

STUDIES OF INORGANIC-ORGANIC INTERFACE FORMATION

A Dissertation

Presented to the Faculty of the Graduate School
of Cornell University

in Partial Fulfillment of the Requirements for the Degree of
Doctor of Philosophy

by

Abhishek Dube

May 2007

© Abhishek Dube 2007

STUDIES OF INORGANIC-ORGANIC INTERFACE FORMATION

Abhishek Dube, Ph.D.

Cornell University 2007

Inorganic-organic interfaces are playing a key role in a number of emerging technologies. For instance, formation of a robust interface between organic and inorganic materials will play an important role in the successful fabrication of “molecular electronic” devices. Self-assembly has been successfully used to make the so-called “bottom contact”. The techniques for “top contact” formation are still not very well developed. Physical vapor deposition of the top contact metal is the most common approach but it has the disadvantages that it causes penetration and disruption of the organic layer. An alternative strategy has been employed here, where a transition metal coordination complex has been used as the interface initiator. The formation of an interface between tetrakisdimethyl(amido)titanium, $\text{Ti}[\text{N}(\text{CH}_3)_2]_4$, and conjugated oligo(phenylene-ethynylene) self-assembled monolayers (SAMs) possessing iso-propylamine terminal functional groups on polycrystalline gold was studied. Extent of reaction and stoichiometry at the interface has also been investigated in this study.

In the ever evolving field of semiconductor manufacturing, organic materials are becoming increasingly important. Copper is now the choice for metallization, and there is a drive to incorporate carbon-containing, possibly

purely organic, and/or porous low dielectric constant (κ) interlayer dielectrics to reduce the capacitive cross talk. The deposition of barrier layers between the Cu and the low- κ materials is challenging, particularly for carbon-containing, porous dielectrics. Self-assembled monolayers have been utilized to modify dielectric surfaces in order to activate them for the deposition of a smooth and conformal diffusion barrier. More specifically, the atomic layer deposition (ALD) of titanium nitride (TiN) employing molecular beams of $\text{Ti}[\text{N}(\text{CH}_3)_2]_4$, and ammonia, NH_3 has been investigated. Deposition was achieved on silane SAMs on SiO_2 possessing different terminations and chain lengths. Nucleation and growth stages were studied by making use of a variety of metrology and surface analysis techniques, namely: ellipsometry, X-ray photoelectron spectroscopy, Rutherford backscattering spectrometry, atomic force microscopy, and scanning transmission electron microscopy. The nature of the interactions between the SAM terminal group and $\text{Ti}[\text{N}(\text{CH}_3)_2]_4$ was pivotal in determining the growth pattern. The growth behavior was also investigated on hyperbranched polymeric films on SiO_2 as well as porous low κ substrates modified using these polymeric films.

BIOGRAPHICAL SKETCH

Abhishek Dube was born on February 22, 1979 in Varanasi (also known as Kashi), India. He spent most of the first 22 years of his life in Kanpur, India; where he attended Kendriya Vidyalaya (IIT-Kanpur) and finished high school in 1997. Inspired by his father, who is a Metallurgical Engineer and a Professor in the Department of Materials and Metallurgical Engineering at the Indian Institute of Technology (IIT-Kanpur), he pursued the B.Tech degree in Chemical Engineering at IIT- Kanpur where he made the Dean's list. During the four years spent at IIT-Kanpur he developed an interest in the area of surfaces and interfaces in materials. He did his senior year dissertation on the degradation of organic light-emitting diodes and decided to further pursue his interests in the materials science world by coming to Cornell University in fall 2001. At Cornell, he was a graduate student in Chemical and Biomolecular Engineering where his work focused on fabricating inorganic-organic interfaces for interconnect and molecular electronics applications. During his stay at Cornell he was awarded the Outstanding Teaching Assistant award for the 2002-03 academic year. He was an Applied Materials Fellow during the 2004-05 academic year. He also received the Best Paper in session award at the Semiconductor Research Corporation Student Symposium held at Cary, NC in October 2006. Abhishek was awarded a PhD in Chemical and Biomolecular Engineering in May 2007. He went on to work as a Process Engineer for IBM in East Fishkill, NY.

*Dedicated to Lord Hanuman,
my parents, and brother*

ACKNOWLEDGEMENTS

First of all, I would like to express utmost gratitude towards my advisor Prof. James R. Engstrom. He has been a great mentor, teacher, and motivator throughout my stay here at Cornell. His constant pursuit of doing precise and careful surface science experiments to come up with the right answers has been instrumental in molding my research career. I am also grateful to my special committee members, Prof. Paulette Clancy and Prof. George G. Malliaras for all their help and support. I would also like to express my gratitude towards Brian Ford and Glenn Swan for their prompt help regarding various issues in the lab.

Within the Engstrom Research Group, I would like to thank Dr. Paul Ma for teaching me how to use the complex scientific equipment in our labs. I am most thankful to Dr. Aravind Killampalli for not only training me on the XPS system but for all the useful and stimulating discussions I had with him. He was a tremendous source of information inside the lab and a great friend outside. I would also like to thank Dr. Todd Schroeder for his input during the formative years of my graduate studies. Amongst the younger members of the group, I would first like to sincerely thank Manish Sharma. He worked with me on numerous projects during the past three years and was a great team member. I really appreciate his help with all the synthesis work he has done to make these projects a success. I would also like to thank Kevin Hughes and Jared Mack for their help during the latter days of my PhD career.

Outside the group, I would like to sincerely thank Dr. Andrew Chadeayne for synthesizing the thiophene ligands and Prof. Peter Wolczanski

for all the useful discussions related to the thiophene manuscript. Peter Ercius and Prof. David Muller are also owed a debt of gratitude for the STEM work. Dr. Mohit Haran, from Prof. Clancy's group, was a great collaborator and friend. I will remember all the interesting discussions we had during the course of my stay at Cornell.

I would also like to thank Kunal, Sourav, Ashish, Devashish, Dhananjay, and Erik, who are all great friends. I have a lot of fond memories of the time I spent with them. A special note of thanks to my childhood friends: Piyush, Sheel, and Jaideep. Our friendship has been great over all these years.

In the end, I would like to express my eternal gratitude towards my parents. They have been a constant source of love, inspiration, and support and whatever I have been able to achieve in life is a result of their blessings. I would also like to thank my younger brother, Nikhil, for being the most caring, loving, and supportive sibling.

I would like to acknowledge the Semiconductor Research Corporation (SRC), National Science Foundation (NSF-NIRT), and the Applied Materials Graduate Fellowship for financial support. The Cornell University experimental facilities: CNF, CCMR, and NBTC and their staff's help are also acknowledged.

TABLE OF CONTENTS

1. Introduction.....	1
1.1 Integrated circuit technology: Current and future trends.....	1
1.1.1 MOSFETs at the scaling limit: Material issues at the front end.....	3
1.1.2 Back end of line (BEOL) technology: Novel interconnect structures.....	8
1.2 Emerging approaches and technologies.....	13
1.2.1 Self-assembly.....	13
1.2.2 Molecular electronics.....	15
1.3 Thin film deposition techniques.....	16
1.3.1 Physical vapor deposition.....	16
1.3.2 Chemical vapor deposition.....	18
1.3.3 Atomic layer deposition.....	20
1.4 Nucleation and morphology of thin films.....	25
1.4.1 Capillarity theory.....	25
1.4.2 Atomistic nucleation.....	29
1.5 Molecular beam techniques.....	31
1.5.1 Beam characterization.....	32
1.5.1.1 Effusive beams.....	32
1.5.1.2 Supersonic beams.....	33
1.5.3 Thin film deposition employing molecular beams.....	39
1.6 Analytical techniques.....	40

1.6.1	Ellipsometry.....	40
1.6.2	X-ray photoelectron spectroscopy.....	43
1.6.3	Rutherford backscattering spectrometry.....	46
1.6.4	Atomic force microscopy.....	48
1.6.5	Scanning transmission electron microscopy.....	50
1.6.6	Electron energy loss spectroscopy.....	51
1.7	References.....	53
2.	Experimental methods.....	56
2.1	Inorganic-organic interfaces for molecular electronics.....	56
2.1.1	Description of the vacuum system and gas delivery setup..	56
2.1.2	Sample preparation.....	60
2.1.2.1	Materials.....	60
2.1.2.2	Synthesis of thiophene ligands.....	60
2.1.2.3	Preparation of self-assembled monolayers.....	65
2.1.3	Characterization of self-assembled monolayers.....	65
2.1.3.1	Contact angle measurements.....	66
2.1.3.2	Ellipsometry.....	66
2.1.3.3	X-ray photoelectron spectroscopy.....	66
2.1.4	Adsorption kinetics experiments.....	67
2.1.4.1	Experimental apparatus.....	67
2.1.4.2	Experimental procedures.....	67
2.2	TiN atomic layer deposition on SiO ₂ and modified SiO ₂	69
2.2.1	Description of the thin film deposition system.....	69
2.2.2	Beam generation and characterization.....	75
2.2.3	Sample preparation.....	77
2.2.3.1	Chemical oxide.....	78

2.2.3.2 SAM synthesis.....	78
2.2.3.2.1 Linear SAMs.....	79
2.2.3.2.2 Branched SAMs.....	80
2.2.3.2.3 SAM characterization.....	81
2.2.3.2.3.1 XPS.....	82
2.2.3.2.3.2 AFM	83
2.2.4 Deposition and characterization of TiN thin films.....	83
2.2.5 Deposition and characterization of TiN thin films on hyper- branched polymeric films and low κ dielectric substrates.....	86
2.2.5.1 Hyperbranched polymers.....	86
2.2.5.2 Low κ dielectric substrates.....	87
2.3 References.....	88
3. Covalent attachment of a transition metal coordination complex to functionalized oligo(phenylene-ethynylene) self-assembled monolayers.....	90
3.1 Overview.....	90
3.2 Introduction.....	91
3.3 Experimental methods.....	95
3.4 Results and discussion.....	96
3.4.1 Characterization of the SAMs.....	96
3.4.2 Reaction of $\text{Ti}[\text{N}(\text{CH}_3)_2]_4$ with the SAMs.....	104
3.5 Conclusions.....	136
3.6 References.....	138

4. Nucleation and growth during TiN atomic layer deposition on silicon dioxide and silicon dioxide modified using interfacial organic layers.....	145
4.1 Overview.....	145
4.2 Introduction.....	146
4.3 Experimental procedures.....	150
4.3.1 Sample preparation.....	150
4.3.2 TiN ALD process.....	151
4.3.3 Characterization methods.....	153
4.3.3.1 Ellipsometry.....	153
4.3.3.2 Atomic force microscopy.....	153
4.3.3.3 X-ray photoelectron spectroscopy.....	155
4.3.3.4 Rutherford backscattering spectrometry.....	155
4.3.3.5 Scanning transmission electron microscopy.....	156
4.4 Results and discussion.....	156
4.4.1 Characterization of the SAMs.....	156
4.4.2 TiN ALD on SiO ₂ and modified SiO ₂	156
4.5 Conclusions.....	211
4.6 References.....	213
5. Atomic layer deposition of TiN on hyperbranched polymeric films and low κ dielectric substrates.....	219
5.1 Overview.....	219
5.2 Introduction.....	220
5.3 Results and discussion.....	226
5.3.1 Characterization of poly-G films.....	226
5.3.2 TiN ALD: Film growth and characterization.....	226

5.4	Conclusions.....	261
5.5	References.....	263
6.	Summary and future work.....	266
7.	Appendices.....	272
7.1	Appendix A: Vapor pressure curve for $\text{Ti}[\text{N}(\text{CH}_3)_2]_4$	272
7.2	Appendix B: ARXPS curve fitting results.....	273
7.3	Appendix C: RBS simulation methodology.....	274

LIST OF FIGURES

Figure 1-1	Feature size vs. time in silicon ICs	2
Figure 1-2	MOSFET schematic.....	4
Figure 1-3	SEM image for cross sectional view of a multilayer interconnect structure.....	10
Figure 1-4	Schematic representation of a self-assembled monolayer.....	14
Figure 1-5	Schematic representation of atomic layer deposition.....	22
Figure 1-6	Cross-sectional TEM image of a MOSFET with layers deposited using atomic layer deposition.....	23
Figure 1-7	Illustration demonstrating the interfacial energies (surface tensions) and transport phenomena during the growth of thin films.....	27
Figure 1-8	Illustration of three thin film growth modes.....	28
Figure 1-9	Illustration of the surface processes and characteristic energies relevant in nucleation and film growth.....	30
Figure 1-10	Schematic representation of effusive and supersonic molecular beam systems.....	35
Figure 1-11	Illustration of the structures formed during a supersonic expansion.	38
Figure 1-12	Schematic of an ellipsometry setup.....	41
Figure 1-13	Angle-resolved XPS schematic.....	45
Figure 1-14	Typical schematic of an atomic force microscope.....	49
Figure 2-1	Schematic drawing of molecular beam scattering system with X-ray photoelectron spectroscopy capability.....	57

Figure 2-2	Schematic for synthesis of the thiophene ligands.....	61
Figure 2-3	AUTOCAD™ rendering of the thin film deposition system employed for the atomic layer deposition experiments.....	70
Figure 2-4	Original schematics of the thin film deposition system.....	71
Figure 2-5	Schematic of Ti[N(CH ₃) ₂] ₄ delivery setup.....	76
Figure 2-6	Schematic illustrating the technique of producing multiple areas of different exposure times on a single sample.....	85
Figure 3-1	Integrated peak areas as a function of take-off angle for the 1P (filled symbols) and 2P SAMs (open symbols) on polycrystalline Au for the (a) Au(4f), (b) S(2p) and (c) C(1s) features from XPS at T _s = 30 °C.....	100
Figure 3-2	XP spectra of the Ti(2p) feature for clean Au and 2P SAM surfaces, both exposed to Ti[N(CH ₃) ₂] ₄ at T _s = 30 °C.....	106
Figure 3-3	Coverage-exposure relationships, deduced from XPS, for the adsorption of Ti[N(CH ₃) ₂] ₄ on (a) the 1P SAM, and (b) the 2P SAM, both for T _s = -50 and 30 °C.....	108
Figure 3-4	Integrated peak areas for the Ti(2p) region as a function of take-off angle for a saturation exposure of the 1P (filled symbols) and 2P SAMs (open symbols) to Ti[N(CH ₃) ₂] ₄ at T _s = 30 °C.....	111
Figure 3-5	Integrated peak areas as a function of take-off angle for the 1P (filled symbols) and 2P SAMs (open symbols) subsequent to saturation exposures to Ti[N(CH ₃) ₂] ₄ at T _s = 30 °C for the (a) Au(4f), (b) S(2p) and (c) C(1s) features from XPS.....	113
Figure 3-6	Relationship between the concentration of Ti in the saturated adlayers and the concentration of molecules (and functional endgroups) in the self-assembled monolayers.....	119

Figure 3-7	Integrated peak areas as a function of take-off angle for the 4-aminothiophenol SAM on polycrystalline Au, prior (open symbols) and subsequent (closed symbols) to a saturation exposure to $\text{Ti}[\text{N}(\text{CH}_3)_2]_4$ at $T_s = 30\text{ }^\circ\text{C}$ for the (a) Au(4f), (b) S(2p) and (c) C(1s) features from XPS.....	124
Figure 3-8	Integrated peak area for the Ti(2p) region as a function of take-off angle for a saturation exposure of the 4-aminothiophenol SAM to $\text{Ti}[\text{N}(\text{CH}_3)_2]_4$ at $T_s = 30\text{ }^\circ\text{C}$	128
Figure 3-9	Possible reaction pathways for $\text{Ti}[\text{N}(\text{CH}_3)_2]_4$ reacting with the 1P and 2P SAM.....	134
Figure 4-1	Schematic representation of the atomic layer deposition process employing modulated molecular beams.....	154
Figure 4-2	(a) Deposited thickness per cycle vs. exposure time to $\text{Ti}[\text{N}(\text{CH}_3)_2]_4$ for ALD of TiN on two surfaces: chemical oxide, SiO_2 ($T_s = 167$ and $207\text{ }^\circ\text{C}$), and SiO_2 modified with a $-\text{NH}_2$ terminated SAM ($T_s = 167\text{ }^\circ\text{C}$, Gen-1-3C). (b) Deposited thickness per cycle as a function of substrate temperature for the ALD of TiN on chemical oxide, SiO_2	157
Figure 4-3	(a) TiN thin film thicknesses, measured using ellipsometry, as a function of the number of reactant cycles for ALD on several substrates: clean chemical oxide, SiO_2 , and SiO_2 modified by four different SAMs. (b) TiN thin film thicknesses, measured using ellipsometry, as a function of the number of reactant cycles for ALD SiO_2 modified by four different SAMs.....	161

Figure 4-4	(a) Atomic force microscope images for TiN ALD at 167 °C on SiO ₂ . In each case the field of view is 0.5 μm × 0.5 μm. The images presented are for the untreated SiO ₂ as well as TiN films which have been grown for 30, 60, 80, 90, and 150 cycles. (b) Select cross sectional line scans which have been offset by the ellipsometric thickness values; at 0, 30, 80, 90, and 150 cycles and depict the evolution of RMS roughness.....	164
Figure 4-5	TiN thin film thickness, measured using ellipsometry, as a function of the number of reactant cycles for ALD on several substrates: clean chemical oxide, SiO ₂ , and SiO ₂ modified by four different SAMs.....	168
Figure 4-6	Growth attenuation factor as a function of thickness of the SAM (T _s = 167 °C). Plotted are the results for SAMs possessing either reactive endgroups (-OH or -NH ₂ , open symbols) or unreactive endgroups (-CH ₃ or CF ₃ , filled symbols).....	170
Figure 4-7	RB spectrum for a 190 Å thick TiN film on a Gen-1-3C SAM modified SiO ₂ substrate.....	171
Figure 4-8	Comparison of the measured ellipsometric and modeled RBS thicknesses for SiO ₂ and the SAMs.....	173
Figure 4-9	Growth attenuation factor as a function of thickness of the SAM (T _s = at 167 and 207 °C).....	174
Figure 4-10	XP spectra, after a Shirley background subtraction, as a function of number of cycles for TiN ALD on the -NH ₂ terminated branched Gen-1-3C SAM at T _s = 167 °C for the (a)Ti(2p), and (b)Si(2p) features.....	176

- Figure 4-11** (a) Atomic force microscope images for TiN ALD at 167 °C on Gen-1-3C SAM. In each case the field of view is 0.5 μm × 0.5 μm. The images presented are for the SAM as well as films which have been grown for 50, 100, 200, and 300 cycles. (b) Selected cross-sectional line scans which have been offset by the ellipsometric thickness values, at 0, 50, 150, and 300 cycles to depict the evolution of RMS roughness.....179
- Figure 4-12** XP spectra, after a Shirley background subtraction after 300 cycles for TiN ALD on the -CH₃ terminated branched OTS and TTS SAM at T_s = 167 °C for the (a) Ti (2p), and (b) Si (2p) features.....182
- Figure 4-13** (a) Atomic force microscope images for TiN ALD at 167 °C on TTS SAM. In each case the field of view is 0.5 μm × 0.5 μm. The images presented are for the SAM as well as TiN films which have been grown for 50, 150, 200, and 300 cycles. (b) Selected cross sectional line scans which have been offset by the ellipsometric thickness values, at 0, 50, 100, and 200 cycles and depict the evolution of RMS roughness.....185
- Figure 4-14** (a) Atomic force microscope images for TiN ALD at 167 °C on HMDS SAM. In each case the field of view is 0.5 μm × 0.5 μm. The images presented are for the SAM as well as TiN films which have been grown for 50, 100, 200, and 300 cycles. (b) Selected cross sectional line scans which have been offset by the ellipsometric thickness values, at 0, 50, 100, 200, and 300 cycles and depict the evolution of RMS roughness.....189

Figure 4-15	(a) Atomic force microscope images for TiN ALD at 167 °C on the -OH SAM. In each case the field of view is 0.5 μm × 0.5 μm. The images presented are for the SAM as well as TiN films which have been grown for 50, 100, 200, and 300 cycles. (b) Selected cross sectional line scans which have been offset by the ellipsometric thickness values, at 0, 50, 100, 200, and 300 cycles and depict the evolution of RMS roughness.....	192
Figure 4-16	AFM determined root-mean-square (RMS) roughness as a function of measured ellipsometric thickness for TiN ALD.....	196
Figure 4-17	Evolution of the one dimensional power spectral density (1DPSD) as a function of spatial frequency.....	198
Figure 4-18	Correlation length ξ (in μm) as a function of TiN film thickness ($T_s = 167$ °C). ξ is obtained from the intersection of the self-affine region and the plateau region in the 1DPSD spectra for SiO ₂ (open circles), Gen-1-3C SAM, -OH SAM, HMDS, and TTS.....	200
Figure 4-19	Correlation length ξ (in Å) as a function of TiN RMS roughness ($T_s = 167$ °C). ξ is obtained from the intersection of the self-affine region and the plateau region in the 1DPSD spectra for SiO ₂ (open circles), Gen-1-3C SAM, -OH SAM, HMDS, and TTS.....	201
Figure 4-20	(a) Roughness exponent α plotted as a function of TiN film thickness, for the TTS and HMDS SAMs ($T_s = 167$ °C). α is extracted from the slope of the self-affine portion of the 1DPSD spectrum. (b) Roughness exponent α plotted as a function of TiN film thickness.....	202

Figure 4-21	Dark field scanning transmission electron micrograph for a film grown on Gen-1-3C SAM for 300 cycles ($T_s = 167\text{ }^\circ\text{C}$). High resolution electron energy loss spectra for carbon, titanium, and silicon. Plotted are the intensities as a function of distance from the surface.....	207
Figure 4-22	Growth attenuation factor plotted as a function of Ti saturation densities after room temperature saturation exposures to a 2.07 eV $\text{Ti}[\text{N}(\text{CH}_3)_2]_4$ beam.....	210
Figure 5-1	Typical schematic for a hyperbranched polymer film.....	222
Figure 5-2	Measured ellipsometric thickness for poly-G films on SiO_2 as a function of deposition time in glycidol.....	227
Figure 5-3	TiN ellipsometric thickness as a function of ALD cycles ($T_s = 167\text{ }^\circ\text{C}$) on SiO_2 and poly-G films of varying thickness.....	228
Figure 5-4	Ti (2p) XP spectra after 300 ALD cycles on poly-G films (15, 30, and 60 min deposition time on SiO_2).....	230
Figure 5-5	Si (2p) XP spectra after 300 ALD cycles on poly-G films (15, 30, and 60 min deposition time on SiO_2).....	231
Figure 5-6	N (1s) XP spectra after 300 ALD cycles on poly-G films (15, 30, and 60 min deposition time on SiO_2).....	233
Figure 5-7	Atomic force microscope images for TiN ALD at $167\text{ }^\circ\text{C}$ on 15 min poly-G films. In each case the field of view is $0.5\text{ }\mu\text{m} \times 0.5\text{ }\mu\text{m}$. The images presented are for the unreacted poly-G IOL as well as TiN films which have been grown for 150, 200, 250, and 300 cycles.	235
Figure 5-8	Atomic force microscope images for TiN ALD at $167\text{ }^\circ\text{C}$ on 60 min poly-G films. In each case the field of view is $0.5\text{ }\mu\text{m} \times 0.5$	

	μm . The images presented are for the unreacted poly-G IOL as well as TiN films which have been grown for 200, 250, and 300 cycles.....	236
Figure 5-9	AFM determined root-mean-square (RMS) roughness as a function of measured ellipsometric thickness for TiN ALD at $T_s = 167^\circ\text{C}$ on poly-G films.....	237
Figure 5-10	Roughness exponent α plotted a a function of TiN film thickness for growth on the poly-G substrates.....	239
Figure 5-11	Correlation length plotted a a function of TiN film thickness for growth on the poly-G substrates.....	240
Figure 5-12	Dark and bright field scanning transmission electron micrographs (STEM) for a 160 \AA thick TiN film grown on 15 min poly-G IOL at 167°C	242
Figure 5-13	High resolution electron energy loss spectra (HREELS) for carbon, titanium, and silicon. Plotted are the intensities as a function of distance from the SiO_2 / Ti interface.....	243
Figure 5-14	Ellipsometric thickness as a function of ALD cycles for TiN deposition on untreated low κ surface at $T_s = 167^\circ\text{C}$	245
Figure 5-15	Atomic force microscope images for TiN ALD at 167°C on untreated low κ films. In each case the field of view is $0.5 \mu\text{m} \times 0.5 \mu\text{m}$. The images presented are for the unreacted surface as well as TiN films which have been grown for 50, 150, and 300 cycles.....	247
Figure 5-16	RB spectrum for a 420 \AA thick (300 ALD cycle) TiN film on an untreated low κ substrate.....	249

Figure 5-17	Bright and dark field scanning transmission electron micrographs (STEM) for a 280 Å thick TiN film grown on untreated low κ at 167 °C.....	251
Figure 5-18	High resolution electron energy loss spectra (HREELS) for titanium at three different positions on the specimen.....	252
Figure 5-19	Ellipsometric thickness as a function of ALD cycles for TiN deposition on 15 min poly-G treated low κ surface at $T_s = 167$ °C.....	253
Figure 5-20	Atomic force microscope images for TiN ALD at 167 °C on poly-G treated low κ films. In each case the field of view is 0.5 $\mu\text{m} \times$ 0.5 μm . The images presented are for the clean poly-G IOL modified surface as well as TiN films which have been grown for 100,150, and 300 cycles. Also included is the RMS roughness vs. thickness data.....	256
Figure 5-21	RB spectrum for a 240 Å thick (300 ALD cycle) TiN film on an poly-g (15 min) treated low κ substrate.....	257
Figure 5-22	Bright and dark field scanning transmission electron micrographs (STEM) for a 240 Å thick TiN film grown on poly-G treated low κ at 167 °C. Also shown is the HREELS data for Ti, Si, and C.....	258
Figure 5-23	Roughness exponent α plotted as a function of TiN film thickness, for the untreated and 15 min poly-G treated low κ substrates ($T_s = 167$ °C).....	259
Figure 5-24	Correlation length ξ as a function of TiN thickness ($T_s = 167$ °C) for films deposited on untreated and 15 min poly-G treated low κ substrates.....	260

Figure 7-1 Vapor pressure curve for $\text{Ti}[\text{N}(\text{CH}_3)_2]_4$272

Figure 7-2 Example RB spectrum and simulation carried out with RUMP.....277

LIST OF TABLES

Table 1-1	ITRS data regarding critical device dimensions	6
Table 3-1	Properties of self-assembled monolayers.....	97
Table 7-1	Parameters from fits to ARXPS data in chapter 3.....	273

LIST OF ABBREVIATIONS

AACVD	aerosol-assisted CVD
AFM	atomic force microscopy
ALD	atomic layer deposition
APCVD	atmospheric pressure CVD
ARXPS	angle-resolved XPS
BEOL	back end of the line
CMOS	complementary metal-oxide-semiconductor
CVD	chemical vapor deposition
DLICVD	direct liquid injection CVD
DRAM	dynamic random access memory
EELS	electron energy loss spectroscopy
eV	electron volt
FET	field effect transistor
FEOL	front end of the line
FOTS	tridecafluoro-1,1,2,2-tetrahydrooctyltrichlorosilane
HMDS	hexamethyldisilazane
HOMO	highest occupied molecular orbital
IC	integrated circuit
IGFET	insulated gate field effect transistors
IOL	interfacial organic layer
ITRS	international technology roadmap for semiconductors
IUPAC	international union of pure and applied chemistry
LPCVD	low pressure CVD

LUMO	lowest unoccupied molecular orbital
MBE	molecular beam epitaxy
MOCVD	metal-organic CVD
MOSFET	Metal oxide semiconductor field effect transistor
OFG	organic functional group
OTS	octadecyltrichlorosilane
PECVD	plasma enhanced CVD
PSD	power spectral density
PVD	physical vapor deposition
QMS	quadrupole mass spectrometry
RBS	Rutherford backscattering spectrometry
RC	resistance-capacitance
RPECVD	remote plasma-enhanced CVD
SAM	self-assembled monolayer
SEM	scanning electron microscopy
STEM	scanning transmission electron microscopy
TEM	transmission electron microscopy
TOF	time of flight
TTS	triacontyltrichlorosilane
UHV	ultra-high vacuum
UHVCVD	ultra-high vacuum CVD
XPS	x-ray photoelectron spectroscopy

LIST OF SYMBOLS

α	roughness exponent
	function or parameter characterizing the velocity distribution of a molecular beam
$\acute{\alpha}$	growth rate attenuation factor
β	growth exponent
c	stream velocity of a molecular beam
$\langle C_p \rangle$	mole fraction mean heat capacity of a mixture of gases
C_p	specific heat capacity at constant pressure
C_v	specific heat capacity at constant volume
d	nozzle orifice diameter
E_D	activation energy for desorption
E_{i^*}	critical cluster dissociation energy
E_i	incident kinetic energy
E_S	activation energy for surface diffusion
F	incident flux of molecules in a supersonic beam
γ	interfacial energy
	ratio of C_p to C_v
ΔG	Gibbs free energy
λ	mean free path of a molecule
κ	dielectric constant
Kn	Knudsen number
$\langle m \rangle$	mole fraction mean mass of a mixture of gases
m	molecular weight

Ma	Mach number
P_0	stagnation pressure
P_n	nozzle pressure or stagnation pressure
T_n	nozzle temperature
T_s	substrate temperature
v	velocity
w	root mean square roughness
ξ	correlation length

1. Introduction

1.1 Integrated circuit technology: Current and future trends

For more than 30 years, the integrated circuit (IC) industry has followed a steady path of constantly shrinking device geometries. This strategy has been driven by the increased performance that smaller devices make possible and the increased functionality that these chips provide. Together, these performance and functionality improvements have resulted in a history of new technology generations every two to three years, commonly referred to as “Moore’s Law” [1]. Each new generation has approximately doubled logic circuit density and increased performance by about 40% while quadrupling memory capacity. The increase in components per chip comes from three key factors first identified by Gordon Moore. The factor of two in component density comes from a $\sqrt{2}$ shrink in each lithography dimension. An additional factor of $\sqrt{2}$ comes from an increase in chip area and a final factor of $\sqrt{2}$ from device and circuit cleverness, providing the overall quadrupling in chip capacity. The apparent ease with which all this has happened has led to an expectation that faster and more powerful chips will continue to be introduced on the same schedule for the foreseeable future. In fact, the semiconductor industry itself has developed a “roadmap” based on exactly this idea. The International Technology Roadmap for Semiconductors (ITRS) [2] now extends this device scaling and increased functionality scenario to the year 2014, upto which point minimum feature sizes are projected to scale according to Moore’s law and chips with components are expected to be available. Figure 1-1 summarizes the trends in feature size over time.

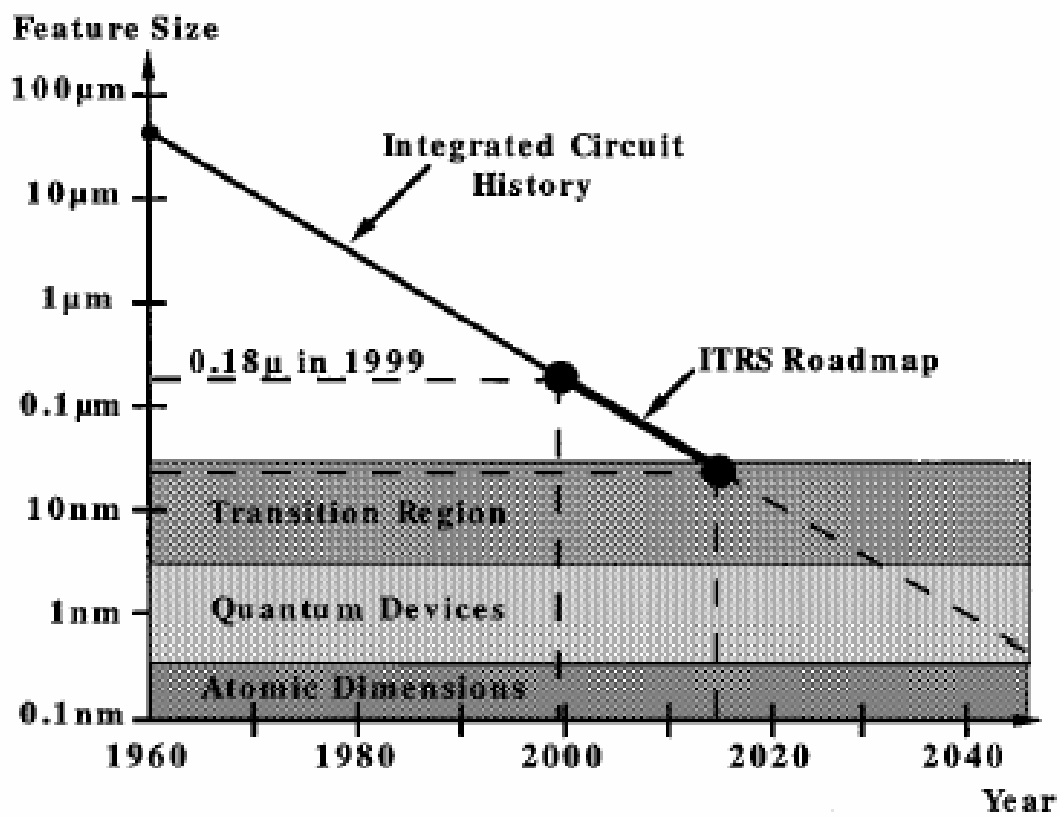


Figure 1-1: Feature size vs. time in silicon ICs (source: www.itrs.net).

Progress has been achieved using the same basic switching element (the metal–oxide–semiconductor [MOS] transistor), the same circuit topology (complimentary metal–oxide–semiconductor [CMOS]), and with a limited number of materials (Si, SiO₂, Cu, Si₃N₄, TiSi₂, TiN, TaN, and W, primarily). Over the past 40 years, progress in these areas has been straightforward in many respects in the sense that no fundamentally new inventions have been needed. Obviously, manufacturing practices have improved. However, the device structures of 30–40 years ago and the manufacturing processes used then are quite recognizable in today’s IC industry. If the ITRS is a correct predictor of the next 15 years, superficially, much will remain the same as it has for the past 30–40 years. However, there are many reasons to believe that continued device scaling will not be as straightforward in the future as it has been in the past. Practical and /or fundamental limits are being approached and substantial changes to device technologies and structures are going to be required. While “inventions” and new materials have largely not been needed for the past 30 years, they surely will be needed over the next 15 years. This period will likely be the most challenging that the IC industry has faced because it is likely that during this period the extendability of Moore’s Law will really be tested. In fact, without new materials and inventions, Moore’s Law can end within this period. It is likely, however, that solutions will be found to the difficult problems that lie ahead.

1.1.1 MOSFET at the scaling limit: Material issues at the front end

Figure 1-2 schematically illustrates the basic metal–oxide–semiconductor field-effect transistor (MOSFET) device used in today’s chips.

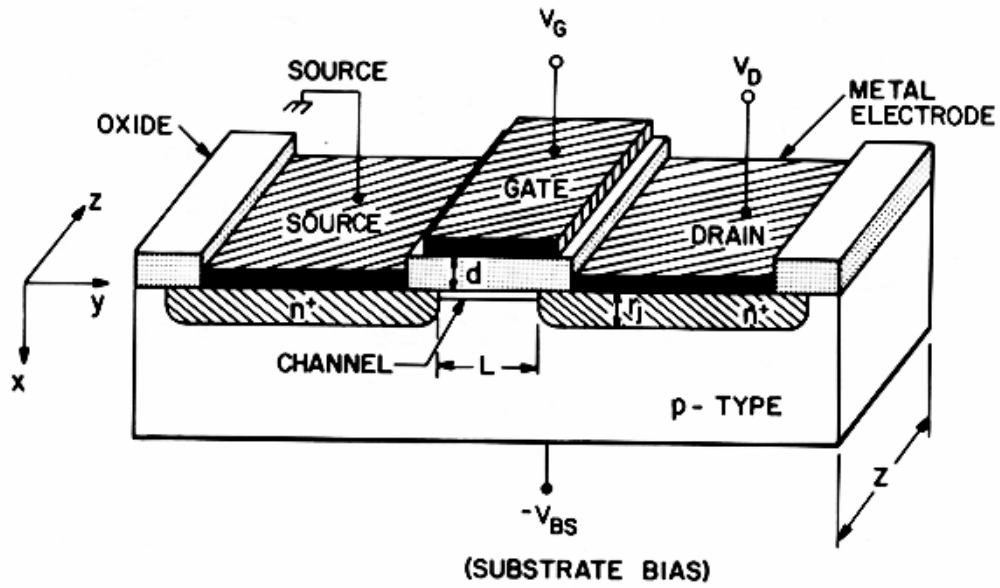


Figure 1-2: A schematic diagram of a metal oxide semiconductor field effect transistor (MOSFET). The substrate is usually single crystal silicon, source, drain and gate electrodes are metals, the gate oxide is currently silicon dioxide the structure is built through a sequence of lithography and deposition steps (source: Ref. [3])

These transistors are formed as a “sandwich” consisting of a semiconductor layer, usually a slice, or wafer, from a single crystal of silicon; a layer of silicon dioxide (the oxide) and a layer of metal. These layers are patterned in a manner which permits transistors to be formed in the semiconductor material (the “substrate”). Silicon dioxide is a very good insulator, so only a very thin layer, currently 1.6 nm thick, is required. These transistors use polycrystalline silicon (poly) for the gate electrode. Polysilicon gate FET's have replaced virtually all of the older devices using metal gates in large scale integrated circuits. (Both metal and polysilicon FET's are sometimes referred to as IGFET's --- insulated gate field effect transistors, since the silicon dioxide under the gate is an insulator. Electrical charge, or current, can flow from the source to the drain depending on the charge applied to the gate region. The semiconductor material in the source and drain regions is “doped” with a different type of material than in the region under the gate, so an NPN or PNP type structure exists between the source and drain region of a MOSFET. The source is the terminal, or node, which acts as the source of charge carriers; charge carriers leave the source and travel to the drain. The area under the gate oxide is called the “channel”. The MOSFET can operate as a very efficient switch for current flowing between the source and drain region. There are no serious competitors to replace this device in the foreseeable future. The basic structure will continue to evolve to allow continued performance improvements, but fundamental changes are unlikely in the next 15 years. However there are challenges which need to be addressed soon as per the ITRS roadmap. Selected data from the roadmap is shown in Table 1-1. The first issue is the gate dielectric thickness.

Table 1-1: Selected data from ITRS regarding critical device dimensions
(adapted from: Ref. [2])

Year of 1st DRAM Shipment	1997	1999	2002	2005	2008	2011	2014
Minimum Feature Size	250 nm	180 nm	130 nm	100 nm	70 nm	50 nm	35 nm
Isolated Gate Length	-	100 nm	70 nm	50 nm	35 nm	25 nm	18 nm
DRAM Bits/Chip	256M	1G	(3G)	8G	(24G)	64G	(192G)
DRAM Chip Size (mm ²)	280	400	460	530	630	710	860
Equivalent Physical Gate Oxide Thickness (nm)	3-5	1.9-2.5	1.5-1.9	1.0-1.5	0.8-1.2	0.6-0.8	0.5-0.6
Dielectric Constant of DRAM Capacitor		22	50	250	700	1500	1500
Max Gate Electrode Resistivity ($\mu\Omega$ cm)		60	43	33	23	16	11

By purely geometric arguments, the gate insulator in a MOSFET needs to be thin compared to the device channel length in order for the gate to exert dominant control over the channel potential. This avoids “short channel effects,” which are largely the result of the drain electric field penetrating throughout the channel and influencing the channel potential at the source side of the device. Practical MOSFET structures generally require the gate dielectric thickness to be a few percent of the channel length. Oxides thinner than about 1.0–1.5 nm conduct direct-tunneling currents too large for most IC applications at the supply voltages listed in the table. A “higher κ ” material system will allow a physically thicker dielectric layer to have an “equivalent SiO_2 thickness” corresponding to the entries in Table 1-1. Higher κ materials are also needed for dynamic random access memory (DRAM) storage capacitors. However, the requirements are quite different in this application because only a charge storage function is required. The two-dimensional (2-D) effects in a logic device that arise because of the difference in permittivity between the silicon channel and the gate insulator make the dielectric requirements very different in logic devices [4]. Generally, the highest dielectric constant possible is needed for DRAM capacitors as shown in Table 1-1, whereas materials with dielectric constants up to 30 or so are needed for active transistor gate insulators. The gate electrode itself also presents some significant challenges. Polysilicon has been used for more than 25 years as the gate electrode material. However, decreasing its resistivity, as shown in Table 1-1, implies increasing the doping levels in the polysilicon, which minimizes the resistivity of the gate electrode and helps avoid polysilicon depletion effects. But this approach is limited by dopant solubility limits and by dopant out-diffusion from the poly through the thin gate dielectric and into the silicon. This latter problem is

particularly acute with P gates because boron diffuses rapidly through SiO₂. The likely solution is again new materials—metal gate electrodes. But there are no known materials solutions that are known to work in manufacturing. All these issues are associated with the creation of transistors on a silicon die commonly called the Front End of the Line (FEOL) in the semiconductor industry. An important, exploratory research area trying to address some of these issues deals with the use of devices constructed at the molecular level, a field popularly known as Molecular Electronics.

1.1.2 Back end of line (BEOL) technology: Novel interconnect structures

There is constant drive to make computers work faster. The most direct way to increase the speed of an IC is to pack in more transistors that are smaller and faster. For the last two decades, device feature size has decreased from 1 μm down to 65 nm, increasing the working frequency of microprocessors from 66 MHz to 4 GHz. However, not all IC components work faster when decreased in size. While continuous shrinking makes transistors faster, it makes interconnections between transistors work slower due to signal delay. The wiring of these transistors to the outside world is also referred to as the Back End of the Line (BEOL). Any interconnection can be represented as a chain of resistors (wires) and capacitors (insulating dielectric between wires). A good figure of merit to characterize interconnects is resistance-capacitance (RC), which is a unit of time. A signal propagating through the interconnection experiences RC delay. Shrinking the cross-section of a wire increases its resistance and bringing wires closer together increases capacitance between the wires. As a result, RC delay increases as device size decreases. It is predicted

that RC delay will soon exceed transistor speed, becoming a serious limitation to performance improvement. Since scaling down dimensions works against RC delay, the only way to bring down resistance and capacitance is to use other metals (with lower resistivity) and dielectrics (with lower dielectric constant) instead of the conventional Al and SiO₂, respectively. The replacement of Al with Cu (36% decrease in resistivity) was the first step taken to address RC delay. The best conductor, Ag, has a resistivity only 6% lower than that of Cu. Considerable effort was put in to successfully integrate Cu into IC manufacturing. Figure 1-3 shows scanning electron micrograph (SEM) images of such Cu-based typical interconnect structures. Changing materials in IC processing requires intensive research, development, and integration engineering.

Replacing SiO₂ has not been a straightforward process and is a major undertaking in materials design and engineering. In principle, any material with a dielectric constant, κ , lower than 4.2 is of interest (so called low κ dielectrics), but the κ value is only one of many required properties. There are two possible ways of reducing κ : decreasing dipole strength or the number of dipoles [5]. This means using materials with chemical bonds of lower polarizability than Si-O or lower density materials. The two methods can be combined to achieve even lower κ values. The IC industry has already moved to certain low κ materials, where some silica Si-O bonds have been replaced with less polar Si-F or Si-C bonds. A more fundamental reduction can be achieved by using virtually all nonpolar bonds, such as C-C or C-H, for example, in materials like organic polymers.

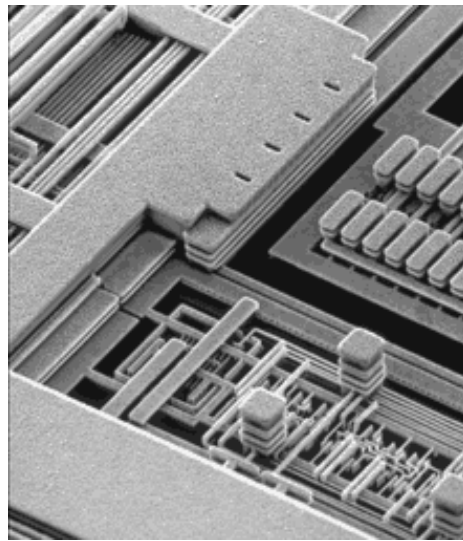
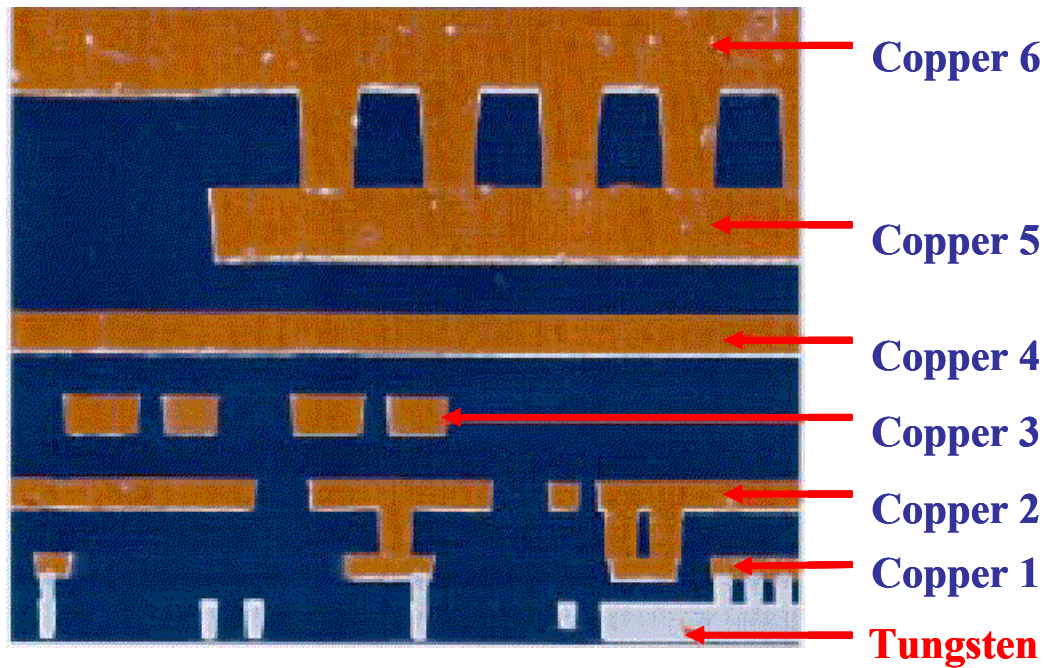


Figure 1-3: Scanning electron micrographs (SEM) of two Cu interconnection schemes. The top SEM image shows a cross-sectional view of a multilayer interconnect structure. In the lower SEM, the dielectric material has been etched away to show only the Cu metal in the interconnect structure (source: IBM)

The density of a material can be decreased by increasing the free volume through rearranging the material structure or introducing porosity. Porosity can be constitutive or subtractive. Constitutive porosity refers to the self organization of a material. After manufacturing, such a material is porous without any additional treatment. Constitutive porosity is relatively low (usually less than 15%) and pore sizes are ~ 1 nm in diameter. According to the International Union of Pure and Applied Chemistry (IUPAC) classification, pores less than 2 nm are denoted ‘micropores’. Subtractive porosity involves selective removal of part of the material. This can be achieved via an artificially added ingredient (e.g., a thermally degradable substance called a “porogen”, which is removed by annealing to leave behind pores) or by selective etching (e.g. Si-O bonds in SiOCH materials removed by HF). Subtractive porosity can be as high as 90% and pore sizes vary from 2 nm to tens of nanometers (pores larger than 2 nm are denoted ‘mesopores’). A mesoporous organic polymer can combine all three approaches: low polarizability, inherent free volume (constitutive porosity), and use of porogens (subtractive porosity). The ultimate case would be the use of air as a dielectric with the lowest possible κ of 1, so called ‘air gaps’.

In IC manufacturing, low κ materials are used as thin films of around 500 nm [5]. There are two main methods of deposition: spin coating and chemical vapor deposition (CVD). Spin-coated films can be constitutively as well as subtractively porous. Low temperatures allow the introduction of thermally degradable porogens into the mixture, which can be removed by a thermal anneal step. The anneal step also induces chemical cross-linking, producing a rigid film structure regardless of subtractive or constitutive porosity. Typically, CVD films are constitutively porous. The introduction of a

porogen is possible, but it is complicated by the fact that deposition usually occurs at elevated temperatures ($\sim 300^\circ\text{C}$) and is often enhanced by plasma. A more detailed discussion of porous low κ materials and their integration in traditional semiconductor manufacturing is given in chapter 5.

Cu has been shown to diffuse rapidly into Si and SiO_2 forming copper silicides. These Cu silicides then act as gettering sites for charges and severely hinder the performance of the device. Also, with the ever decreasing amount of material present in the metal lines of the future interconnects, diffusion of Cu into the dielectric material could also result in failure of the metal lines [6]. A barrier layer is required to prevent Cu diffusion. The main requirements for the barrier layer material are: 1) The ability to prevent the diffusion of Cu into the surrounding dielectric, 2) a relatively low electrical resistivity since the effective resistivity of a metal line is a combination of the resistivity of the metal plus the barrier layer material and 3) interactions with Cu which permits good adhesion and nucleation properties. To this end, transition metals and their nitrides have emerged as the most promising materials for this application, namely, Ti/TiN and Ta/TaN. Furthermore, at the same thickness, the nitrides have been found to be better diffusion barriers compared to pure metals. In previous studies, TiN has been found to prevent Cu diffusion for up to 2 hours at a temperature of 575°C [7] whereas TaN films have been shown to retain barrier properties for a 5 minute rapid thermal anneal at 700°C [8]. As a result, TiN and TaN deposition has also received much attention. The traditional method of deposition has been reactive plasma sputtering in a N_2 atmosphere. More recently, CVD of TiN using TiCl_4 and NH_3 as reactants has shown promise for depositing conformal films in high aspect ratio trenches [9]. However the temperature required ($> 500^\circ\text{C}$) for this reaction is too high for

subsequent processing steps. Organo-metallic precursors of Ti and Ta have recently been shown to be good candidates for use in low temperature conformal deposition of TiN [10] and TaN [11].

1.2 Emerging approaches and technologies

1.2.1 Self-assembly

Conventional microelectronic technologies have involved “top-down” fabrication approaches that make use of conventional lithography, deposition, and etch steps to build nanostructures. More recently, attention has shifted to the so-called “bottom-up”, or self-assembly, approaches where one starts from individual atoms and combines them into complex units of large variety and functionality. This approach can lead to the fabrication of so-called “molecular electronic” devices where individual molecules are used as active components. Self-assembly, in a general sense, might be defined as the spontaneous formation of complex hierarchical structures from pre-designed building blocks, typically involving multiple energy scales and multiple degrees of freedom. Self-assembly is also a very general principle in nature, as seen in the formation of, e.g., membranes from lipid molecules, or the living cell as probably the most important paradigm [12]. Self-assembled monolayers (SAMs) are ordered molecular assemblies that are formed spontaneously by the adsorption of a surfactant with a specific affinity of its headgroup to a substrate. Figure 1-4 shows a schematic, including the constituents of a SAM-molecule (headgroup, chain or backbone, endgroup).

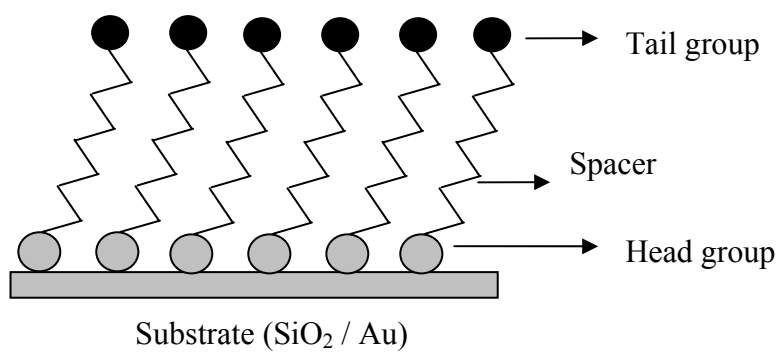


Figure 1-4: A typical schematic of a self-assembled monolayer. The illustration shows the tail group with a straight chain hydrocarbon connection to the head group.

Thiols (R-SH, where R denotes the rest of the molecule) on Au [13] and silane-based systems on SiO₂ [14] were identified as model systems. The general interest in organic thin films was one reason for these choices. In addition, SAMs are particularly attractive for the following reasons:

- ease of preparation;
- tunability of surface properties via modification of molecular structure and functions;
- use of SAMs as building blocks in more complex structures, e.g., for “docking” additional layers to a surface;
- possibility of lateral structuring in the nanometer regime;
- applications made possible by these features.

1.2.2 Molecular electronics

The concept of miniaturization is governed by “Moore’s law”, which suggests that the number of transistors on a chip doubles every 18 months. As the projected sizes of the transistors go down to 20 nm or below it, the end of “Moore’s law” is predicted. Below this size, the physics of the transistors lead to unacceptable power dissipation. In addition, there is, at present, no technology based on lithography to fabricate devices of this small size. As the total transistor size comes down to a few nanometers – implying that only few atoms would work as a transistor - a shift in paradigm for the manufacturing and integration of microelectronics components becomes necessary. This signals the emergence of “molecular electronics” whereby one is looking for the design of an individual molecule or group of molecules that have a specific electronic functionality.

Organic molecules, owing to their size, mechanical flexibility and chemical tenability, are expected to play a key role in molecular electronics. The electrical properties of organic monolayers were first measured by Mann and Kuhn in 1971 [15]. The first theoretical concept of using a single organic molecule as a rectifier was proposed by Aviram and Ratner in 1974 [16]. They showed that if one could couple a readily oxidizing group to a readily reducing group, the alignment of the lowest unoccupied molecular orbital (LUMO) and highest occupied molecular orbital (HOMO) would be such that electronic conduction would be easier in one direction than the other, which results in a molecular diode. SAMs have been extensively used as model organic surfaces for making these device structures. Self-assembly is very useful to form the so-called “bottom contact”. In all cases involving the use of organics in device structures, the deposition of a so-called “top contact” in the form of a thin metallic or inorganic film is essential. The deposition of a top contact is very challenging due to the fact that organic molecules are unstable at high temperatures and mechanically fragile to further processing steps. In addition, molecular devices could be quite challenging as the number of molecules, their configuration, purity and numerous other important variables are not easily known and not amenable to known characterization tools.

1.3 Thin film deposition techniques

1.3.1 Physical vapor deposition (PVD)

Physical vapor deposition (PVD) involves the transfer of atoms from a condensed (solid) phase through the gas phase onto a substrate. The transfer

from the solid phase to the gas phase is typically caused by one of two methods: sputtering or evaporation. In evaporation, the charge of the material to be deposited is loaded into a crucible. The crucible is heated by embedded heaters and as the crucible heats up, the material either evaporates or sublimates. The atoms typically travel without collision to the surface of the substrate where they accumulate to form a film. One commonly used design of evaporators is the effusion cell. The material flux is solely controlled by the temperature of the crucible. Shutters are usually used to provide on/off control for the source.

In sputtering, the source target is bombarded with high energy gas phase ions emitting atoms which are then deposited on the substrate surface. To produce the high energy ions, a plasma is created by applying a large voltage across a gap containing a low pressure gas. Once the plasma is formed, ions in the plasma are accelerated toward the negatively charged target thus causing sputtering. One commonly used method is magnetron sputtering. Magnetic fields cause electrons to spiral following the direction of the magnetic field. The orbital motion of the electrons increases the possibility for the electrons to ionize a neutral gas species. The increase in efficiency allows for lower chamber pressures for deposition.

The major advantages of PVD processes are the high deposition rates achievable and the ability to deposit a wide range of materials. Also, the substrates are typically close to room temperature during deposition which is desirable from the perspective of process integration. For PVD processes, the sticking coefficient of atoms on the substrate surface is unity which results in poor step coverage. This inability to cover complicated surface topology is the major limitation of PVD processes for future film deposition requirements in the microelectronics industry. Other drawbacks of PVD techniques include

difficulties of controlling the composition of alloy materials, non-selective nature of the deposition, and difficulty in depositing insulating and semiconductor materials.

1.3.2 Chemical vapor deposition (CVD)

Chemical vapor deposition (CVD) is a chemical process often used in the semiconductor industry for the deposition of thin films of various materials. In a typical CVD process the substrate is exposed to one or more volatile precursors, which react and / or decompose on the substrate surface to produce the desired deposit. Frequently, volatile byproducts are also produced, which are removed by gas flow through the reaction chamber. CVD is widely used in the semiconductor industry, as part of the semiconductor device fabrication to deposit various films including: polycrystalline, amorphous, and epitaxial silicon, carbon fiber, filaments, carbon nanotubes, SiO₂, Si-Ge, tungsten, silicon nitride, titanium nitride, and various high κ dielectrics. The CVD process is also used to produce synthetic diamonds.

A number of forms of CVD are in wide use and frequently referenced in the literature. These processes differ in the means by which chemical reactions are initiated (e.g. activation process) and process conditions.

- Atmospheric pressure CVD (APCVD) - CVD process at atmospheric pressure.
- Atomic layer CVD (ALCVD) - A CVD process in which two complementary precursors (e.g. Al(CH₃)₃ and H₂O) are alternatively introduced into the reaction chamber. Typically, one of the precursors will

adsorb onto the substrate, but cannot completely decompose without the second precursor. The precursor adsorbs until it saturates the surface and further growth cannot occur until the second precursor is introduced. Thus the film thickness is controlled by the number of precursor cycles rather than the deposition time as is the case for conventional CVD processes. In theory ALCVD allows for extremely precise control of film thickness and uniformity.

- Aerosol-assisted CVD (AACVD) – A CVD process in which the precursors are transported to the substrate by means of a liquid/gas aerosol, which can be generated ultrasonically. This technique is suitable for use with low volatility precursors.
- Direct liquid injection CVD (DLICVD) – A CVD process in which the precursors are in liquid form. Liquid solutions (mainly metal-organic precursors are used) are injected in a vaporization chamber towards injectors (typically car injectors). Then the precursor vapors are transported to the substrate in classical CVD process. This technique is suitable for use with liquid or solid precursors. High growth rates can be reached using this technique.
- Low pressure CVD (LPCVD) - CVD processes at sub-atmospheric pressures. Reduced pressures tend to reduce unwanted gas phase reactions and improve film uniformity across the wafer. Most modern CVD processes are either LPCVD or UHVCVD.
- Metal-organic CVD (MOCVD) – CVD processes based on metal-organic precursors, such as tantalum ethoxide, $\text{Ta}(\text{OC}_2\text{H}_5)_5$, to create Ta_2O_5 .
- Plasma-enhanced CVD (PECVD) – CVD processes that utilize plasma to enhance chemical reaction rates of the precursors. PECVD processing

allows deposition at lower temperatures, which is often critical in the manufacturing of semiconductors.

- Remote plasma-enhanced CVD (RPECVD) – Similar to PECVD except that the wafer substrate is not directly in the plasma discharge region. Removing the wafer from the plasma region allows processing temperatures down to room temperature.
- Ultrahigh vacuum CVD (UHVCVD) – CVD processes at a very low pressure, typically below 10^{-8} Torr.

1.3.3 Atomic layer deposition (ALD)

Atomic layer deposition (ALD) is a self-limiting film growth method characterized by the alternate exposure of chemical species. This is achieved by using two self-limiting surface reactions alternatively in an A-B-A-B.... scheme. The substrate is exposed to reactant A for a period of time to allow the adsorption of a monolayer on the surface. This is followed by exposure to reactant B which reacts with the adsorbed monolayer to leave a single layer of product C on the surface. Reactant B is not reactive with product C and should desorb readily from the surface, leaving a starting surface for reactant A to adsorb on the next cycle. Hence, a complete cycle in ALD is defined as exposure to both reactant A and B. In this ideal scheme, a single layer of C can be deposited per cycle and the thickness can be controlled simply by repeating the number of cycles. Shown in Fig. 1-5 is the schematic of an ALD process proceeding via alternate pulsing of precursors separated by a purge step. ALD was developed in the 1970s by Suntola and co-workers, and its first successful application was for the deposition of materials used for display devices [17].

Originally, the deposition technique was called atomic layer epitaxy, emphasizing the sequentially controlled arrangement of atomic layers through surface reaction following a previously deposited layer. Until the early 1990s, ALD had been considered only for very limited applications, such as the deposition of II–VI materials for display devices and III–V compound, or elemental semiconductor (SiGe) thin films [17-21]. With the continued dimensional scaling down in semiconductor devices, now clearly entering the nanoscale node, the need for a deposition technique to produce very conformal, ultrathin films at low growth temperatures has increased which makes ALD very attractive. Shown in Fig. 1-6 is the cross sectional transmission electron micrograph (TEM) of a MOSFET showing several layers which can be deposited using ALD [22]. In addition, the increase in Si wafer size to 300 mm diameter requires deposition techniques with good, intrinsic uniformity. The process temperature limitation for all deposition technologies has become more severe by the introduction of novel low κ dielectric materials for interconnect applications. This restriction in deposition temperature depends strongly on the choice of the low κ dielectric as well as the various integration schemes used in production. Generally, this puts an absolute upper limit of around 400 °C on all the processes. The major advantages offered by ALD are:

- good uniformity
- great conformality in high aspect ratio features
- good chemical composition
- can seal porous structures (Plasma enhanced ALD)
- better purity than MOCVD which usually leads to carbon contamination
- low particulate content
- lower thermal budget than CVD

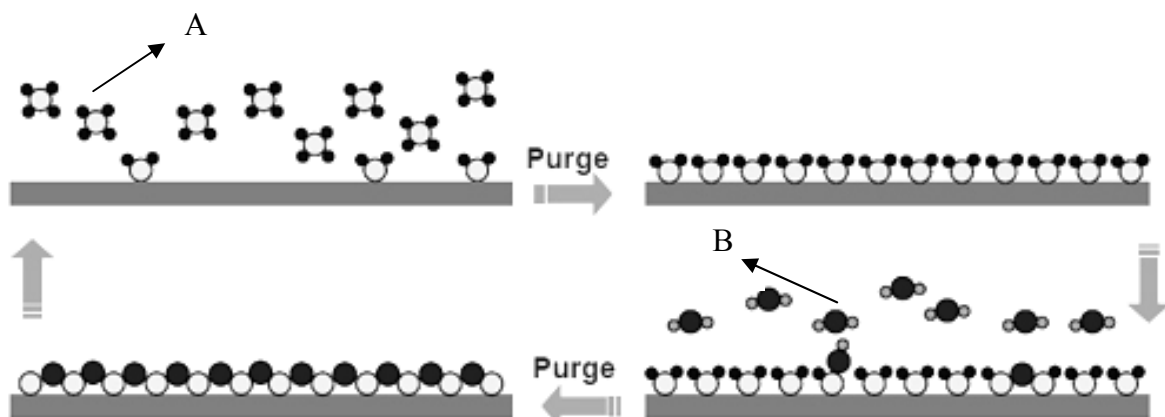


Figure 1-5: Schematic illustration of the ALD process where alternating pulses of two different precursors, separated by a purge pulse of an inert gas, constitute a typical ALD cycle. Multiple ALD cycles are used to deposit a film. (source: IBM)

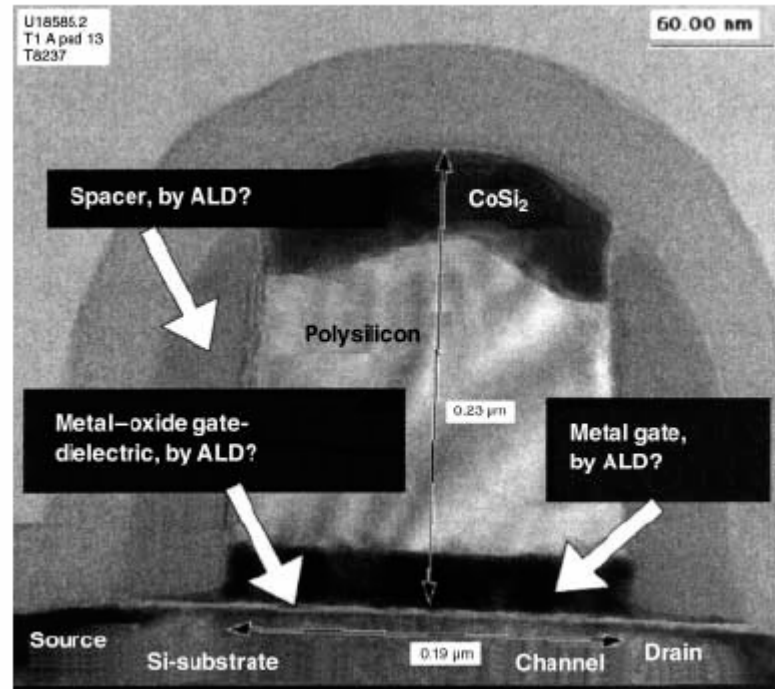


Figure 1-6: A cross-sectional TEM image of a MOSFET (channel length = 0.19 μm) showing three application areas where ALD film could be used (adapted from [22]).

The major disadvantages are generally slower deposition rates compared to CVD or PVD and an initial nucleation behavior strongly dependent on starting surface. However, with continued shrinking of device dimensions, film thicknesses are also decreasing and ALD is becoming a more viable technique for depositing ultra thin films.

Although a variety of films have been deposited using ALD, there is very little fundamental insight into the surface reactions and intermediates involved in this process. The reaction of tetrakis(dimethylamido)titanium ($\text{Ti}[\text{N}(\text{CH}_3)_2]_4$) with self-assembled thiophene monolayers terminated in isopropyl amine groups is described in Chapter 3. The kinetics of adsorption on these self-assembled monolayers is examined explicitly as a function of substrate temperature. In addition, the stoichiometry of the interface formed by the reaction of $\text{Ti}[\text{N}(\text{CH}_3)_2]_4$ with these functionalized monolayers is described in detail. Described in chapters 4 and 5, are the results for TiN ALD employing $\text{Ti}[\text{N}(\text{CH}_3)_2]_4$ and NH_3 , on SiO_2 , SiO_2 modified using interfacial organic layers (IOLs) and porous low κ dielectric substrates.

Chemical processes during thin film deposition are crucial steps in the fabrication of today's semiconductor devices. Fundamental insight into atomistic processes involved in the nucleation and deposition of these films is therefore critical to understanding these processes in order to scale films to smaller dimensions for the next generation of integrated circuits.

1.4 Nucleation and morphology of thin films

1.4.1 Capillarity theory

As the requisite thickness of thin films becomes thinner and thinner, the requirements of conformality become more stringent. Also the morphological evolution of thin films becomes extremely important and more difficult to control. While the differences between different types of films and methods of growth play a large role in determining morphology, it is useful to examine some of the models developed concerning the evolution of thin films before the results of any novel studies are presented. Perhaps one of the simplest models, yet still very useful in illustrating some of the more relevant issues associated with thin film growth is that of capillarity. Much of this model is based on the thermodynamic properties of the deposited film the underlying substrate and the interfacial energies. The free energy ΔG of such a system may be expressed as:

$$\Delta G = a_3 r^3 \Delta G_v + a_1 r^2 \gamma_{vf} + a_2 r^2 \gamma_{fs} - a_2 r^2 \gamma_{sv} \quad (1-1)$$

where ΔG_v is the chemical free-energy change per unit volume, r is the radius of a cap shaped island such as that illustrated in Fig. 1-7, and γ is the interfacial energy between two materials designated by the subscripts v , f and s indicating vapor, film and substrate, respectively [23]. Under conditions of supersaturation ΔG_v is negative driving the equilibrium towards the condensation of atoms. However, the interfacial energies (γ), or tensions as they are often indicated, complicate the picture. Considering for a moment the balance of forces generated by these tensions at the boundary of the growing

island gives some insight into the growth mode expected. This balance is governed by the mathematical relation known as Young's equation:

$$\gamma_{sv} = \gamma_{fs} + \gamma_{vf} \cos \Theta \quad (1-2)$$

In the case that Θ is greater than 0, i.e., the film growth is characterized by the deposition of islands, $\gamma_{sv} < \gamma_{fs} + \gamma_{vf}$. This mode of growth in epitaxial systems is known as Volmer Weber growth and is 3-dimensional in nature. In contrast, when Θ is exactly 0, or more precisely when the film growth is 2-dimensional, $\gamma_{sv} = \gamma_{fs} + \gamma_{vf}$. This is known as Frank van-der Merwe type growth and is most often the goal for film deposition. A third type of growth known as Stranski-Krastanov growth occurs when $\gamma_{sv} > \gamma_{fs} + \gamma_{vf}$. When this condition is satisfied and the strain energy per unit area of film is high with respect to γ_{vf} then the film initially wets the surface before islands begin to nucleate on the surface of the film. These three modes of growth are shown illustratively in Fig. 1-8. By differentiating Eqn. 1-1, the critical nucleus size can be obtained:

$$r^* = \frac{-2(a_1\gamma_{vf} + a_2\gamma_{fs} - a_3\gamma_{sv})}{3a_3\Delta G_v} \quad (1-3)$$

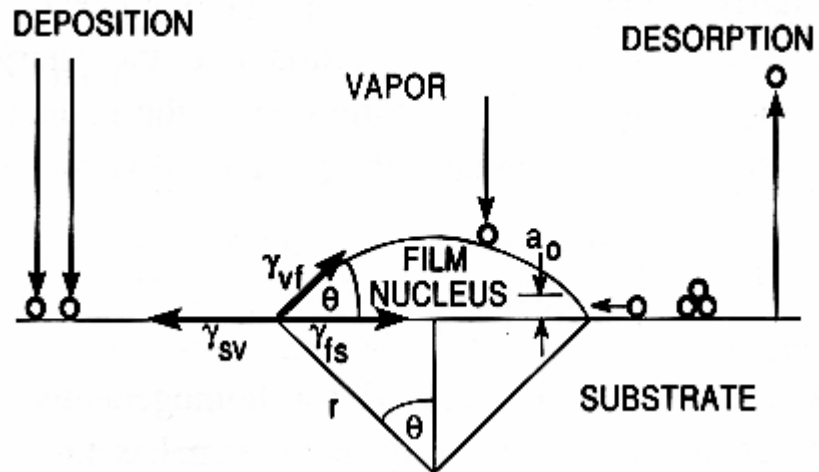


Figure 1-7: Illustration demonstrating the interfacial energies (surface tensions) and transport phenomena during the growth of thin films. Shown on the left side of the island is the balance of interfacial energies which leads to Young's equation (from [23])

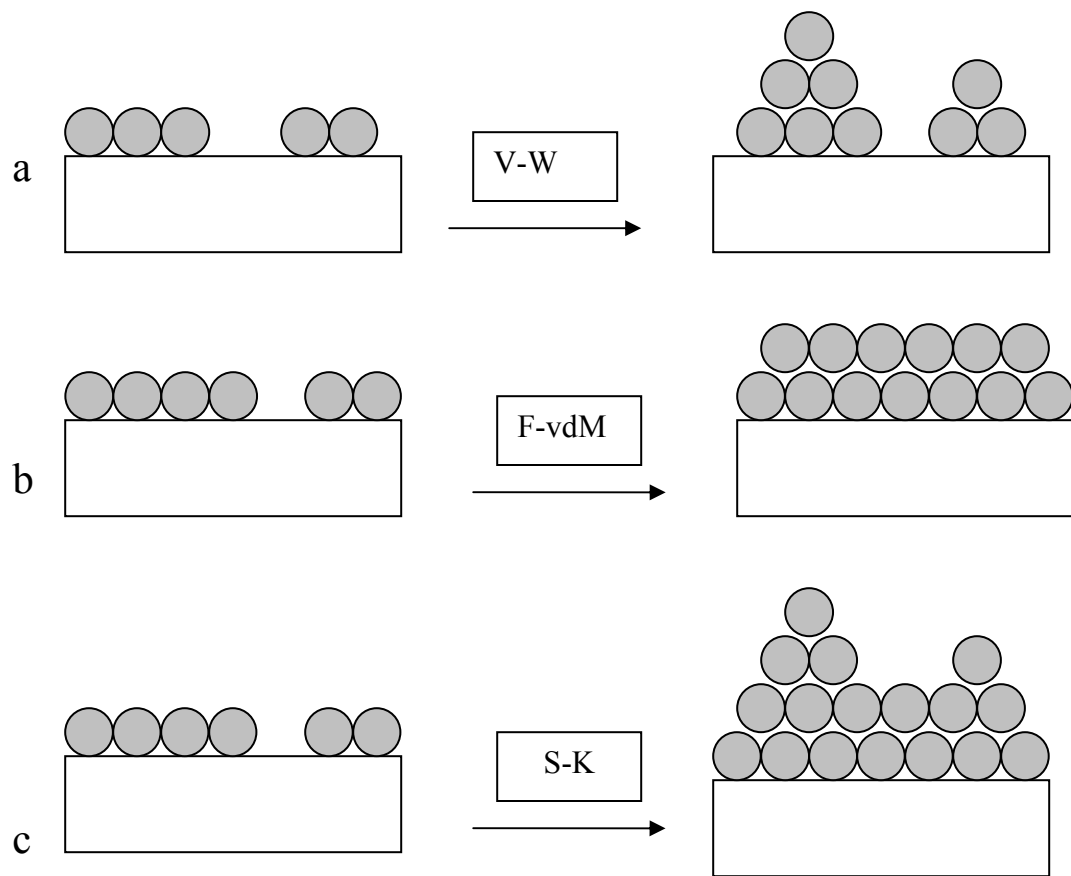


Figure 1-8: Illustration of three thin film growth modes (a) island, or Volmer-Weber (VW) growth; (b) layer-by-layer, or Frank-van der Merwe (F-vdM) growth; (c) layer-plus-island, or Stranski-Krastanov (S-K) growth.

By substituting r^* back into Eqn. 1-1 along with the geometric constants, it can be shown that the energy barrier for nucleation ΔG^* is:

$$\Delta G^* = \left(\frac{16\pi\gamma_{vf}^3}{3\Delta G_v^2} \right) \left(\frac{2 - 3\cos\theta + \cos^3\theta}{4} \right) \quad (1-4)$$

The critical nucleus size r^* defines the size of stable nuclei. Nuclei above the size of r^* tend to grow in size while nuclei smaller than r^* will disappear by shrinking in size. The first factor in Eqn. 1-4 is the energy barrier for homogeneous nucleation and is the upper limit for the case of heterogeneous nucleation. A relationship for the rate of nucleation can be derived using the critical nucleus size r^* , energy barrier for nucleation ΔG^* , an estimate of the overall impingement flux, surface diffusion and desorption rates.

1.4.2 Atomistic nucleation

Capillarity theory provides a conceptually simple qualitative model of film nucleation; however, it lacks detailed atomistic assumptions which render it quantitatively inaccurate. Atomistic nucleation models are based on the Walton-Rhodin theory [23] which incorporates the critical dissociation energy, E_i , for a critical cluster size, i . Figure 1-9 illustrates the relevant surface processes and energies involved in the atomistic nucleation model. The critical dissociation energy is basically the energy required to disintegrate a cluster of i atoms into i separated adatoms.

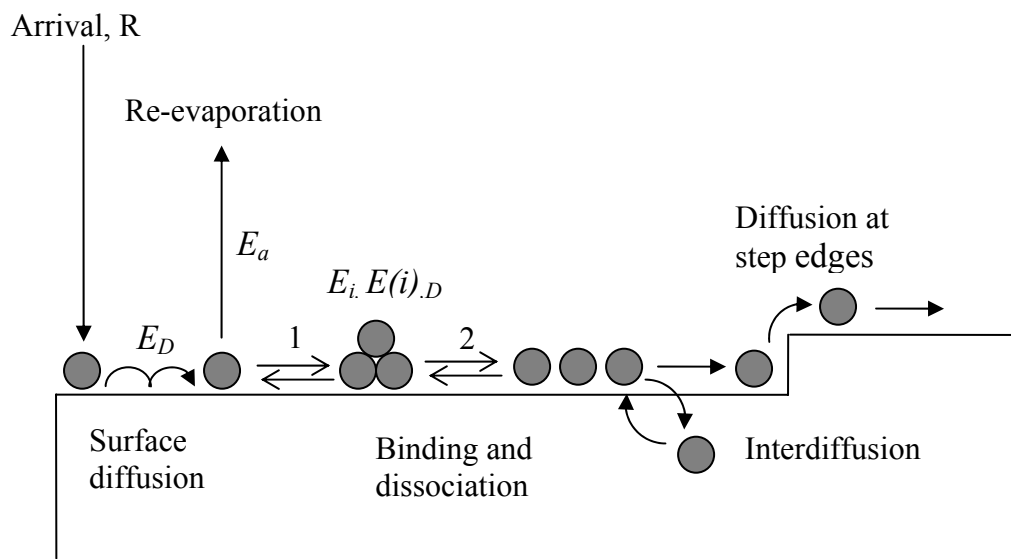


Figure 1-9: Illustration of the surface processes and characteristic energies relevant in nucleation and film growth. Processes 1 and 2 are the binding and dissociation processes, respectively (adapted from [24])

As opposed to the nucleation model based on capillarity theory, atomistic models have the advantage of expressing the nucleation rate in terms of measurable parameters rather than macroscopic quantities such as ΔG^* , γ , or θ , which are not known with certainty and are difficult to estimate. Venables [24] has summarized nucleation behaviors for cases where i is any integer value. The general expression for the maximum cluster density, N_{\max} is given by:

$$N_{\max} = An_0 \left| \frac{R}{n_0\nu} \right|^p \exp \frac{E}{kT} \quad (1-5)$$

where A is a coverage dependant dimensionless constant, n_0 is the total number of surface adsorption sites, ν is the effective vibrational frequency of an adatom, R is the arrival rate of atoms to the substrate surface, and p and E are parameters dependant on the condensation regime.

1.5 Molecular beam techniques

A molecular beam can be defined as a stream of neutral molecules produced by expanding a gas through an orifice into a region of low pressure. Molecular beams can be broadly classified into two categories: effusive (oven) beams and supersonic (nozzle) beams [25, 26]. This classification is based on the nature of the gas flow emanating from the orifice, as characterized by the Knudsen number (Kn), which is defined in Eq. 1-6 below:

$$Kn = \frac{\lambda}{d} \quad (1-6)$$

Kn is the ratio of the molecular mean free path (λ) to the characteristic length of the system, in this case, the diameter of the nozzle (d). Kn essentially describes the degree of inter-molecular interaction that a molecule experiences in a system, in this case, the expansion through an orifice. In the case of $Kn \gg 1$, the molecules tend to travel through the aperture with a small number of collisions and are in molecular flow. In this case, the resultant expansion is termed effusive. On the other hand, if Kn is $\ll 1$, the molecules encounter many collisions traveling through the aperture and the flow in the orifice is termed continuum flow. In this case, the expansion is termed supersonic. The following sections provide a more detailed description of both types of beams.

1.5.1 Beam characterization

1.5.1.1 Effusive beams

As mentioned above, for an effusive beam there are few inter-molecular collisions occurring during the expansion process compared to collisions with the wall. Due to this, the velocity distribution of the beam is characterized by Maxwell-Boltzmann distribution and is a function of the source temperature (T_n). The flux-weighted velocity distribution, $I(v)$, is given by:

$$I(v) = \left(\frac{2}{\alpha^4} \right) v^3 \exp\left(-\frac{v^2}{\alpha^2} \right) \quad (1-7)$$

where $\alpha^2 = 2k_B T_n / m$, k_B is the Boltzmann constant, and m is the molecular weight. From this expression the average translational energy, $\langle E_i \rangle$ can be calculated by the integration of the individual molecular kinetic energies over

the flux weighted velocity distribution. This results in $\langle E_i \rangle = 2k_B T_n$, which demonstrates the low energy nature of effusive beams. For example, for typical nozzle temperatures of a few hundred °C, $\langle E_i \rangle$ is still in the range of a few meV. The flux distribution of the effusive beam can also be expressed by using Boltzmann statistics, or the cosine angular distribution:

$$F_i = \frac{P_n}{\sqrt{2\pi m k_B T_n}} \frac{\pi r_n^2}{\pi x^2} \cos \theta \quad (1-8)$$

where F_i is the flux arriving at a point in space in the effusive beam, P_n and r_n are the source pressure and nozzle radius ($d_n/2$) respectively, and x is the distance between the source and substrate. The major advantages of effusive beams over supersonic beams are the ease of production and characterization. However, with the low and limited range of incident kinetic energies achievable, wide beam energy distributions, difficulties in producing high flux intensities and difficulties in producing a high beam to background intensity, the use of effusive beams are somewhat limited to large area dosing of surfaces.

1.5.1.2 Supersonic beams

A supersonic beam is formed when an adiabatic (isentropic) expansion occurs from a region of high pressure into a low pressure region. The Kn in this case is $\ll 1$ which means many more inter-molecular collisions occur compared to collisions with the wall. The result of these inter-molecular collisions is to convert random thermal molecular motion into directed translational motion, producing a nearly mono-energetic beam. The beam produced is more focused and intense and has a peaked flux distribution compared to the effusive beam.

The difference between the production methodologies of the two beams is shown schematically in Fig 1-10. The energy of the molecules can be further enhanced with the use of seeding techniques, where an inert, fast moving light gas such as H₂ or He accelerates slow moving heavier gas molecules. The energy of the molecules in a supersonic beam can thus be tuned to a much wider range compared to the effusive beams. The flux-weighted velocity distribution, $I(v)$, of a supersonic molecular beam is given by:

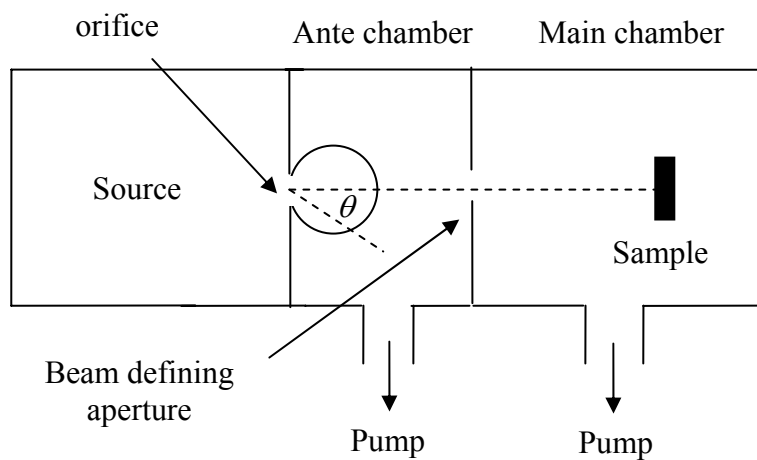
$$I(v) = N(c, \alpha)v^3 \exp\left(-\frac{(v-c)^2}{\alpha^2}\right) \quad (1-9)$$

where $N(c, \alpha)$ is a normalization constant, and c is the most probable velocity, defined as:

$$c = \left[\frac{2\gamma k_B T_n}{(\gamma - 1)m} \right]^{0.5} \quad (1-10)$$

where $\gamma = C_p/C_v$ is the ratio of heat capacities, T_n is the nozzle temperature and α^2 is a measure of spread in the velocities of the gas parallel to the flow direction defined as $2k_B T_{ax}/m$, where T_{ax} is the axial translational temperature, and m is the mass of the reactant gas. Equation 1-10 reduces to an effusive beam Maxwell distribution when $c = 0$ and $\alpha^2 = 2k_B T_n/m$ and goes to a commonly used representation for the velocity distribution of a supersonic beam. The resultant beam has a centerline flux 2-3 times higher than the effusive beam and the angular distribution is peaked with a $\cos^4\theta$ distribution for a pure gas under ideal conditions.

a)



b)

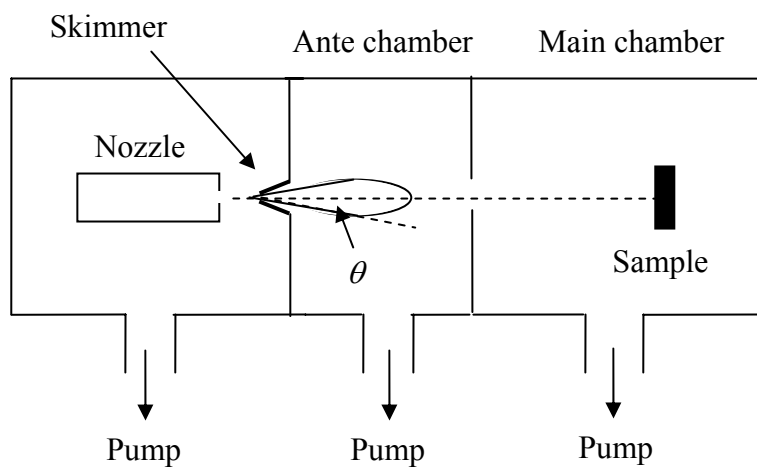


Figure 1-10: Schematic representation of: a) effusive and b) supersonic molecular beam systems. The closed curves downstream of the orifice and the skimmer represent the relative intensity distribution (from [25]).

As the molecules travel from the high pressure region through the orifice, the random motion of the molecules (rotational and vibrational energies) are converted into translational motion in the beam direction. Once the gas passes through the orifice, it expands and cools. This results in a drop in the number of collisions and also a narrower velocity distribution. Ideally, no energy is lost from the beam during expansion and is instead completely converted to a directed translational energy.

In order for supersonic expansion to occur, the ratio of the pressure upstream of the nozzle, P_0 , with the pressure in the evacuated chamber downstream of the nozzle, P_1 , must be:

$$\frac{P_0}{P_1} \geq \left[\frac{(\gamma + 1)}{2} \right]^{\gamma/(\gamma-1)} \quad (1-11)$$

When this condition is satisfied, the velocity of the gas at the nozzle is equal to the speed of sound given by $s = (\gamma k_B T_n / m)^{0.5}$. A characteristic of the expansion is the Mach number (Ma), defined as the ratio of the gas velocity to the speed of sound, v/s . Therefore, in order for the expansion to be supersonic, the pressure ratio must be high enough to make $\text{Ma} = 1$. Otherwise, the expansion would tend toward a Maxwell-Boltzmann distribution. In the limit of the expansion gas temperature being much less than the nozzle temperature, the terminal velocity, v_∞ , may be derived to be:

$$v_\infty = \sqrt{\frac{2k_B}{m} \left(\frac{\gamma}{\gamma-1} \right) T_n} \quad (1-12)$$

In a seeded supersonic beam, the different gases in the mixture are accelerated to the same velocity rather than energy. This is the basis for the

ability to enhance the kinetic energy of a heavy molecule with a light molecule. In a mixture, assuming ideal molar heat capacities, the maximum possible translational energy of a reactant in a mixture is given by:

$$\langle E_i \rangle = \frac{m_i}{\langle m \rangle} \langle C_p \rangle T_n \quad (1-13)$$

where m_i is the mass of the reactant gas, $\langle m \rangle$ is the mole fraction mean mass of the gas mixture, $\langle C_p \rangle$ is the mole fraction mean heat capacity of the mixture, and T_n is the nozzle temperature. In most cases, the expansion is not ideal and both velocity and temperature of the reactant gas deviate from their ideal values. The non-idealities from these cases are referred to as velocity and temperature slip, respectively. For both cases, it results in a lower than expected energy from Eq. 1-13. Thus Eq. 1-13 can only be used as an upper limit for the average beam energy.

As illustrated in Fig. 1-10, in practice, the extraction of a supersonic beam requires a skimmer placed a short distance downstream of the nozzle. An illustration of the expansion region right after the nozzle is given in Fig. 1-11. The molecules traveling beyond the expansion in a supersonic beam are traveling in excess of the speed of sound. The molecules are not able to adjust to the boundary conditions downstream of the expansion since information travels in fluids at the speed of sound. As a result, shock structures eventually develop and these structures have the property of high density gradients. This shock structure is to be avoided in a supersonic beam and in practice, a skimmer is typically used to “extract” or sample the expansion in the so-called zone of silence.

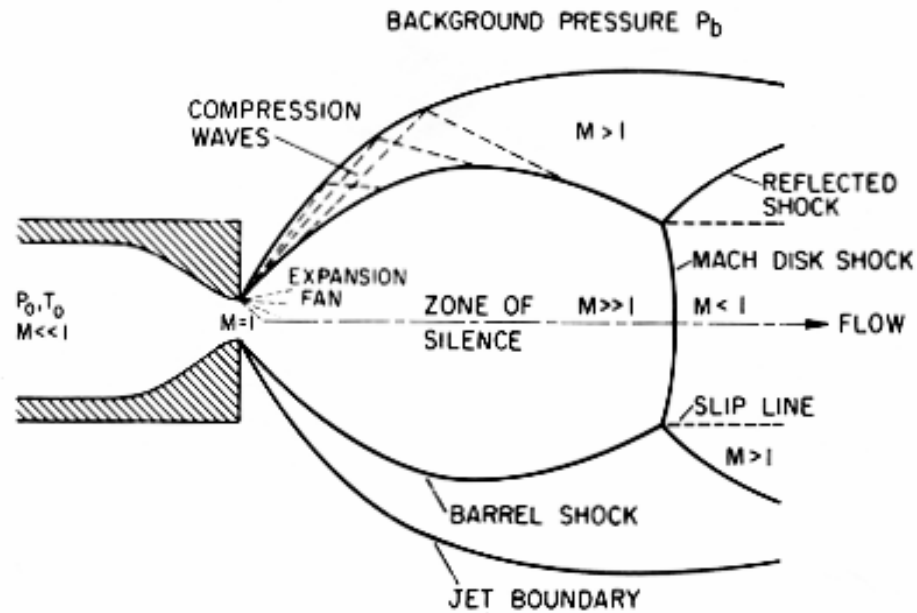


Figure 1-11: Illustration of the structures formed during a supersonic expansion. The figure shows what is commonly known as a “Free Jet” expansion which is produced without any downstream structures affecting the boundary conditions of the expansion (from [26]).

The skimmer is usually conical in shape with a small aperture at the apex. This shape minimizes the backscattering of skimmed molecules into the free jet stream out of the nozzle. After the extraction, the beam can be further pumped in a separate chamber to minimize scattering and inter-molecular collisions in the beam. Furthermore, collimation can be carried out with apertures placed before the main chamber. The result is a spatially well-defined beam with a narrow energy distribution and allows a unique experimental technique involving translation of the beam relative to the sample. This technique is described in detail in chapter 2. Supersonic beams can also be used for thin film growth and the details will be discussed in chapters 4 and 5. Besides the velocity and temperature slip problems mentioned previously, other factors such as mass focusing in a seeded beam can affect the flux distribution of the supersonic beam. Even for expansions of pure gases, theoretical evaluations of the flux is complicated by the number of variables that can affect the expansion i.e. T_n , P_n , d_n , experimental configuration and pumping conditions in each separate chamber. Although empirical models have been developed to estimate the effects of velocity and temperature slip [27] and mass focusing [28], it is difficult to extend these models to more complex molecules. Currently, the only exact method of determining the energy of reactant molecules in a supersonic beam is to measure them using time of flight techniques.

1.5.3 Thin film deposition employing molecular beams

A supersonic molecular beam provides a reactant flux with an initial state that is well defined in energy, angle of incidence, composition and flux. Molecular beams provide much higher fluxes than typical vapor

deposition processes and hence prove to be useful sources for growing thin films. In addition, excellent control over the translational energy, angle and flux of incident molecules can be obtained. As a result, thin film deposition techniques can be developed which may be activated or strongly influenced even at low substrate temperatures. Several of these techniques have already been outlined in the previous discussions of the future of electronic materials processing and include plasma-enhanced CVD which activates process chemistries through the ionization of the process gases and atomic layer deposition (ALD) which employs self limiting chemistries activated at low process temperatures. Chapters 4 and 5 contain the details of an ALD process for TiN films employing supersonic molecular beams.

1.6 Analytical techniques

1.6.1 Ellipsometry

Ellipsometry measures the change of polarization of light upon reflection or transmission. Typically, ellipsometry is done only in the reflection setup. The exact nature of the polarization change is determined by the sample's properties (thickness, complex refractive index or dielectric function tensor) [29, 30]. Although optical techniques are inherently diffraction limited, ellipsometry exploits phase information and the polarization state of light, and can achieve angstrom resolution. In its simplest form, the technique is applicable to thin films with thickness less than a nanometer to several micrometers.

The basic setup for an ellipsometry measurement is shown in Fig. 1-12.

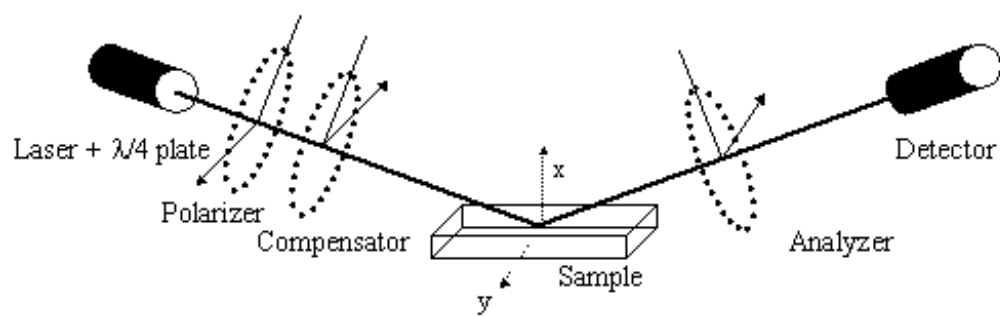


Figure 1-12: Schematic of an ellipsometry setup (source: Ref. [30])

Electromagnetic radiation is emitted by a light source and linearly polarized by a polarizer, it can then pass an optional compensator (retarder, quarter wave plate), and fall onto the sample. After reflection, the radiation passes a compensator (optional) and a second polarizer, which is called an analyzer, and falls into the detector. Ellipsometry is a specular optical technique (the angle of incidence equals the angle of reflection). The incident and the reflected beam span the plane of incidence. Light, which is polarized parallel or perpendicular to the plane of incidence, is called *p*- or *s*- polarized, respectively. Ellipsometry measures two of the four Stokes parameters, which are conventionally denoted by Ψ and Δ . The polarization state of the light incident upon the sample may be decomposed into an *s* and a *p* component (the *s* component is oscillating perpendicular to the plane of incidence and parallel to the sample surface, and the *p* component is oscillating parallel to the plane of incidence). The amplitudes of the *s* and *p* components, after reflection and normalized to their initial value, are denoted by R_s and R_p , respectively. Ellipsometry measures the ratio of R_s and R_p , which is described by the fundamental equation of ellipsometry:

$$\rho = \frac{R_p}{R_s} = \tan(\Psi)e^{i\Delta} \quad (1-14)$$

Here, $\tan \Psi$ is the amplitude ratio upon reflection, and Δ is the phase shift (difference). Since ellipsometry is measuring the ratio (or difference) of two values (rather than the absolute value of either), it is very robust, accurate, and reproducible. Ellipsometry is an indirect method, i.e., in general the measured Ψ and Δ cannot be converted directly into the optical constants of the sample. Normally, a model analysis must be performed. Direct inversion of Ψ and Δ is only possible in very simple cases of isotropic, homogeneous and infinitely

thick films. In all other cases, a layer model must be established which considers the optical constants (refractive index or dielectric function tensor) and thickness parameters of all individual layers of the sample including the correct layer sequence. Using an iterative procedure (least-squares minimization), unknown optical constants and/or thickness parameters are varied, and Ψ and Δ values are calculated using the Fresnel equations. The calculated Ψ and Δ values, which match the experimental data best, provide the optical constants and thickness parameters of the sample.

1.6.2 X-ray photoelectron spectroscopy (XPS)

X-ray Photoelectron Spectroscopy (XPS) is a quantitative spectroscopic technique that measures the empirical formula, chemical and electronic state of the elements that exist within a material. XPS spectra are obtained by irradiating a material with a beam of X-rays while simultaneously measuring the kinetic energy (KE) and number of electrons that escape from the top 1 to 10 nm of the material being analyzed. XPS requires ultra-high vacuum (UHV) conditions.

A typical XP spectrum is a plot of the number of electrons detected (Y-axis, abscissa) versus the binding energy of the electrons detected (X-axis, ordinate). Each element produces a characteristic set of XPS peaks at characteristic binding energy values that directly identify each element that exist in or on the surface of the material being analyzed. These characteristic peaks correspond to the configuration of the electrons within the atoms, e.g., 1s,

2s, 2p, 3s, etc. The number of detected electrons in each of the characteristic peaks is directly related to the amount of element within the area (volume) irradiated. To generate atomic percentage values, each raw XPS signal must be corrected by dividing its signal intensity (number of electrons detected) by a "relative sensitivity factor" and normalized over all of the elements detected [31].

To count the number of electrons at each KE value, with the minimum of error, XPS must be performed under ultra-high vacuum (UHV) conditions because electron-counting detectors in XPS instruments are typically one meter away from the material irradiated with X-rays. It is important to note that XPS detects only those electrons that have actually escaped into the vacuum of the instrument. The photo-emitted electrons that have escaped into the vacuum of the instrument are those that originated from within the top 10 to 12 nm of the material. All of the deeper photo-emitted electrons, which were generated as the X-rays penetrated 1–5 micrometers of the material, are either recaptured or trapped in various excited states within the material. For most applications, it is, in effect, a non-destructive technique that measures the surface chemistry of any material.

To make the technique more surface-sensitive, reducing the photoelectron take-off angle (measured from the sample surface) reduces the depth from which the XPS information is obtained. Thus, the analysis is more surface sensitive for grazing take-off angles than for angles close to the surface normal. The most important application of angle resolved XPS (ARXPS) is in the estimation of the thickness of thin films, e.g., contamination, implantation, sputtering altered and segregation layers. A basic setup of an ARXPS experiment is shown in Fig. 1-13.

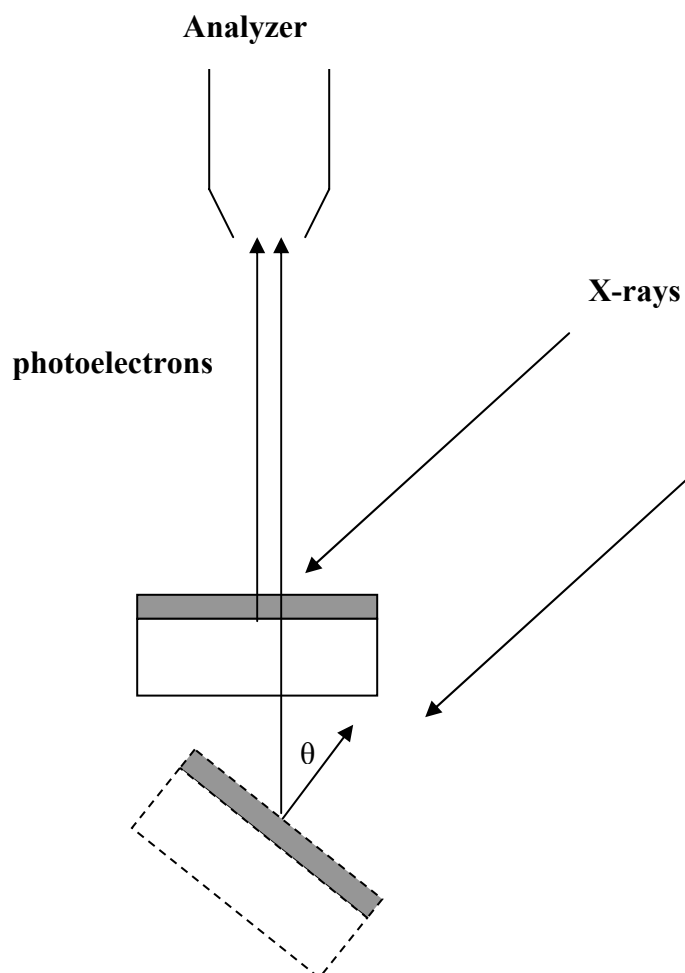


Figure 1-13: Schematic showing the setup of an ARXPS experiment. Higher take-off angle enhances surface sensitivity.

1.6.3 Rutherford backscattering spectrometry (RBS)

Rutherford Backscattering (RBS) is based on collisions between atomic nuclei. It involves measuring the number and energy of ions in a beam which backscatter after colliding with atoms in the near-surface region of a sample at which the beam has been targeted. With this information, it is possible to determine atomic mass and elemental concentrations versus depth below the surface. RBS is ideally suited for determining the concentration of trace elements heavier than the major constituents of the substrate [32]. Its sensitivity is poor for light masses, and for the makeup of samples well below the surface.

When a sample is bombarded with a beam of high energy particles, the vast majority of particles are implanted into the material and do not escape. This is because the diameter of an atomic nucleus is on the order of 10^{-15} m while the spacing between nuclei is on the order of 2×10^{-10} m. A small fraction of the incident particles do undergo a direct collision with a nucleus of one of the atoms in the upper few micrometers of the sample. This "collision" does not actually involve direct contact between the projectile ion and target atom. Energy exchange occurs because of Coulombic forces between nuclei in close proximity to each other. However, the interaction can be modeled accurately as an elastic collision using classical physics. The energy measured for a particle backscattering at a given angle depends upon two processes. Particles lose energy while they pass through the sample, both before and after a collision. The amount of energy lost is dependent on that material's stopping power. A particle will also lose energy as the result of the collision itself. The collisional loss depends on the masses of the projectile the target atoms. The number of backscattering events that occur from a given element in a sample depend upon

two factors: the concentration of the element and the effective size of its nucleus.

There is much greater separation between the energies of particles backscattered from light elements than from heavy elements, because a significant amount of momentum is transferred from the incident particle to a light target atom. As the mass of the target atom increases, less momentum is transferred to the target atom and the energy of the backscattered particle asymptotically approaches the incident particle energy. This means that RBS is more useful for distinguishing between two light elements than it is for distinguishing between two heavy elements. RBS has good mass resolution for light elements, but poor mass resolution for heavy elements. For example, when He^{++} strikes light elements such as C, N, or O, a significant fraction of the projectile's energy is transferred to the target atom and the energy recorded for that backscattering event is much lower than the energy of the beam. It is usually possible to resolve C from N or P from Si, even though these elements differ in mass by only about 1 amu. However, as the mass of the atom being struck increases, a smaller and smaller portion of the projectile energy is transferred to the target during collision, and the energy of the backscattered atom asymptotically approaches the energy of the beam. It is not possible, for instance, to resolve W from Ta, or Fe from Ni when these elements are present at the same depths in the sample, even though these heavier elements also differ in mass by only about 1 amu.

An important related issue is that He will not scatter backwards from H or He atoms in a sample. Elements as light as, or lighter than, the projectile element will instead scatter at forward trajectories with significant energy. Thus, these elements cannot be detected using classical RBS. However, by

placing a detector so that these forward scattering events can be recorded, these elements can be quantitatively measured using the same principles as RBS [32].

1.6.4 Atomic force microscopy (AFM)

The atomic force microscope (AFM) is a very high-resolution scanning probe microscope, with demonstrated resolution of fractions of an Angstrom, more than a 1000 times better than the optical diffraction limit [33]. The AFM consists of a microscale cantilever with a sharp tip (probe) at its end that is used to scan the specimen surface. The cantilever is typically silicon or silicon nitride with a tip radius of curvature on the order of nanometers. When the tip is brought into proximity of a sample surface, forces between the tip and the sample lead to a deflection of the cantilever according to Hooke's law. Depending on the situation, forces that are measured in AFM include mechanical contact force, Van der Waals forces, capillary forces, chemical bonding, electrostatic forces, magnetic forces etc. Typically, the deflection is measured using a laser spot reflected from the top of the cantilever into an array of photodiodes. A typical AFM schematic is presented in Fig. 1-14.

The AFM probes are fabricated with piezoresistive elements that act as a strain gauge. Most commonly, a feedback mechanism is employed to adjust the tip-to-sample distance to maintain a constant force between the tip and the sample. Traditionally, the sample is mounted on a piezoelectric tube that can move the sample in the z direction for maintaining a constant force, and the x and y directions for scanning the sample.

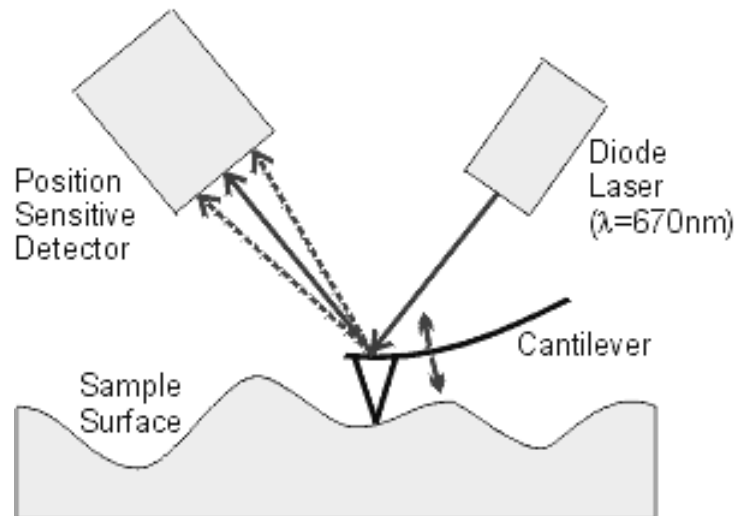


Figure 1-14: Typical schematic of an atomic force microscope (AFM) (source: Ref. [33])

Alternately a 'tripod' configuration of three piezo crystals may be employed, with each responsible for scanning in the x,y and z directions. This eliminates some of the distortion effects seen with a tube scanner. The resulting map of the area represents the topography of the sample.

The AFM can be operated in a number of modes, depending on the application. The primary modes of operation are static (contact) mode and dynamic mode. In the static mode operation, the static tip deflection is used as a feedback signal. The measurement of a static signal is prone to noise and drift, hence low stiffness cantilevers are used to boost the deflection signal. However, close to the surface of the sample, attractive forces can be quite strong, causing the tip to 'snap-in' to the surface. Thus static mode AFM is almost always done in contact where the overall force is repulsive. Consequently, this technique is typically called "contact mode". In contact mode, the force between the tip and the surface is kept constant during scanning by maintaining a constant deflection. In the dynamic mode (or the tapping mode), the cantilever is externally oscillated at or close to its resonance frequency. The oscillation amplitude, phase and resonance frequency are modified by tip-sample interaction forces. These changes in oscillation with respect to the external reference oscillation provide information about the sample's characteristics. This mode is very useful for soft materials like polymers as the contact mode can be invasive.

1.6.5 Scanning transmission electron microscopy (STEM)

The original form of electron microscopy, transmission electron microscopy (TEM) involves a high voltage electron beam emitted by a cathode

and formed by magnetic lenses. The electron beam that has been partially transmitted through the very thin specimen carries information about the inner structure of the specimen. The spatial variation in this information (the "image") is then magnified by a series of magnetic lenses until it is recorded by hitting a fluorescent screen, photographic plate, or light-sensitive sensor such as a CCD (charge-coupled device) camera. The image detected by the CCD may be displayed in real time on a monitor or computer. Resolution of the high-resolution TEM (HRTEM) is limited by spherical and chromatic aberration. The ability to determine the positions of atoms within materials has made the HRTEM an indispensable tool for nanotechnology research and development in many fields, including heterogeneous catalysis and the development of semiconductor devices for electronics and photonics [34].

In a STEM, an electron transparent sample is studied in much the same way as in TEM. However, instead of continuously illuminating the sample, a small electron probe is scanned over the area to be studied. The transmitted electrons are then collected by an annular detector mounted a long way from the specimen. This signal is displayed as a function of probe position to form an image which has a very high intensity. Another important advantage of STEM is that any analytical signal, such as X-ray fluorescence spectroscopy and electron energy loss spectroscopy (EELS), can also be obtained at high resolution (0.1 nm in the very best STEM) [34].

1.6.6 Electron energy loss spectroscopy (EELS)

In electron energy loss spectroscopy (EELS), a material is exposed to a beam of electrons with a known, narrow range of kinetic energies. Some of the

electrons will lose energy by inelastic scattering, which is primarily an interaction of the beam electron with an electron in the sample. This inelastic scattering results in both a loss of energy and a change in momentum. These interactions may be phonon excitations, inter and intra band transitions, plasmon excitations or inner shell ionizations [34]. The latter are particularly useful for detecting the elemental components of a material.

There are several basic flavors of EELS, primarily classified by the geometry and by the kinetic energy of the incident electrons (typically measured in keV). Probably the most common today is transmission EELS, in which the kinetic energies are typically 100 to 300 keV and the incident electrons pass entirely through the material sample. Usually this occurs in a scanning transmission electron microscope (STEM).

1.7 References

1. Moore, G. E. *Electron.* **1965**, *19*, 114.
2. International Technology Roadmap for Semiconductors (www.itrs.net), **2005**.
3. *Physics of Semiconductor Devices, Second Edition*; Sze S. M.; John Wiley and Sons: NY, **1981**.
4. Frank, D. J.; Taur, Y.; Wong, H. -S. P. *IEEE Electron Device Lett.*, **1998**, *19*,385.
5. Maex, K.; Hoyas, A. M. *J. Appl. Phys.* **2003**, *93*, 8793.
6. *Copper interconnect technology*; Steinbrüchel, C.; Chin, B. L., SPIE Press :Washington, **2001**.
7. Rha, S. -K.; Lee, W. -J.; Lee, S. -Y.; Hwang, Y. -S.; Lee, Y. -J.; Kim, D. -I.; Kim, D. -W.; Chun, S. -S.; Park, C. -O. *Thin Solid Films* **1998**,*320*, 134.
8. Chen, G. S.; Chen, S. T. *J. Appl. Phys.* **2000**, *87*, 8473.
9. Mathad, G. S.; Rathore, H. S.; Arita, Y. *Interconnect and Contact Metallization for ULSI proceedings* **2000**, 46.
10. Dube, A.; Sharma, M.; Ma, P. F.; Engstrom, J. R. *Appl. Phys. Lett.* **2006**, *89*,164108.
11. Park, J.-S.; Lee, M. J.; Lee, C.-S.; Kang, S.-W. *Electrochem. Solid-*

State Lett. **2001**, 4, C17.

12. Ulman, A. *Chem. Rev.* **1996**, 96, 1533.
13. Nuzzo, R. G.; Allara, D. L. *J. Am. Chem. Soc.* **1983**, 105, 4481.
14. Sagiv, J. *J. Am. Chem. Soc.* **1980**, 102, 92.
15. Mann, B.; Kuhn, H. *J. Appl. Phys.* **1971**, 42, 4398.
16. Aviram, A.; Ratner, M. A. *Chem. Phys. Lett.* **1974**, 29, 277.
17. Suntola, T. *Mater. Sci. Rep.* **1989**, 4, 265.
18. Suntola, T. *Thin Solid Films* **1992**, 216, 84.
19. Goodman C. H.; Pessa, M. V. *J. Appl. Phys.* **1986**, 60, R65.
20. Bedair, S. M. *J. Vac. Sci. Technol. B* **1994**, 12, 179.
21. Leskela, M.; Ritala, M. *J. Phys. IV* **1999**, 9, Pr8-837.
22. Leskela, M.; Ritala, M. *Angew Chem. Int.* **2003**, 42, 5548.
23. *The materials science of thin films*; Ohring M.; Academic Press: Boston, **1992**.
24. *Introduction to Surface and Thin Film Processes*; Venables, J. A.; Cambridge University Press: Cambridge, UK, **2000**.
25. *Molecular and Low density Gas Dynamics*; Wegener R. P., Ed.; Deckker: New York, **1974**.
26. *Atomic and Molecular Beam Methods Vol. 1*; Scoles, G.; Oxford University Press: NY, **1988**.

27. Xia, L. -Q.; Jones, M. E.; Maity, N.; Engstrom, J. R. *J. Vac. Sci. Technol. A* **1995**, *13*, 2651.
28. de la Mora, J. F.; Rosell-Llompart, J. *J. Chem. Phys.* **1989**, *91*, 2603.
29. *Handbook of Ellipsometry*; Tompkins, H. G; Irene, E. A., Eds; William Andrews Publications: Norwich, NY, **2005**.
30. *A Users's Guide to Ellipsometry*, Tompkins, H. G.; Academic Press Inc: London, U.K., **1993**.
31. *Practical Surface Analysis: Volume I, Auger and X-ray Photoelectron Spectroscopy, 2nd ed.*; Seah, M. P., Briggs, D., Eds.; John Wiley and Sons: Chichester, England, **1990**.
32. *Fundamentals of Surface and Thin Film Analysis*; Feldman, L. C.; Mayer, J. W.; North Holland-Elsevier: NY, **1986**.
33. Giessibl, F. *Rev. Mod. Phys.* **2003**, *75*, 949.
34. *Introduction To Scanning Transmission Electron Microscopy, 1st ed.*; Keyse, R. J.; Garratt-Reed, A. J.; Goodhew, P. J.; Lorimer, G. W.; BIOS Scientific Publishers Ltd : Oxford, UK, **1998**.

2. Experimental methods

2.1 Inorganic-organic interfaces for molecular electronics

2.1.1 Description of the vacuum system and gas delivery setup

The formation of an interface between transition metal co-ordination complex tetrakisdimethyl(amido)titanium, $\text{Ti}[\text{N}(\text{CH}_3)_2]_4$, and oligo(phenylene-ethynylene) self-assembled monolayers possessing iso-propylamine terminal functional groups was studied in a custom designed ultra-high vacuum (UHV) molecular beam system [1]. Schematics for this system are provided in Fig. 2-1. This system was initially designed for beam scattering experiments employing a supersonic molecular beam.

The main chamber (volume ~ 40 L) is pumped by a 400 L/s turbomolecular pump equipped with magnetic bearings (Leybold 340M). A base pressure of 2×10^{-9} Torr is routinely achieved after a 24 hour bake-out at 150 °C. Substrates are mounted on a sample manipulator (Thermionics) capable of 5 degrees of freedom (x, y, z, translations, polar rotation and tilt), which allows the sample to be transported between two foci within the system. Both foci lie on the axis of the supersonic molecular beam. The first focal point positions the sample at the intersection of the foci of a hemispherical energy analyzer, a twin anode (Mg/Al) X-ray source (VSW), a doubly-differentially pumped ion gun, the supersonic beam and the effusive beam. The second focal point positions the sample at the intersection of the axis of rotation of a quadrupole mass spectrometer (QMS, Extrel EX-800).

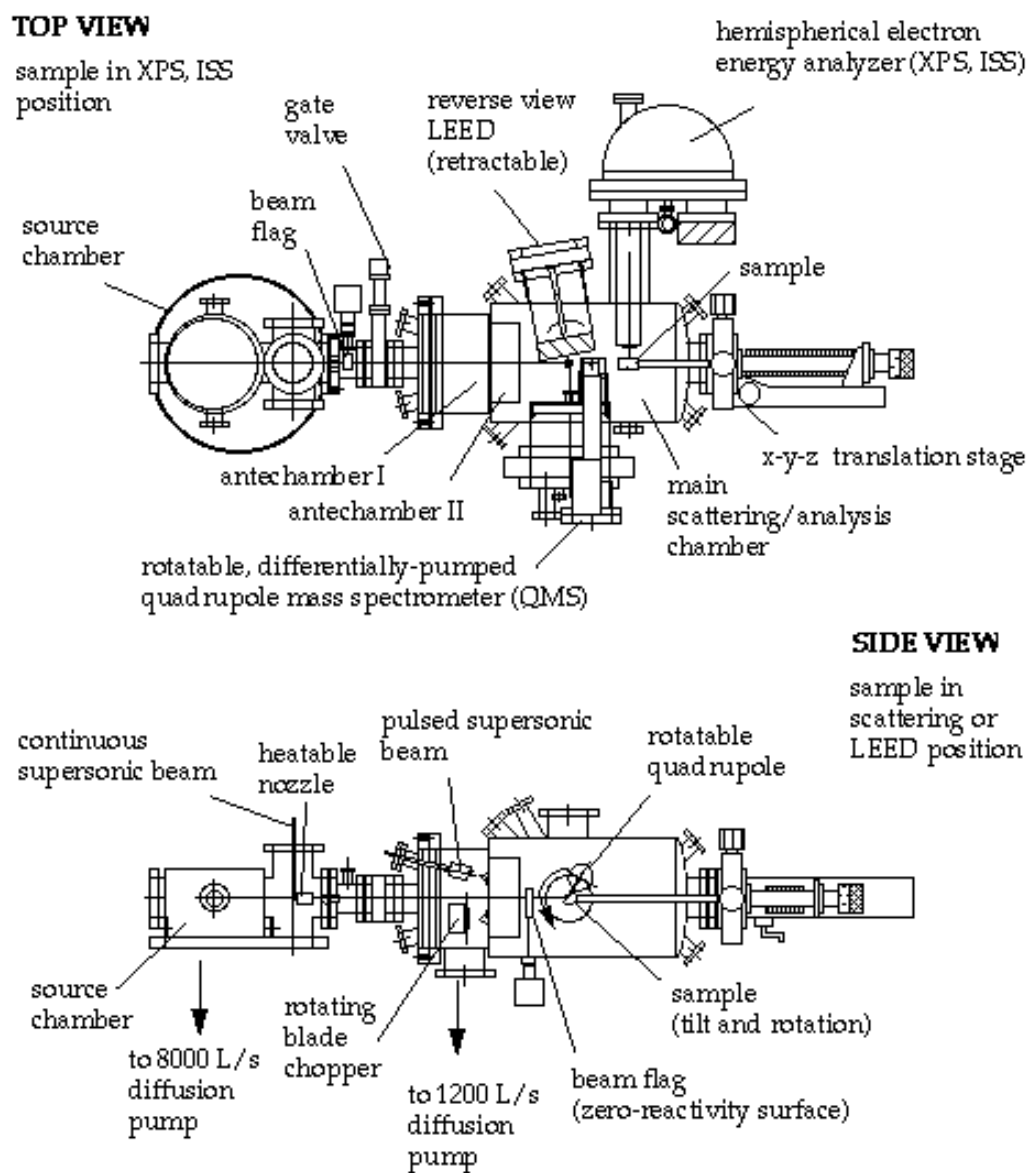


Figure 2-1: Schematic drawing of molecular beam scattering system with X-ray photoelectron spectroscopy (XPS) capability

The ionization source for the spectrometer is located 5.7 cm from the sample, the focal point of a set of retractable rear-view low-energy electron diffraction (LEED) optics, the supersonic beam and the effusive source can be moved (to flange) to reach this focal point. The quadrupole is mounted off-axis on a 10" rotatable platform, equipped with differentially-pumped spring-loaded teflon seals (Thermionics), in a separately pumped chamber at 90° to the line of flight of the molecular beam. The mass spectrometer chamber is pumped by a 60 L/s turbomolecular pump and the seals are pumped by a 10 L/s ion pump. This detector chamber is isolated from the main chamber by an additional spring-loaded teflon seal such that the turbomolecular pump can be mounted in a permanently fixed position. The flange that isolates the main and detector chambers is equipped with a cylindrical reservoir, cooled with liquid nitrogen that surrounds the ionization region of the quadrupole. This configuration allows measurement of time-of-flight (TOF) and/or angular distribution of molecules scattered from the sample surface using a supersonic beam source or, with sample retracted, the molecular beams themselves.

Above the second focal point is the load-lock pumped by a 240 L-s⁻¹ corrosive turbo pump (Pfeiffer TPU 240H). Samples are transferred into the loadlock which is pumped down to below 1×10^{-6} Torr before introducing them through a gate valve onto the manipulator in the main chamber. The load-lock mechanism consists of a sample transfer arm and fork employing a STLC (Thermionics) type transfer system which mates to the sample manipulator. Solid back or "picture frame" type Mo platens can be used. The picture frame assembly utilizes a retaining ring to minimize thermal stresses incurred and to provide temperature uniformity during experiments studying the effect of substrate temperature. Its open back design allows for direct radiant heating

using a tungsten ribbon mounted behind the sample, while cooling to approximately 170 K is provided by contact, through copper braids to a liquid nitrogen cooled reservoir. The solid back platen is useful for samples of smaller size and/or custom shapes. The temperature at the surface of the substrate is calibrated using a chromel-alumel (type – K) thermocouple wedged between the retaining ring and the substrate; the reference is another thermocouple attached to the back of the manipulator.

A vapor delivery source was designed and constructed to produce an effusive beam of $\text{Ti}[\text{N}(\text{CH}_3)_2]_4$, details of which are given elsewhere [2]. A microcapillary array doser (Burle Technologies Inc., Lancaster, PA) made of lead silicate glass, (0.3 mm thick, 18 mm diameter of capillary area, 5 μm pore size, 6 μm center to center spacing with solid border) was used to deliver a uniform flux of $\text{Ti}[\text{N}(\text{CH}_3)_2]_4$ to the surface of the sample, without producing a significant rise in the background partial pressure. The doser was mounted on a 2-3/4" flange with a 4" translation stage. As a result, it was translated to be 25.4 mm from the center of the sample during exposures and retracted during analysis using XPS. A 1/4 in. silver plated 316 SS VCR gasket with an aperture 178.8 μm in diameter and $125 \pm 25 \mu\text{m}$ long was placed upstream of the doser. For most experiments, the flow of $\text{Ti}[\text{N}(\text{CH}_3)_2]_4$ through the doser was metered by controlling the temperature of the bubbler (set at 0 °C for all experiments), and using the gasket as a flow-limiting orifice. Vapor in the bubbler was drawn to the doser in the main chamber, through 1/4" stainless steel tubing (ID: 0.18") via a three way pneumatically operated bellows valve. Switching the valve resulted in either transporting TDMAT to the main chamber or to the 240 L/s corrosive turbomolecular pump. In order to minimize transients associated with the end of an exposure, a liquid nitrogen cooled glass tube was located

downstream of the three-way valve, acted as a cryopump and was used to shunt exposures through a manually operated valve.

2.1.2 Sample preparation

2.1.2.1 Materials

The following chemicals were purchased from Sigma-Aldrich Corp. (St. Louis, MO) and used as received: tetrahydrofuran (THF), > 99%, A.C.S. reagent; 4-aminothiophenol, 97% purity; ethanol, $\geq 99.5\%$, anhydrous grade. Tetrakis(dimethylamido)titanium, $\geq 99.9999\%$ purity based on metals analyzed, and $\geq 99\%$ purity based on an assay by NMR, was obtained from Schumacher (Carlsbad, CA). The following chemicals were used as received from Mallinckrodt Baker Inc. (Phillipsburg, NJ): CMOSTM grade acetone, and CMOSTM grade 2-propanol. Nanostrip from Cyantek Corp. (Fremont, CA) was also used as received.

2.1.2.2 Synthesis of thiophene ligands

The synthesis was carried out by Dr. Andrew R. Chadeayne (Wolczanski Research Group). The brief schematics of the synthetic procedure are given in Fig. 2-2. Copper (I) iodide (98%), CuI, and, tetrakis(triphenylphosphine) palladium (0) (99.9+%), Pd(PPh₃)₄ were purchased from Strem and used as received. 3-ethynylthiophene, **2** [3], 1-Bromo-4-trimethylsilylethynylbenzene, **3** [4], and 4-iodo-*N*-isopropylaniline were synthesized using reference [5].

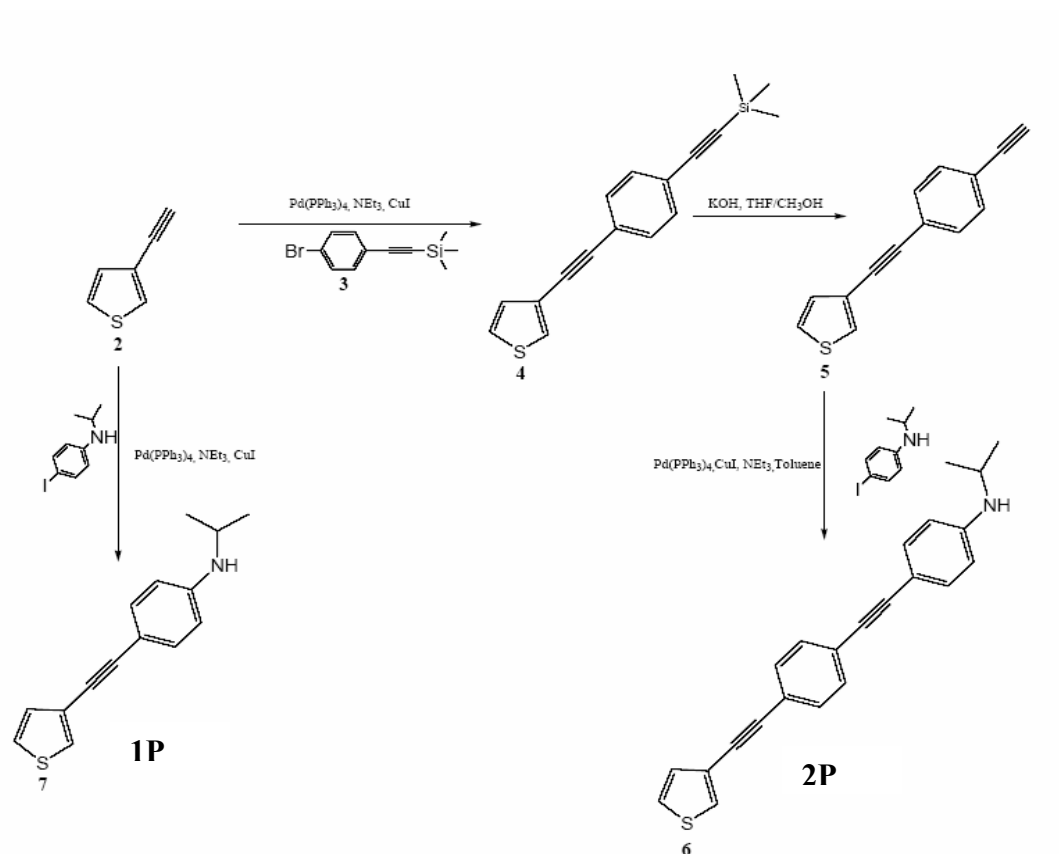


Figure 2-2: Schematic for synthesis of the thiophene SAM ligands

NMR spectra were obtained using Varian XL-400, INOVA-400 and Unity-500 spectrometers, and chemical shifts are reported relative to benzene-d₆ (¹H, δ 7.15; ¹³C{¹H}, δ 128.00). Where shifts within a conjugated ring system are reported, the following nomenclature is adapted: The thiophene ring is herein described as ring “A” and subsequent rings “B,” and, where applicable, “C.”

Preparation of (4): A 250 mL 3-neck round bottom flask was charged with 125 mL of triethylamine and sparged with argon for 20 min. 6.60 g, (26 mmol) of **3** and 3.10 g (28 mol) of **2** were added, resulting in a suspension. Pd(PPh₃)₄ (0.50g, 0.43 mmol) and CuI (0.20g, 1.1 mmol) were added under argon purge. The flask was equipped with a reflux condenser and the system was refluxed under argon for 12 h. The reaction mixture turned from pale yellow to dark brown and a white solid precipitated. After cooling to 23 °C, saturated aqueous ammonium chloride was added and the aqueous layer assumed a deep blue color while the organic layer remained amber brown. Chloroform was added to this mixture and the resulting organic layer was separated and washed three times with 200 mL of saturated aqueous ammonium chloride. The organic layer was then dried over magnesium sulfate, filtered and concentrated via rotary evaporation to yield a crude yellow solid. The crude solid was put into warm ethanol and allowed to cool to room temperature and stand for 16 h, after which time 5.90 g (81%) of white crystals were collected, ¹H NMR (400 MHz, C₆D₆) δ 0.22 (s, 9H, SiCH₃), 6.67 (dd, 1H, J= 3.2Hz, J=5.2Hz, A₄), 7.00 (dd, 1H, J=1.2Hz, J=5.2Hz, A₅), 7.16 (dd, 1H, J=1.2Hz, J=3.2Hz, A₂), 7.25 (q, 4H, J=10.8Hz, J=8.8Hz, B_{2,3,5,6}) ¹³C{¹H} NMR (100.5 MHz, C₆D₆) δ -0.05 (SiCH₃), 87.21 (A-CC-B), 89.13 (A-CC-B), 96.37 (B-CC Si), 105.49 (B-CC-Si), 122.54 (B₄), 123.34 (A₂), 123.85 (A₅), 125.70 (B₂), 129.14 (A₃), 129.92 (A₄), 131.68 (B₃), 132.22 (B₁).

Preparation of (5): A 250 mL round bottom flask was charged with 6.00 g (21.4 mmol) of **4**, 2.40 g of KOH (42.8 mmol), 200 mL of methanol and 100 mL of THF, which resulted in a light amber solution. The solution was stirred at 23 °C for 24 h. 400 mL of distilled water were added and the resulting suspension was extracted three times with 100 mL portions of chloroform. The combined chloroform extracts were dried with magnesium sulfate and filtered. The resulting filtrate was concentrated via rotary evaporation, resulting in an off-white amorphous solid. The solid was dissolved in boiling benzene and filtered while hot. The filtrate was cooled to room temperature. After 1 h, an off-white precipitate formed, which was collected (4.99 g, 89%) via vacuum filtration. ^1H NMR (400 MHz, C_6D_6) δ 2.74 (s, 1H, B-CCH), 6.65 (dd, 1H, $J=3.2, 5.2\text{Hz}$, A_4), 7.00 (dd, 1H, $J=4.8\text{Hz}, 1.2\text{Hz}$, A_5), 7.15 (dd, 1H, $J=2.8, 1.2\text{Hz}$, A_2), (q, 4H, $J= 3.6\text{Hz}, 8.4\text{Hz}$, $\text{B}_{2,3,5,6}$). $^{13}\text{C}\{\text{H}\}$ NMR (100.5 MHz, C_6D_6) δ 79.50 (B-CCH), 83.42 (A-CC-B), 87.18 (B-CCH), 88.97 (A-CC-B), 122.36 (B_1), 122.46 (B_4), 124.07 (A_2), 125.70 (A_5), 129.21 (A_3), 129.91 (A_4), 131.67 (B_2), 132.37 (B_3).

Preparation of (6 - 2P SAM ligand): To a 250 mL round bottom flask was added 1.73 g (6.63 mmol) of 4-Iodo-*N*-isopropylaniline, 1.56 g (7.29 mmol), 0.2 g (1.1 mmol) of copper(I) iodide, 0.5 g (0.43 mmol) of $\text{Pd}(\text{PPh}_3)_4$, 50 mL of toluene and 10 mL of triethylamine. The resulting mixture was stirred at 23 °C. A white precipitate formed. After 12 h, 40 mL of saturated ammonium chloride and 50 mL of chloroform were added to the mixture, resulting in a deep blue aqueous layer and a yellow-brown organic layer. The organic layer was separated, washed three times with saturated ammonium chloride, dried over magnesium sulfate, filtered and concentrated via rotary evaporation to yield a crude tan solid. This solid was washed with benzene and

then hexanes to remove impurities and then dried *in vacuo* to give 2.00 g (88%) of a light tan powder. ^1H NMR (400 MHz, C_6D_6) δ .77 (d, 6H, J = 8.4Hz, $\text{NC}(\text{CH}_3)_2$), 3.02 (br s, 1H, NH), 3.15 (sept, 1H, J = 8.4Hz, $\text{NCH}(\text{CH}_3)_2$), 6.20 (d, 2H, J =11.2Hz, $\text{C}_{2,6}$), 6.66 (dd, 1H, J = 6.8Hz, 4.4Hz, A_4), 7.02 (d, 1H, J = 6.8Hz, A_5), 7.37 (q, 4H, J =10.8Hz, $\text{B}_{2,3,5,6}$), 7.55 (d, 2H, J = 11.2Hz, $\text{C}_{3,5}$). The resonance for A_2 was obscured by the solvent peak. $^{13}\text{C}\{\text{H}\}$ NMR (100.5MHz, THF-d_8) δ 23.08 ($\text{NCH}(\text{CH}_3)_2$), 44.45 ($\text{NCH}(\text{CH}_3)_2$), 87.00 (A-CC-B), 87.35 (A-CC-B), 89.47(B-CC-C), 94.36 (B-CC-C), 110.23 (C_2), 113.14 (C_4), 123.10 (B_1), 123.32 (B_4), 125.57 (A_2), 126.71 (A_5), 129.87 (A_3), 130.65 (A_4), 131.93(B_2), 132.23 (B_3), 133.77 (C_3), 149.70 (C_1).

Preparation of (7- 1P SAM ligand): To a 250mL round bottom flask was added 4 g (15.3 mmol) of 4-Iodo-*N*-isopropylaniline, 1.65 g (15.3 mmol) of 3-thionylacetylene and 100 mL of triethylamine. The resulting solution was sparged with argon for 30 min and 0.2 g (1.1 mmol) of Copper(I) iodide and 0.5 g (0.43 mmol) of $\text{Pd}(\text{PPh}_3)_4$ were added. The reaction was stirred at 23 °C for 12 h and worked up as **6**. The brown solid was crystallized from ethanol to yield 2.98 g (81%) of red-brown crystals, which were collected via vacuum filtration. ^1H NMR (400 MHz, C_6D_6) δ .79 (d, 6H, J = 6.4Hz $\text{NC}(\text{CH}_3)_2$), 3.06 (br s, 1H, NH), 3.15 (sept, 1H J =6.4Hz, $\text{NCH}(\text{CH}_3)_2$), 6.20 (d, 2H, J =8.8Hz, $\text{B}_{2,6}$), 6.70 (dd, 1H, J = 4.8Hz, 3.2Hz, A_4), 7.10 (dd, 1H, J = 5.2Hz, 1.2Hz, A_5), 7.21 (dd, 1H, J = 2.8Hz, 1.2Hz, A_2), 7.50 (d, 2H, 8.8Hz, $\text{B}_{3,5}$), $^{13}\text{C}\{\text{H}\}$ NMR (100.5MHz, C_6D_6) δ 22.52 ($\text{NCH}(\text{CH}_3)_2$), 43.63 ($\text{NCH}(\text{CH}_3)_2$), 82.96 (A-CC-B), 90.91 (A-CC-B), 111.19 (B_4), 112.99 (B_2), 123.85 (A_2), 125.32 (A_5), 127.60 (A_3), 130.15 (A_4), 133.29 (B_3), 147.74 (B_1).

2.1.2.3 Preparation of self-assembled monolayers

The starting substrates were 100 mm single side polished, 500-550 μm thick Si (100) wafers, doped with B to a resistivity of 38-63 $\Omega\text{-cm}$. The substrates were scribed with a diamond scribe and subsequently cleaved into 16 samples, each a square of $16.75 \times 16.75 \text{ mm}^2$. After cleaving, the samples were cleaned in Nanostrip solution at 75 $^{\circ}\text{C}$, to remove the organic contaminants on the surface. These samples were immediately transferred to a CVC- SC4500 evaporation system (Cornell Nanoscale Facility). E-beam evaporation was employed to deposit 100 \AA of Cr (at 1 \AA-s^{-1}) as an adhesion layer followed by 2000 \AA of Au (at 2 \AA-s^{-1}). Self-assembled monolayers were formed via a liquid phase deposition process. 1 mM solutions, for both the thiophene ligands, were prepared in THF. The typical deposition time employed was 24 hours. After deposition, the substrates were rinsed in THF for 10 minutes to remove any physisorbed species and/or multilayers. For the 4-aminothiophenol, 1mM solutions in anhydrous ethanol were prepared and the deposition time employed was 24 hours. After deposition, the substrates were rinsed in anhydrous ethanol for 10 minutes to remove any physisorbed species and/or multilayers.

2.1.3 Characterization of self-assembled monolayers

Three different analytical techniques were employed to characterize the ordering, thickness, and composition of these monolayers.

2.1.3.1 Contact angle measurements

Measurements, made with a NRL CA Goniometer (Ramé-Hart inc., Mountain Lakes, NJ), were performed with an advancing droplet volume of at least 3 μL and a receding droplet volume of about 2 μL . Contact angles were measured on each side of the droplet and in five different areas on each sample, and the average of these values is reported.

2.1.3.2 Ellipsometry

A Gaertner L-120A ellipsometer, which employs a He-Ne (632.8 nm) laser light source incident at 70° with respect to the surface normal, was employed to measure film thickness. A refractive index of 1.45 [6] was used to calculate the film thickness, and the index was assumed to be isotropic, which introduces some additional uncertainty (anisotropy is expected for the SAMs). Typically, measurements were made on five different areas of each sample and then averaged. To compare thicknesses measured via ellipsometry, computer models of the molecular structures were made using ACD/ChemSketchTM package from Advanced Chemistry Development Inc. (Toronto, ON, Canada).

2.1.3.3 X-ray photoelectron spectroscopy (XPS)

The spectra were acquired using a VSW twin anode x-ray source (Mg/Al) and a VSW CLASS 100 concentric hemispherical energy analyzer (VSW Worldwide, Cheshire, U.K.). Mg $K\alpha$ x-rays ($h\nu = 1253.6$ eV) were used throughout this study. Survey scans (e.g. 100-1200 eV kinetic energy) were

carried out in the fixed retardation ratio (FRR) mode. Detailed scans (range of ~ 20 eV over a single feature) were carried out in the fixed analyzer transmission (FAT) mode. The emission current for the source was 20 mA and the electron voltage was 12 kV. The take-off angle for photoelectrons was 38.5° , unless noted otherwise. For background subtraction, a method first proposed by Shirley [7] was used. Peak areas and peak positions were obtained by fitting the spectra to a product Gaussian-Lorentzian (G-L) function. Specifically during the adsorption kinetics experiments, for the Ti(2p) peak, the data was fit to a G-L function where a ratio of 0.45:1 was assumed for the relative areas of the $2p_{1/2}$ and $2p_{3/2}$ peaks [8].

2.1.4 Adsorption kinetics experiments

2.1.4.1 Experimental apparatus

Characterization of the SAMs via XPS, and their reactions with $\text{Ti}[\text{N}(\text{CH}_3)_2]_4$ were carried out in a custom built ultra-high vacuum (UHV) chamber described in detail earlier in the chapter. Other details of this setup as well as a procedure for determining an absolute flux have been described elsewhere [2]. In the study conducted here, an absolute flux of 2.798×10^{13} molecules- $\text{cm}^{-2}\text{-s}^{-1}$ was calculated. The uncertainty in this flux is on the order of $\pm 30\%$.

2.1.4.2 Experimental procedures

Polycrystalline Au substrates, prepared as described above, were used as a reference standard for XPS. After analysis of a clean Au substrate using XPS [scanning the Au (4f) peak], an Au substrate with the self-assembled monolayer was transferred into the ultrahigh vacuum chamber via a fast-entry load-lock. The sample was brought to temperature (-50 °C or 30 °C) and a base pressure of $< 7 \times 10^{-9}$ Torr was achieved before spectra were obtained to characterize the unreacted SAM, and to quantify its coverage. Subsequently the SAM surface was exposed to $\text{Ti}[\text{N}(\text{CH}_3)_2]_4$ using the doser, where exposures ranged from 60 to 600s. After each exposure, the Ti(2p) peak was scanned in order to quantify the adsorption of $\text{Ti}[\text{N}(\text{CH}_3)_2]_4$ on the SAM surface. This was repeated until saturation of the adlayer was apparent. After saturation was attained, detailed scans of the C(1s), N(1s) and S(2p) peaks were also acquired. For studies of the adsorption kinetics the take-off angle of the photoelectrons was fixed at 38.5°, and a 5mm diameter circular spot on the sample was analyzed. For the experiments involving a variable (0°-64°) take-off angle, a $1 \times 10 \text{ mm}^2$ rectangular slit was used to maintain maximum field of focus. All experiments involving ARXPS were conducted at $T_s = 30 \text{ °C}$. Angle-resolved XP spectra of the Au(4f), S(2p), and C(1s) peaks were also acquired for the unexposed SAMs to probe for the nature of the SAM-substrate chemical interaction. Ti(2p) ARXPS data was acquired after $\text{Ti}[\text{N}(\text{CH}_3)_2]_4$ exposures, to probe the spatial extent of the reaction. Peak areas were obtained by numerical integration following a Shirley background subtraction.

2.2 TiN atomic layer deposition on SiO₂ and modified SiO₂

2.2.1 Description of the thin film deposition system

The TiN thin film deposition experiments employing Ti[N(CH₃)₂]₄ and NH₃ were carried out in a custom made ultra-high vacuum (UHV) chamber designed and constructed by previous members of the Engstrom research group. A more detailed description of the original design and capabilities of the chamber can be found in [9]. AUTOCAD™ has since being used to make a 3D rendering of this chamber [10]. The 3D rendering of the chamber as well as the original schematics of the chamber are shown in Figs. 2-3 and 2-4.

The system is separated into four main compartments plus a load-lock system: the source, ante, main and analysis chambers. A gate valve is placed between the analysis and main chambers and also the source and ante chambers. The valves allow isolation of the separate chambers to facilitate maintenance and modifications of section of the chambers without having to vent the entire system. A translation stage is mounted on the source chamber which has the nozzle at its end. This is the chamber where the supersonic expansion occurs to produce the molecular beam. The center line portion of this supersonic molecular beam is extracted into the ante chamber using a skimmer. After passing through the skimmer, the supersonic beam enters the ante chamber where it is differentially pumped by a high throughput turbomolecular pump (Balzers TPU 62H). The beam is then collimated by a beam defining aperture before entering the main chamber. An effusive component is present due to the partial pressure of the precursor in the ante chamber.

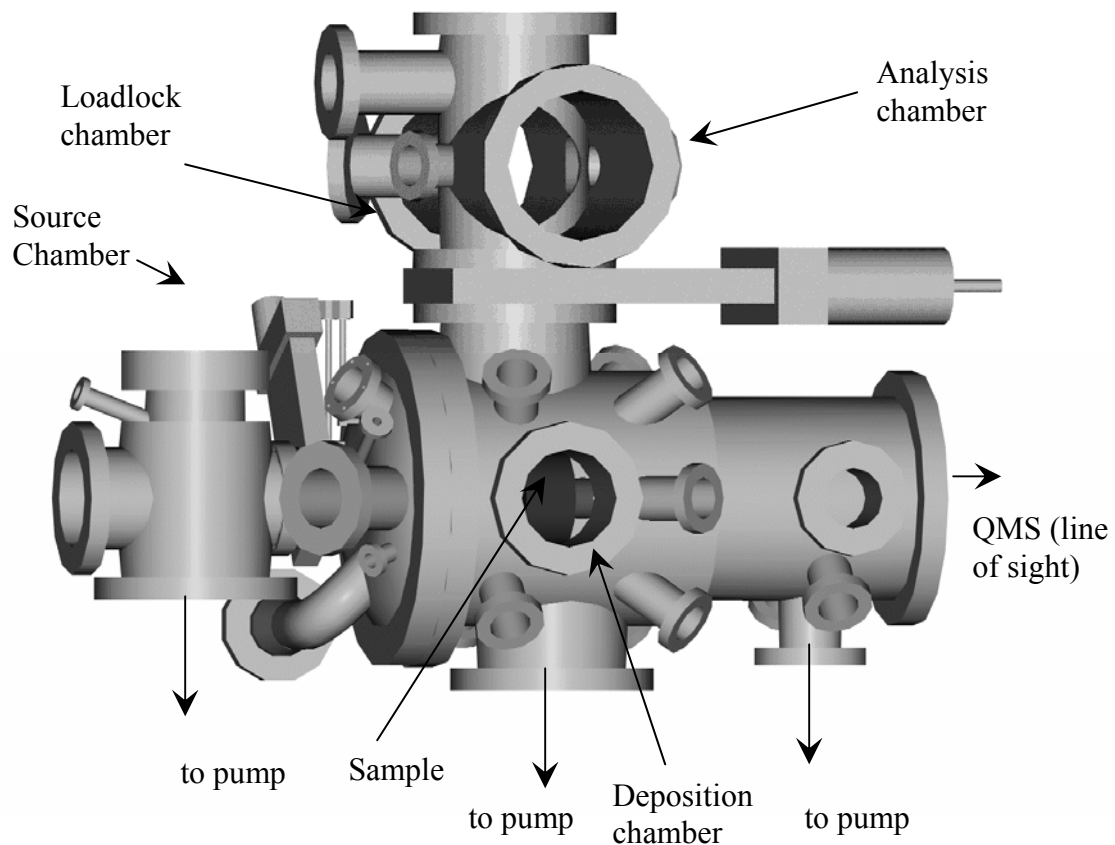


Figure 2-3: AUTOCAD™ rendering of the thin film deposition system employed for the Atomic layer deposition (ALD) experiments (Ref. [10])

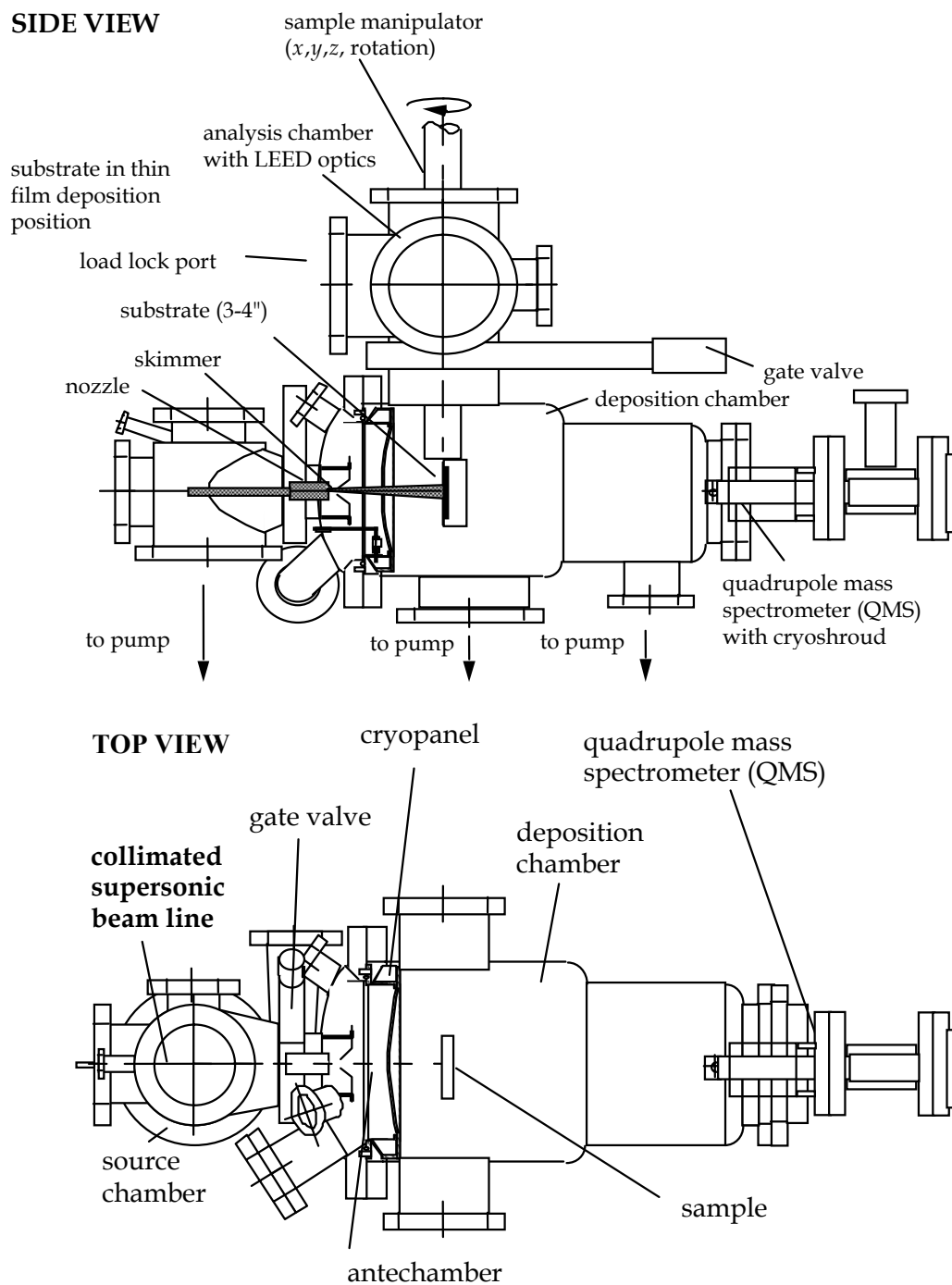


Figure 2-4: Original schematics of the thin film deposition system (Ref.[9])

To further improve the beam to background ratio, a cryoshroud is present in the ante chamber to allow liquid nitrogen cooling. The main chamber is located immediately after the ante chamber and is pumped by a $400 \text{ L}\cdot\text{s}^{-1}$ magnetically levitated turbomolecular pump (Osaka TG 403M). After bakeout at $120 \text{ }^\circ\text{C}$ for 24 - 48 hours, the pressure in the main chamber can routinely reach a base pressure of $< 5 \times 10^{-10}$ Torr.

A Hiden 3F/EPIC quadrupole mass spectrometer (QMS) (Hiden Analytical, UK) is also mounted on the main chamber. The QMS was initially designed to be utilized to perform time-of-flight experiments and can be mounted in a direct line-of-sight position at the end of the chamber or in a cross beam position normal to the beam axis. In the case of TiN deposition experiments, however, the QMS has been mounted in the cross beam position as it is only used to perform routine residual gas analysis and beam intensity/flux measurements. The QMS is mounted in a position that is directly behind the substrate during experiments and is 11.95 inches from the substrate surface and 14.63 inches from the aperture plate separating the main and ante chambers.

The substrates were mounted on platens made out of molybdenum (Mo), which were held in place on a sample manipulator (Thermionics, WA). The manipulator is capable of movements in the x, y, z directions as well as rotational motion in the azimuthal (along the beam axis) and polar (normal to the beam axis) directions. All motions are controlled by stepper motors (except for the y-direction) which are operated using software written in visual basic. The manipulator is capable of moving between the analysis and main chamber using the z translation which has an approximate travel of 16 inches.

The x and y directions have approximately 1 inch travel while the rotational degrees of freedom are capable of complete 360° rotations inside the main chamber.

Two focal points are of interest to this system; focal point 1 located in the main chamber is the exposure position of the sample to the supersonic beam. Focal point 2 is the position in the analysis chamber where the sample can be analyzed by a reverse view low energy electron diffraction (LEED) system (Omicron) as well as placed in position for sample transfer to the loadlock. In focal point 1, the sample is 2.68 inches from the final beam defining aperture along the beam axis. In this position, ports can be utilized to provide close to line of sight gas sources such as atomic hydrogen [11] and NH₃. At focal point 2, the sample can be rotated to face the LEED the load-lock for transfer of sample in and out of the system.

The loadlock is pumped by a 300 L-s⁻¹ magnetically levitated turbo pump (Seiko STPH 300C), and after bakeout for approximately 12 hours, is routinely pumped to 5×10^{-9} Torr. The loadlock and the analysis chambers are separated by a gate valve. Mo platens capable of holding 3- and 4- inch wafers as well as samples of dimensions 1×1 cm² and 1.7×1.7 cm² can be used for different sample sizes. The latter size was used for the experiments described here due to compatibility issues with X-ray photoelectron spectroscopy (XPS) system described earlier. The design of the platens exposes the back of the samples for radiative heating.

The substrates were heated by a 3-inch, 3 kW graphite heater encapsulated in pyrolytic BN for chemical resistance. The heating of samples is achieved by direct radiative heating; no direct contact is made between the sample and the heater. The heater is capable of heating 3- and 4- inch wafers to

temperatures exceeding 850 °C and to as high as 950 °C for short periods of time during annealing processes. A chromel-alumel (K-type) thermocouple is also mounted on the back of the manipulator and is calibrated to the surface temperature by clamping a second thermocouple to the sample surface. The thermocouple is held in place using the retaining rings allowing calibration of the surface temperature to the temperature on the back of the manipulator to be achieved. Details are given elsewhere [10].

The supersonic nozzles are made from 125 μm stainless steel plates with holes of 150 μm diameter. The plates are welded to 1/4 inch electropolished stainless steel tubes with the connections to delivery line made through a 1-1/3 inch CF flanges. The design of the chamber allows the skimmer plate to be positioned in either a forward or back position. The forward position allows for a higher flux of reactants to the substrate and brings the nozzle to approximately 7 inches from focal point 1. The back position can be used for experiments where high flux was not desired and is approximately 14 inches from focal point 1. The forward position was used for all experiments carried out in this study. The skimmers are made from Ni and are 1.5 mm diameter at the opening. The temperature of the nozzle is controlled by a home made heater made from threading Ta ribbon (H-Cross, NJ) through ceramic tubing and wrapping a series of ceramic tubing around the end of the nozzle. The nozzle temperature, T_n , is monitored by spot welding K-type thermocouple wires toward the end of the nozzle. Due to the low vapor pressure of the precursors used, in general, all delivery lines wetted by the precursor were heated to approximately 20°C higher than the bubbler temperature using Ta ribbon. The stagnation pressure was measured using a capacitance manometer (MKS) located approximately 25 inches upstream of the nozzle orifice.

The nozzle assembly is mounted on an x-y-z manipulator to allow alignment of the nozzle.

2.2.2 Beam generation and characterization

The precursor used for TiN deposition was $\text{Ti}[\text{N}(\text{CH}_3)_2]_4$. The vapor pressure curve of this precursor is given in Appendix A. Shown in Fig. 2-5 is a schematic of the bubbler setup. The temperature of the bubbler was controlled by a digital water bath (Precision Instruments). Carrier gas flow was controlled by a 50 sccm mass flow controller (MKS). The entrainment of the precursor in the carrier gas is dependant on the bubbler temperature and the carrier gas flow rate. The carrier gas used was ultra high purity (99.999%) H_2 .

The kinetic energy of the $\text{Ti}[\text{N}(\text{CH}_3)_2]_4$ supersonic beam seeded in H_2 were measured using time-of-flight, TOF, technique in a separate chamber described elsewhere [12]. Briefly, a QMS can be mounted on a translation stage in the axis of the molecular beam. This allows a direct measurement of the velocity, v , of the molecules by measuring the time, t , it takes for the molecules to reach two different positions separated by a distance, L by using $v = L/t$. In an ideal situation where the velocities of all the molecules in a supersonic beam are the same, i.e. the velocity distribution is a delta function; the kinetic energy, E_i , of the molecules is given by:

$$E_i = \frac{1}{2} m_i v^2 \quad (2-1)$$

where, m_i is the weight of the molecule. In real systems, molecules detected at the QMS do not travel at the same velocity and will thus have a distribution of velocities.

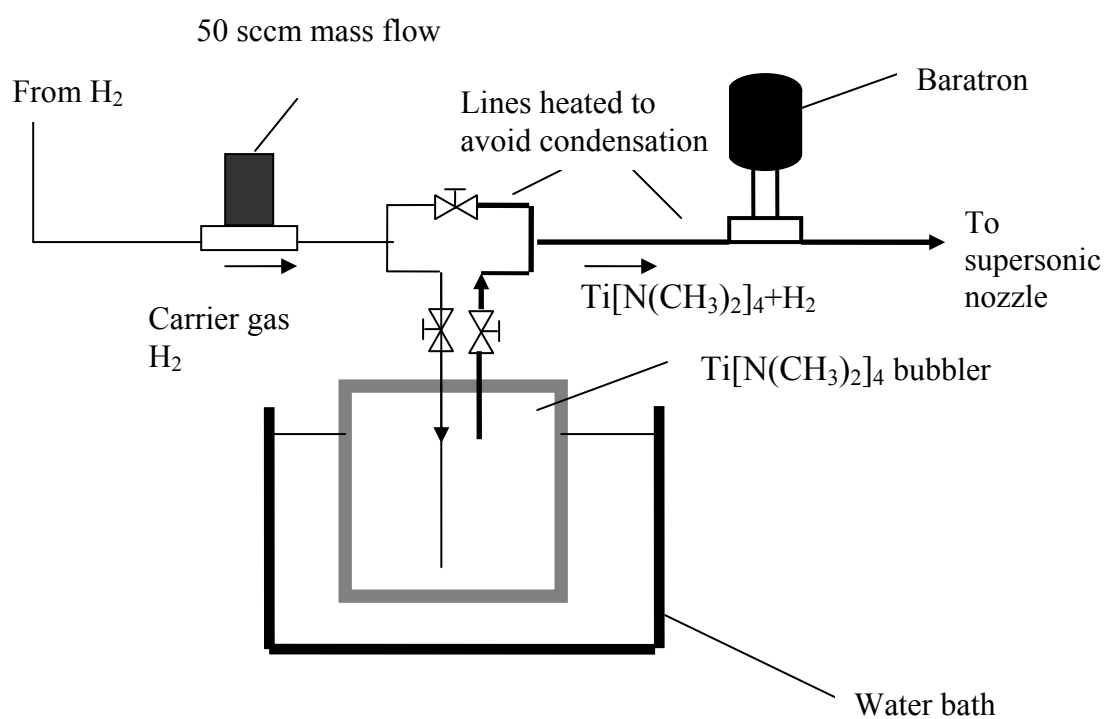


Figure 2-5: Schematic of $\text{Ti}[\text{N}(\text{CH}_3)_2]_4$ delivery setup

Fitting of the velocity distribution to Gaussian functions to calculate the peak velocity and width is required to determine the average translational energy of the molecules. Details of this procedure are given elsewhere [12]. The flux of the $\text{Ti}[\text{N}(\text{CH}_3)_2]_4$ supersonic beam was calibrated against an effusive beam source mounted directly on the main chamber. By measuring the partial pressure produced by a direct effusive beam using the QMS, a calibration curve was made by calculating the corresponding molecular flux from the effusive beam [10]. The effusive beam was produced using a 150 μm nozzle connected directly to the outlet of the $\text{Ti}[\text{N}(\text{CH}_3)_2]_4$ bubbler and connected to a 2-3/4" flange on the main chamber. Pure $\text{Ti}[\text{N}(\text{CH}_3)_2]_4$ was required for the effusive source, therefore no carrier gas was used and the inlet/ dip-tube of the bubbler was sealed off. In this gas flow setup $\text{Kn} \gg 1$ and hence the flow regime is molecular and the flux of gas, F , through the orifice is given by:

$$F = \frac{n}{4} \left(\frac{8kT_{noz}}{\pi m} \right)^{1/2} = \frac{P_{noz}}{(2kT_{noz}\pi m)^{1/2}} \quad (2-2)$$

where m is the mass of a $\text{Ti}[\text{N}(\text{CH}_3)_2]_4$ molecule. By increasing the bubbler temperature T_B , a series of nozzle pressures P_{noz} were produced at a constant T_{noz} of 30 °C. The QMS was used to detect the intensity corresponding to an effusive flux calculated from Eq. 2-2. This calibration was used to get a flux for the supersonic beam from the line of sight intensity QMS measurements.

2.2.3 Sample preparation

Clean SiO_2 substrates were prepared described in detail elsewhere [2], including the formation of the so-called chemical oxide, which possesses a high

density of $-OH$ (*a*) groups. This is the starting surface for the formation of all of the SAMs considered here, which include four SAMs with generally unreactive endgroups and backbones, and four SAMs with reactive endgroups.

2.2.3.1 Chemical oxide

The chemical silicon dioxide samples, or chemical oxide in short, were prepared on single-side polished 4" Si(100) B-dopes wafers. The wafers were scribed and cleaved using a diamond scribe into 16-20 samples of 16.75×16.75 mm size. The samples were then sonicated in chloroform, washed with de-ionized (DI) water, dried with N_2 and dipped in buffered oxide etch (BOE: buffered HF solution) for approximately 1 min. to remove the native oxide. The samples were then immediately dipped in NanostripTM solution (a stabilized mixture of sulfuric acid and hydrogen peroxide) at 75 °C. After 15 min, a thin layer of silicon dioxide (the so-called chemical oxide) is formed on the surface. The etch and oxidation steps are repeated once more. The first step serves as a cleaning step and the second step produces the desired surface. This procedure is believed to produce a consistent chemical oxide film with a thickness of 20-25 Å as measured by ellipsometry.

2.2.3.2 SAM synthesis

All the SAMs used in this work differed not only in film thickness and the surface organic functional group (OFG) but also their microstructure. SAMs possessing both linear and branched back bones were studied. All the synthesis protocol development work involving linear SAMs was done by Dr. Aravind S.

Killampalli [2], and the protocols for branched SAMs were developed by Manish Sharma [13].

2.2.3.2.1 Linear SAMs

In all cases using solution based chemistry, deposition was carried out in a glove box (Unilab, M. Braun Inc.) at the Cornell Nanobiotechnology center (NBTC). The glove box possessed a refrigeration unit capable of $-35\text{ }^{\circ}\text{C}$ and a N_2 atmosphere with < 1 ppm O_2 . All SAM precursors were purchased from Gelest Inc. For octadecyltrichlorosilane [$\text{Cl}_3\text{-Si-(CH}_2\text{)}_{17}\text{-CH}_3$, OTS] and triacontyltrichlorosilane [$\text{CH}_3(\text{CH}_2)_{29}\text{-SiCl}_3$, TTS], a 10 mM solution in anhydrous toluene (Sigma Aldrich, St. Louis, MO) was used. Deposition time was typically 24 - 48 hours. After deposition, the samples were rinsed in toluene, acetone (Sigma Aldrich), and chloroform (Sigma Aldrich) for 5 minutes each. This was followed by a de-ionized (DI) water rinse and dry. SiO_2 modification with $\text{HN}[\text{Si}(\text{CH}_3)_3]_2$, hexamethyldisilazane (HMDS), the thinnest $-\text{CH}_3$ terminated layer, was done from vapor phase using a YES LP-III Vapor Prime Oven (CNF) after successive evacuation and purge cycles to dehydrate the substrate held at $150\text{ }^{\circ}\text{C}$. The other vapor-deposited SAM was the $-\text{CF}_3$ terminated tridecafluoro-1,1,2,2-tetrahydrooctyltrichlorosilane [$\text{CF}_3(\text{CF}_2)_5(\text{CH}_2)_2\text{SiCl}_3$, FOTS]. The MVD-100 (Applied Microstructures Inc., San Jose, CA – CNF tool), was used to deposit the FOTS SAM, where the FOTS vapor (0.6 Torr) and water vapor (7 Torr) were let into the deposition chamber, and the SiO_2 substrates allowed to react for 20 minutes.

For 11-cyanoundecyltrichlorosilane ($\text{Cl}_3\text{-Si-(CH}_2\text{)}_{11}\text{-CN}$) and 10-undecenyltrichlorosilane ($\text{Cl}_3\text{-Si-(CH}_2\text{)}_9\text{-CH=CH}_2$) SAMs, bicyclohexyl (Acros organics, Belgium) was used as the solvent. The former is a precursor to the -NH_2 terminated SAM whereas the latter is used for synthesizing the -OH terminated SAM. For the -CH=CH_2 terminated SAM, chemical oxide substrates were dipped in a SAM solution with approximately 2.5 mM concentration of SAM precursors for 1 hour while for the -CN terminated SAM, the deposition time was 3 minutes. Post deposition, the substrates were washed in DI water and dried with N_2 .

The final step for the -OH and -NH_2 SAMs was the transformation from a -CN terminated SAM to the desired functional group. For the -OH SAM, the -CN terminated SAM was placed in $> 99\%$ pure 1.0 M borane-tetrahydrofuran ($\text{BH}_3\text{-THF}$: Sigma Aldrich) for 2 hours followed by a dry tetrahydrofuran (THF : Sigma Aldrich) rinse, and a 2 min. dip in a 30% H_2O_2 : 0.1 M NaOH (Sigma Aldrich) solution. This final dip forms the OH termination and the substrates were then washed with DI water and dried with N_2 . For the NH_2 SAM, the CN terminated SAM was placed in 1.0 M $\text{BH}_3\text{-THF}$ solution for 4 hours followed by a 1 hour dip in methanol and finally a 15 min. dip in 10% HCl to deprotonate the amine group.

2.2.3.2.2 Branched SAMs

The two SAMs with branched microstructure: $\text{OSi(CH}_3\text{)}_2\text{-(CH}_2\text{)}_3\text{N-}[(\text{CH}_2\text{)}_2\text{CONH(CH}_2\text{)}_2\text{NH}_2\text{]}_2$ (termed here, Gen-1-3C) and $\text{-(O)}_3\text{Si(CH}_2\text{)}_{12}\text{N-}[(\text{CH}_2\text{)}_2\text{CONH(CH}_2\text{)}_2\text{NH}_2\text{]}_2$ (termed here, Gen-1-12C) were formed using a synthetic procedure that is similar to that used to make dendritic

polymers[13,14]. Briefly, the two SAMs differ as to their “anchor” group, 3-aminopropyldimethylethoxysilane (Gelest Inc.) is used for Gen-1-3C, whereas the previously described linear $-\text{NH}_2$ SAM, $(-\text{O})_3\text{Si}(\text{CH}_2)_{12}\text{NH}_2$ is used for Gen-1-12C. The substrates, treated with either anchor, are sequentially reacted with methyl acrylate ($\text{CH}_2=\text{CH}(\text{CO})\text{OCH}_3$, >99% stabilized, Sigma Aldrich), and ethylenediamine ($\text{H}_2\text{N}(\text{CH}_2)_2\text{NH}_2$, >99.5%, redistilled, SigmaAldrich) to get to the so called Gen-1 (first generation dendrimer) SAM, with a higher density of terminal $-\text{NH}_2$ OFGs. Again, the starting surface in all these cases was chemical oxide.

2.2.3.2.3 SAM characterization

Contact angle measurements, ellipsometry, X-ray photoelectron spectroscopy, and atomic force microscopy (AFM) were employed to characterize the SAMs. The details for contact angle measurements can be found in the characterization section for thiophene SAMs (section 2.1.3.1). Ellipsometry measurements are also described in detail earlier. For these measurements differences are in the value of optical constants chosen compared to the case of thiophene SAMs. A value of 1.46 has been reported for the refractive index of chemical oxide [15]. A refractive index of 1.46 was used in this work for chemical oxide and SAM taken together. The sensitivity of the measured thickness to the value assumed for refractive index was small – change of 0.05 in the latter resulted in less than 1 Å change in the former. The measurements were taken at four different spots on each sample. The thickness values are the average increase in thickness in going from chemical oxide to the SAM in each case. The estimated error in these measurements is $\pm 2\text{Å}$.

2.2.3.2.3.1 X-ray photoelectron spectroscopy (XPS)

XPS was carried out using a VSW twin anode x-ray source (Mg/Al) and a VSW CLASS 100 concentric hemispherical energy analyzer (VSW Worldwide, Cheshire, U.K.). Mg K α x-rays (1253.6 eV) were used throughout this study. Survey scans (e.g. 0-1200 eV kinetic energy) were carried out in the fixed retardation ratio mode, whereas detailed scans (range of ~ 20 eV over a single feature) were carried out in the fixed analyzer transmission mode. The emission current for the source was 20 mA and the electron voltage was 12 kV. Short scans (0.5 eV/s, 10 cycles) were used for C (1s), O (1s) and Si (2p) peaks. The take-off angle for photoelectrons was 38.5 $^\circ$ with respect to the surface normal for experiments examining the kinetics of adsorption. The Shirley background subtraction method was used in all analyses of the peaks. Peak areas and peak positions were obtained by fitting the spectra to a product Gaussian-Lorentzian (G-L) function of the form:

$$f(x) = \frac{h}{[1 + M(x - x_0)^2 / \beta^2] \exp\left\{(1 - M)[(\ln 2)(x - x_0)^2] / \beta^2\right\}} \quad (2-3)$$

where h is peak height, M is the mixing ratio or the fractional contribution of the Gaussian and Lorentzian components, x_0 is the peak center and β is a parameter that is nearly 0.5 (FWHM). A value of 0.9 was used for M for all peaks.

2.2.3.2.3.2 Atomic force microscopy (AFM)

Images were acquired with a Dimension 3100 scanning probe microscope (Veeco Instruments, Woodbury, NY) in tapping mode using Tap 300 SPM probes (Nanodevices Inc., Santa Barbara, CA). Typical images obtained were $0.5 \times 0.5 \mu\text{m}^2$ and subjected to a second order plane fit using Nanoscope software (v 5.3)

2.2.4 Deposition and characterization of TiN thin films

The experiments were carried out in a custom-built ultra-high (UHV) chamber that has been described in detail earlier. The base pressure of the chamber is typically below 1×10^{-9} Torr. A few crucial modifications were made to the system in order to carry out the ALD experiments, namely, the addition of an effusive beam doser for the delivery of NH_3 which consists of a glass microcapillary array (GCA, Burle Technologies Inc., Lancaster, PA). With the high number of cycles (>200) likely involved in ALD experiments, automation of the reactant cycling was necessary. Automation software was developed using LabView 6.0 (National Instruments, Austin, TX)[10]. $\text{Ti}[\text{N}(\text{CH}_3)_2]_4$ was delivered to the supersonic beam nozzle (150 μm orifice) using H_2 as a carrier gas. The doubly differentially pumped beam passes through a skimmer (1.5 mm aperture, Precision Instrument Services, Inc.) into an ante chamber and through an aperture ($9 \times 9 \text{ mm}^2$), producing a well defined beam spot on the substrate at normal incidence. The beam could be blocked using a shutter in the antechamber, facilitating precise exposures to the substrate. In this study, the kinetic energy of the $\text{Ti}[\text{N}(\text{CH}_3)_2]_4$ molecules was

fixed at 2.07 eV. The flux was 2.2×10^{15} molecules-cm⁻²-s⁻¹. The reactant NH₃ (Airgas, VLSI grade) was introduced via an effusive beam doser, which consists of a glass microcapillary array (GCA, Burle Technologies Inc., Lancaster, PA), and produces a uniform flux over the substrate surface (2.8×10^{18} molecules-cm⁻²-s⁻¹) while achieving a good beam-to-background ratio. The gating of the NH₃ flux was achieved by employing a vent-run configuration controlled by a pneumatic valve. In these experiments, the total pressure was typically no greater than 10⁻⁵ Torr (i.e., molecular flow regime). Thus, a simple pump out period was used to separate the flows of the two reactants, as a purge gas step is nonsensical in this flow regime. Cycle times of the reactants were computer controlled, and a typical cycle was: 10 s {Ti[N(CH₃)₂]₄} / 15 s (pump-out) / 30 s (NH₃) / 100 s (pump-out). During the experiments the sample could be periodically translated perpendicular to the Ti[N(CH₃)₂]₄ beam axis. If this is done during the Ti[N(CH₃)₂]₄ cycle, it produces areas / terraces on the substrate surface representing different exposure times to Ti[N(CH₃)₂]₄. If it is done subsequent to “n” total cycles, areas representing a different total number of cycles will be produced. Such terraces for a typical TiN ALD experiment have been illustrated in Fig. 2-6.

Measurements of the thickness of TiN films were performed with an ellipsometer. For TiN, a refractive index value of 1.7 was used. AFM images obtained were of size $0.5 \times 0.5 \mu\text{m}^2$ and subjected to a second order plane fit using Nanoscope software (v 5.0). *Ex situ* XPS employed to determine the composition of the TiN films. Rutherford backscattering spectrometry (RBS) was also employed for film thickness and composition measurements. A 4 MeV He⁺ beam was employed at a total dose of 5×10^8 counts. The analysis of the acquired spectra was carried out using the RUMP simulation program [16].

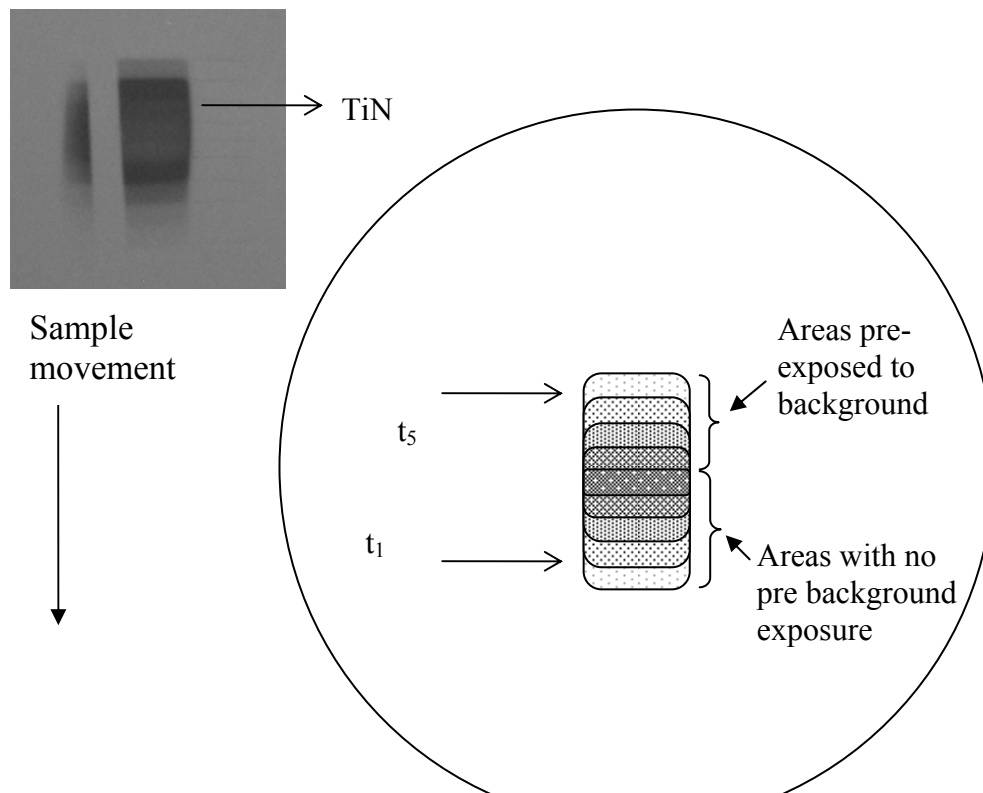


Figure 2-6: Schematic illustrating the technique of producing multiple areas of different exposure times on a single sample. Also shown is an example of a TiN film grown on SiO₂ at a substrate temperature of 257 °C with five such terraces corresponding to different Ti[N(CH₃)₂]₄ exposure times.

An FEI Tecnai TF20 high resolution scanning transmission electron microscope (STEM) was employed to further characterize the films. This microscope was also used to acquire high energy resolution electron energy loss spectroscopy (HREELS) data.

2.2.5 Deposition and characterization of TiN thin films on hyperbranched polymeric films and low κ dielectric substrates

2.2.5.1 Hyperbranched polymers

In this work, a different strategy was used to multiply and/or amplify the density of nucleation sites for the subsequent deposition of inorganic (metallic, oxide, carbide or nitride) thin films. Interfacial organic layers (IOLs) possessing branched molecular backbones, where each branch is terminated by a reactive functional group were studied. Here a covalently grafted hyperbranched polyglycidol (poly-G) thin film is grown on SiO₂ surface using anionic ring-opening multibranching polymerization of glycidol [17]. The protocol was developed by Manish Sharma. SiO₂ was prepared as described earlier in this chapter. The surface was first activated with a strong base, sodium methoxide (Sigma Aldrich), following which branched poly-G thin films were grown on the surface by a treatment with glycidol (Sigma Aldrich) at 120 °C. The thickness of the film was obtained using ellipsometry and was found to be linearly dependent on the reaction time in glycidol. The poly-G layers were further characterized using contact angle measurements and X-ray photoelectron spectroscopy. The nucleation and growth of titanium nitride (TiN, using Ti[N(CH₃)₂]₄ and NH₃) thin films on these branched microstructure

IOLs using atomic layer deposition was attempted as described earlier. The TiN films were again characterized employing ellipsometry, XPS, RBS, AFM, and STEM.

2.2.5.2 Low κ dielectric substrates

Low κ substrates were supplied by our collaborator at Intel Corporation (Dr. Adrian Lavoie, Components Research Group, Hillsboro, OR). The films were characterized employing contact angle measurements, ellipsometry, XPS, and AFM. The as received films had the following specifications: 4500 Å thickness, 25% porosity, 2.6 nm pore diameter, and $\kappa = 2.5$.

ALD TiN was attempted on as received / untreated low κ substrates and the films were characterized using ellipsometry, AFM, and STEM. The deposition experiments were also performed on 15 min poly-G films (deposited as described earlier) on the low κ substrates. To facilitate the poly-G deposition, low κ substrates were activated with 2 s oxygen plasma (Harrick plasma cleaner, NBTC). This duration of plasma exposure was found to be the optimum for activating the surface without changing the properties of the low κ films significantly. The motivation behind this work was to study the efficacy of using these hyperbranched poly-G films as pore sealants for preventing TiN from penetrating the porous dielectric films. The TiN films were again characterized using ellipsometry, AFM, and STEM.

2.3 References

1. Xia, L. -Q.; Jones, M. E.; Maity, N.; Engstrom, J. R. *J. Vac. Sci. Technol. A* **1995**, *13*, 2651.
2. Killampalli, A. S.; Ma, P. F.; Engstrom, J. R. *J. Am. Chem. Soc.* **2005**, *127*, 6300.
3. Sarkar, A.; Kamath, S.P.M; Bhagwat, L.; Babu, K.N.; Rajalakshmi, K.; Talwar, S.S. *Indian J. Chem.* **1991**, *30B*, 360.
4. *Molecular Electronics: Commercial Insights, Chemistry, Devices, Architecture and Programming*; Tour, J. M.; World Scientific: New Jersey, **2003**.
5. Borch, R.F.; Hassid, A. I. *J. Org. Chem.* **1972**, *37*, 1673.
6. Walczak, M. M.; Chung, C.; Stole, S. M.; Widrig, C. A.; Porter, M. D. *J. Am. Chem. Soc.* **1991**, *113*, 2370.
7. Shirley, D. A. *Phys. Rev. B* **1972**, *5*, 4709.
8. Lee, H.; Lee, S. M.; Ada, E. T.; Kim, B.; Weiss, M.; Perry, S. S.; Rabalais, J. W. *Nuclear Instruments and Methods in Physics Research B* **1999**, *157*, 226.
9. Roadman, S. E.; Maity, N.; Carter, J. N.; Engstrom, J. R. *J. Vac. Sci. Technol. A* **1998**, *16*, 3423.
10. Paul F. Ma, PhD thesis, Cornell University, **2004**.

11. Schroeder, T. W.; Lam, A. M.; Ma, P. F.; Engstrom, J. R.; *J. Vac. Sci. Technol. A* **2004**, *22*, 578.
12. Todd W. Schroeder, PhD thesis, Cornell University, **2003**.
13. Sharma, M.; Dube, A.; Engstrom, J. R., in preparation
14. Tomalia, D. A.; Baker, H.; Dewald, J.; Hall, M.; Kallos, G.; Martin, S.; Roeck, J.; Ryder, J.; Smith, P. *Polym. J.* **1985**, *17*, 117.
15. *Handbook of Optical Constants of Solids*; Palik, E.D., Ed.; Academic Press: New York, **1985**.
16. Dolittle, L. R. *Nucl. Instrum. and Meth.* **1986**, *15*, 227.
17. Khan, M.; Huck, W. T. S. *Macromolecules* **2003**, *36*, 5088.

3. Covalent attachment of a transition metal coordination complex to functionalized oligo(phenylene-ethynylene) self assembled monolayers

3.1 Overview

The reaction of tetrakis(dimethylamido)titanium, $\text{Ti}[\text{N}(\text{CH}_3)_2]_4$, with *N*-isopropyl-*N*-[4-(thien-3-ylethynyl) phenyl] amine and *N*-isopropyl-*N*-(4-{[4-(thien-3-ylethynyl) phenyl]ethynyl}phenyl) amine self-assembled monolayers (SAMs), on polycrystalline Au substrates, has been studied. The structure of the SAMs themselves has also been investigated. Both molecules form SAMs on polycrystalline Au bound by the thiophene group. The longer molecular backbone molecule forms a denser SAM, with molecules characterized by a smaller tilt angle. X-ray photoelectron spectroscopy (XPS) and angle-resolved XPS have been employed to examine the kinetics of adsorption, the spatial extent of reaction, and the stoichiometry of reaction. For both SAMs, adsorption is described well by first-order Langmuirian kinetics, and adsorption is self-limiting from $T_s = -50$ to 30 °C. The use of angle-resolved XPS clearly demonstrates that the $\text{Ti}[\text{N}(\text{CH}_3)_2]_4$ reacts exclusively with the iso-propylamine end group via ligand exchange, and there is no penetration of the SAM, followed by reaction at the SAM-Au interface. Moreover, the SAM molecules remain bound to the Au surface via their thiophene functionalities. From XPS it was concluded that, in both cases, approximately one $\text{Ti}[\text{N}(\text{CH}_3)_2]_4$ is adsorbed per two SAM molecules.

3.2 Introduction

Most modern electronic devices are solid state devices, the active components of which are constructed essentially entirely of inorganic materials—semiconductors, metals, various oxides, nitrides and silicides. To date, excepting important applications such as photo-resists in lithography, organic materials have played a rather secondary role in this technology. This situation is changing and considerable interest has developed in the past 5-10 years concerning the use of small molecules in active components of electronic circuitry—the field is known as molecular scale electronics or molecular electronics [1]. A major challenge in this area is devising chemistries and processes that can bring together these two diverse materials sets, inorganic and organic, without doing damage to the delicate organic structures and functionalities.

Attempts to construct devices incorporating molecules have taken many designs: break junctions, formed mechanically [2] and electrically [3], nanopores [4] and cross-bar arrays [5] are perhaps the most well-known examples. In all these cases, the so-called bottom contact is formed using chemically specific adsorption, alternatively referred to as self-assembly. The solution phase deposition of organothiols on gold [6] is a well-developed chemistry for forming well ordered self-assembled monolayers (SAMs). These SAMs can have rigid backbones comprised of aromatic fragments [7] or “floppy” backbones comprised of aliphatic fragments [8]. The former, including oligo(phenylene-ethynylene) SAMs, have attracted interest due to their structure, which should promote facile electrical conduction along their molecular backbone. Indeed, conjugated SAMs have been used for making

sensors [9], rectifiers [10, 11], and molecular switches [12]. A common motif in these devices is an electrode/molecule/electrode microstructure, formed by sequential deposition and patterning steps [4, 5, 11, 12].

It is important to note, however, that with all these approaches a second or top contact with the SAM (an inorganic-on-organic interface) is required to fabricate functional molecular electronic devices. The tip of either a conducting atomic force microscope (c-AFM) or a scanning tunneling microscope (STM) has been used to make this contact [13-15]. This approach can work well for fundamental studies of single to several hundred molecules, but it obviously does not make a permanent contact and is, in general, unsuitable for fabricating arrays of devices. Formation of inorganic or metal thin films on SAMs, whether explicitly for top contacts or not, has mostly involved evaporative deposition in vacuum or liquid phase deposition. Vapor deposition of elemental metals (e.g., Ag, Cu, Ti, Al, Fe, Cr and Au) on SAMs possessing different terminal organic functional groups (OFGs) such as $-\text{CH}_3$, $-\text{OH}$, $-\text{COOH}$, $-\text{COOCH}_3$, $-\text{CN}$ and $-\text{SH}$ has been studied extensively [16-24]. In many cases, due to the rather unspecific reactions of many of these elemental metals, mixed adlayers were formed because reactions occurred not only with the OFG tail, but also apparently with the SAM backbone and head groups. Such penetration of the organic monolayer by the metal species, the extent of which depended on the terminal OFG as well as the metal studied, is unacceptable concerning most devices envisaged for molecular electronics. Formation of inorganic-on-organic interfaces via liquid phase thin film deposition has also been problematic. TiO_2 thin films have been deposited on alkyltrichlorosilane SAMs possessing different terminal OFGs [25-28]. The films, in most instances, were rough and exhibited poor adhesion, while molecular level details concerning the

interfaces were absent from these studies. Finally, X-ray photoelectron spectroscopy (XPS) revealed that the films suffered from carbon and chlorine contamination [28]. Formation of inorganic-organic interfaces via the use of transition metal coordination complexes holds tremendous promise. A key is to tailor both the terminal OFG and the transition metal complex such that they react with each other in a specific fashion. Growth that is self-limiting may also be desirable and feasible with this approach, as uncontrolled continuous deposition might lead to degradation of the interface. There are a handful of studies that have examined the deposition of metal thin films on SAMs (thiols), including Au growth via $[(\text{CH}_3)_3\text{P}]\text{AuCH}_3$ [29], Pd growth via $\text{Cp}(\text{allyl})\text{Pd}$ [29, 30], and Al growth via $[(\text{CH}_3)_3\text{N}]\text{AlH}_3$ [31, 32]. In the case of Au and Pd deposition, the selectivity of growth and film morphology were examined. In the case of Al deposition [31], interfacial chemistry was examined using XPS, but an explicit examination of the kinetics of adsorption was not attempted. Recently, the reaction of a transition metal coordination complex with SAMs [33], in this case, the reaction of tetrakis(dimethylamido)titanium, $\text{Ti}[\text{N}(\text{CH}_3)_2]_4$, a TiN precursor [34-41], with alkyltrichlorosilane SAMs possessing $-\text{OH}$, $-\text{NH}_2$ and $-\text{CH}_3$ terminal OFGs was reported. Using XPS it was found that the reaction was self-limiting in all these cases. Using angle-resolved XPS (ARXPS), to probe the spatial extent of the reaction, it was found that penetration of the SAM followed by reaction at the SAM/substrate interface occurred in the case of the $-\text{CH}_3$ SAM. In case of the $-\text{NH}_2$ SAM, however, no evidence of penetration was found, and reaction was confined to the terminal $-\text{NH}_2$ group.

In this work, the reaction of $\text{Ti}[\text{N}(\text{CH}_3)_2]_4$ with adsorbed molecules that possess specially chosen head and tail groups, and backbone, has been

considered. In particular, a thiophene headgroup has been chosen for its affinity for Au surfaces, an isopropylamine terminal OFG to react with $\text{Ti}[\text{N}(\text{CH}_3)_2]_4$, and a phenylene ethynylene backbone for electrical conduction. Although a specific device function is not assumed here, this scheme leads to the aforementioned electrode/molecule/electrode structural motif used in molecular switches [5, 12], and rectifiers [11]. Thiophenes offer potential advantages over the related thiols. For example, thiols may be reduced to thiolates [42] or oxidized to disulfides [43], whereas the likelihood of a thiophene group participating in reactions other than simple molecular adsorption, under our reaction conditions, is quite small due to its stable ring structure. Comparative studies of thiophene SAMs and thiol SAMs on Au are relatively scarce. STM has been used to demonstrate that thiophene can form well-ordered monolayers on Au(111)[44]. In another study, the structural evolution of a thiophene SAM on Au(111) was examined by Fourier-transform infrared reflection absorption spectroscopy [45]. The formation of the SAM was found to occur in two stages: in the first stage, thiophene orients parallel to the Au surface; in the second stage, the molecular orientation changes to upright. In another work [46], XPS revealed that the sulfur in thiophene chemically interacts with Au, indicated by a shift in the binding energy of the $\text{S}(2p_{3/2})$ by 2-3 eV.

Herein is described a detailed study of the following: the synthesis and formation of SAMs possessing a molecular backbone that should facilitate facile electrical conduction and an endgroup that should bind in a specific fashion to a Au substrate; the reactions between the organic functional tailgroups of these SAMs [$-\text{NH}(i\text{-C}_3\text{H}_7)$] and a transition metal coordination complex, $\text{Ti}[\text{N}(\text{CH}_3)_2]_4$. XPS was used to probe the nature of SAMs that were formed, quantify the kinetics of adsorption of the Ti complex on these layers,

and determine the specificity and/or spatial extent of reaction between the Ti complex and the SAMs. Ultimately, this strategy could be used to make “sandwich” structures comprising electrode/molecule/electrode, or any of a variety of structures where precisely fabricated inorganic-organic interfaces are key structural elements.

3.3 Experimental methods

Complete details concerning the experimental procedures employed here are given in chapter 2, and only give brief summary is given here. The thiophene ligands, *N*-isopropyl-*N*-[4-(thien-3-ylethynyl) phenyl] amine and *N*-isopropyl-*N*-(4-{[4-(thien-3-ylethynyl) phenyl]ethynyl}phenyl) amine were synthesized by Dr. Andrew Chadeayne. Details of the synthetic procedure, as well as all assignments of the chemical shifts from NMR, are provided in chapter 2. One ligand has one phenyl ring in its backbone whereas the other has two. From now on, a shorthand notation of **1P** for the former and **2P** for the latter will be use, in an obvious reference to the number of phenyl groups in the molecule. Self-assembled monolayers of these thiophene ligands and 4-aminothiophenol (Sigma Aldrich) were prepared on evaporated gold substrates via a liquid phase deposition process. Contact angle measurements, ellipsometry, and X-ray photoelectron spectroscopy (XPS) were employed to characterize the order, thickness, and composition of these monolayers. Characterization of the SAMs via XPS, and their reactions with $\text{Ti}[\text{N}(\text{CH}_3)_2]_4$ were carried out in a custom built ultra-high vacuum (UHV) chamber that is described in detail elsewhere [47].

3.4 Results and discussion

3.4.1 Characterization of the SAMs

Contact-angle measurements, ellipsometry and XPS were used to characterize the layers formed from the adsorption of the two molecules of interest on polycrystalline Au. In Table 3-1, the data is presented for advancing and receding contact angles of water, as well as the hysteresis for both of the SAMs. As may be seen, a smaller contact angle was observed for the **1P** SAM in comparison to the **2P** SAM. These results are in qualitative agreement with results reported for thiol SAMs possessing conjugated backbones of varying length [48]. In particular, in this work, it was reported that increasing the chain length of the conjugated thiols reduced the tilt angle, which in turn, resulted in a more hydrophobic character of the longer ring system. Indeed, the ellipsometric data, also shown in Table 3-1, confirms this picture. The measured ellipsometric thicknesses for the **1P** and **2P** SAMs are $6.6 \pm 0.4 \text{ \AA}$, and $16.6 \pm 0.8 \text{ \AA}$ respectively, vs. estimated lengths (from molecular models) of 12.6 \AA and 19.6 \AA for the molecules themselves. These results are in good qualitative agreement with data for other conjugated thiol SAMs [48], and the larger tilt angle implicated for the shorter **1P** SAM can be attributed to weaker intermolecular forces due to fewer aromatic rings in the backbone [49].

Survey XP spectra have been collected from both SAMs and the following peaks have been observed: Au(4f), N(1s), C(1s) and S(2p). The survey scan was followed by detailed scans for all of these. The C(1s) feature can be used to estimate the absolute coverage of the SAMs.

Table 3-1: Properties of self-assembled monolayers

SAM	Contact angle			Thickness (ellipsometry)	Molecular length	Density (cm ⁻² , XPS)
	advancing	receding	hysteresis			
1P	56° ± 3°	41° ± 2°	15°	6.6 ± 0.4 Å	12.6 Å	2.11 ± 0.87 × 10 ¹⁴
2P	66° ± 1°	56° ± 2°	10°	16.6 ± 0.8 Å	19.6 Å	3.42 ± 0.79 × 10 ¹⁴
4-aminothiophenol	27° ± 3°			10.7 ± 0.8 Å	5.6 Å	3.24 ± 0.91 × 10 ¹⁴

To accomplish this one needs to account for the photoelectron cross-sections, σ , for the C(1s) and the Au(4f_{7/2}) peaks, the analyzer transmission, T(E), which is inversely proportional to the kinetic energy (E=968.6 and 1169.6 eV, respectively), the atomic density of the two elements, N , and the inelastic mean free path, λ , for the photoelectrons. Concerning these, $\sigma_{\text{Au}}/\sigma_{\text{C}} = 9.8$ [50], $N_{\text{Au}} = 5.88 \times 10^{22}$ atoms-cm⁻³ [51], and $\lambda_{\text{Au}} = 15.5$ Å [52]. The atomic density of C in the SAM depends on the density of the SAM, n_{SAM} (molecules-cm⁻²), and the mean spacing between C in the backbone, d_{C} . The integrated intensity of the Au (4f_{7/2}) peak for a clean Au substrate is proportional to $\sigma_{\text{Au}}N_{\text{Au}}\lambda_{\text{Au}}T(E_{\text{Au}})$. For the C(1s) peak, the finite thickness of the layer must be accounted for, and the integrated intensity is proportional to $\sigma_{\text{C}}(n_{\text{SAM}}/d_{\text{C}})\lambda_{\text{C}}T(E_{\text{C}})[\exp(-n d_{\text{C}}/\lambda_{\text{C}} \cos \theta)]$, where n is the number of C in the SAM backbone and θ is the takeoff angle. For the inelastic mean free path of the C(1s) photoelectrons $\lambda_{\text{C}} = 24.5$ Å was used [53]. Making use of these expressions, the density, n_{SAM} , was computed for both the SAMs and these values are also given in Table 3-1. Given the assumptions made here to calculate these values, the absolute accuracy is estimated to be approximately $\pm 30\%$. A higher density (3.4×10^{14} vs. 2.1×10^{14} molecules-cm⁻²) is observed for the **2P** SAM. This can again be attributed to the fact that more aromatic rings lead to higher intermolecular forces which, in turn, account for the smaller tilt and higher packing density [49]. A density of 4.5×10^{14} molecules-cm⁻² has been reported for a SAM of 4-[4'-(phenylethynyl)-phenylethynyl]-benzenethiol on Au [54], which has a similar molecular structure to the **2P** SAM, but possesses a different head group, and lacks the terminal isopropyl amine group, which in this case may hinder packing of the molecules. For a molecule similar to the **2P** molecule, but

lacking the isopropylamine terminal group, molecular dynamics simulations done by Haran [55], predict the coverage to be $\sim 4.01 \times 10^{14}$ molecules-cm⁻².

Angle-resolved XPS has been used to probe the SAMs, which is particularly valuable concerning non-invasive depth profiling of the layers. ARXPS of the Au(4f), S(2p), and C(1s) peaks have been obtained. The take-off angle was varied from 0° to 64°. Plotted in Fig. 3-1(a) are the Au(4f) integrated intensities as a function of the take-off angle, for both the SAMs considered here. The data can be modeled as a semi-infinite (Au) substrate that is covered by a uniform two dimensional SAM film: $I(\theta) = I_0 \exp(-d_{\text{SAM}}/\lambda \cos\theta)$, where I_0 is the unattenuated emission achieved at normal take-off angle. The smaller integrated intensities for the **2P** SAM at all take-off angles are consistent with the fact that more attenuation of the Au (4f) photoelectrons is occurring due to the presence of a thicker (and denser) overlayer. In terms of the parameters, from these data we find $d_{\text{SAM}}/\lambda = 0.47 \pm 0.01$ and 0.49 ± 0.02 for the **1P** and **2P** SAM, respectively. These values for the parameters, as well as all values obtained in this work from ARXPS, are also given in Appendix B. In Fig. 3-1(b) the S(2p) integrated intensity is displayed as a function of the take-off angle for both SAMs. In this case, it is assumed that sulfur atoms are arranged in a 2-D plane at a distance d from the SAM-vacuum interface. The expression is given by $I(\theta) = (I_0 / \cos\theta) \exp(-d/\lambda \cos\theta)$, where again I_0 is the unattenuated emission achieved at normal take-off angle. A fit to the data shown in Fig. 3-1(b) gives $d/\lambda = 1.69 \pm 0.57$ and 2.05 ± 0.65 for the **1P** and **2P** SAM, respectively. These values indicate that the sulfur is a significant distance beneath the surface, presumably at the SAM-Au interface. A discussion of the physical meaning of the absolute values is given later. Results from ARXPS of the C(1s) peak for both the SAMs are presented in Fig. 3-1(c).

Figure 3-1: Integrated peak areas as a function of take-off angle for the **1P** (filled symbols) and **2P** SAMs (open symbols) on polycrystalline Au for the (a) Au(4f), (b) S(2p) and (c) C(1s) features from XPS at $T_s = 30$ °C. The smooth curves represent fits of the data to models that are described in the text. The parameters found from these fits are given in the text or Appendix B.

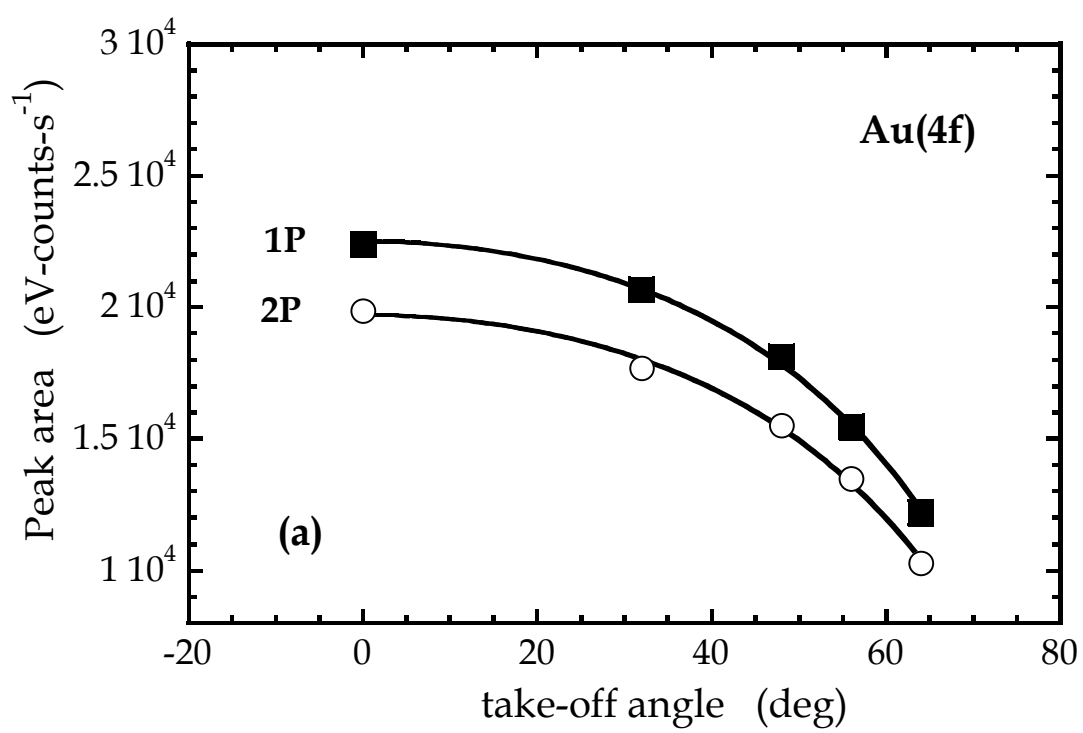
(a)

Figure 3-1 (continued)

(b)

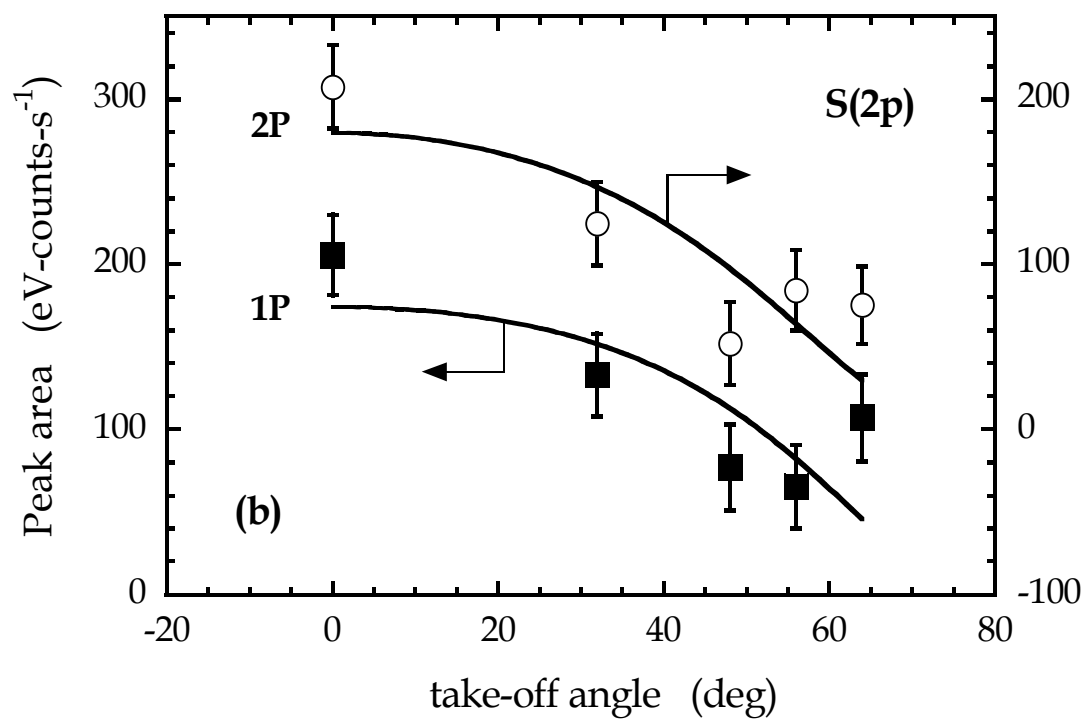
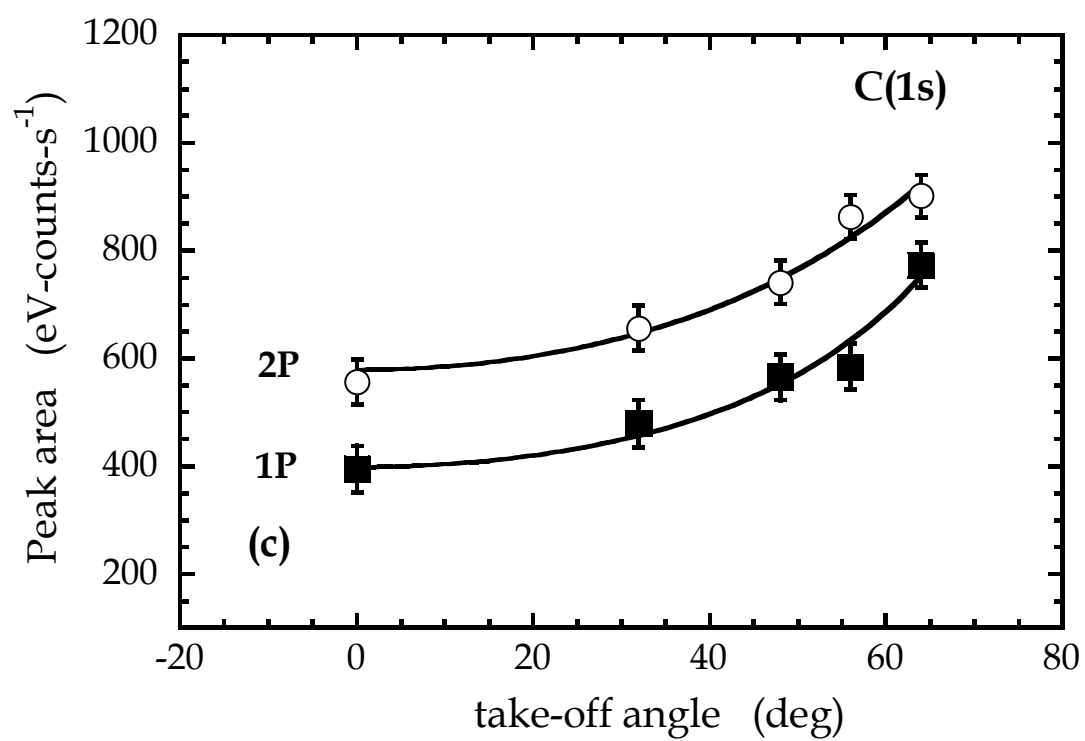


Figure 3-1 (continued)

(c)



The following model was used: $I(\theta) = I_0 [1 - \exp(-d_{\text{SAM}} / \lambda \cos\theta)]$, which assumes the C is present at some constant density in a thin film at the surface and where I_0 is the C(1s) emission from a semi-infinite SAM film. Here it was found that $d_{\text{SAM}}/\lambda = 0.32 \pm 0.14$ and 0.68 ± 0.12 for the **1P** and **2P** SAM, respectively. One final set of experiments was conducted to further characterize the SAMs. In these experiments, first a scan for Au(4f) was completed on a clean Au substrate, and this was followed directly by another scan on a Au substrate covered by the SAM. Again assuming the SAM covers the surface uniformly this gives directly the quantity: $I(\theta)/I_0 = \exp(-d_{\text{SAM}}/\lambda \cos\theta)$. We find that $d_{\text{SAM}}/\lambda = 0.21 \pm 0.01$ for the **1P** SAM and 0.29 ± 0.01 for the **2P** SAM. These values are in qualitative agreement with those found in Fig. 3-1(a), (b) and (c). One explanation for the disparity in d_{SAM}/λ values could be a difference in attenuation between the Au photoelectrons and those arising from C and S. For example, as C and S are both part of the SAM molecules, attenuation by the remaining portion of the molecule is assured. Such is not the case for the Au substrate, particularly for a less than well packed SAM overlayer. In any event these results are consistent with a SAM where the molecules are bound exclusively by the thiophene end of the molecule.

3.4.2 Reaction of $\text{Ti}[\text{N}(\text{CH}_3)_2]_4$ with the SAMs

The reaction of $\text{Ti}[\text{N}(\text{CH}_3)_2]_4$ with the clean Au substrate, and the **1P** and **2P** SAMs has been examined using XPS. In previous work on trichlorosilane based SAMs [33], the starting substrate was found to be the most reactive. In this work the substrate was “chemical” silicon oxide, which has a high density of silanol groups at the surface. To determine if similar phenomenon was

possible in the systems examined here, the reaction of $\text{Ti}[\text{N}(\text{CH}_3)_2]_4$ with a clean Au substrate at $T_s = 30\text{ }^\circ\text{C}$ was studied. After a 1 hour exposure to $\text{Ti}[\text{N}(\text{CH}_3)_2]_4$ (dose of $\sim 1.01 \times 10^{17}$ molecules- cm^{-2}) a Ti(2p) spectra was acquired, which is displayed in Fig. 3-2. In Fig. 3-2 the results of a 30 min. exposure of the **2P** SAM to $\text{Ti}[\text{N}(\text{CH}_3)_2]_4$ are also displayed. It can be clearly seen that there are only trace amounts of Ti present on the clean Au substrate in comparison to the surface with the **2P** SAM. The area of the peaks can be used to estimate the surface density of Ti. First, a Ti(2p) spectrum was obtained from a reference single crystal TiO_2 surface. The area under this peak is proportional to $\sigma_{\text{Ti}} N_{\text{Ti}} \lambda_{\text{Ti}} T(E_{\text{Ti}})$, where $\lambda_{\text{Ti}} = 20.67\text{ \AA}$ [56], and $N_{\text{Ti}} = 3.2 \times 10^{22}$ atoms- cm^{-3} . The Ti atoms in the $\text{Ti}[\text{N}(\text{CH}_3)_2]_4$ adlayer are modeled as a thin film of thickness d_{Ti} and atomic density N'_{Ti} . The area under the peak from such an adlayer is proportional to $\sigma_{\text{Ti}} N'_{\text{Ti}} d_{\text{Ti}} T(E_{\text{Ti}})/\cos\theta$, assuming $d_{\text{Ti}} \ll \lambda_{\text{Ti}}$. Thus, the quantity, $N'_{\text{Ti}} d_{\text{Ti}}$, which represents the Ti surface density (atoms- cm^{-2}), can be calculated directly. The (temperature averaged) saturation Ti densities on the three substrates are: $0.073 \pm 0.03 \times 10^{14}$ (clean Au), $1.2 \pm 0.2 \times 10^{14}$ (**1P** SAM), and $2.1 \pm 0.2 \times 10^{14}$ atoms- cm^{-2} (**2P** SAM). A higher Ti saturation coverage for the **2P** SAM is in agreement with the results given above where a higher coverage of SAM molecules, and hence reactive endgroups, was implicated.

In order to examine the kinetics of adsorption coverage-exposure data was acquired for both the SAMs at two different values of T_s ($30\text{ }^\circ\text{C}$ and $-50\text{ }^\circ\text{C}$). This data has been fit to first-order Langmuirian kinetics, $n_s(d\theta/dt) = S_{R,0}F(1 - \theta)$, where, n_s is the density of reactive sites (molecules- cm^{-2}), θ is the fractional surface coverage of $\text{Ti}[\text{N}(\text{CH}_3)_2]_4$, $S_{R,0}$ is the initial reaction probability, and F is the incident flux of $\text{Ti}[\text{N}(\text{CH}_3)_2]_4$ (molecules- cm^{-2} - s^{-1}).

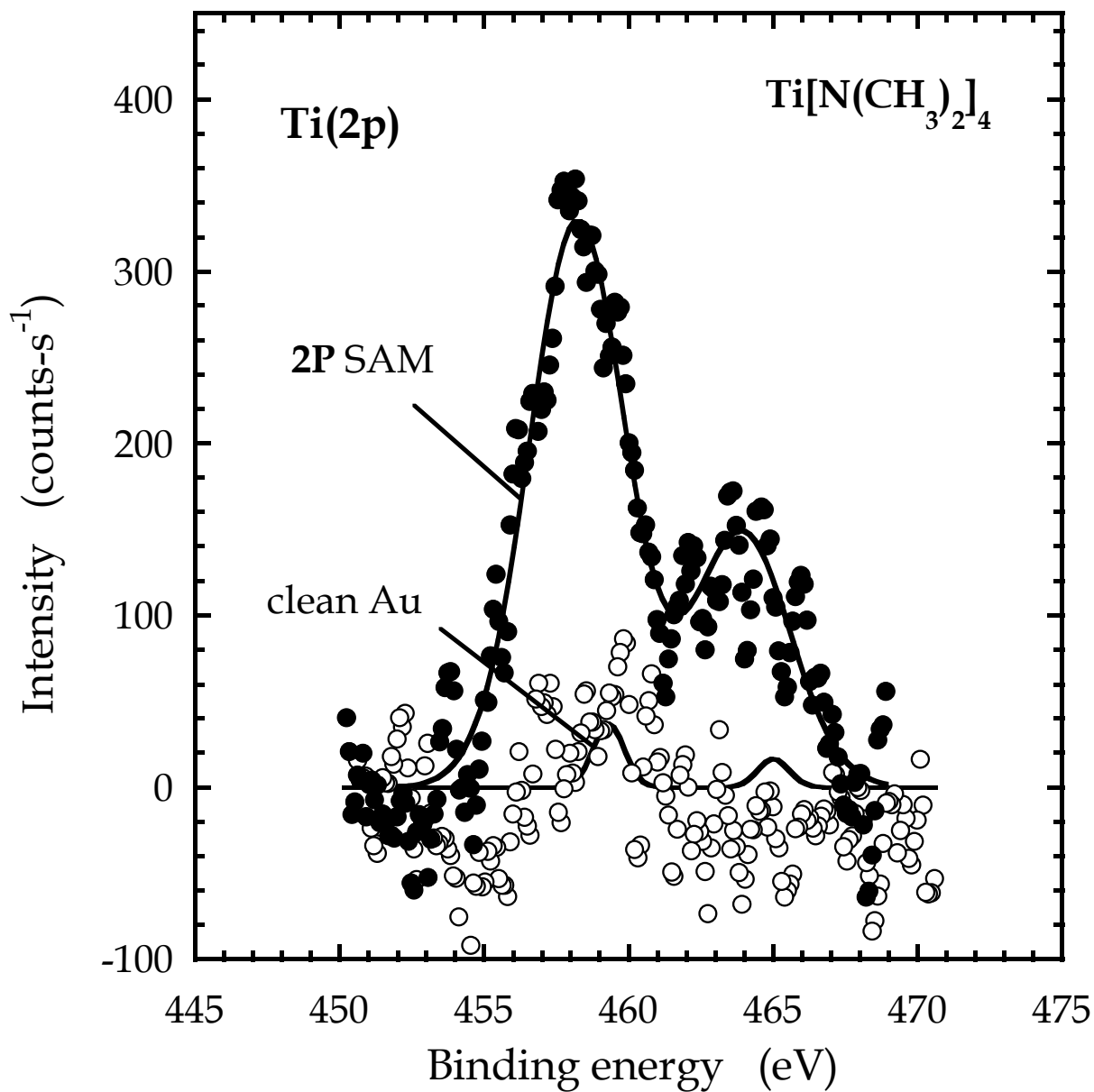


Figure 3-2: XP spectra of the Ti(2p) feature for clean Au and 2P SAM surfaces, both exposed to $\text{Ti}[\text{N}(\text{CH}_3)_2]_4$ at $T_s = 30^\circ\text{C}$. Exposures were 1.01 and 0.50×10^{17} molecules- cm^{-2} , respectively. Spectra have been fit to two peaks using Gaussian-Lorentzian product functions.

The data and the fits thereof are presented in Fig. 3-3 for the **1P** and **2P** SAM. Using the estimates for the absolute densities of Ti and the estimated incident flux of $\text{Ti}[\text{N}(\text{CH}_3)_2]_4$ $S_{\text{R},0}$ was calculated. At $T_s = 30\text{ }^\circ\text{C}$, $S_{\text{R},0}$ is 0.024 and 0.028 for the **1P** and **2P** SAM, respectively. At $T_s = -50\text{ }^\circ\text{C}$ the values are 0.010 and 0.020, respectively. Whereas the uncertainties in the absolute values are on the order of $\pm 50\%$, the uncertainties in the relative values are much less, perhaps on the order of $\pm 10\%$. Given these estimates, it can be concluded that the initial reaction probability in three of the four cases is within the experimental uncertainties. For the case that appears to deviate, the **1P** SAM at $T_s = -50\text{ }^\circ\text{C}$ ($S_{\text{R},0} = 0.010$), it can be said that the fit to the model at low coverage is not particularly good, and a simple linear fit of the first 3-4 data points would have revealed a larger $S_{\text{R},0}$, closer to that implicated in the other three cases.

Angle-resolved XPS has been used to probe the spatial extent of the reaction between $\text{Ti}[\text{N}(\text{CH}_3)_2]_4$ and the SAMs, similar to that conducted for the SAMs themselves (Fig. 3-1). To probe for the spatial location of Ti in the adlayer, XP spectra for the Ti(2p) features have been acquired at four different take-off angles from 0° to 64° . In Fig. 3-4 the Ti(2p) integrated intensity is plotted as a function of take-off angle, for both SAMs after saturation exposures to $\text{Ti}[\text{N}(\text{CH}_3)_2]_4$. Clearly, for both adlayers the intensity increases as a function of take-off angle, which points to the presence of Ti at the SAM-vacuum interface, as opposed to being buried at the SAM-Au interface. The Ti (2p) has been fit to the expression used for the S(2p) peak above [Fig. 3-1(b)], namely, $I(\theta) = (I_0 / \cos\theta) \exp(-d/\lambda \cos\theta)$. Here quantity d/λ is forced to be a positive definite. A fit of the data (shown by the smooth curves) gives $d/\lambda = 0.0003 \pm 0.3$ for the **1P** SAM and $d/\lambda = 0.0003 \pm 0.2$ for the **2P** SAM.

Figure 3-3: Coverage-exposure relationships, deduced from XPS, for the adsorption of $\text{Ti}[\text{N}(\text{CH}_3)_2]_4$ on (a) the **1P** SAM, and (b) the **2P** SAM, both for $T_s = -50$ and 30 °C. The fits to the data, shown as smooth curves, are for first-order Langmuirian kinetics.

(a)

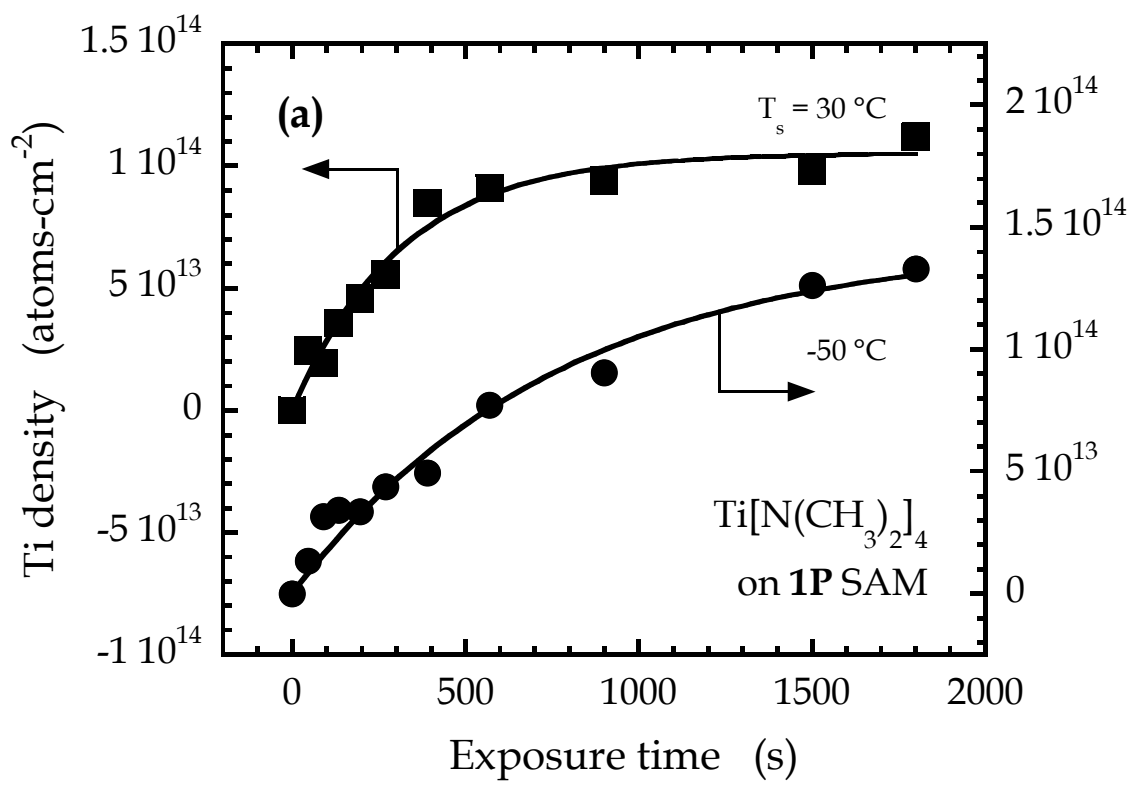
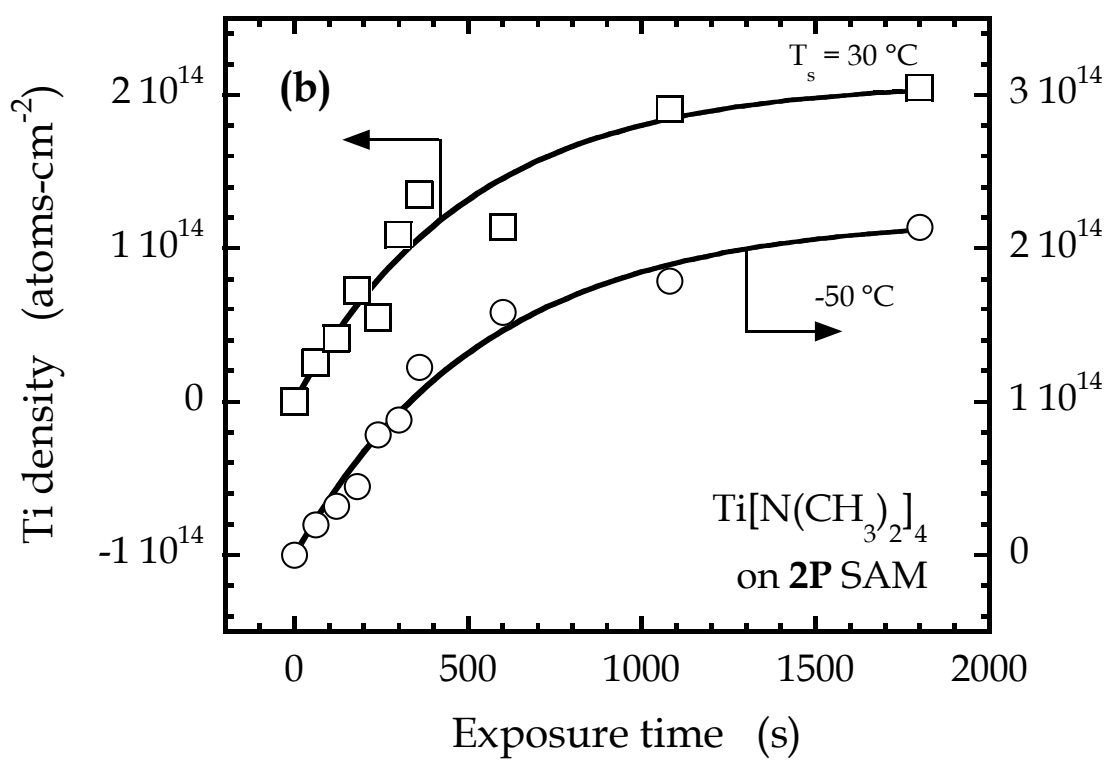


Figure 3-3 (continued)

(b)



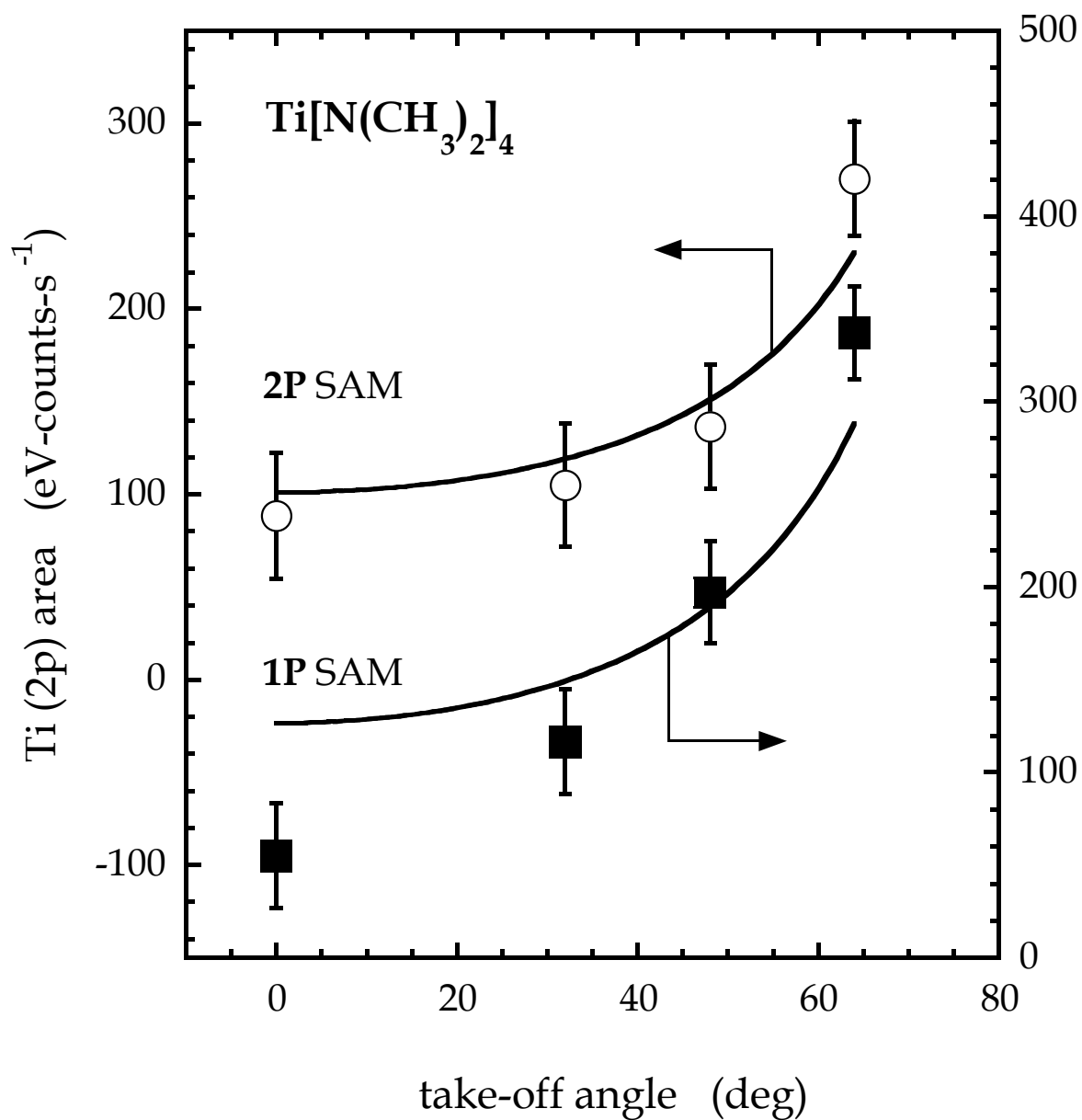


Figure 3-4: Integrated peak areas for the Ti(2p) region as a function of take-off angle for a saturation exposure of the **1P** (filled symbols) and **2P** SAMs (open symbols) to $\text{Ti}[\text{N}(\text{CH}_3)_2]_4$ at $T_s = 30\text{ }^\circ\text{C}$. The smooth curves represent fits of the data to a model that is described in the text. The parameters found from these fits are given in the text or Appendix B.

From these values it can be safely concluded that all the Ti is present at the SAM-vacuum interface in both cases. Penetration, followed by reaction at the SAM-Au interface, can be ruled out based on these data, and is unlikely due to the negligible reactivity observed for $\text{Ti}[\text{N}(\text{CH}_3)_2]_4$ on the clean Au substrate. In summary, these results indicate that the Ti is at the SAM-vacuum interface, bound to the $-\text{NH}(i\text{-C}_3\text{H}_7)$ SAM endgroup in both cases. Angle-resolved XP spectra of the Au(4f), S(2p), and C(1s) peaks have also been acquired from adlayers representing saturation exposures of both SAMs to $\text{Ti}[\text{N}(\text{CH}_3)_2]_4$. These experiments were conducted to determine if exposure of the SAMs to $\text{Ti}[\text{N}(\text{CH}_3)_2]_4$ resulted in significant changes in the adlayer other than reaction with the endgroup, possibly including displacement/desorption of the adsorbed molecules. These data are shown in Figs. 3-5(a), (b) and (c), which are identical in layout to those shown in Fig. 3-1, and have been fit to the corresponding functional forms indicated above. A number of things are apparent upon comparison of Figs. 3-1 and 3-5. First, the qualitative trends for all three peak areas for both SAMs are unchanged subsequent to exposure to $\text{Ti}[\text{N}(\text{CH}_3)_2]_4$ —the Au(4f) and S(2p) peaks are attenuated, whereas the C(1s) increases in intensity at more glancing take-off angles. These results are consistent with a situation in which significant structural rearrangement and/or ligand displacement has not occurred upon $\text{Ti}[\text{N}(\text{CH}_3)_2]_4$ chemisorption, leaving the molecules still bound to the Au surface via the thiophene linkage. Indeed, some changes in features are minimal. For example, a fit of the data for the Au(4f) peaks shown in Fig. 3-5(a) gives $d_{\text{SAM}}/\lambda = 0.46 \pm 0.01$ and 0.43 ± 0.04 for the **1P** and **2P** SAM, respectively, values essentially unchanged from those for the bare SAMs (*cf.* Appendix B).

Figure 3-5: Integrated peak areas as a function of take-off angle for the **1P** (filled symbols) and **2P** SAMs (open symbols) subsequent to saturation exposures to $\text{Ti}[\text{N}(\text{CH}_3)_2]_4$ at $T_s = 30\text{ }^\circ\text{C}$ for the (a) Au(4f), (b) S(2p) and (c) C(1s) features from XPS. The smooth curves represent fits of the data to models that are described in the text. The parameters found from these fits are given in the text or Appendix B.

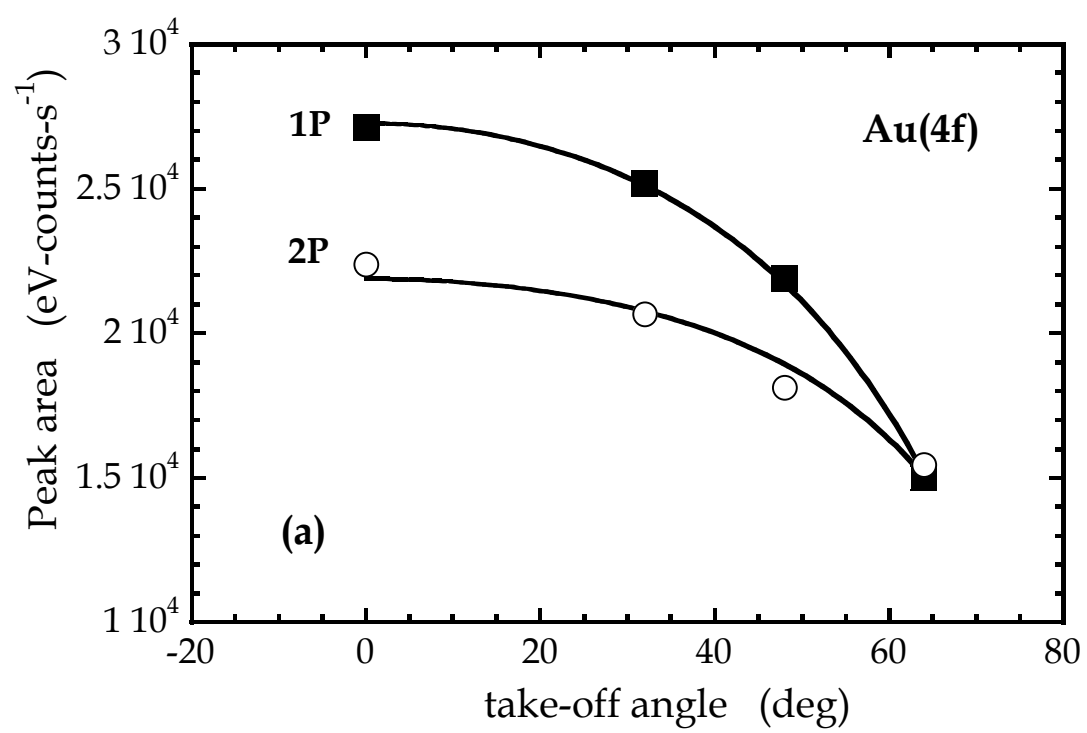
(a)

Figure 3-5 (continued)

(b)

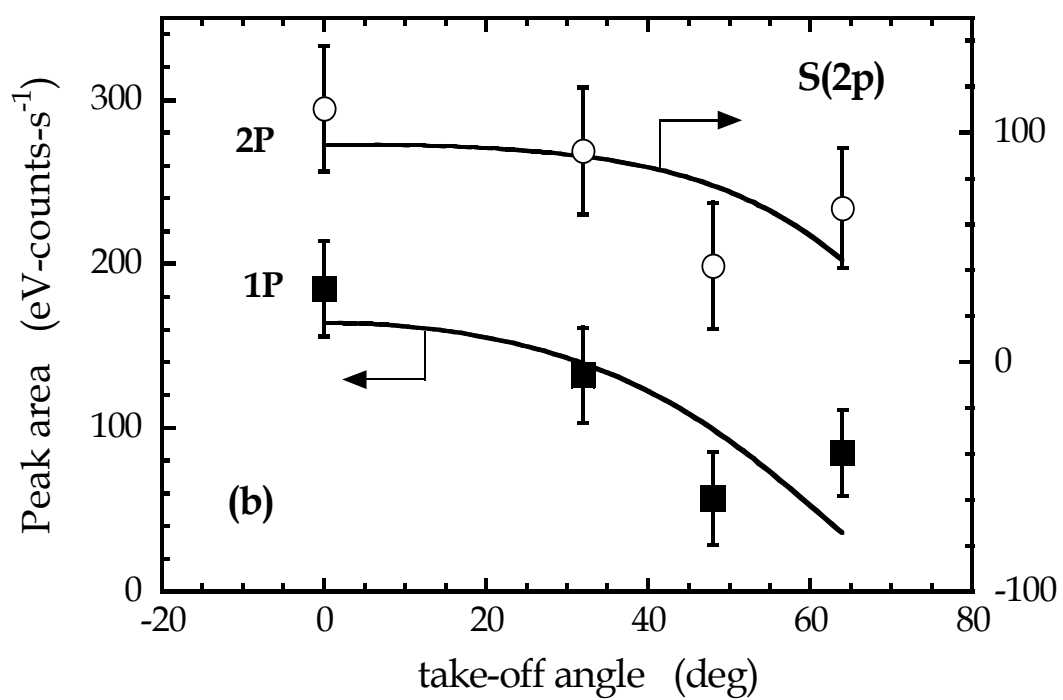
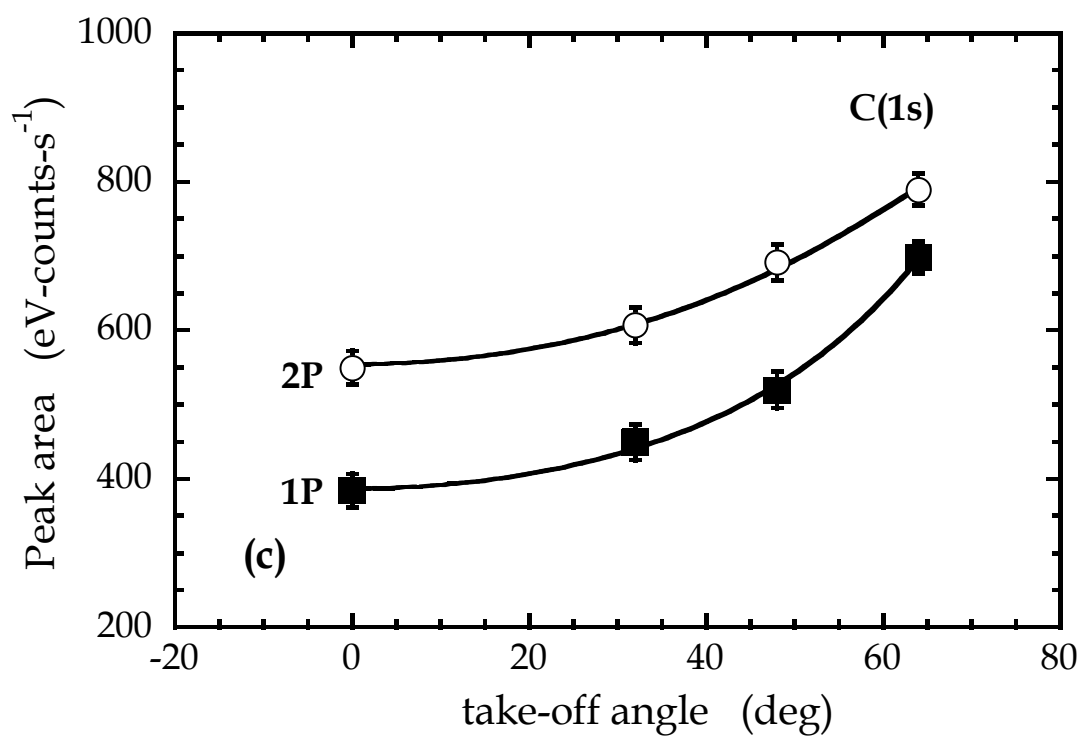


Figure 3-5 (continued)

(c)



Closer inspection of the data, however, does reveal some important differences. In particular, for the **2P** SAM, exposure to $\text{Ti}[\text{N}(\text{CH}_3)_2]_4$ resulted in a rather small increase of $\sim 6\%$ in the Au(4f) intensity at all take-off angles, whereas a more substantial increase of $\sim 21\%$ occurred on the **1P** SAM. Although $\text{Ti}[\text{N}(\text{CH}_3)_2]_4$ chemisorption might produce SAM desorption, this seems very unlikely because the Ti species does not compete with the SAM for adsorption sites, but rather exhibits a propensity to react with the endgroup on the SAM itself. A more plausible explanation is that reaction between the Ti species and the SAM has changed the orientation of these species, making them more upright and less able to cover the underlying Au substrate. This scenario is consistent with the larger change seen for the **1P** SAM, which, from ellipsometry, consists of a monolayer that is less dense and less upright.

For the S(2p) peak, *cf.* Fig. 3-5(b), there is a small change in the absolute intensities for the **1P** SAM upon reaction with $\text{Ti}[\text{N}(\text{CH}_3)_2]_4$, whereas there appears to be a much more substantial ($\sim 50\%$ at 0° take-off angle) attenuation of this peak for the **2P** SAM. Given the results for the Au(4f) peak discussed above, differing behavior of the two layers is not unexpected. For example, restructuring of the **1P** adlayer upon reaction into a sparser adlayer, which is also thicker, might produce minimal changes in the intensity. On the other hand, reaction and deposition leading to minimal restructuring of the **2P** SAMs, could further attenuate the S(2p) signal coming from the Au-SAM interface. Finally, for the C(1s) peak, *cf.* Fig. 3-5(c), there is minimal change in the absolute intensities (less than 5%), and fits to the data give $d_{\text{SAM}}/\lambda = 0.42 \pm 0.04$ and 0.98 ± 0.05 for the **1P** and **2P** SAM, respectively. These somewhat larger values for d_{SAM}/λ might reflect a thicker C layer due to the presence of the $\text{N}(\text{CH}_3)_2$ ligands from the $\text{Ti}[\text{N}(\text{CH}_3)_2]_4$.

To obtain more insight into the structure and composition of the adlayer formed at saturation exposure, the results from XPS are considered further. In particular, from the C(1s) feature of the (bare) SAMs the SAM density has been computed. Likewise, following a saturation exposure to $\text{Ti}[\text{N}(\text{CH}_3)_2]_4$, the density of adsorbed Ti has also been computed. Combining these results allows the calculation of a Ti:SAM ratio for both SAMs. In Fig. 3-6 the Ti density vs. the SAM density at saturation is plotted. Also plotted is the data for the reaction of $\text{Ti}[\text{N}(\text{CH}_3)_2]_4$ with a trichlorosilane based alkylamine SAM on SiO_2 (from Ref. [33]). As may be seen the ratio is $\sim 1:2$ in both cases considered here and for the alkylamine ($-\text{NH}_2$ endgroup), a result that is consistent with different scenarios. In one scenario it can be argued that each $\text{Ti}[\text{N}(\text{CH}_3)_2]_4$ molecule is reacting with two SAMs via the $-\text{NH}(i\text{-C}_3\text{H}_7)$ group, effectively occupying all possible reactive endgroups. In another scenario one could argue that on an average only $\frac{1}{2}$ of the $-\text{NH}(i\text{-C}_3\text{H}_7)$ groups are reacting with $\text{Ti}[\text{N}(\text{CH}_3)_2]_4$. This situation is also plausible because the SAM ligands considered here are bulky and possess a relatively inflexible backbone, where steric hindrance might limit $\text{Ti}[\text{N}(\text{CH}_3)_2]_4$ to react only with every alternate reactive endgroup.

Additional insight into the stoichiometry of the adlayer can be gained by examining the N:Ti ratio. Concerning the scenarios considered above, for $\text{Ti}[\text{N}(\text{CH}_3)_2]_4$ reacting with only $\frac{1}{2}$ of the SAMs present, and simple ligand exchange for chemisorption [loss of one $\text{N}(\text{CH}_3)_2$ ligand via formation of $\text{HN}(\text{CH}_3)_2$], a ratio of 5:1 would be expected, in the absence of attenuation effects. Alternatively, for the case where each $\text{Ti}[\text{N}(\text{CH}_3)_2]_4$ reacts with two SAMs, again by simple ligand exchange, a ratio of 4:1 would be expected.

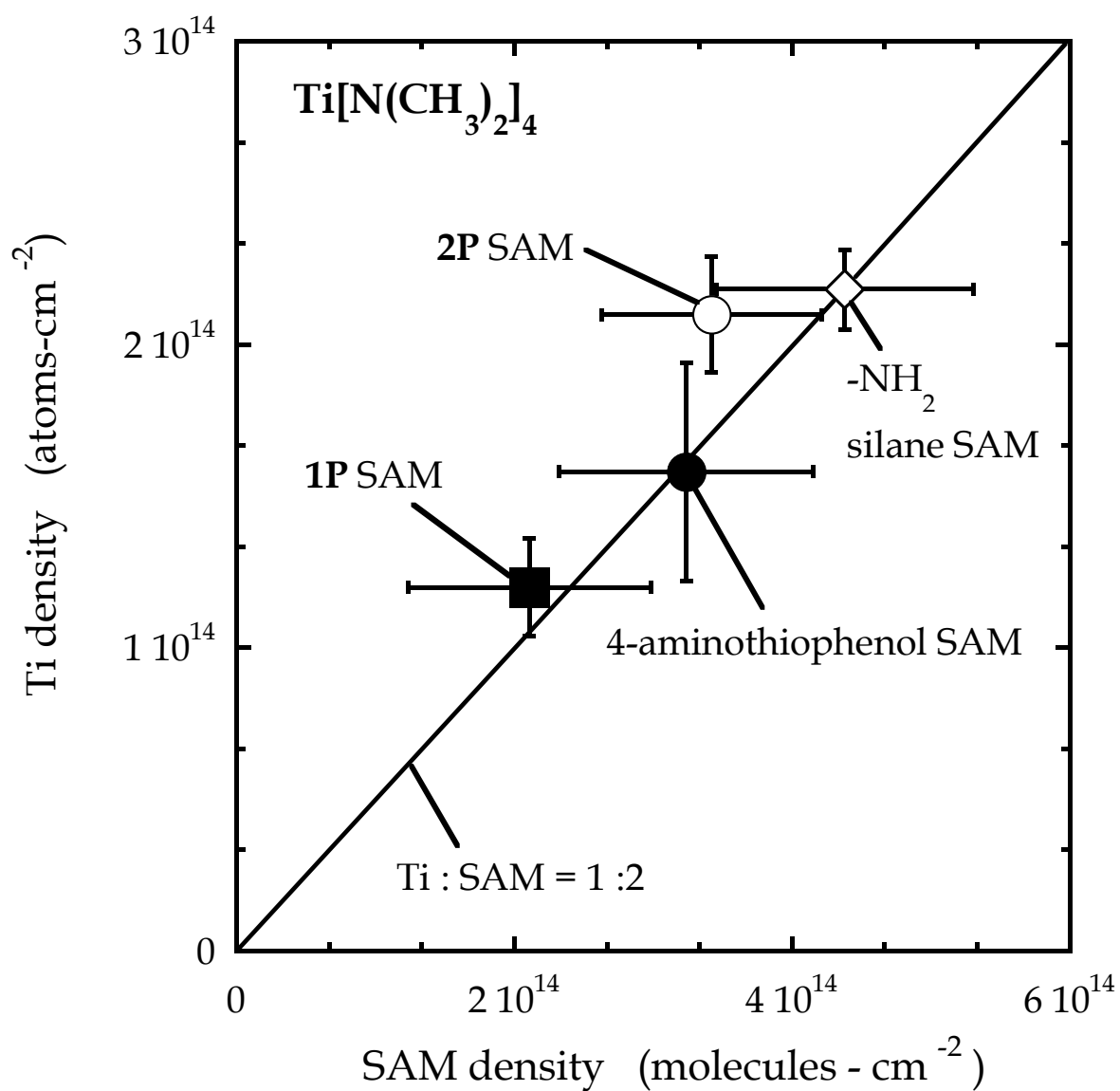


Figure 3-6: Relationship between the concentration of Ti in the saturated adlayers and the concentration of molecules (and functional endgroups) in the self-assembled monolayers. The datum for the -NH₂ terminated alkylsilane is from [33].

In Table 3-2, shown are the N:Ti ratios for the saturated adlayers for both SAMs and for our previous results on the alkylamine. Also indicated in Table 3-2 are the substrate temperatures at which the experiments were conducted. The N:Ti ratios have been calculated after making suitable corrections for the photoelectron cross-sections. Clearly, a N:Ti ratio of approximately 3:1 is observed for both the SAMs considered here, independent of substrate temperature. At $T_s = -50$ °C a ratio of $\sim 4:1$ is observed for the alkylamine. The ratio of 3:1 is unexpected, but nonetheless in poor agreement with the scenario where only $\frac{1}{2}$ of the SAMs react with $\text{Ti}[\text{N}(\text{CH}_3)_2]_4$. Alternatively, exclusively attenuation effects would also seem to be insufficient to explain a reduction in the theoretical ratio of 4:1 for $\text{Ti}[\text{N}(\text{CH}_3)_2]_4$ bound to two SAMs. One remaining possibility is the additional loss of ligand via pathways that do not involve ligand exchange.

As a final point of comparison the adsorption of 4-aminothiophenol (4-ATP) on polycrystalline Au was examined along with its reaction with $\text{Ti}[\text{N}(\text{CH}_3)_2]_4$. This molecule, which has been examined by a number of groups concerning its use as an adhesion promoter [57-59], possesses a much simpler structure, -SH and $-\text{NH}_2$ groups separated (para) by a phenyl group. In one study [59], from electrochemical deposition, a saturation coverage of $5.5 \pm 0.4 \times 10^{14}$ molecules- cm^{-2} was reported. As with the molecules of primary interest here (the **1P** and **2P** SAMs), an adlayer of the SAM itself was first prepared and characterized using contact angle measurements, ellipsometry, and ARXPS. Subsequently this layer was exposed to $\text{Ti}[\text{N}(\text{CH}_3)_2]_4$ and the layer was again characterized using ARXPS. For this adlayer, a characterization of the kinetics of adsorption was not attempted. The results of the contact angle and ellipsometry studies are displayed in Table 3-1.

Table 3-2: Stoichiometry of the saturated adlayers, $\text{Ti}[\text{N}(\text{CH}_3)_2]_4$ on SAMs

Substrate	SAM	Substrate temperature	N:Ti
polycrystalline Au	1P	-50 °C	2.9 ± 0.2
	1P	30 °C	3.0 ± 0.2
	2P	-50 °C	3.3 ± 0.4
	2P	30 °C	2.9 ± 0.2
	4-aminothiophenol	30 °C	4.0 ± 0.3
SiO ₂ (Ref. [33])	-NH ₂ terminated alkylsilane	-50 °C	4.0 ± 0.3
	-NH ₂ terminated alkylsilane	30 °C	3.0 ± 0.2

The contact angle (sessile drop method) of 26.9 ± 3.1 is smaller than that observed for the **1P** and **2P** SAMs. The ellipsometric thickness of 10.7 ± 0.8 Å, unlike the results for the 1P and 2P SAMs, is larger than expected, even for a molecule bound to the surface upright (calculated length of 5.6 Å). One expects this molecule to be bound upright, and if it is bound with a higher density than the **1P** and **2P** SAMs then it could produce a larger apparent thickness from ellipsometry due to the assumptions concerning the dielectric constant.

Concerning ARXPS of 4-aminothiophenol, the results are presented in Figs. 3-7(a), (b) and (c), for the Au(4f), S(2p) and C(1s) peaks (pre- and post-exposure), and in Fig. 3-8 for the Ti(2p) peak (exposure was $\sim 1.01 \times 10^{17}$ molecules-cm⁻²). As shown Fig. 3-7, the results for ARXPS on the unreacted SAM is qualitatively similar to that observed for the **1P** and **2P** SAMs: increasing attenuation of the Au(4f) and S(2p) features with increasing takeoff angle, higher intensity for the C(1s). Again these features have been fit to the models used to fit the data in Figs. 3-1 and 3-5. Shown in Figs. 3-7 and 3-8 are the results for ARXPS on the SAM, subsequent to reaction with Ti[N(CH₃)₂]₄. In Fig. 3-8, the data for the Ti(2p) peak were fit to the form used above in connection with Fig. 3-5, which yields a value of $d/\lambda = 0.11 \pm 0.10$ for Ti[N(CH₃)₂]₄ on aminothiophenol. This indicates that all of the Ti is present at the SAM-vacuum interface.

Examining the results shown in Fig. 3-7, the following is observed: for the Au(4f) feature, a fit of the data shown in Fig. 3-7(a) gives $d_{\text{SAM}}/\lambda = 0.49 \pm 0.02$ (bare SAM) and 0.45 ± 0.01 (reacted SAM), a minimal change. More interesting is the fact that an increase was observed in the Au(4f) emission at all take-off angles subsequent to exposure to Ti[N(CH₃)₂]₄, where the percentage

increase (21.5%) is essentially that seen for the **1P** SAM (21.2%) in the same situation. As indicated above, if chemisorption results in local densification of the adlayer about the Ti center then this could occur in the absence of SAM desorption. For the S(2p) peak displayed in Fig. 3-7(b), it can be seen that exposure to $\text{Ti}[\text{N}(\text{CH}_3)_2]_4$ has changed the photoemission intensity only perhaps a small amount. These results would seem to confirm that the S-Au bond is intact, even in the presence of reaction with the $-\text{NH}_2$ tailgroup. Finally, for the C(1s) feature, from Fig. 3-7(c) it can be seen that the intensity increases with increasing exposure to $\text{Ti}[\text{N}(\text{CH}_3)_2]_4$. This situation is consistent with an increased amount of C in the layer due to the $\text{N}(\text{CH}_3)_2$ ligands. As discussed above in connection with Fig. 3-5(c), a modest ($\sim 20\%$) decrease was seen in the C(1s) intensity for both the **1P** and **2P** SAMs upon exposure to $\text{Ti}[\text{N}(\text{CH}_3)_2]_4$. It is important to note that there is considerably less C in the 4-ATP (6 atoms vs. 16 and 23), and a larger relative increase is expected. In terms of the parameters used to fit Fig. 3-7(c), the increase in the C fraction is about 0.88 ± 0.41 , or 5.3 ± 2.5 C atoms, if no SAM is lost to desorption.

As with the results for the **1P** and **2P** SAMs, XPS can also be used to quantify the stoichiometry of the adlayer: the ratios Ti:SAM and Ti:N at saturation. Following a procedure identical to that used for the **1P** and **2P** SAMs the absolute coverage of 4-ATP for our conditions was calculated to be $3.24 \pm 0.91 \times 10^{14}$ molecules- cm^{-2} . For Ti, saturation coverage of $1.58 \pm 0.36 \times 10^{14}$ molecules- cm^{-2} was estimated. These results are plotted in Fig. 3-6, and they are in good agreement with the other systems have been studied with $-\text{NHR}$ termination: a Ti:SAM ratio of $\sim 1:2$. For the N:Ti ratio a value of $\text{N:Ti} = 4.03 \pm 0.25$ was found for 4-ATP, and $\text{Ti}[\text{N}(\text{CH}_3)_2]_4$ adsorption at $T_s = 30$ °C.

Figure 3-7: Integrated peak areas as a function of take-off angle for the 4-aminothiophenol SAM on polycrystalline Au, prior (open symbols) and subsequent (closed symbols) to a saturation exposure to $\text{Ti}[\text{N}(\text{CH}_3)_2]_4$ at $T_s = 30$ °C for the (a) Au(4f), (b) S(2p) and (c) C(1s) features from XPS. The smooth curves represent fits of the data to models that are described in the text. The parameters found from these fits are given in the text or Appendix B.

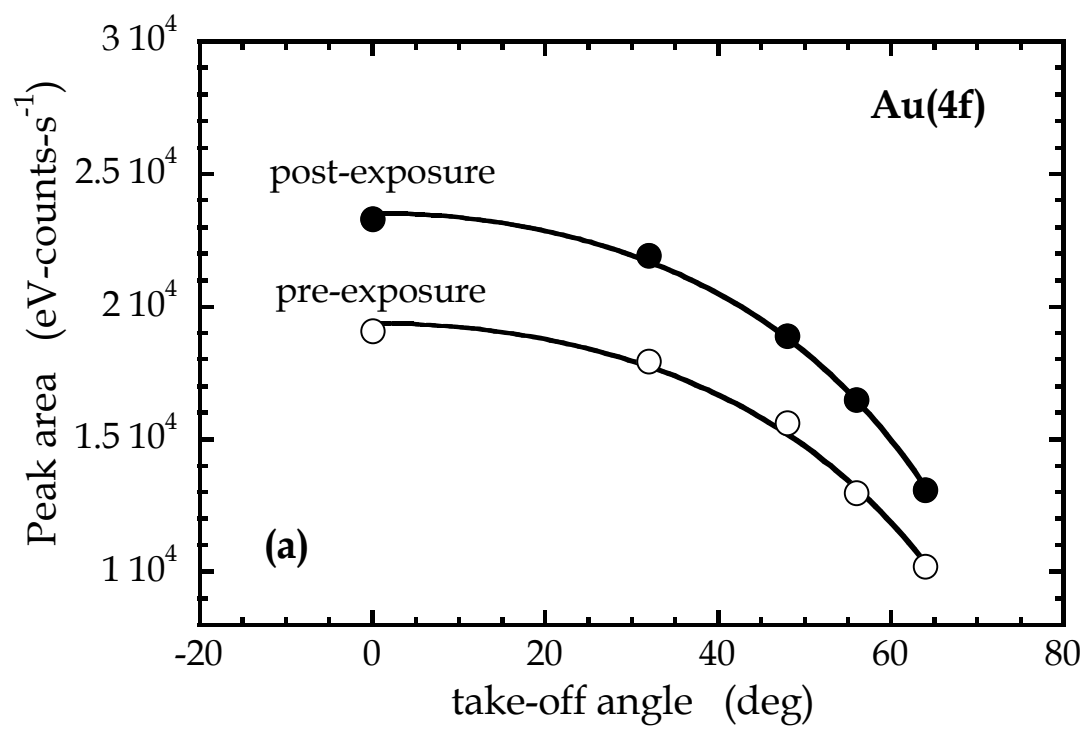
(a)

Figure 3-7 (continued)

(b)

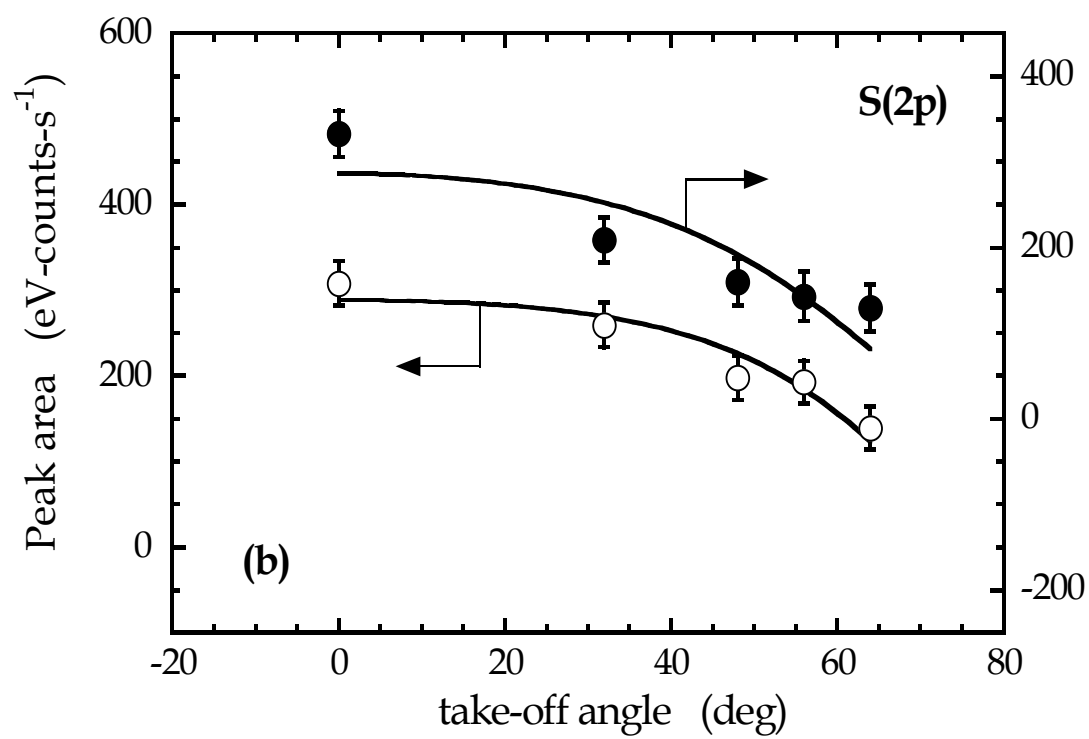
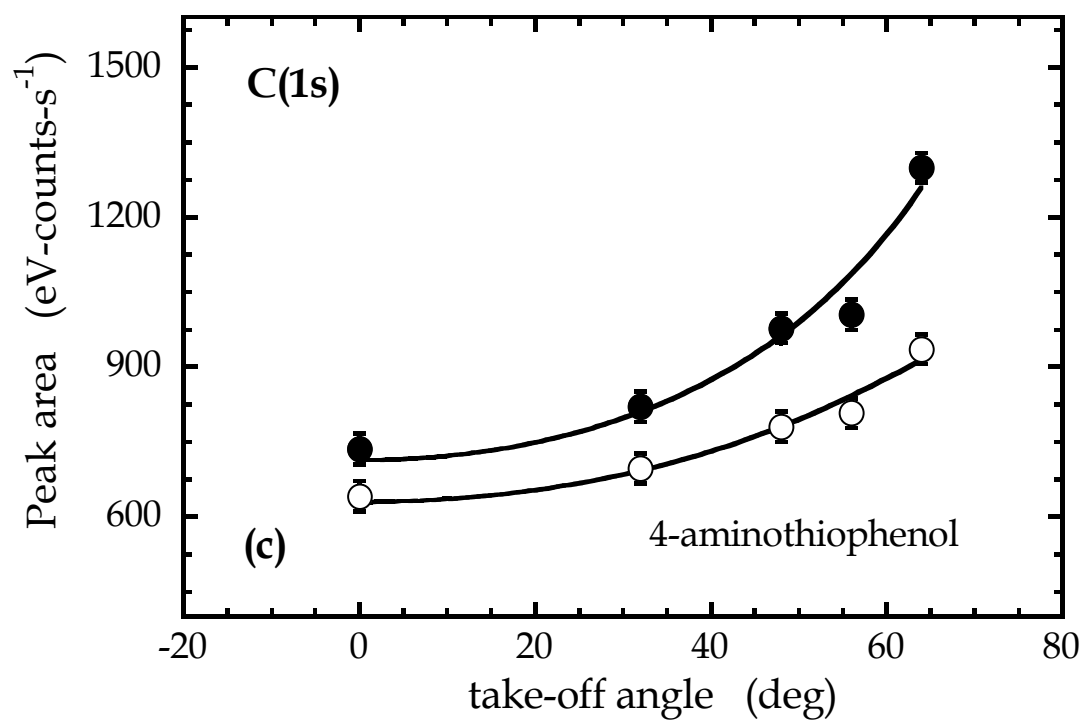


Figure 3-7 (continued)

(c)



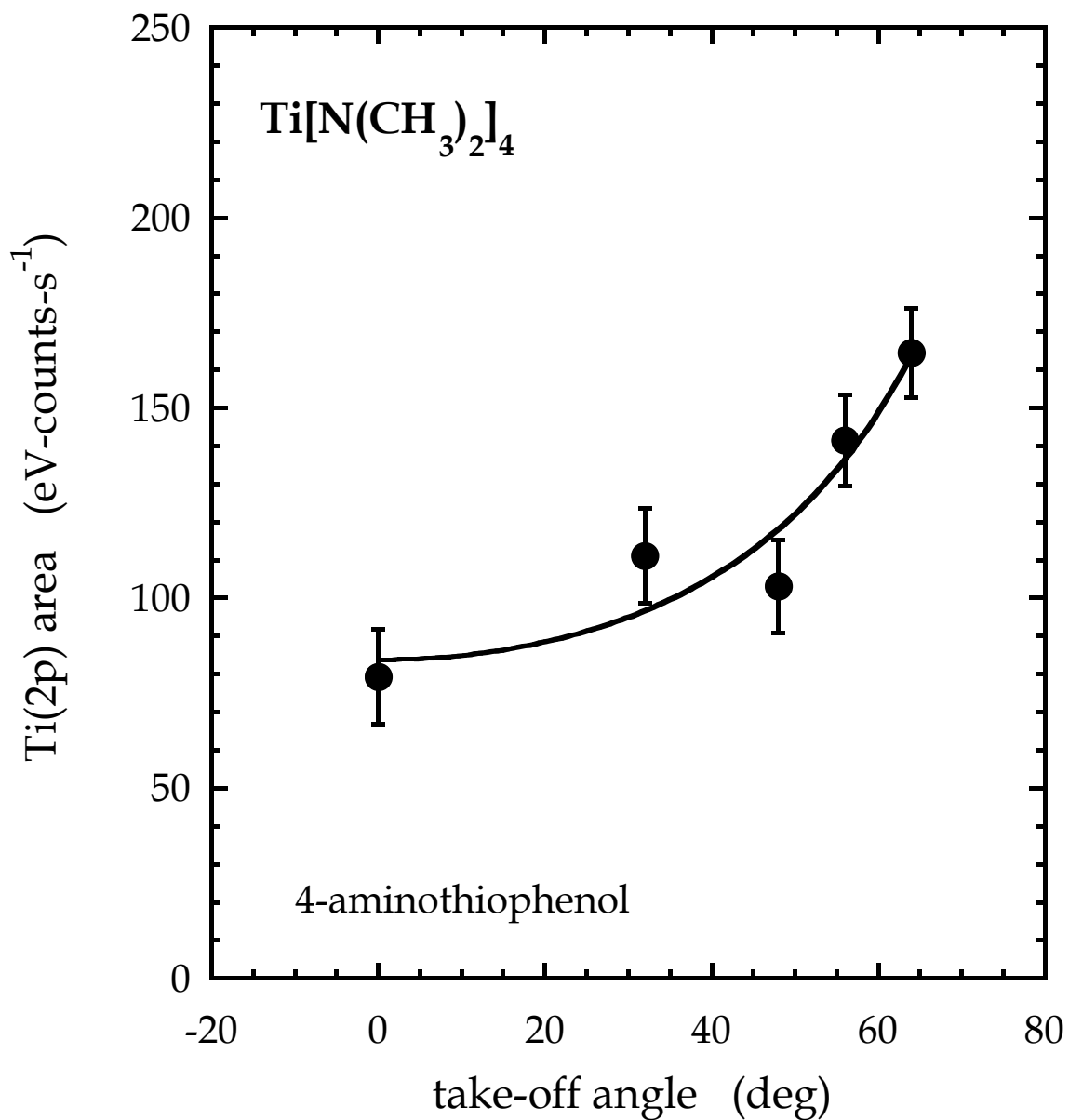


Figure 3-8: Integrated peak area for the Ti(2p) region as a function of take-off angle for a saturation exposure of the 4-aminothiophenol SAM to $\text{Ti}[\text{N}(\text{CH}_3)_2]_4$ at $T_s = 30\text{ }^\circ\text{C}$. The smooth curves represent fits of the data to a model that is described in the text. The parameters found from these fits are given in the text or Appendix B.

This is essentially the result achieved with an $-\text{NH}_2$ terminated alkylsilane SAM on SiO_2 , but seems to differ from the results reported here for the **1P** and **2P** SAMs, and the alkylsilane at $T_s = 30\text{ }^\circ\text{C}$, where the apparent stoichiometry was $\sim 3:1$.

Reviewing the results as a whole the focus will be on the following three important issues: (i) the kinetics of adsorption; (ii) the structure of the reacted and unreacted SAMs; and (iii) the stoichiometry of the saturated adlayer. Concerning the first of these, in previous work [33] the reactions of $\text{Ti}[\text{N}(\text{CH}_3)_2]_4$ on alkylsilane SAMs on SiO_2 were examined. For a $-(\text{CH}_2)_{12}\text{-NH}_2$ SAM, the initial reaction probabilities were ~ 0.13 , 0.10 , and 0.14 for $T_s = -50$, 30 , and $110\text{ }^\circ\text{C}$. Focusing on the results at $T_s = 30\text{ }^\circ\text{C}$, for the **1P** and **2P** SAMs the values of $S_{R,0}$ were 0.024 and 0.028 , respectively. Although the absolute accuracy of both sets of results may be no better than $\pm 50\%$, a relative comparison can be made with more confidence, as the method of calculating $S_{R,0}$ was identical in both cases. Thus, a difference in reactivity in the two cases is a factor of $3.6\text{-}4.2$, with the primary alkylamine being more reactive. One expects some difference between the $-\text{R-NH}_2$ group compared to the $[-\text{Ar-NH}(i\text{-C}_3\text{H}_7)]$ group. First, the N-H bond dissociation energy of the former is expected to be higher by about $6\text{-}7\text{ kcal}\cdot\text{mol}^{-1}$ [60], suggesting lower reactivity for the $-\text{R-NH}_2$ group. Additionally, a monoalkylamine species is less acidic than an *N*-alkyl aniline. Hence, if the transamination reaction were mediated by deprotonation of the incoming ligand then the long alkyl chain $-\text{R-NH}_2$ species would be moderately less reactive toward substitution. On the other hand, steric effects will certainly be in play for the **1P** and **2P** SAMs (e.g., the bulkier *i*- C_3H_7 , and phenyl groups), in comparison to the long alkyl chain $-\text{R-NH}_2$. Based on these results it appears that these steric effects dominate the

substitution chemistry in the system described here, probably influencing both the preexponential factor and the barrier to reaction. Haran et al. [55, 77] also investigated these steric effects by exploring the reaction of $\text{Ti}[\text{N}(\text{CH}_3)_2]_4$, with isopropyl-aniline and 1-methylaniline attached to a Si (100) surface cluster. The reaction mechanism was found to be similar to the corresponding deposition on aniline. If the size of the side ligand is increased to isopropylamine, the activation barrier and reaction energy are each increased. Repeating this for a branched *alkyl* SAM, the reaction of $\text{Ti}[\text{N}(\text{CH}_3)_2]_4$ on methyl-ethylamine ($\text{CH}_3\text{NHC}_2\text{H}_5$), an increase in activation barrier was observed with respect to an unbranched alkyl SAM. This suggests that branched side ligands significantly reduce kinetic and thermodynamic favorability and agrees well with the experimental observations here.

Concerning the structure of the SAMs, both before and after exposure to $\text{Ti}[\text{N}(\text{CH}_3)_2]_4$, work on related systems is very limited. Most relevant are structural studies of thiophene [46, 61], and oligo(phenylene-ethynylene) [62] monolayers. STM studies [61] suggest that thiophene forms an ordered paired-row structure on Au(111), with a density of $\sim 5.2 \times 10^{14}$ molecules- cm^{-2} . However, adding methyl groups to the molecule in the case of 2,5-dimethylthiophene destroys the ability to form this ordered structure, and no ordered monolayers are observed. In the case of oligo(phenylene-ethynylene) monolayers (thiol head group, un-functionalized phenyl tail group), based on results from contact mode AFM [62], a $(\sqrt{3} \times \sqrt{3})R30^\circ$ structure was formed, which would correspond to a density of $\sim 4.6 \times 10^{14}$ molecules- cm^{-2} . Addition of a $-\text{NO}_2$ group at the central phenyl group did not seem to affect ordering of this monolayer. Finally, in this study, based on results from infrared spectroscopy [62], an average tilt angle of $\sim 32\text{-}39^\circ$ was reported.

In the work reported here, XPS was employed to deduce structural properties of the monolayers. For the **2P** SAM, the saturation density is estimated to be 3.4×10^{14} molecules-cm⁻², which would represent a coverage of 0.245 on Au(111), consistent with a (2 × 2) overlayer. The ellipsometric data implies a tilt angle of $\theta = \cos^{-1}(16.6/19.6) = 32.1^\circ$, remarkably close to that reported elsewhere for the oligo(phenylene-ethynylene). This data again agrees remarkably well with molecular dynamics simulations carried out by Haran et al. [55], where an average tilt angle of 27-32 ° was predicted for a molecule similar to the **2P** molecule. How do the results for the **1P** SAM fit into this picture? Assume that the **1P** SAM forms a (2 × *m*) overlayer, where a larger tilt angle results in *m* > 2. Also assume that as the tilt angle increases, the spacing between adjacent chains perpendicular to their molecular axis does not. Again making use of the ellipsometric data, a tilt angle of 58.4° is implicated for the **1P** SAM. If the spacing between the molecular axes has not changed from that for the **2P** SAM, then the increase in tilt angle would make $m \sim 2 \cos(32.1^\circ)/\cos(58.4^\circ) = 3.23$. The density of such a layer of the **1P** SAM would be 2/3.23 that of the **2P** SAM layer, or $(2/3.23)(3.4 \times 10^{14}) = 2.1 \times 10^{14}$ molecules-cm⁻², exactly the result which was estimated from XPS. Although this result fits perfectly into the structural model just described, too much quantitative importance can not be assigned to it. This is mostly due to the use of XPS as a quantitative measure. In a relative sense, however, XPS is quite reproducible and reliable, and these results certainly highlight the important differences in the **1P** and **2P** SAMs. In particular, the lower density and larger tilt angle implicated for the **1P** SAM, whatever the exact structure may be.

A final point of discussion concerns the stoichiometry and structure of the reacted adlayer, and the possible scenarios are considered in Fig. 3-9.

Chemisorption most likely involves transamination ligand exchange reactions with the $-\text{Ar-NH}(i\text{-C}_3\text{H}_7)$ and $-\text{Ar-NH}_2$ groups at the SAM-vacuum interface [forming $\text{HN}(\text{CH}_3)_2(\text{g})$], and these may be facile at $T_s \leq 30$ °C. Perhaps the most striking result described here is the implied stoichiometry of the adlayer, $\text{Ti}:\text{SAM} \sim 1:2$, for four rather different amine-terminated monolayers (*cf.* Fig. 3-6). The best explanation for these results is successive ligand exchange reactions with adjacent molecules in the SAM ($-\text{L-NHR}$), forming a $(-\text{L-NR})_2\text{-Ti}[\text{N}(\text{CH}_3)_2]_2(a)$ species. This model is a perfect fit for the results for 4-aminothiophenol and the $-\text{NH}_2$ terminated alkylsilane at $T_s = -50$ °C, based on the implicated N:Ti ratios (*cf.* Table 3-2). It is also consistent with results reported by Scott and co-workers for $\text{Ti}[\text{N}(\text{CH}_3)_2]_4$ reacting on silica surfaces [63, 64], where $(\equiv\text{Si-O})_2\text{-Ti}[\text{N}(\text{CH}_3)_2]_2(a)$ species were implicated. However, for both the **1P** and **2P** SAMs, and the alkylsilane at $T_s = 30$ °C, a stoichiometry of 3:1 is indicated.

A further loss of dimethylamine from $(\text{L-N}(i\text{-C}_3\text{H}_7))_2\text{Ti}[\text{N}(\text{CH}_3)_2]_2$ is a plausible way in which the predicted 4:1 ratio of N:Ti can be lowered. As discussed elsewhere [33], if the kinetics of gas phase unimolecular decomposition of $\text{Ti}[\text{N}(\text{CH}_3)_2]_4$ is used as a guide, then decomposition of $\text{Ti}[\text{N}(\text{CH}_3)_2]_x(a)$ species forming metallacycles and/or imines [65] is likely not kinetically feasible at $T_s \leq 30$ °C. However, for the $\text{Ti}[\text{N}(\text{CH}_3)_2]_2(a)$ fragment bound by siloxane bridges examined by Beaudoin and Scott [64], just such a mechanism was proposed for prolonged (~ 10 h) “exposure” to vacuum at room temperature. Thus, including this mechanism, two pathways appear reasonable based on precedent. First, a dimethylamide could abstract a hydrogen from the adjacent $\text{Ti-N}(\text{CH}_3)_2$ functionality to generate free $\text{HN}(\text{CH}_3)_2$ and an azametalacyclopropane (alternately described as a bound imine), $(\text{L-N}(i-$

$C_3H_7)_2Ti(\eta^2-CH_2NCH_3)$) (pathway A, Fig. 3-9). β -Abstractions from dialkylamide groups are well established in early transition metal chemistry [64, 66-71]. A second possible route involves abstraction of an isopropyl group hydrogen to afford $HN(CH_3)_2$ and the azametalcyclobutane, $(L-N(i-C_3H_7))(L-\kappa^2-N,C-NCH(CH_3)CH_2)Ti(N(CH_3)_2)$ (pathway B, Fig. 3-9). While not as common, in complexes that are sterically crowded, abstractions of peripheral hydrogens can occur concomitant with cyclometalation of the ligand [72-74]. Subsequent loss of propene from the azametalcyclobutane might occur to give $(L-N(i-C_3H_7))(L-N=)Ti(N(CH_3)_2)$, and this 3-coordinate species would be expected to add any number of CH bonds --either intra- or intermolecularly -- across the imido linkage [75,76] In these scenarios, the ultimate N:Ti ratio would be 3:1.

The feasibility of these two mechanisms has also been investigated using quantum chemistry calculations by Haran et al. [55, 77]. The kinetics of competing side unimolecular decomposition reactions plays a key role in defining the composition of the developing surface, demonstrating the influence of steric hindrance on kinetics. Metallacycle formation was found to be kinetically and thermodynamically the least favorable with a further decrease in kinetic favorability as steric hindrance is increased and with the placement of aromatic side ligands on the metal center. This pathway was found to be kinetically limited below 350 K, suggesting that this is an upper processing temperature limit to prevent the incorporation of “carbide” Ti-C. β -elimination of the dimethylamine group to form an azametalcyclobutane or hydrogen abstraction from a α -carbon to form azametalcyclopropane with the side branched group were found to be kinetically the most competitive, though the latter is thermodynamically less favorable.

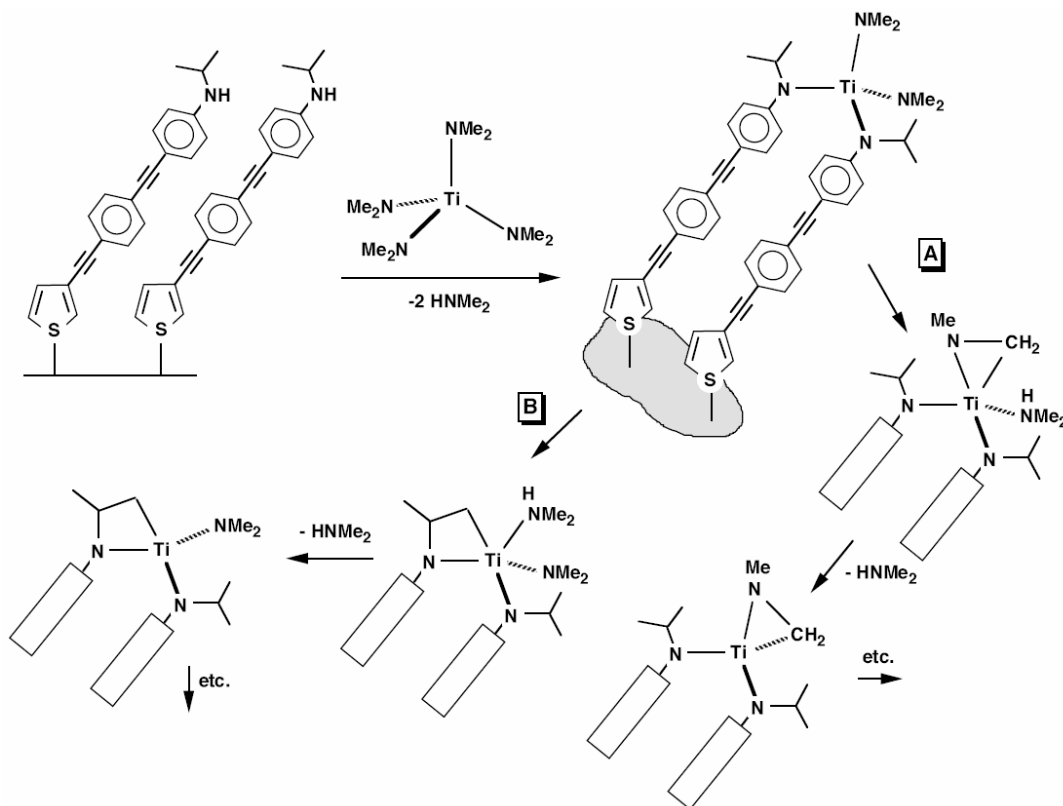


Figure 3-9: Possible reaction pathways for $\text{Ti}[\text{N}(\text{CH}_3)_2]_4$ reacting with the **1P** and **2P** SAM (source: Prof. P. T. Wolczanski)

Pathways involving side ligands were kinetically competitive with transamination at temperatures as low as 250 K, leading to a Ti:N ratio of 1:3 at low temperatures. The kinetic favorability of these pathways increased with an increase in steric hindrance. Similar β -elimination in gas phase unimolecular decomposition of $\text{Ti}[\text{N}(\text{CH}_3)_2]_4$ to form metallacycles and imines was not kinetically favorable for substrate temperatures below 200°C, demonstrating a significant influence of steric hindrance and of the aromatic substrate in reducing the activation barrier.

Independent of this proposition, however, is the unambiguous preference of $\text{Ti}[\text{N}(\text{CH}_3)_2]_4$ to react with these layers via two successive ligand exchange reactions. As discussed above, our results for the **1P** SAM seem to indicate that the bare SAM is a low density layer characterized by molecules closer to parallel to the surface, rather than perpendicular. Reaction with $\text{Ti}[\text{N}(\text{CH}_3)_2]_4$ would likely change that, particularly if two molecules are bound to the same Ti center. Indeed, a more upright $(\text{-L-NR})_2\text{-TiN}(\text{CH}_3)_2(a)$ species might be expected to occupy a smaller area of the Au surface, and lead to less attenuation of the Au signal. This is, of course, exactly what we see from XPS. In contrast, the more upright **2P** layer, may lead to species covering similar amounts of the Au surface, leading to little change in attenuation of the Au signal—again, this is what is observed in XPS. More definitive conclusions concerning the structure of the reacted adlayers await direct structural studies using techniques such as STM.

3.5 Conclusions

The synthesis and characterization of conjugated thiophene self-assembled monolayers with an isopropylamine endgroup, and their reaction with tetrakis(dimethylamido)titanium has been investigated. Using contact angle measurements and ellipsometry, it was found that the shorter **1P** SAM produces an adlayer that is less dense than the longer **2P** SAM. This may be due to the nature of the intermolecular interactions in the **2P** SAM, which lead to an adlayer that involves molecules that are more upright than the **1P** SAM. These results are confirmed by results from XPS, which also indicate a higher density for the **2P** SAM. Angle-resolved XPS indicates that the molecules for both SAMs are bound to the Au surface via the thiophene headgroup, with the amine termination at the SAM-vacuum interface. Reaction of these SAMs with $\text{Ti}[\text{N}(\text{CH}_3)_2]_4$ in both cases is self-limiting, and the kinetics of adsorption are in good agreement with first-order Langmuirian kinetics. The initial probability of reaction on these SAMs is about a factor of 4 smaller than that observed on a $-\text{NH}_2$ terminated alkylsilane, which is attributed to steric effects caused by the *i*- C_3H_7 group on these SAMs. Angle-resolved XPS conducted after the reaction of the SAMs with $\text{Ti}[\text{N}(\text{CH}_3)_2]_4$ shows clearly that the reaction occurs cleanly with the terminal isopropylamine group, and there is no reaction at the SAM-Au interface. From XPS it was found that the stoichiometry in the saturated adlayers for both SAMs is $\sim 1:2$ for Ti:SAM, and $\sim 3:1$ for N:Ti. These results are best explained by a model where chemisorption involves ligand exchange reactions resulting in one $\text{Ti}[\text{N}(\text{CH}_3)_2]_x$ fragment bound to two SAMs via the isopropylamine group. Taken as a whole, these results indicate that transition metal complexes can bind very specifically and non-invasively to the endgroups

on self-assembled monolayers that possess a backbone that may be useful in fields such as molecular electronics.

3.6 References

1. Reed, M. A.; Tour, J. M. *Scientific American*, **2000**, 86.
2. Reed, M. A.; Zhou, C.; Muller, C. J.; Burgin, T. P.; Tour, J. M. *Science* **1997**, 278, 252.
3. Park, J.; Pasupathy, A. N.; Goldsmith, J. I.; Chang, C.; Yaish, Y.; Petta, J. R.; Rinkoski, M.; Sethna, J. P.; Abruña, H. D.; McEuen, P. L.; Ralph D. C. *Nature* **2002**, 417, 722.
4. Ralls, K. S.; Buhrman, R. A.; Tiberio, R. C. *Appl. Phys. Lett.* **1989**, 55, 2459.
5. Chen, Y.; Ohlberg, D. A. A.; Li, X.; Stewart, D. R.; Williams, R. S.; Jeppesen, J. O.; Nielsen, K.A.; Stoddart, J. F.; Olynick, D. L.; Anderson, E. *Appl. Phys. Lett.* **2003**, 82, 1610.
6. Nuzzo, R. G.; Allara, D. L. *J. Am. Chem. Soc.* **1983**, 105, 4481.
7. Bain, C. D.; Troughton, E. B.; Tao, Y-T.; Evall, J.; Whitesides, G. M.; Nuzzo, R. G. *J. Am. Chem. Soc.* **1989**, 111, 321.
8. Tour, J. M.; Jones II, L.; Pearson, D. L.; Lamba, J. J. S.; Burgin, T. P.; Whitesides, G. M.; Allara, D. L.; Parikh, A. N.; Atre, S. V. *J. Am. Chem. Soc.* **1995**, 117, 9529.
9. Hutchinson, J. E.; Postlethwaite, T. A.; Murray, R. W. *Langmuir* **1993**, 9, 3277.

10. Martin, A. S.; Sambles, J. R.; Ashwell, G. J. *Phys. Rev. Lett.* **1993**, *70*, 218.
11. Metzger, R. M.; Xu, T.; Peterson, I. R. *J. Phys. Chem. B* **2001**, *105*, 7280.
12. Chen, J.; Reed, M. A.; Rawlett, A. M.; Tour, J. M. *Science* **1999**, *286*, 1550.
13. Cui, X. D.; Primak, A.; Zarate, X.; Tomfohr, J.; Sankey, O. F.; Moore, A. L.; Moore, T. A.; Gust, D.; Harris, G.; Lindsay, S. M. *Science* **2001**, *294*, 571.
14. Ng, M. K.; Lee, D. C.; Yu, L. *J. Am. Chem. Soc.* **2002**, *124*, 11862.
15. Bumm, L. A.; Arnold, J. J.; Cygan, M. T.; Dunbar, T. D.; Burgin, T. P.; Jones II, L.; Allara, D. L.; Tour, J. M.; Weiss, P. S. *Science* **1996**, *271*, 1705.
16. Jung, D. R.; Czanderna, A. W. *Crit. Rev. Solid State Mater. Sci.* **1994**, *19*, 1.
17. Herdt, G. C.; Jung, D. R.; Czanderna, A. W., *Prog. Surf. Sci.* **1995**, *50*, 103.
18. Tarlov, M. J. *Langmuir* **1992**, *8*, 80.
19. Ohgi, T.; Sheng, H.-Y.; Dong, Z.-C.; Nejoh, H. *Surf. Sci.* **1999**, *442*, 277.
20. Fisher, G. L.; Hooper, A. E.; Opila, R. L.; Allara, D. L.; Winograd, N. *J. Phys. Chem. B* **2000**, *104*, 3267.

21. Konstadinidis, K.; Zhang, P.; Opila, R. L.; Allara, D. L. *Surf. Sci.* **1995**, *338*, 300.
22. Hooper, A. E.; Fisher, G. L.; Konstadinidis, K.; Jung, D.; Nguyen, H.; Opila, R.L.; Collins, R. W.; Winograd N.; Allara, D. L. *J. Am. Chem. Soc.* **1999**, *121*, 8052.
23. Fisher, G. L.; Walker, A. V.; Hooper, A. E.; Tighe, T. B.; Bahnck, K. B.; Skriba, H. T.; Reinard, M. D.; Haynie, B. C.; Opila, R. L.; Winograd, N.; Allara, D. L. *J. Am. Chem. Soc.* **2002**, *124*, 5528.
24. Carlo, S. R.; Wagner, A. J.; Fairbrother, D. H. *J. Phys. Chem. B* **2000**, *104*, 6633.
25. Shin, H.; Collins, R. J.; De Guire, M. R.; Heuer, A. H.; Sukenik, C. N. *J. Mater. Res.* **1995**, *10*, 692.
26. Shin, H.; Collins, R. J.; De Guire, M. R.; Heuer, A. H.; Sukenik, C. N. *J. Mater. Res.* **1995**, *10*, 699.
27. Niesen, T. P.; Bill, J.; Aldinger, F. *Chem. Mater.* **2001**, *13*, 1552.
28. Masuda, Y.; Jinbo, Y.; Yonezawa, T; Koumoto, K. *Chem. Mater.* **2002**, *14*, 1236.
29. a) Wohlfart, P.; Weiss, J.; Kashammer, J.; Winter, C.; Scheumann, V.; Fischer, R. A.; Mittler-Nehera, S. *Thin Solid Films* **1999**, *340*, 274. b) Winter, C.; Weckenmann, U.; Fischer, R. A.; Kashammer, J.; Scheumann, V.; Mittler, S. *Chem. Vap. Depn.* **2000**, *6*, 199. c) Fischer, R.A.; Weckenmann, U.; Winter, C.; Kāshammer, J.; Scheumann, V.; Mittler, S. *Journal de Physique IV: Proceedings* **2001**, *11*, Pr3/1183.

30. Weckenmann, U.; Mittler, S.; Krämer, S.; Aliganga, A. K. A.; Fischer, R.A. *Chem. Mater.* **2004**, *16*, 621.
31. Weiss, J.; Himmel, H. J.; Fischer, R. A.; Woell, C. *Chem. Vap. Depn.* **1998**, *4*, 17.
32. Wohlfart, P.; Weiss, J.; Käshmmmer, J.; Kreiter, M.; Winter, C.; Fischer, R.; Mittler-Neher, S. *Chem. Vap. Depn.* **1999**, *5*, 165.
33. Killampalli, A. S.; Ma, P. F.; Engstrom, J. R. *J. Am. Chem. Soc.* **2005**, *127*, 6300.
34. Fix, R.; Gordon, R. G.; Hoffman, D. M. *Chem. Mater.* **1991**, *3*, 1138.
35. Musher, J. N.; Gordon, R. G. *J. Mater. Res.* **1996**, *11*, 989.
36. Ritala, M.; Asikainen, T.; Leskelä, M.; Jokinen, J.; Lappalainen, R.; Utriainen, M.; Niinistö, L.; Ristolainen, E. *Appl. Surf. Sci.* **1997**, *120*, 199.
37. Berry, A.; Mowery, R.; Turner, N.H.; Seitzman, L.; Dunn, D.; Ladouceur, H. *Thin Solid Films* **1998**, *323*, 10.
38. Min, J. -S.; Park, J. -S.; Park, H. -S.; Kang, S. -W. *J. Electrochem. Soc.*, **2000**, *147*, 3868.
39. Ritala, M.; Asikainen, T.; Leskelä, M.; Dekker, J. -P.; Mutsaers, C.; Soininen, P. J.; Skarp, J. *Chem. Vap. Dep.*, **1999**, *5*, 7.
40. Elam, J. W.; Wilson, C. A.; Schuisky, M.; Sechrist, Z.A.; George, S. M. *J. Vac. Sci. Technol. B* , **2003**, *21*, 1099.

41. Elam, J. W.; Schuisky, M.; Ferguson, J. D.; George, S. M. *Thin Solid Films*, **2003**, *436*, 145.
42. Biebuyck, H. A.; Bain, C. D.; Whitesides, G. M. *Langmuir* **1994**, *10*, 1825.
43. Fenter, P.; Eberhardt, A.; Eisenberger, P. *Science* **1994**, *266*, 1216.
44. Dishner, M. H.; Hemminger, J. C.; Feher, F. J. *Langmuir*, **1996**, *12*, 6176.
45. Matsuura, T.; Nakajima, M.; Shimoyama, Y. *Jpn. J. Appl. Phys.* **2001**, *40*, 6945.
46. Noh, J.; Ito, E.; Nakajima, K.; Kim, J.; Lee, H.; Hara, M. *J. Phys. Chem. B* **2002**, *106*, 7139.
47. Xia, L. -Q.; Jones, M. E.; Maity, N.; Engstrom, J. R. *J. Vac. Sci. Technol. A*, **1995**, *13*, 2651.
48. De Boer, B.; Meng, H.; Perepichka, D. F.; Zheng, J.; Frank, M. M.; Chabal, Y.; Bao, Z. *Langmuir* **2003**, *19*, 4272.
49. Frey, S.; Stadler, V.; Heister, K.; Eck, W.; Zharnikov, M.; Grunze, M. *Langmuir* **2001**, *17*, 2408.
50. *Practical Surface Analysis: Volume I, Auger and X-ray Photoelectron Spectroscopy, 2nd ed.*; Seah, M. P., Briggs, D., Eds.; John Wiley and Sons: Chichester, England, **1990**.
51. *Solid State Physics*; Ashcroft, N. W., Mermin, N. D., Harcourt Brace College Publishers: U.S.A., **1976**.

52. Powell, C. J.; Jablonski, A. *J. Vac. Sci. Technol. A* **1999**, *17*, 1122.
53. Lamont, C. L. A.; Wilkes, J. *Langmuir* **1999**, *15*, 2037.
54. Walker, A. V.; Tighe, T. B.; Stapleton, J.; Haynie, B. C.; Upilli, S.; Allara, D. L.; Winograd, N. *Appl. Phys. Lett.* **2004**, *84*, 4008.
55. M. Haran, PhD thesis, Cornell University, **2006**.
56. Seah, M. P.; Dench, W. A. *Surf. Interface Anal.* **1979**, *1*, 2.
57. Schlieben, O.; Hormes, J. *J. Synchrotron Rad.* **1999**, *6*, 793.
58. Hooper, A. E.; Werho, D.; Hopson, T.; Palmer, O. *Surf. Interface Anal.* **2001**, *31*, 809.
59. Batz, V.; Schneeweiss, M. A.; Kramer, D.; Hagenström, H.; Kolb, D. M.; Mandler, D. *J. Electroanal. Chem.* **2000**, *491*, 55.
60. Gomes, Jose' R. B.; Ribeiro da Silva, Maria D. M. C.; Ribeiro da Silva, Manuel A. V. *J. Phys. Chem. A* **2004**, *108*, 2119.
61. Noh, J.; Eisuke, I.; Araki, T.; Hara, M. *Surface Science* **2003**, 532-535, 1116.
62. Stapleton, J. J.; Harder, P.; Daniel, T. A.; Reinard, M. D.; Yao, Y.; Price, D. W.; Tour, J. M.; Allara, D. L. *Langmuir* **2003**, *19*, 8245.
63. Bouh, A. O.; Rice, G. L.; Scott, S. L., *J. Amer. Chem. Soc.* **1999**, 121, 7201.
64. Beaudoin, M.; Scott, S. L. *Organometallics* **2001**, *20*, 237.

65. Dubois, L. H.; Zegarski, B. R.; Girolami, G. S. *J. Electrochem. Soc.* **1992**, *139*, 3603-3609; Driessen, J. P. A. M.; Schoonman, J.; Jensen, K. F. *J. Electrochem. Soc.* **2001**, *148*, G178.
66. Nugent, W. A.; Ovenall, D. W.; Holmes, S. J. *Organometallics* **1983**, *2*, 161.
67. Mayer, J. M.; Curtis, C. J.; Bercaw, J. E. *J. Am. Chem. Soc.* **1983**, *105*, 2651.
68. Groysman, S.; Goldberg, I.; Kol, M.; Genizi, E.; Goldschmidt, Z. *Organometallics* **2004**, *23*, 1880.
69. Coles, N.; Harris, M. C. J.; Whitby, R. J.; Blagg, J. *Organometallics* **1994**, *13*, 190.
70. Maury, F.; Ossola, F. *Appl. Organomet. Chem.* **1998**, *12*, 189.
71. Chiu, H. T.; Huang, C. C. *Materials Letters* **1993**, *16*, 194.
72. Simpson, S. J.; Andersen, R. A. *Inorg. Chem.* **1981**, *20*, 3627.
73. Rothwell, I. P. *Acc. Chem. Res.* **1988**, *21*, 153.
74. Rothwell, I. P. *Polyhedron* **1985**, *4*, 177.
75. Bennett, J. L.; Wolczanski, P.T. *J. Am. Chem. Soc.* **1997**, *119*, 10696.
76. Slaughter, L. M.; Wolczanski, P. T.; Klinckman, T. R.; Cundari, T. R., *J. Am. Chem. Soc.* **2000**, *122*, 7953.
77. Haran, M.; Engstrom, J. R.; Clancy, P. *J. Am. Chem. Soc.* **2006**, *128*, 836.

4. Nucleation and growth during TiN atomic layer deposition on silicon dioxide and silicon dioxide modified using interfacial organic layers

4.1 Overview

Atomic layer deposition (ALD) of titanium nitride, TiN, on silicon dioxide, and silicon dioxide modified by self-assembled monolayers (SAMs) possessing -NH_2 , -OH , -CF_3 , and -CH_3 functional terminations has been investigated employing molecular beams of tetrakis(dimethylamido) titanium $\{\text{Ti}[\text{N}(\text{CH}_3)_2]_4\}$ and ammonia (NH_3). An ALD “window” was present for growth on SiO_2 at substrate temperatures between $167\text{ }^\circ\text{C}$ and $207\text{ }^\circ\text{C}$. The deposited thickness per cycle saturates around 2 \AA-cycle^{-1} in this temperature range. In the same temperature range, growth is observed on all modified SiO_2 surfaces, and the data do not fit a simple model whereby growth is merely delayed a fixed period of time. On the -CF_3 and -CH_3 terminated SAMs, which are generally unreactive, growth is significantly attenuated over that observed on clean SiO_2 , more so for the thicker SAMs ($>$ a factor of 10), and involves islanded, non-uniform growth. ALD is also observed on SAMs with -NH_2 and -OH endgroups, but growth is uniform, and attenuated only by approximately a factor of three, independent of the thickness of these SAMs. The results seem to suggest highly conformal growth in the case of SiO_2 along with the reactive -NH_2 and -OH terminated SAMs.

4.2 Introduction

In order to be able to continue to increase the density of integrated circuits new materials must be integrated into the device structures [1]. Copper (Cu) is now the choice for metallization, and there is a drive to incorporate carbon-containing, possibly purely organic, and/or porous low κ interlayer dielectrics [2]. The deposition of barrier layers between the Cu and the low κ materials is challenging, particularly for carbon-containing, porous dielectrics. Essentially all barrier layers are inorganic, thus an “inorganic-on-organic” interface must be formed. Interestingly, these interfaces are playing an increasingly important role in several other technologies, including organic light-emitting diodes [3, 4], and molecular electronics [5-8], yet they are not fully understood.

Self-assembly is a popular method for making highly ordered organic monolayer films on metallic and semiconductor substrates [9-11]. These self-assembled “organic-on-inorganic” monolayers (SAMs) have been widely studied as model organic surfaces owing to their ease of formation, self-limiting growth characteristics, and the specificity of their reaction enabling the tailoring of surface properties by varying the organic functional end group (OFG).

Recently, SAMs have been employed as interfacial and/or patterned layers in thin films grown using both solution and gas phase deposition techniques. Formation of inorganic-on-organic interfaces via liquid phase thin film deposition has been reported to be problematic [12, 13]. The films, in most instances, were rough and exhibited poor adhesion, while molecular level details concerning the interfaces were absent from these studies.

Vapor deposition of elemental metals (e.g., Ag, Cu, Ti, Al, Fe, Cr and Au) on SAMs possessing different terminal organic functional groups (OFGs) such as $-\text{CH}_3$, $-\text{OH}$, $-\text{COOH}$, $-\text{COOCH}_3$, $-\text{CN}$ and $-\text{SH}$ has been studied extensively [14-18]. In many cases, due to the rather unspecific reactions of many of these elemental metals, mixed adlayers were formed because reactions occurred not only with the OFG tail groups, but also apparently with the SAM backbone and head groups.

Formation of inorganic-organic interfaces via the use of transition metal coordination complexes holds tremendous promise. A key is to tailor both the terminal OFG and the transition metal complex such that they react with each other in a specific fashion. Growth that is self-limiting may also be desirable, and feasible with this approach, as uncontrolled continuous deposition might lead to degradation of the interface. There are a handful of studies which have employed these types of complexes to initiate the deposition of metal thin films on SAMs in a chemical vapor deposition (CVD) like scheme [19-21]. In all of these studies, the selectivity of growth and film morphology were examined but an explicit examination of the kinetics of adsorption was not attempted. Recently, the Engstrom group (Dr. Aravind S. Killampalli's thesis) has completed what is perhaps the most rigorous study of the reaction of a transition metal coordination complex with SAMs [22], in this case, the reaction of tetrakis(dimethylamido)titanium, $\text{Ti}[\text{N}(\text{CH}_3)_2]_4$, a TiN precursor, with alkyltrichlorosilane SAMs possessing $-\text{OH}$, $-\text{NH}_2$ and $-\text{CH}_3$ terminal OFGs. XPS was employed to conclude that the reaction was self-limiting in all these cases. The choice of TiN was not arbitrary as it is a diffusion barrier candidate in Cu interconnect structures [2]. Angle-resolved XPS (ARXPS) was used to probe the spatial extent of the reaction, and it was found that penetration

of the SAM followed by reaction at the SAM/substrate occurred in the case of the $-\text{CH}_3$ SAM. In case of the $-\text{NH}_2$ SAM, however, no evidence of penetration was found, and reaction was confined to the terminal $-\text{NH}_2$ group. More recently, atomic layer deposition (ALD) has been employed in cases where the SAMs have been used as a mask for selective deposition of HfO_2 [23], Pt [24], TiO_2 [25], and Ru [26]. In all these cases, however, growth was not attempted on the organic layer itself. There are very few studies of ALD initiated thin film growth on SAMs [27, 28]. TiO_2 ALD growth, on mixed alkyltrichlorosilane SAMs on SiO_2 with different ratios of $-\text{OH}$ and $-\text{CH}_3$ OFGs, was attempted employing titanium isopropoxide and water [27]. It was reported that the ALD growth modes (2- dimensional vs. 3-dimensional) can be controlled by varying the composition and hence the surface energy of these mixed SAM substrates. ALD of WC_xN_y films on SAMs derived from bromoundecyltrichlorosilane adsorbed on SiO_2 has also been reported [28]. The monolayer was thermally stable up to a temperature of $550\text{ }^\circ\text{C}$ as suggested by temperature programmed desorption (TPD) results and hence survived multiple ALD cycles at $300\text{ }^\circ\text{C}$. However, the role of bromine termination in initiating ALD growth was not very clear. In summary, among all these techniques, ALD is the most promising because of its self-limiting nature which affords sub-nanometer control of the growth process [29]. More importantly, ALD is characterized by relatively low temperatures and thermal budgets for growth (*vis-a-vis* CVD), making it of interest for deposition on organic materials.

The study of the nucleation state of ALD has received increased attention in recent times, with the great majority of work involving growth of TiN [31], WN_xC_y [32] and HfO_2 [33] from metal halide sources on various oxides, nitrides and carbides of Si. Use of these different forms of Si has

allowed a qualitative assessment of the importance of the $-\text{OH}(a)$ group, and it can both facilitate [31,33] and impede [32] nucleation depending on the chemistry. To investigate nucleation we have used the approach of introducing one of the reactants, $\text{Ti}[\text{N}(\text{CH}_3)_2]_4$, via a well-collimated supersonic molecular beam, and the other, NH_3 , via an effusive beam. A well collimated beam provides the possibility of varying (i) the total number of ALD cycles (to validate the digital nature of the process), or (ii) the length of exposure to the $\text{Ti}[\text{N}(\text{CH}_3)_2]_4$ reactant (to validate the self-limiting nature of growth) on a single sample in a single experiment. This ability is critical for study of the non-steady-state stage of growth [34], i.e., nucleation.

Recently, a report was published regarding preliminary results of TiN nucleation via ALD employing gated molecular beams [30] on both clean SiO_2 and on SiO_2 modified with SAMs with different microstructure, and different OFG terminations. $\text{Ti}[\text{N}(\text{CH}_3)_2]_4$ and ammonia, NH_3 , were employed as precursors. Herein, described in greater detail, are the results for ALD TiN nucleation and growth on SiO_2 and SiO_2 modified using SAMs. *Ex situ* X-ray photoelectron spectroscopy (XPS) and Rutherford backscattering spectrometry (RBS) were used to determine composition, atomic density, and the extent of growth. Atomic force microscopy (AFM) was employed to track the evolution of roughness/morphology during film growth. Additionally, high-resolution scanning transmission electron microscopy (HRSTEM) and high resolution energy electron energy loss spectroscopy (HREELS) were also used to probe the interfaces and hence further characterize the nature of growth.

4.3 Experimental procedures

4.3.1 Sample preparation

Substrates were Si (100) wafers (Wacker-Siltronic, p-type, 4" dia., 500-550 μm thick, 38-63 $\Omega\text{-cm}$) The wafers were scribed with a diamond scribe and subsequently cleaved into 16 samples, each a square of $16.75 \times 16.75 \text{ mm}^2$. Chemical oxide, which refers to SiO_2 possessing a high density of $-\text{OH}$ (a) groups, was prepared as described in chapter 2.. This is the starting surface for formation of all of the SAMs. The SAM precursors: 3-aminopropyldimethylethoxysilane, 11-cyanoundecyltrichlorosilane, 10-undecenyltrichlorosilane, octadecyltrichlorosilane, tridecafluoro-1,1,2,2-tetrahydrooctyltrichlorosilane, and triacontyltrichlorosilane were purchased from Gelest, Inc. (Morrisville, PA) and used as received. SiO_2 modification with $\text{HN}[\text{Si}(\text{CH}_3)_3]_2$, hexamethyldisilazane (HMDS), the thinnest $-\text{CH}_3$ terminated layer, was done from vapor phase using a YES LP-III Vapor Prime Oven after successive evacuation and purge cycles to dehydrate the substrate held at 150 $^\circ\text{C}$. The other vapor deposited SAM was the $-\text{CF}_3$ terminated tridecafluoro-1,1,2,2-tetrahydrooctyltrichlorosilane $[\text{CF}_3(\text{CF}_2)_5(\text{CH}_2)_2\text{SiCl}_3$, FOTS]. The MVD-100 (Applied Microstructures Inc., San Jose, CA), was used to deposit the FOTS SAM, where the FOTS vapor (0.6 Torr) and water vapor (7 Torr) were let into the deposition chamber, and the SiO_2 substrates were allowed to react for 20 minutes. The thicker $-\text{CH}_3$ terminated layers namely: octadecyltrichlorosilane $[\text{CH}_3(\text{CH}_2)_{17}\text{-SiCl}_3$, OTS] and triacontyltrichlorosilane $[\text{CH}_3(\text{CH}_2)_{29}\text{-SiCl}_3$, TTS] SAMs, were solution deposited. Details regarding the

preparation of OTS and TTS SAMs are again provided in chapter 2. Also considered are two other straight-chain SAMs: namely, $(\text{-O-})_3\text{Si}(\text{CH}_2)_{12}\text{NH}_2$, and $(\text{-O-})_3\text{Si}(\text{CH}_2)_{11}\text{OH}$ (preparation details in chapter 2). Briefly, the -CN terminal functionality in 11-cyanoundecyltrichlorosilane was hydroborated to get the -NH_2 terminated SAM. The -CH=CH_2 group in 10-undecenyltrichlorosilane is converted to $\text{-CH}_2\text{-CH}_2\text{-OH}$, again by hydroboration, to synthesize -OH terminated SAM. The two SAMs with branched microstructure: $\text{-O-Si}(\text{CH}_3)_2(\text{CH}_2)_3\text{N}[(\text{CH}_2)_2\text{CONH}(\text{CH}_2)_2\text{NH}_2]_2$ (termed here, Gen-1-3C) and $(\text{-O-})_3\text{Si}(\text{CH}_2)_{12}\text{N}[(\text{CH}_2)_2\text{CONH}(\text{CH}_2)_2\text{NH}_2]_2$ (termed here, Gen-1-12C) were formed using a synthetic procedure that is similar to that used to make dendritic polymers [35, 36]. Briefly, the two SAMs differ as to their “anchor” group, 3-aminopropyldimethylethoxysilane is used for Gen-1-3C, whereas the aforementioned $(\text{-O})_3\text{Si}(\text{CH}_2)_{12}\text{NH}_2$ is used for Gen-1-12C. The substrates, treated with either anchor, are sequentially reacted with methyl acrylate ($\text{CH}_2=\text{CH}(\text{CO})\text{OCH}_3$, >99% stabilized, Sigma-Aldrich Corp., St. Louis, MO), and ethylenediamine ($\text{H}_2\text{N}(\text{CH}_2)_2\text{NH}_2$, >99.5%, redistilled, Sigma-Aldrich Corp., St. Louis, MO) to get to the so called Gen-1 (first generation dendrimer) SAM, with a higher density of terminal -NH_2 OFGs.

4.3.2 TiN ALD process

The experiments were carried out in a custom-built ultra-high (UHV) chamber that has been described in chapter 2 and in more detail elsewhere [37]. The base pressure of the chamber is typically below 1×10^{-9} Torr. A few crucial modifications were made to the system in order to carry out the ALD experiments, namely, the addition of an effusive beam doser for the delivery of

NH₃ which consists of a glass microcapillary array (GCA, Burle Technologies Inc., Lancaster, PA). With the high number of cycles (>200) likely involved in ALD experiments, automation of the reactant cycling was necessary. Automation software was developed using LabView 6.0 (National Instruments, Austin, TX). Ti[N(CH₃)₂]₄ was obtained from Schumacher (Carlsbad, CA) in a stainless steel bubbler, and is delivered to the supersonic beam nozzle (150 μm orifice) using H₂ (Airgas, semiconductor grade) as a carrier gas. The doubly differentially pumped beam passes through a skimmer (1.5 mm aperture, Precision Instrument Services, Inc.) into an ante chamber and through an aperture (9 × 9 mm²), producing a well defined beam spot on the substrate at normal incidence. The beam could be blocked using a shutter in the antechamber, facilitating precise exposures to the substrate. Kinetic energies of the Ti[N(CH₃)₂]₄ molecules were measured using time-of-flight mass spectrometric techniques [38]. In this study, the kinetic energy of the Ti[N(CH₃)₂]₄ molecules in all experiments was fixed at 2.07 eV, and the flux was 2.2 × 10¹⁵ molecules-cm⁻²-s⁻¹. The reactant NH₃ (Airgas, VLSI grade) was introduced via an effusive beam doser, which consists of a glass microcapillary array (GCA, Burle Technologies Inc., Lancaster, PA), and produces a uniform flux over the substrate surface (2.8 × 10¹⁸ molecules-cm⁻²-s⁻¹) while achieving a good beam to background ratio. The gating of the NH₃ flux was achieved by employing a vent-run configuration controlled by a pneumatic valve. In these experiments the total pressure was typically no greater than 10⁻⁵ Torr (i.e., molecular flow regime). Thus, a simple pump out period was used to separate the flows of the two reactants, as a purge gas step is nonsensical in this flow regime. Cycle times of the reactants were computer controlled, and a typical cycle was: 10 s {Ti[N(CH₃)₂]₄} / 15 s (pump out) / 30 s (NH₃) / 100 s (pump

out). During the experiments the sample could be periodically translated perpendicular to the $\text{Ti}[\text{N}(\text{CH}_3)_2]_4$ beam axis. If this is done during the $\text{Ti}[\text{N}(\text{CH}_3)_2]_4$ cycle, it produces areas on the substrate surface representing different exposure times to $\text{Ti}[\text{N}(\text{CH}_3)_2]_4$. If it is done subsequent to “n” total cycles, areas representing a different total number of cycles will be produced. A 3-D AUTOCADTM rendering of this setup is provided in Fig. 4-1.

4.3.3 Characterization methods

4.3.3.1 Ellipsometry

Measurements of the thickness of the SAMs as well as the TiN films were performed with a Gaertner L-120A ellipsometer (He-Ne 632.8 nm laser, incident at 70°). For the refractive indices, a value of 1.46 has been used for the chemical oxide and SAMs. For TiN a refractive index value of 1.7 has been used.

4.3.3.2 Atomic force microscopy (AFM)

Images were acquired with a Dimension 3100 scanning probe microscope (Veeco Instruments, Woodbury, NY) in tapping mode using Tap 300 SPM probes (Nanodevices Inc., Santa Barbara, CA). Typical images obtained were of size $0.5 \times 0.5 \mu\text{m}^2$ and subjected to a second order plane fit using Nanoscope software (v 5.3)

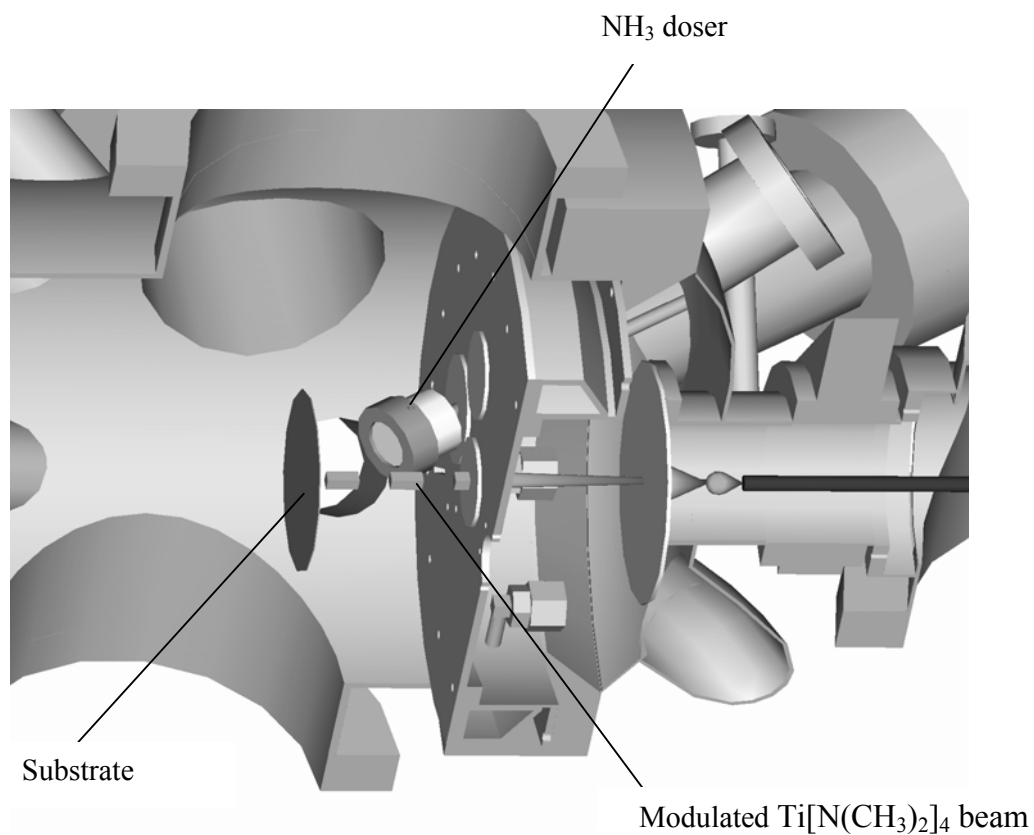


Figure 4-1: Schematic representation of the atomic layer deposition process employing modulated molecular beams. Shown is a cutaway of the deposition chamber with $\text{Ti}[\text{N}(\text{CH}_3)_2]_4$ delivered using a supersonic beam and NH_3 delivered as an effusive beam by using a capillary array doser.

One-dimensional PSD spectra (1DPSD) can be used to characterize the roughness and surface structure and also to obtain scaling exponents. 1DPSDs were calculated using the same software along the fast scan direction and single line PSDs were averaged. For each scan length L , spatial frequencies range between $1/L$ and the Nyquist frequency $256/L$.

4.3.3.3 X-ray photoelectron spectroscopy (XPS)

XPS was carried out using a VSW twin anode X-ray source (Mg/Al) and a VSW CLASS 100 concentric hemispherical energy analyzer (VSW Worldwide, Cheshire, U.K.). Mg $K\alpha$ X-rays (1253.6 eV) were used throughout this study. Survey scans (e.g., 0-1200 eV kinetic energy) were carried out in the fixed retardation ratio mode, whereas detailed scans (range of ~ 20 eV over a single feature) were carried out in the fixed analyzer transmission mode. All the binding energy values were referenced to the C(1s) peak at 285.0 eV [40]. A background subtraction method first proposed by Shirley [39] was used in all analyses of the peaks. Peak areas were obtained by fitting the spectra to a product Gaussian-Lorentzian (G-L) function with a mixing ratio of 0.9 [40, 41].

4.3.3.4 Rutherford backscattering spectrometry (RBS)

A 4 MeV He^+ beam was employed at a total dose of 5×10^8 counts. The analysis of the acquired spectra was carried out using the RUMP simulation program [42]. The areal density/thickness estimates were based on a least squares fit to the actual data.

4.3.3.5 Scanning transmission electron microscopy (STEM)

An FEI Tecnai TF20 high resolution STEM was employed to characterize the TiN films. This microscope was also used to acquire high resolution electron energy loss spectroscopy (HREELS) data.

4.4 Results and discussion

4.4.1 Characterization of the SAMs

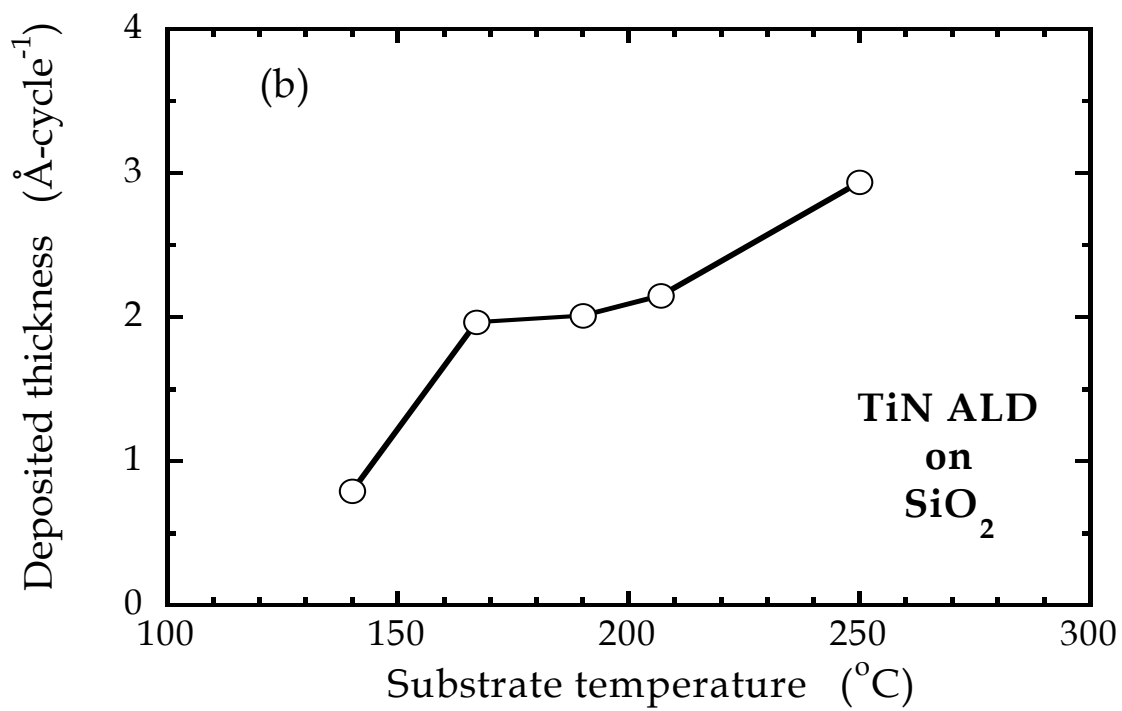
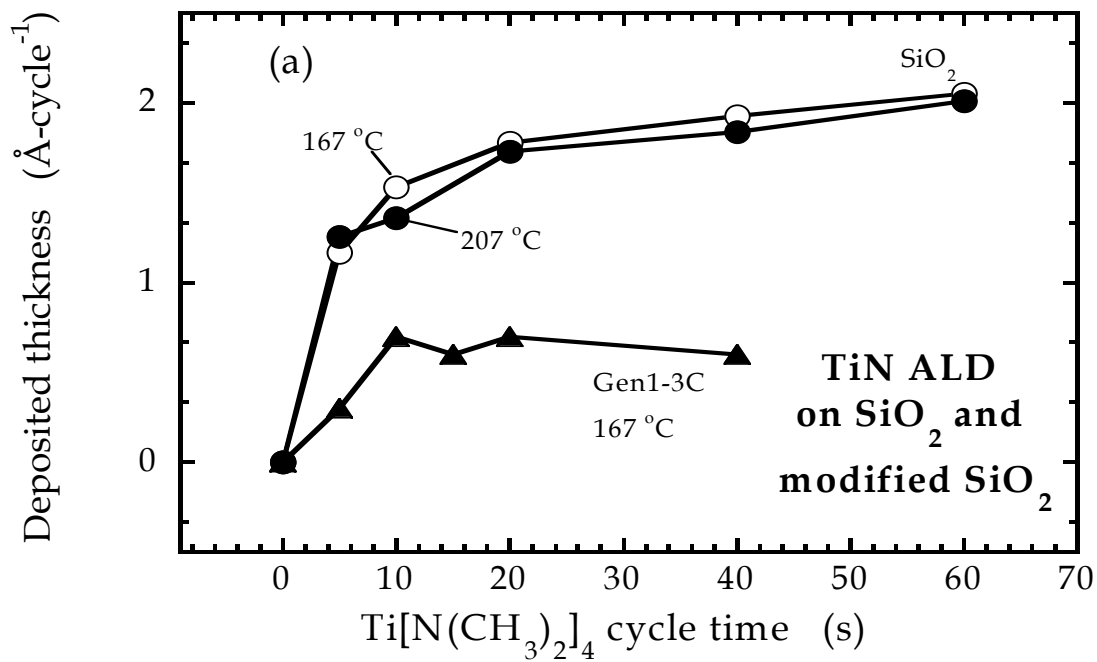
Detailed results regarding SAM characterization employing contact angle measurements, ellipsometry, XPS, and AFM have been described elsewhere [22,35]. The SAMs considered here, include four with generally hydrophobic endgroups (-CH₃ and -CF₃ terminations) and backbones, and four SAMs with relatively hydrophilic endgroups (-OH and -NH₂ terminations).

4.4.2 TiN ALD on SiO₂ and modified SiO₂

First, a discussion regarding the self-limiting nature of the ALD process using gated molecular beam sources is presented. In Fig. 4-2(a) the deposited thickness per cycle is plotted as a function of the exposure to Ti[N(CH₃)₂]₄ (E_i = 2.07 eV) per cycle for growth on chemical oxide at T_s = 167 and 207 °C, and on the branched amine-terminated SAM (Gen-1-3C) at T_s = 167 °C (total cycles : 200 for Gen-1-3C, 150 for oxide).

Figure 4-2: (a) Deposited thickness per cycle vs. exposure time to $\text{Ti}[\text{N}(\text{CH}_3)_2]_4$ for ALD of TiN on two surfaces: chemical oxide, SiO_2 ($T_s = 167$ and 207 °C), and SiO_2 modified with a $-\text{NH}_2$ terminated SAM ($T_s = 167$ °C, Gen-1-3C). Reactants introduced via gated supersonic $\{\text{Ti}[\text{N}(\text{CH}_3)_2]_4\}$ and effusive (NH_3) molecular beams. TiN film thickness was measured using ellipsometry. (b) Deposited thickness per cycle as a function of substrate temperature for the ALD of TiN on chemical oxide, SiO_2 .

(a), (b)



Here, substrate translation was used to vary the exposure time per cycle. It can be clearly seen that the deposited thickness per cycle approaches saturation for all three cases for exposures greater than approximately 4×10^{16} molecules-cm². Saturation for this exposure is consistent with molecular beam scattering studies at similar reaction conditions [43]. The deposited (ellipsometric) thickness per cycle approaches saturation, in all the examined cases (namely SiO₂ at T_s=167 and 207 °C, and Gen1-3C SAM at T_s=167 °C), for exposures greater than approximately 4×10^{16} molecules-cm². What is interesting, and will be revisited, is that the deposited thickness per cycle on the SAM is suppressed with respect to that on the chemical oxide at essentially identical process conditions.

Substrate temperature is also known to be an important factor in ALD, where often a so-called “ALD window” is identified in which growth is constant, typically some fraction of one monolayer (ML)-cycle⁻¹. In Fig. 4-2(b), the deposited thickness per cycle on chemical oxide is plotted as a function of substrate temperature. In a passing note, for experiments conducted at T_s < 140 °C a measurable thickness could not be observed using ellipsometry. In previous work using conventional ALD in a viscous flow reactor (pressure of ~ 1 Torr) [44] growth was observed as low as 60 °C, although these films were extremely porous and very susceptible to oxidation. As may be seen, the deposited thickness per cycle from the process described here increases with increasing T_s, exhibiting a plateau at T_s = 167–207 °C, where it is ~ 2.0 Å-cycle⁻¹. In previous work using conventional ALD, a clear plateau in the deposited thickness was not observed but growth rates were similar (~ 2-3 Å-cycle⁻¹) [44], or the range over it was observed was only 10 or 15 °C in width, with a growth rate of ~ 5 Å-cycle⁻¹ [45].

Both studies, however, report a rapid increase in the deposited thickness above about $T_s = 180\text{ }^\circ\text{C}$ [44] or $210\text{ }^\circ\text{C}$ [45], which is consistent with the results reported here for ALD using gated molecular beams.

A second set of issues and/or requirements of the ALD process are its digital nature, and the existence of an “incubation” period. These are best examined by monitoring the film thickness as a function of the number of cycles. In Fig. 4-3(a) the ellipsometric thickness is plotted as a function of ALD cycles at $T_s = 167\text{ }^\circ\text{C}$ for growth on chemical oxide, and four of the SAMs: two with reactive $-\text{NH}_2$ endgroups (Gen-1-3C, Gen-1-12C); two with unreactive backbones and endgroups (OTS, TTS). Presented in Fig. 4-3(b) are the results for the other four SAMs: reactive ($-\text{OH}$, Gen-0-12C) and unreactive (FOTS, HMDS). For growth on the chemical oxide the data can be fit by a straight line, and the deposited thickness is $1.97\text{ \AA-cycle}^{-1}$, with no observed incubation time. These films were smooth and continuous as deduced from AFM ($\sim 8\text{ \AA}$ RMS roughness at 175 \AA thickness) and cross-sectional scanning electron microscopy (SEM). The AFM images at different stages during growth are shown in Fig. 4-4(a). In Fig. 4-4(b) selected line scans are shown, depicting evolution of RMS roughness with measured ellipsometric thickness are shown. The RMS roughness increases steadily with increase in thickness. These roughness profiles will be compared against those obtained for the SAMs, a little later.

Next the growth on the surfaces modified by the SAMs is examined. In Fig. 4-3(a) and (b), the TiN film thickness is plotted as a function of the number of ALD cycles for the SAMs, all at $T_s = 167\text{ }^\circ\text{C}$. Two immediate observations can be made.

Figure 4-3: (a) TiN thin film thicknesses, measured using ellipsometry, as a function of the number of reactant cycles for ALD on several substrates: clean chemical oxide, SiO₂, and SiO₂ modified by four different SAMs. The SAMs possess two different functional terminations: -NH₂ (Gen-1-3C and Gen-1-12C :filled and open triangles respectively) and -CH₃ (OTS and TTS :filled and open squares respectively), and also represent different chain/backbone lengths. The smooth lines represent a fit to Eq. 4-1 ($T_s = 167$ °C). (b) TiN thin film thicknesses, measured using ellipsometry, as a function of the number of reactant cycles for ALD SiO₂ modified by four different SAMs. The SAMs possess four different functional terminations: -OH (open circles), -NH₂ (Gen-0-12C : open triangles), -CH₃ (HMDS : filled squares), and -CF₃ (FOTS: filled diamonds). The smooth lines represent a fit to Eq. 4-1 ($T_s = 167$ °C).

(a)

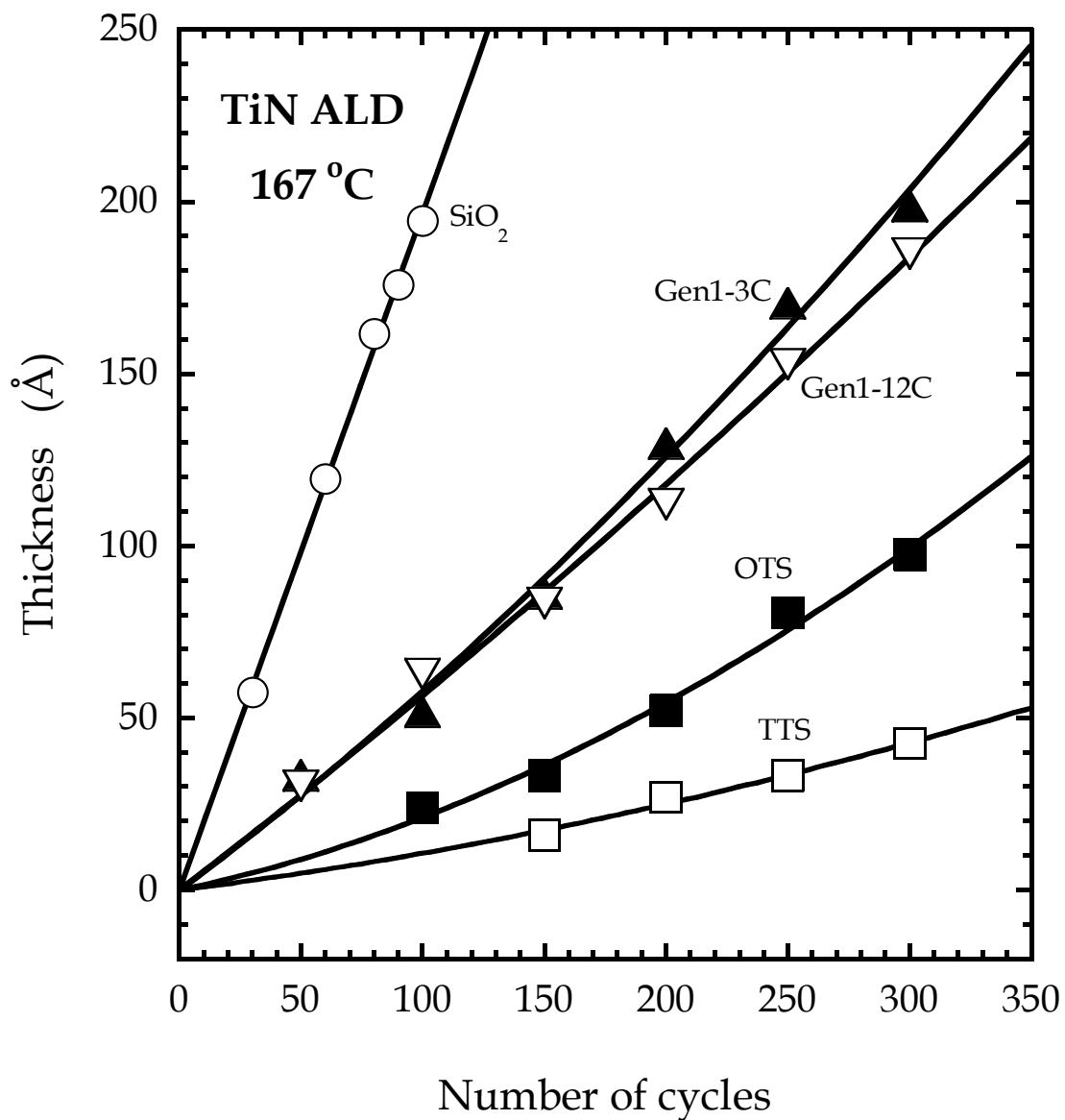


Figure 4-3 (continued)

(b)

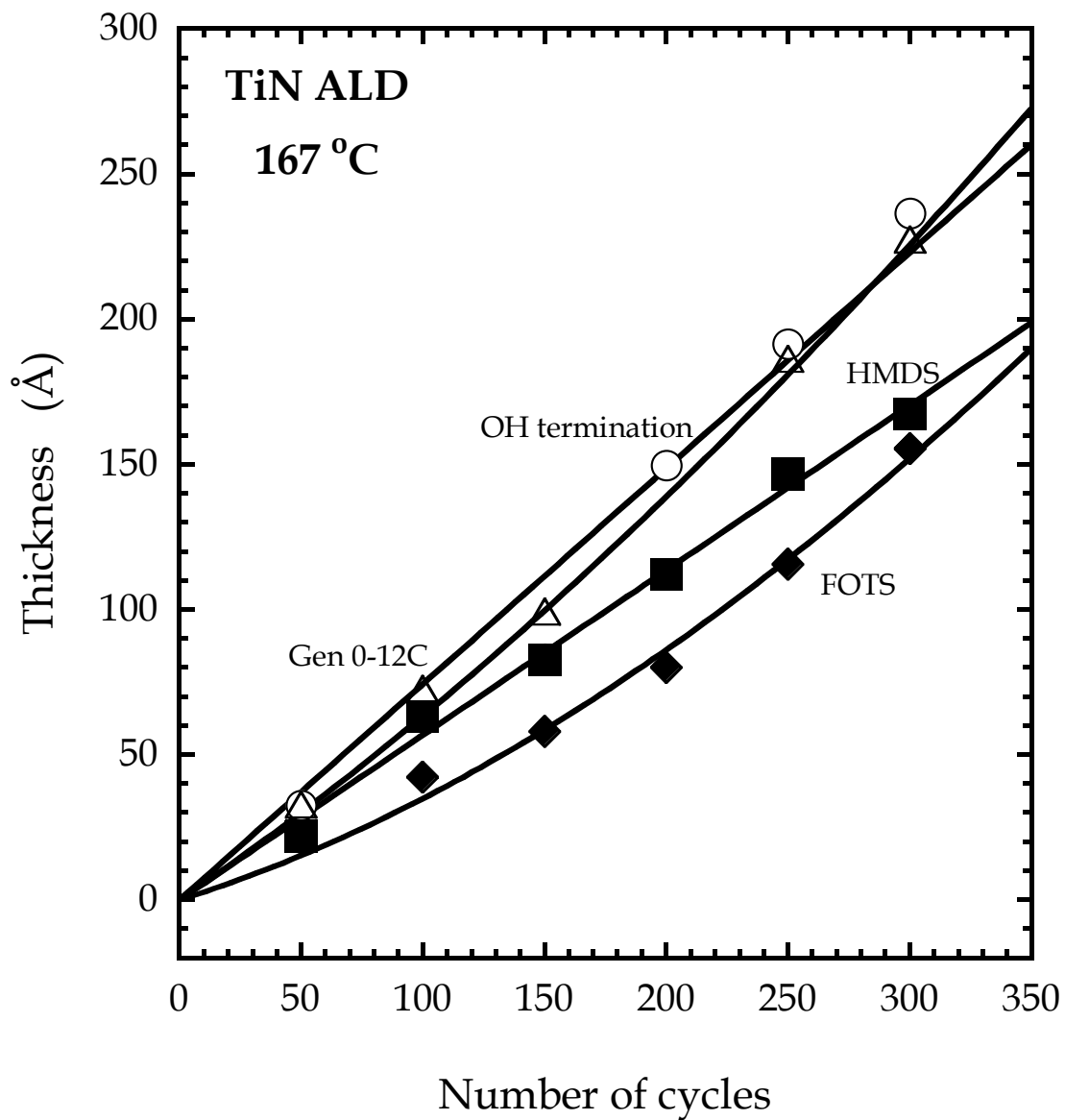


Figure 4-4: (a) Atomic force microscope images for TiN ALD at 167 °C on SiO₂. In each case the field of view is 0.5 μm × 0.5 μm. The images presented are for the untreated SiO₂ as well as TiN films which have been grown for 30, 60, 80, 90, and 150 cycles. (b) Selected cross sectional line scans which have been offset by the ellipsometric thickness values; at 0, 30, 80, 90, and 150 cycles and depict the evolution of RMS roughness.

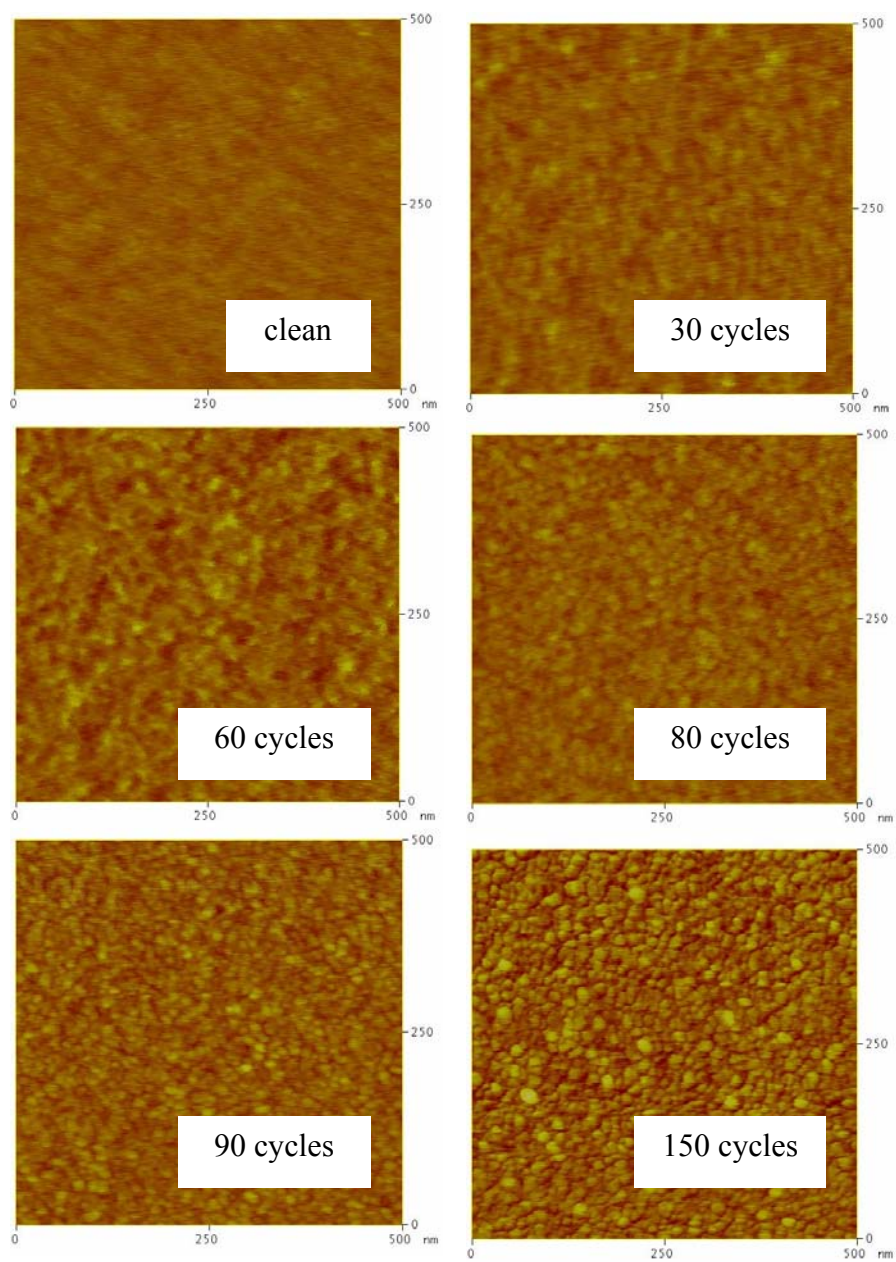
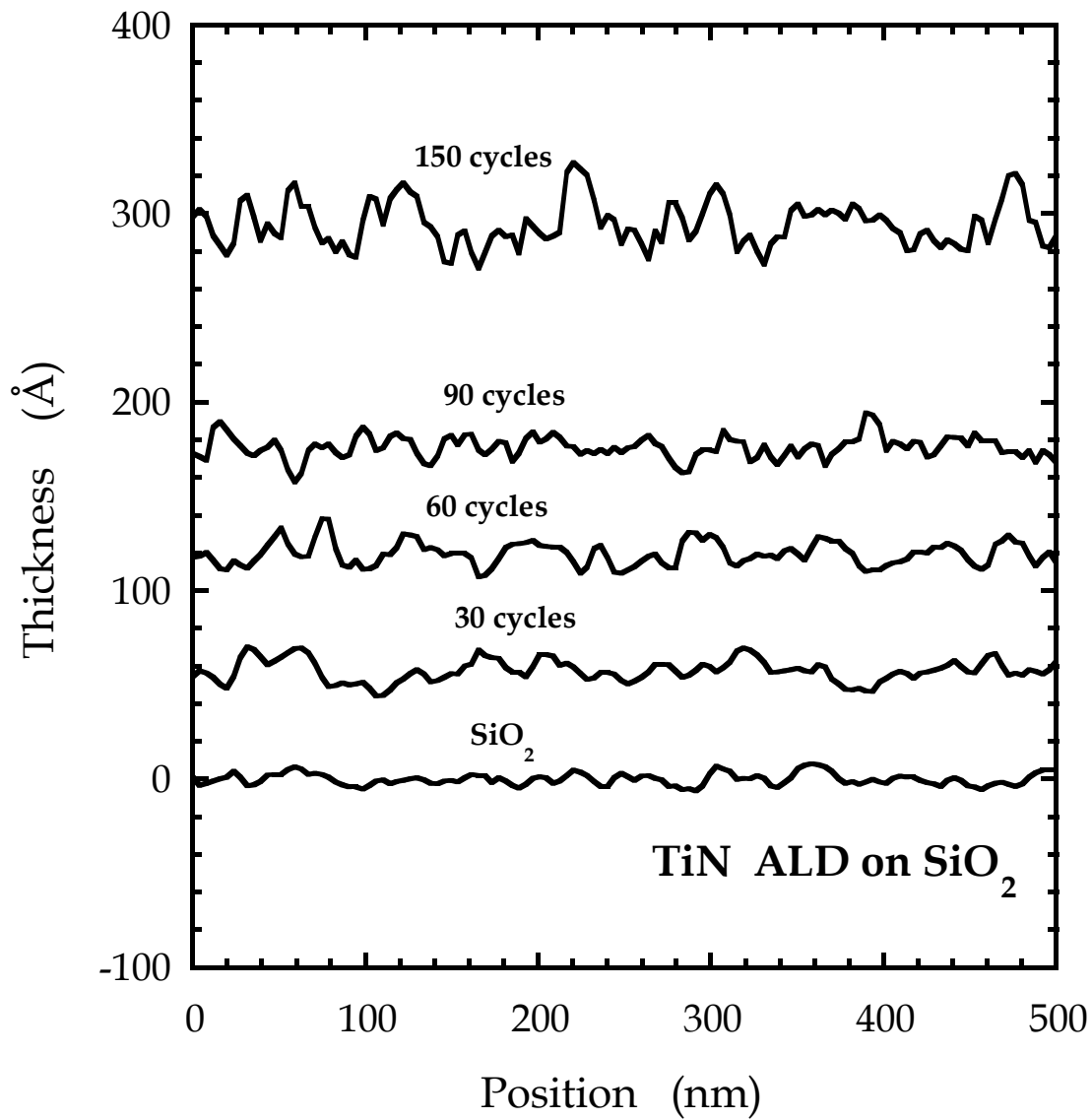
(a)

Figure 4-4 (continued)

(b)



The film thickness at a fixed number of cycles is greatly attenuated for all of the surfaces modified by the SAMs, and second, there is upward curvature in the data for ellipsometric thickness vs. number of cycles. In an effort to quantify the effects of the SAMs on the ALD of TiN from $\text{Ti}[\text{N}(\text{CH}_3)_2]_4$ and NH_3 , these data are fit to the following functional form:

$$D = D_\infty \{n + m(1 - \alpha)[\exp(-n/m) - 1]\} \quad (4-1)$$

where D is the film thickness, n is the number of ALD cycles, D_∞ is the deposited thickness per cycle as $n \rightarrow \infty$, and α and m are parameters. In this model there is no “incubation” time, where the growth is identically zero, and the functional form is essentially that given previously as an asymptotic form by Alam and Green [46]. Shown in Fig. 4-3(a) and (b) are fits of the data to the proposed functional form, where it was assumed that $D_\infty = 1.97 \text{ \AA-cycle}^{-1}$, i.e., the deposited thickness per cycle for the chemical oxide surface at $T_s = 167 \text{ }^\circ\text{C}$. The chemical oxide surface exhibits almost instantaneous nucleation with linear growth and hence can be used a model surface which exhibits steady state growth throughout. As may be seen, the fits to the data for growth on the all the SAMs are excellent. In a similar set of experiments conducted at $T_s = 207 \text{ }^\circ\text{C}$, the data showed similar behavior—essentially linear growth on chemical oxide, while growth on the SAM-terminated surfaces was attenuated and fit well by the proposed functional form. These results are presented in Fig. 4-5, where D_∞ was assumed to be $2.15 \text{ \AA-cycle}^{-1}$ which is the deposited thickness per cycle for the chemical oxide surface at $T_s = 207 \text{ }^\circ\text{C}$. For the sake of brevity, only five sets of data are presented: SiO_2 , Gen-1-3C, Gen-1-12C, FOTS, and TTS SAMs. All the other SAMs also fit this functional form well.

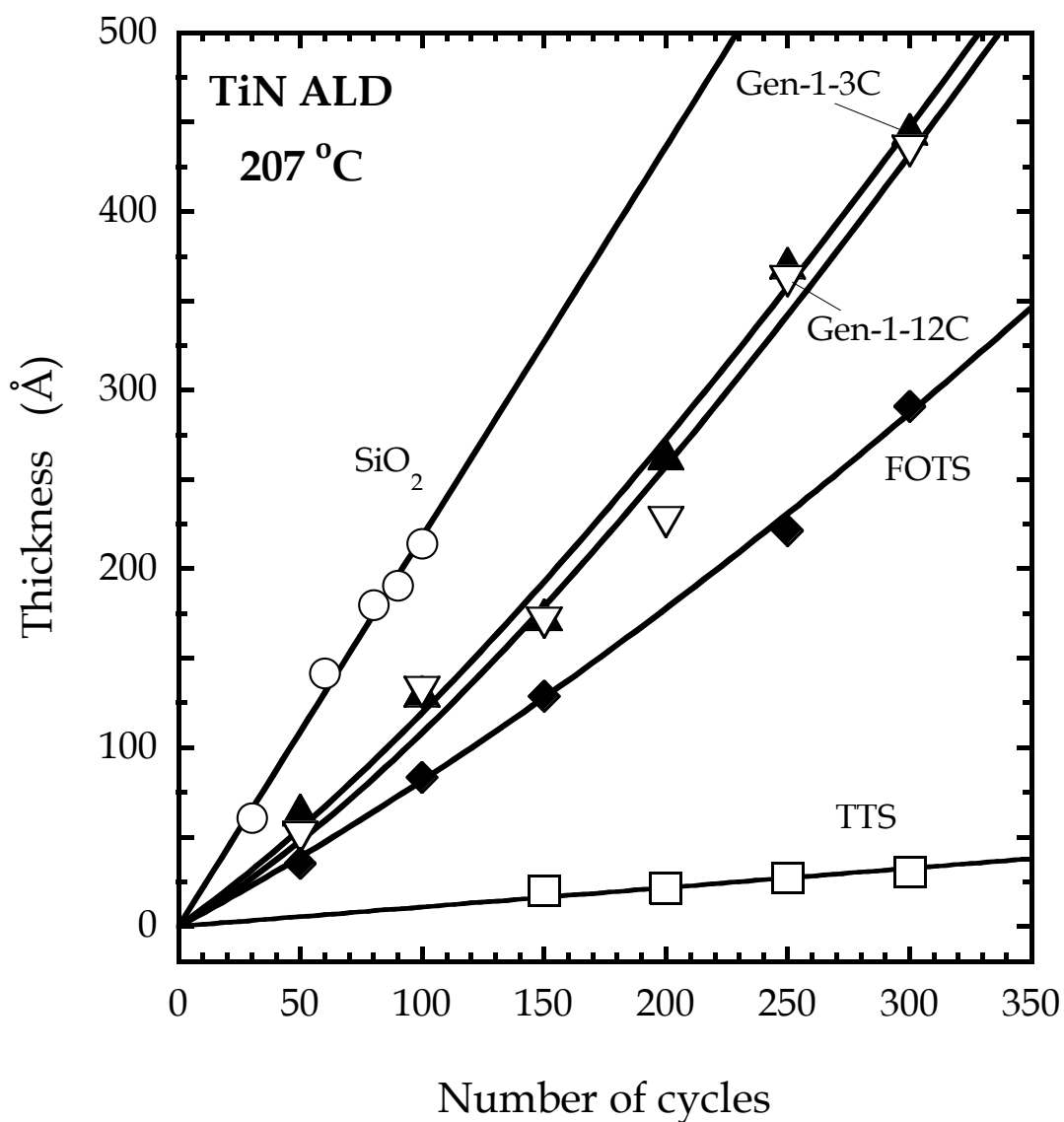


Figure 4-5: TiN thin film thickness, measured using ellipsometry, as a function of the number of reactant cycles for ALD on several substrates: clean chemical oxide, SiO₂; and SiO₂ modified by four different SAMs. The SAMs possess two different functional terminations: -NH₂ (Gen1-3C and Gen1-12C), -CH₃ (TTS), and -CF₃ (FOTS), and also represent different chain/backbone lengths. The smooth lines represent a fit to Eq. (4-1) ($T_s = 207$ °C).

In order to perhaps better understand the effect of the SAMs on the ALD process, in Fig. 4-6 the growth attenuation factor $\acute{\alpha}$ ($\acute{\alpha} = 1$ for SiO_2) has been plotted as a function of the measured ellipsometric thicknesses of the SAMs. The SAMs have been classified into two groups: those possessing reactive {with respect to $\text{Ti}[\text{N}(\text{CH}_3)_2]_4$ ligand exchange reactions} and unreactive end groups (at $T_s = 167$ °C). From the data shown in Fig. 4-6 one can conclude that for the SAMs with reactive end groups, the attenuation factor depends weakly on the thickness of the layer, as $\acute{\alpha} \sim 0.27\text{-}0.29$. Again, these SAMs possess either linear or branched backbones, and $-\text{NH}_2$ or $-\text{OH}$ end groups.

XPS and RBS have also been used to examine the thickness of these layers, and the results for $\acute{\alpha}$ from RBS are shown in Fig. 4-6. For all the reactive SAMs, and the relatively short-chain unreactive HMDS and FOTS SAMs, RBS and ellipsometry give nearly the same thickness. An example RB spectrum, a TiN film grown on a Gen-1-3C SAM for 300 cycles, is shown in Fig. 4-7. All the relevant peaks are also indicated. For the long-chain unreactive OTS and TTS SAMs, RBS indicates formation of much thinner layers, whereas XPS indicates a thickness intermediate between those indicated by RBS and ellipsometry. Film roughness could be a reason behind this disparity. More importantly, the general observations concerning the effects of the SAMs do not change. Due to the *ex situ* nature of composition analysis, O was detected in addition to Ti, N, and C. The data along with a simulation (overlying smooth curve) is shown in Fig. 4-7, represents a result where the stack was modeled as a $\text{TiO}_2 / \text{TiN} / \text{Gen-1-3C} / \text{SiO}_2 / \text{Si}$ (100). The simulation was carried out with the aid of RUMP [49]. A TiO_2 surface layer had to be accounted for due to the fact that there is oxidation of the top few layers once the TiN surface is exposed to air.

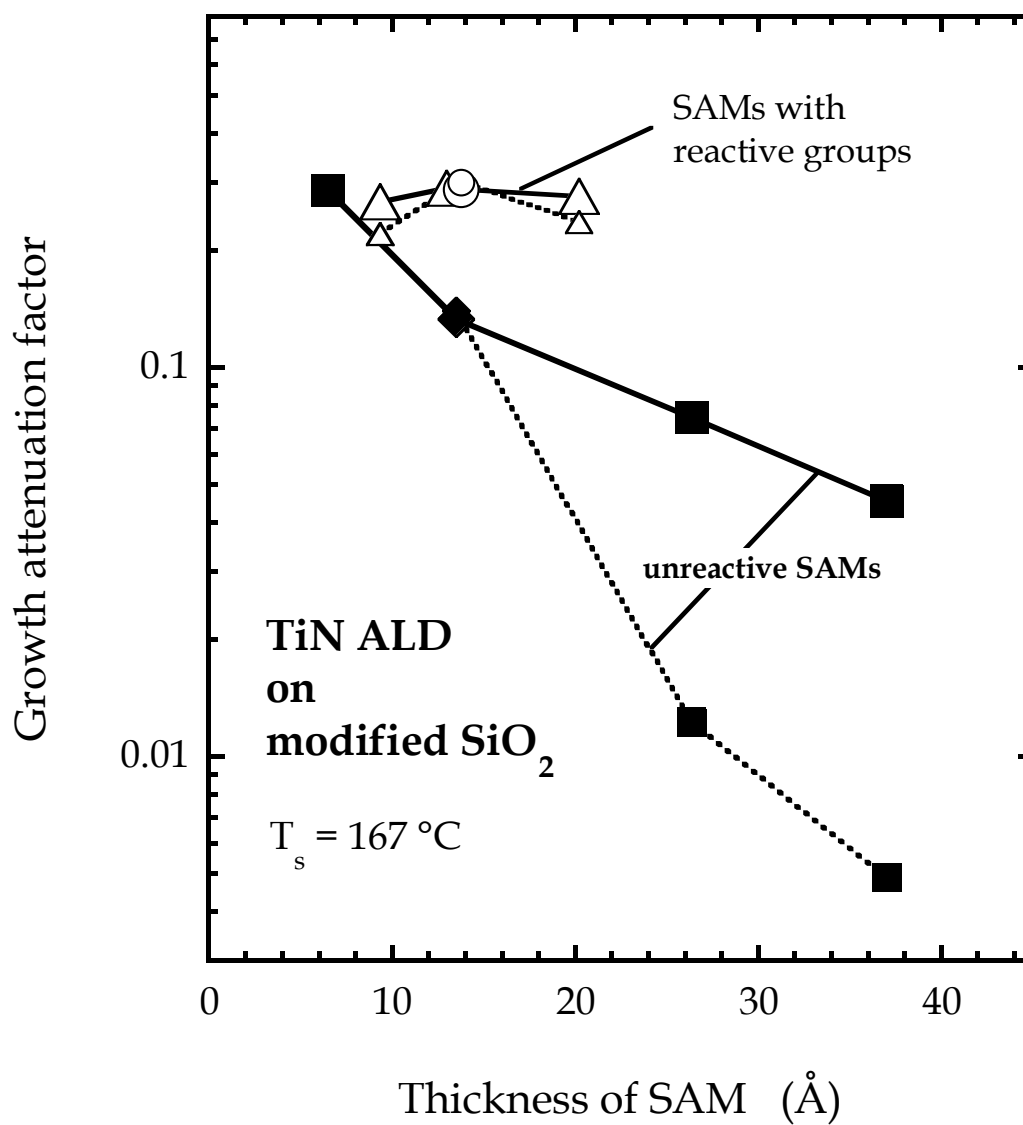


Figure 4-6: Growth attenuation factor as a function of thickness of the SAM ($T_s = 167 \text{ }^\circ\text{C}$). Plotted are the results for SAMs possessing either reactive endgroups ($-\text{OH}$ or $-\text{NH}_2$, open symbols) or unreactive endgroups ($-\text{CH}_3$ or CF_3 , filled symbols). The smaller symbols and dashed lines represent results derived from thicknesses determined from RBS.

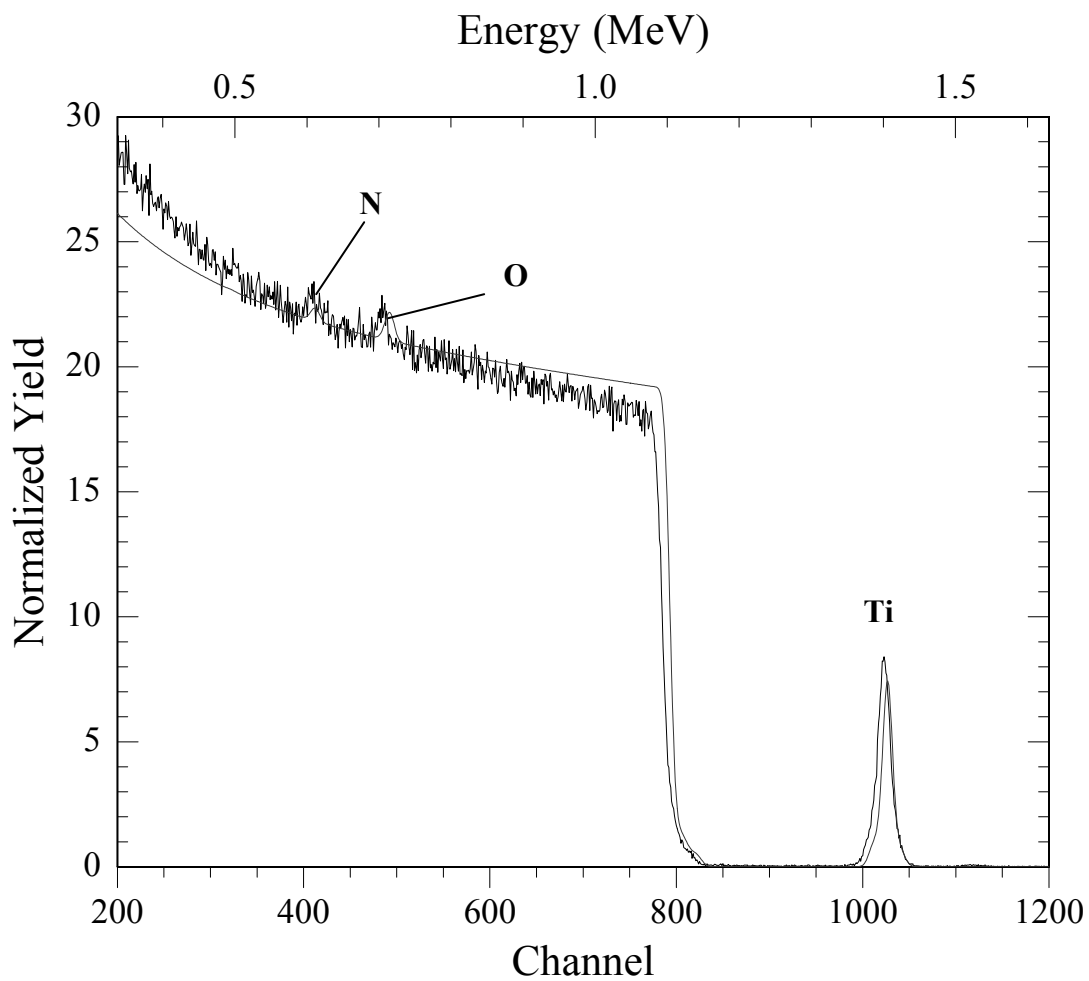


Figure 4-7: RB spectrum for a 190 Å thick TiN film on a Gen-1-3C SAM modified SiO₂ substrate. The data are presented along with the simulation results (overlying smooth curve) carried out with the aid of RUMP. All the elemental peak positions are indicated.

The PERT subprogram was used to search for a "best" fit to the data. It does so by varying one or more parameters of the sample description or experimental parameters (thicknesses, compositions, etc.) and comparing the resulting theoretical spectrum with the actual spectrum. PERT iterates the process until it finds the best set of parameters to match the spectrum. The definition of "best" fit is the one which maximizes the Poisson likelihood function χ^2 between the experimental spectrum and the simulation over a selected region called the error window. In this case the layer compositions were fixed, and the only simulation parameters were the TiN and TiO₂ thickness values. The RBS calculated thickness for the TiO₂ / TiN stack is in very good agreement with the measured ellipsometric thickness in all but two cases. The cases of OTS and TTS show a large deviation. The films in these two cases are the thinnest and roughness can start playing an important role in affecting the measurements. The results are presented in Fig. 4-8. All the measured films, except that on SiO₂ were grown for 300 cycles at 167 °C. The SiO₂ films were grown for 100 cycles. Details regarding the RBS simulation are also given in Appendix C.

To investigate the effect of T_s on growth on SAMs, plotted in Fig. 4-9 are the growth attenuation factors α as a function of the measured ellipsometric thicknesses of the SAMs, both at 167 and 207 °C. From the data shown in Fig. 4-9, one can conclude that for the SAMs with reactive end groups, the attenuation factor depends weakly on the thickness of the layer, and T_s , as $\alpha \sim 0.3-0.5$ in all cases. Thus, for these SAMs, it would seem that nucleation and growth is initiated at the terminal OFGs, and that the length of the backbone of the SAM that anchors it to the surface does not affect the attenuation factor.

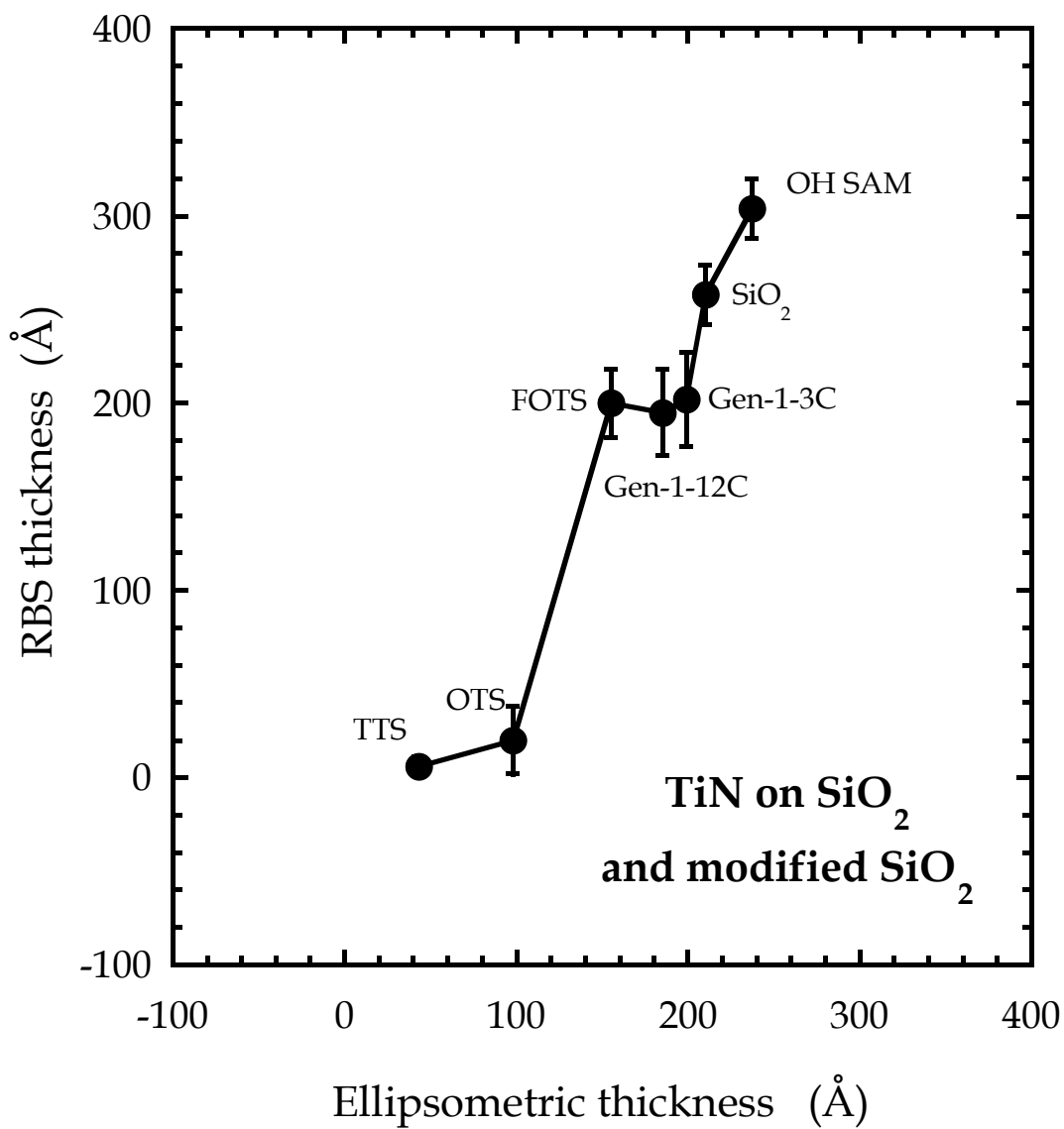


Figure 4-8: Comparison of the measured ellipsometric and the modeled RBS thicknesses, for SiO₂ and six different SAMs. All TiN films were grown at $T_s = 167^\circ\text{C}$.

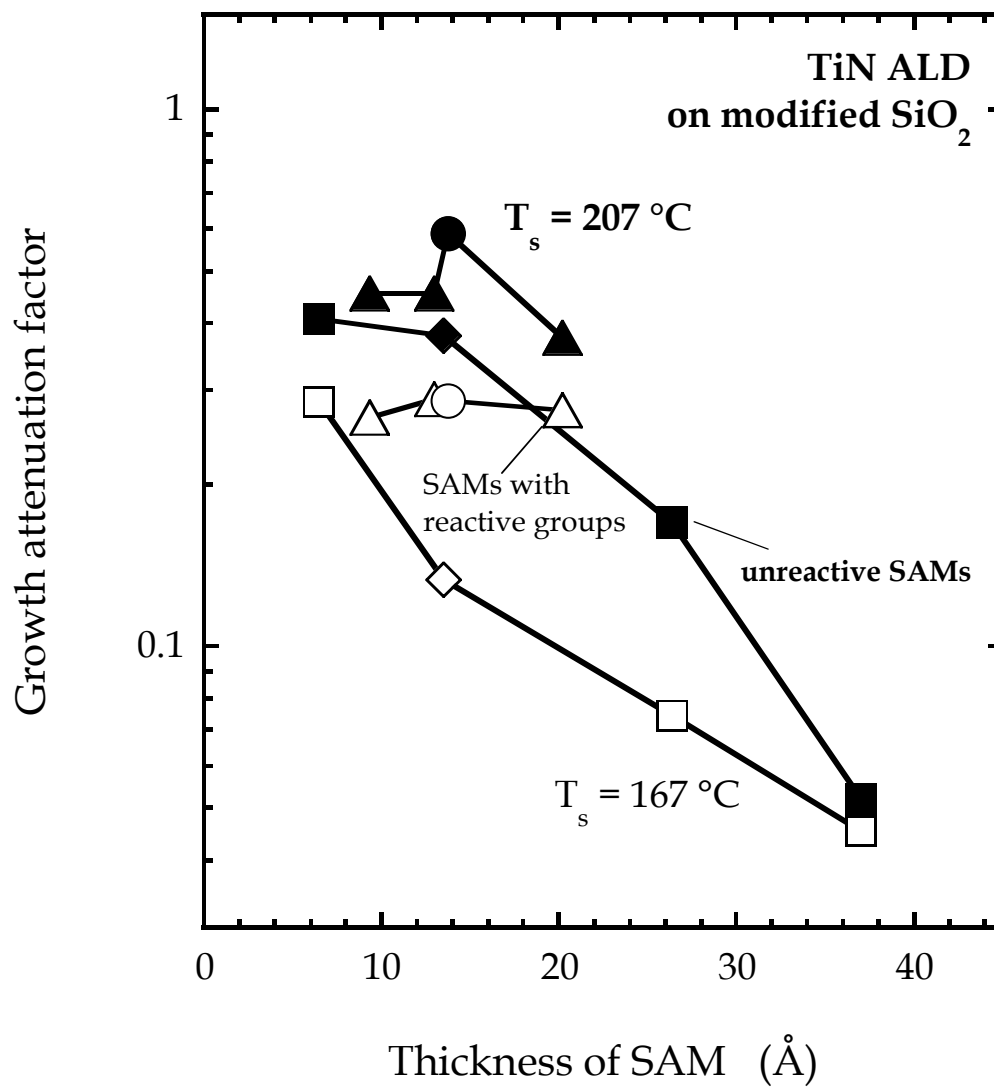


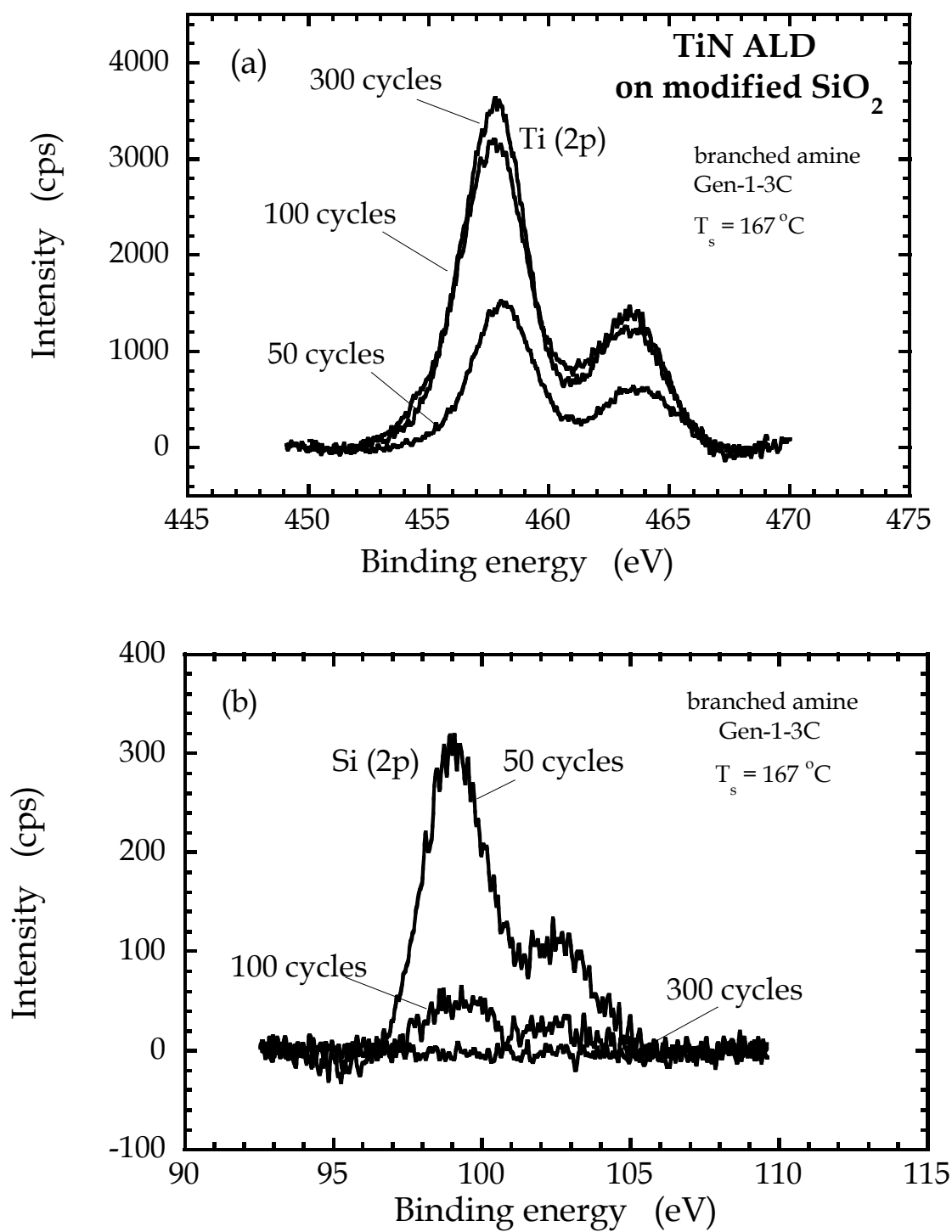
Figure 4-9: Growth attenuation factor as a function of thickness of the SAM ($T_s = 167$ and 207 °C). Plotted are the results for SAMs possessing reactive endgroups ($-\text{OH}$ or $-\text{NH}_2$, open and filled circles and triangles) and unreactive endgroups ($-\text{CH}_3$ or CF_3 , open and filled squares and diamonds).

Ti[N(CH₃)₂]₄ reacting with SAMs bearing -OH and -NH₂ groups has also been seen in previous work done in the Engstrom group, making use of x-ray photoelectron spectroscopy [22], and molecular beam scattering techniques [43]. For the SAMs possessing the unreactive terminal groups the attenuation factor clearly depends on the length of the backbone, at both T_s values. For HMDS, the thinnest layer examined, the behavior is very similar to that on the reactive SAMs. As the likely adsorbed species from HMDS is -Si(CH₃)₃, this group may provide little resistance to penetration by the Ti[N(CH₃)₂]₄ species to reach the SAM/SiO₂ interface, where residual -OH(*a*) is present. An increase in thickness of the unreactive groups will make sure that the Ti[N(CH₃)₂]₄ species will have to penetrate further to find to SAM/SiO₂ interface. The thicker layers will be better packed, and hence more difficult to penetrate and initiate nucleation. Although not too much importance could be attached to this disparity in absolute α value at the two T_s values examined here, it is conceivable that a competing effect comes into play. The SAMs will disorder at a faster rate at 207 °C [47], hence making the defect sites / vacancies in the organic layer much more accessible, thereby reducing its resistance to penetration by Ti[N(CH₃)₂]₄. Thus a higher value of α would be observed, which implies a deposited thickness per cycle value closer to that on SiO₂ under similar conditions.

To further probe the extent of growth and film composition as a function of number of ALD cycles, XPS was employed. The Gen-1-3C SAM has been chosen as an example. Shown in Fig. 4-10(a) are the Ti(2p) spectra from TiN films grown on the Gen-1-3C SAM for 50, 100, and 300 cycles.

Figure 4-10: XP spectra, after a Shirley background subtraction, as a function of number of cycles for TiN ALD on the $-\text{NH}_2$ terminated branched Gen-1-3C SAM at $T_s = 167$ °C for the (a) Ti (2p), and (b) Si (2p) features.

(a),(b)



The Ti signal has nearly reached saturation after 100 cycles. Another way to characterize the growth process would be to look at the Si(2p) spectrum as a function of number of ALD cycles. Plotted in Fig. 4-10(b) are the Si(2p) spectra after 50, 100, and 300 cycles where the Si(2p) signal has been nearly quenched after 100 cycles. This observation points to two possible scenarios: the first, where it can be envisioned that growth is non-uniform or islanded up to 100 cycles. In an alternate scenario, it can be argued that the TiN film is not thick enough, even after 100 cycles, to completely attenuate the Si(2p) signal from the substrate.

Clearly, there is a case here for making use of scanning probe techniques like AFM to track the topography as a function of number of cycles to further characterize the growth process. Shown in Fig. 4-11(a), are $0.5 \times 0.5 \mu\text{m}^2$ AFM images for TiN ALD at 167 °C on Gen-1-3C SAM. The images for the unreacted SAM as well as TiN films which have been grown for 50, 100, 200, and 300 cycles, respectively, have been presented. Plotted in Fig. 4-11(b) are the line scans that depict the evolution of root-mean-square (RMS) roughness as a function of the measured ellipsometric thickness. A quick increase in roughness can be seen from 0 to 50 cycles and it seems to saturate afterwards. From this data it can be concluded that the growth process is relatively uniform and conformal throughout with no evidence for island formation at any stage. This result will be revisited a little later, and compared against other roughness evolution profiles.

An interesting comparison to the just discussed case of Gen-1-3C SAM would be to track growth on an unreactive surface like TTS, which is the thickest interfacial layer examined here. In Fig. 4-12(a), the Ti (2p) spectra have been plotted, after 300 cycles at 167 °C, for the OTS and TTS SAMs.

Figure 4-11: (a) Atomic force microscope images for TiN ALD at 167 °C on Gen-1-3C SAM. In each case the field of view is $0.5 \mu\text{m} \times 0.5 \mu\text{m}$. The images presented are for the SAM as well as films which have been grown for 50, 100, 200, and 300 cycles. (b) Selected cross-sectional line scans which have been offset by the ellipsometric thickness values, at 0, 50, 150, and 300 cycles to depict the evolution of root-mean-square (RMS) roughness.

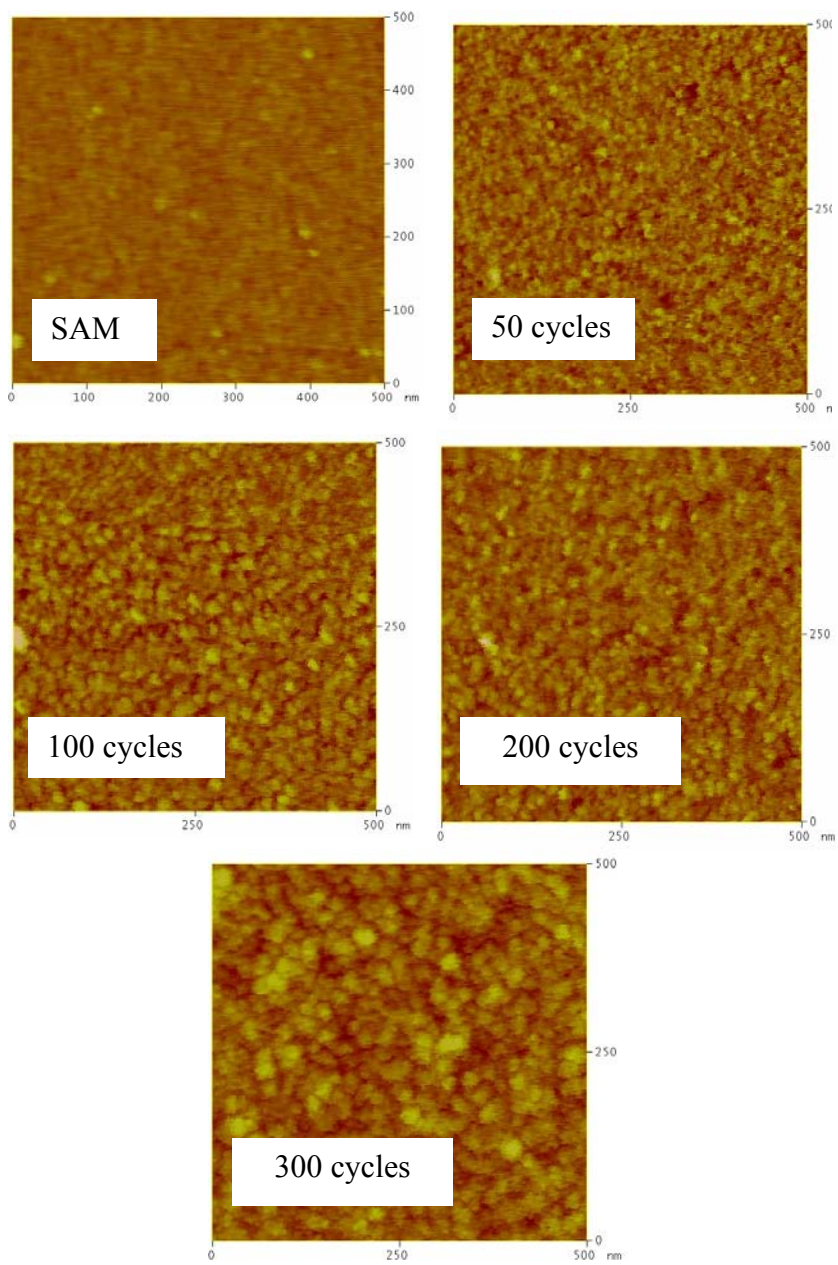
(a)

Figure 4-11 (continued)

(b)

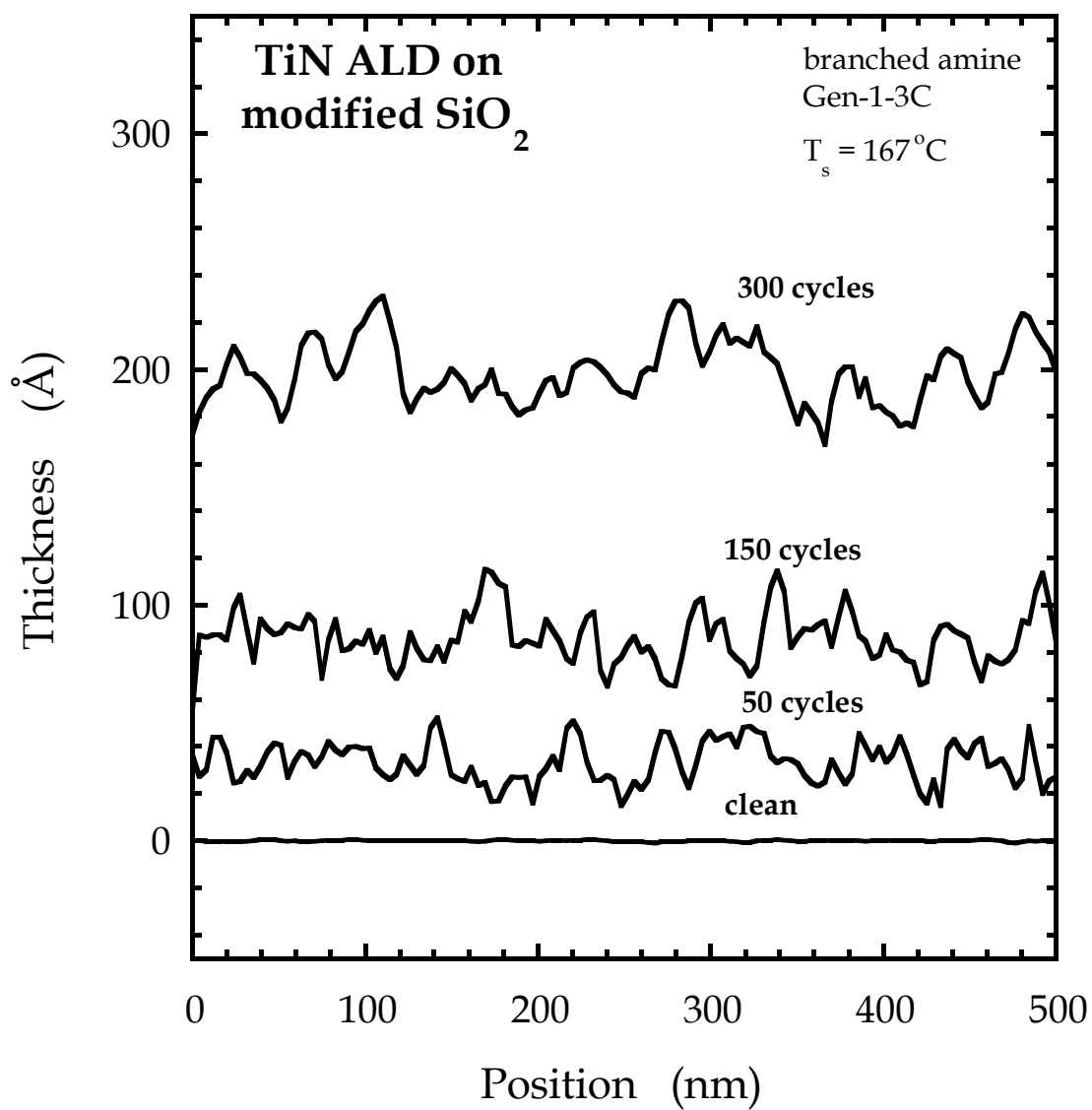
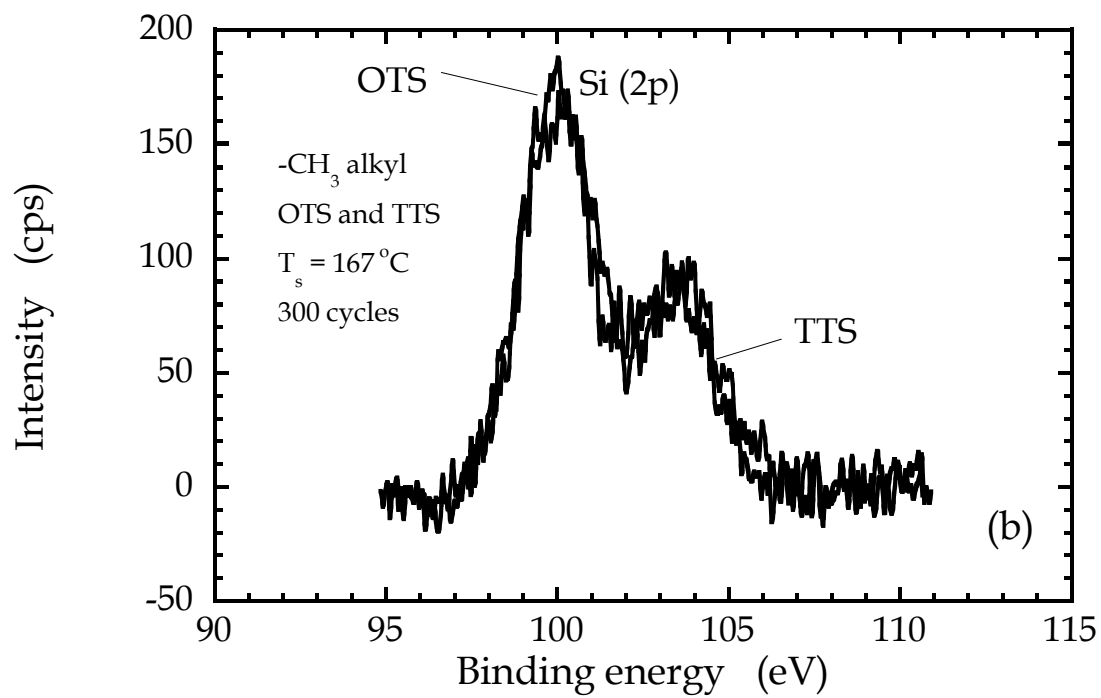
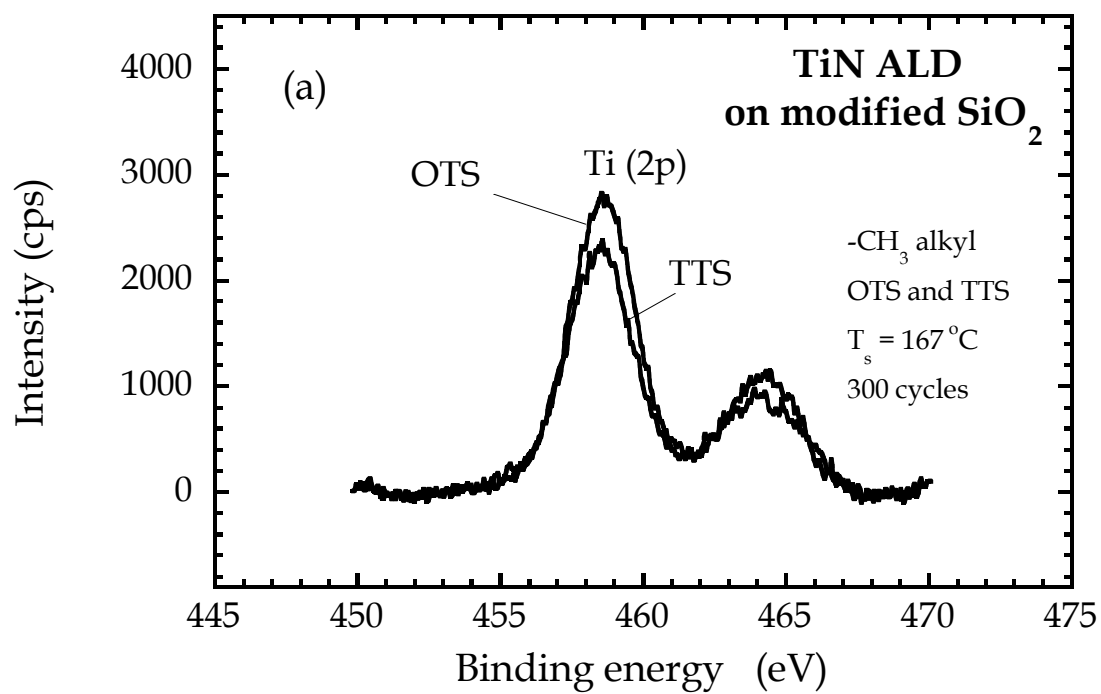


Figure 4-12: XP spectra, after a Shirley background subtraction, after 300 cycles for TiN ALD on the $-\text{CH}_3$ terminated branched OTS and TTS SAM at $T_s = 167^\circ\text{C}$ for the (a) Ti (2p), and (b) Si (2p) features.

(a), (b)



The Ti(2p) intensity, after a Shirley background subtraction, is higher in the case of OTS which is not an entirely unexpected result. The thicker TTS SAM is expected to possess a higher surface coverage and hence a higher density of surface $-CH_3$ groups and fewer vacancies or domain boundaries [11], making it more effective as a nucleation impeding layer. Similar trends have been reported for HfO_2 ALD on silicon dioxide surfaces patterned using $-CH_3$ terminated SAMs [23]. OTS, which was the thickest SAM examined [23], was reported to be the most efficient blocking agent. In Fig. 4-12(b) the Si(2p) spectra are plotted, for the OTS and TTS SAMs after exposure to 300 ALD cycles. The Si(2p) signal, in both cases, is not fully attenuated even after 300 cycles which is in contrast to the results obtained for the case of reactive Gen-1-3C SAM. At this time it is important to note that OTS and TTS are the only two surfaces which exhibit this behavior. For all the reactive SAMs as well as the thinner and unreactive HMDS and FOTS the Si(2p) signal was fully attenuated through the TiN overlayer. Also the Ti(2p) intensities are very close to each other in all these cases. This can only be explained by a growth process which is islanded or three-dimensional in nature, even after 300 cycles, in the case of OTS and TTS SAMs. Further and more conclusive evidence to support this argument can be obtained using AFM. Presented in Fig. 4-13(a), are $0.5 \times 0.5 \mu m^2$ images for the untreated TTS SAM along with TiN films which have been grown for 50, 150, 200, and 300 cycles. It is very clear from these "snapshots" during different stages of growth, that the films are islanded or three-dimensional (3-D) in nature, where the substrate is visible even after 200 growth cycles. In Fig. 4-13(b), selected line scans showing evolution of RMS roughness as a function of measured ellipsometric thickness, have been plotted.

Figure 4-13: (a) Atomic force microscope images for TiN ALD at 167 °C on TTS SAM. In each case the field of view is $0.5 \mu\text{m} \times 0.5 \mu\text{m}$. The images presented are for the SAM as well as TiN films which have been grown for 50, 150, 200, and 300 cycles. (b) Selected cross sectional line scans, which have been offset by the ellipsometric thickness values, at 0, 50, 100, and 200 cycles, depict the evolution of root-mean-square (RMS) roughness.

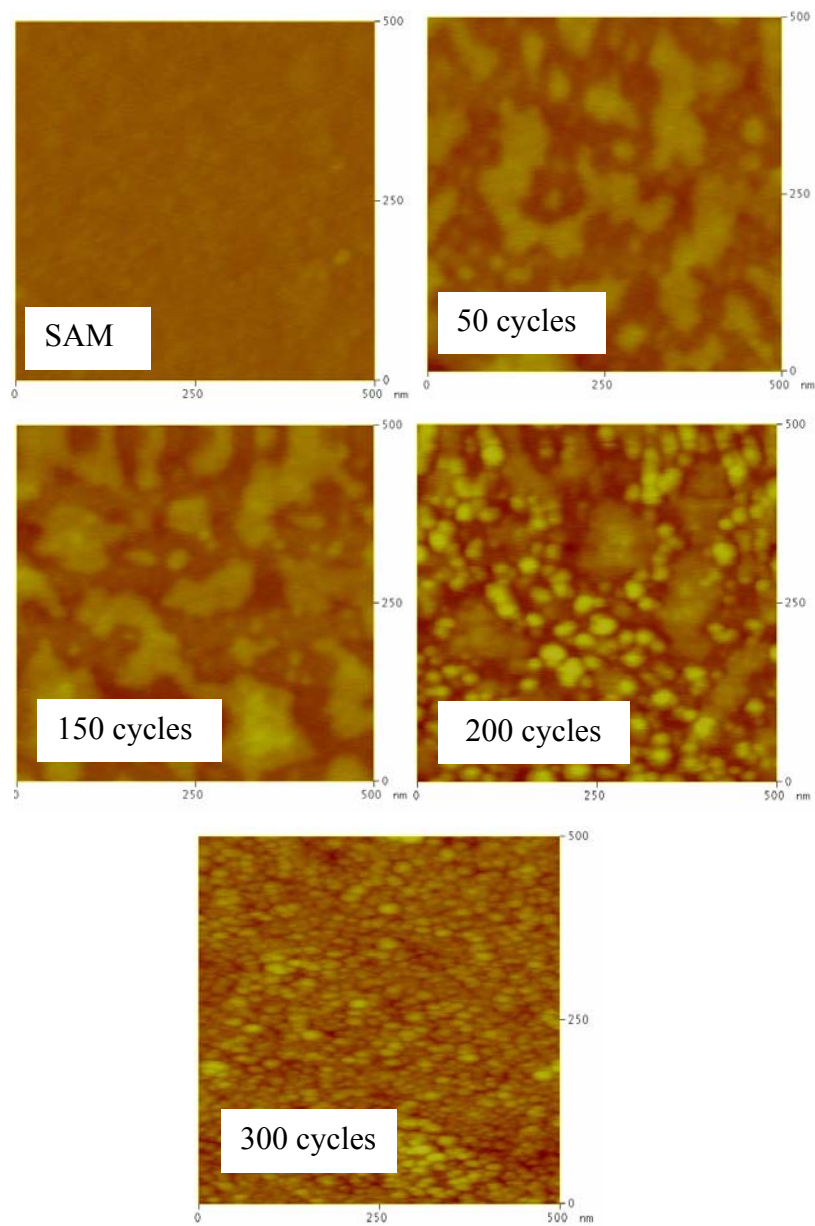
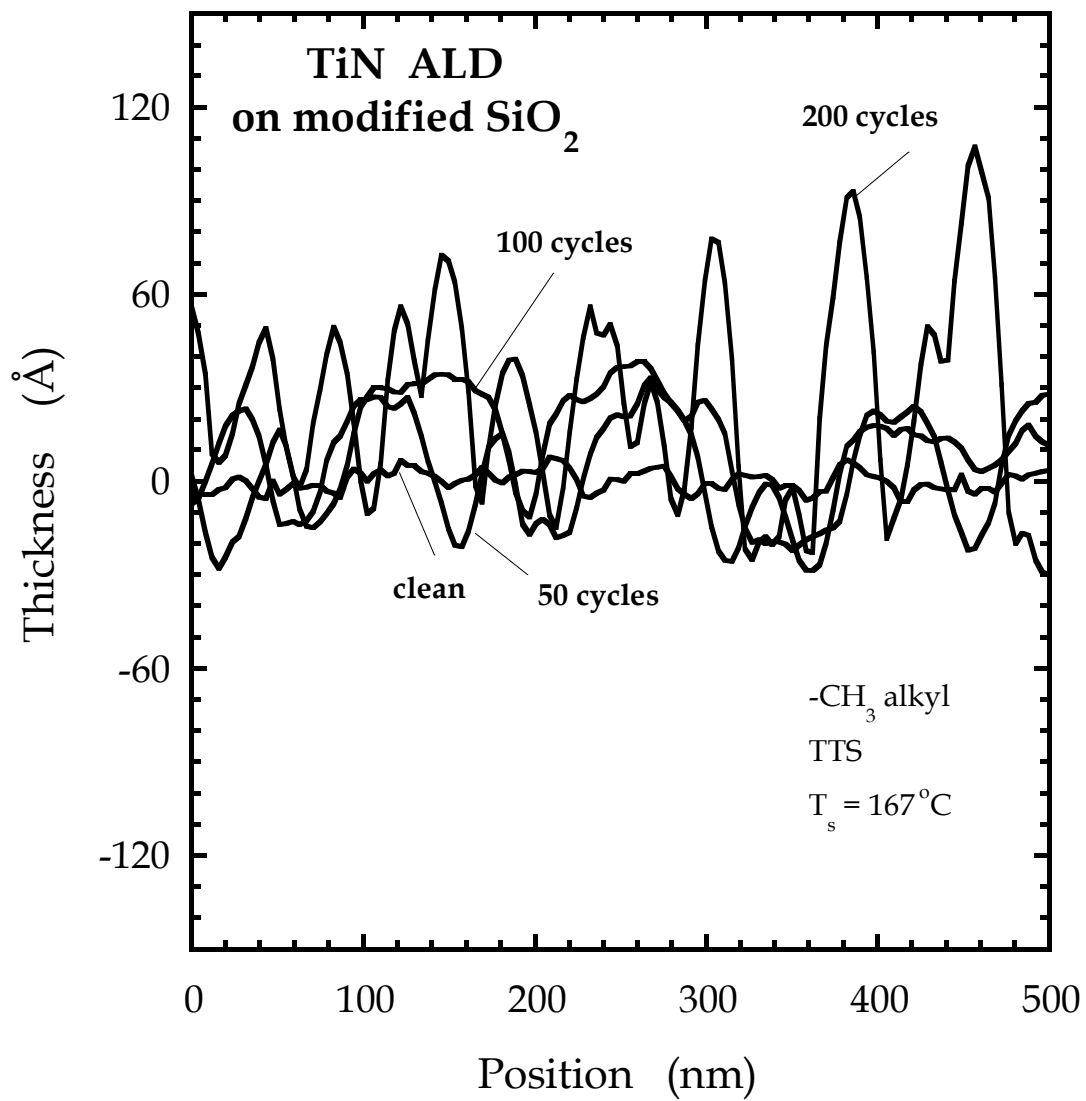
(a)

Figure 4-13 (continued)

(b)



The film roughness goes through a maximum around 200 cycles. However, even after 300 cycles RMS roughness is $\sim 30 \text{ \AA}$ for films of a nominal ellipsometric thickness of 30 \AA . As mentioned earlier, the XPS results would also support this mechanism.

To further support the argument about nucleation occurring at defect sites in case of the so-called unreactive SAMs, growth on the thinnest interfacial layer used has also been examined. HMDS modified SiO_2 has a nominal thickness of $\sim 6.5 \text{ \AA}$, and can be expected to have the highest density of vacancies and defect sites in the form of $-\text{OH}(\text{a})$ groups on the exposed SiO_2 . Shown in Fig. 4-14(a) are $0.5 \times 0.5 \mu\text{m}^2$ AFM images for untreated HMDS and TiN films grown on HMDS, at $167 \text{ }^\circ\text{C}$, for 50, 100, 200, and 300 cycles respectively. The films, purely on a visual inspection, resemble those shown in Fig. 4-11(a) for growth on the Gen-1-3C SAM and the growth is not nearly as non-uniform or islanded as it was in the case of TTS SAM, the other unreactive SAM, TTS, just discussed. Also plotted in Fig. 4-14(b), are the selected line scans which depict the evolution RMS roughness as a function of ellipsometric thickness. It can again be seen that the roughness increases rapidly from 0 to 50 cycles and plateaus afterwards. It is important to note, however, that the RMS roughness is 15 \AA for a nominal thickness of $\sim 20 \text{ \AA}$ after 50 cycles. Thus it can be argued that the growth process is indeed three-dimensional or islanded in the very early stages. It eventually becomes relatively uniform, as suggested by the slight decrease in RMS roughness after 50 cycles.

As a final comparison, it would be useful to look at the effect of a different reactive terminal functional group on TiN growth. Shown in Fig. 4-15(a) are $0.5 \times 0.5 \mu\text{m}^2$ AFM images for unreacted $-\text{OH}$ SAM and TiN films grown on it (at $167 \text{ }^\circ\text{C}$), for 50, 100, 200 and 300 cycles, respectively.

Figure 4-14: (a) Atomic force microscope images for TiN ALD at 167 °C on HMDS SAM. In each case the field of view is $0.5 \mu\text{m} \times 0.5 \mu\text{m}$. The images presented are for the SAM as well as TiN films which have been grown for 50, 100, 200, and 300 cycles. (b) Selected cross sectional line scans which have been offset by the ellipsometric thickness values, at 0, 50, 100, 200, and 300 cycles and depict the evolution of root-mean-square (RMS) roughness.

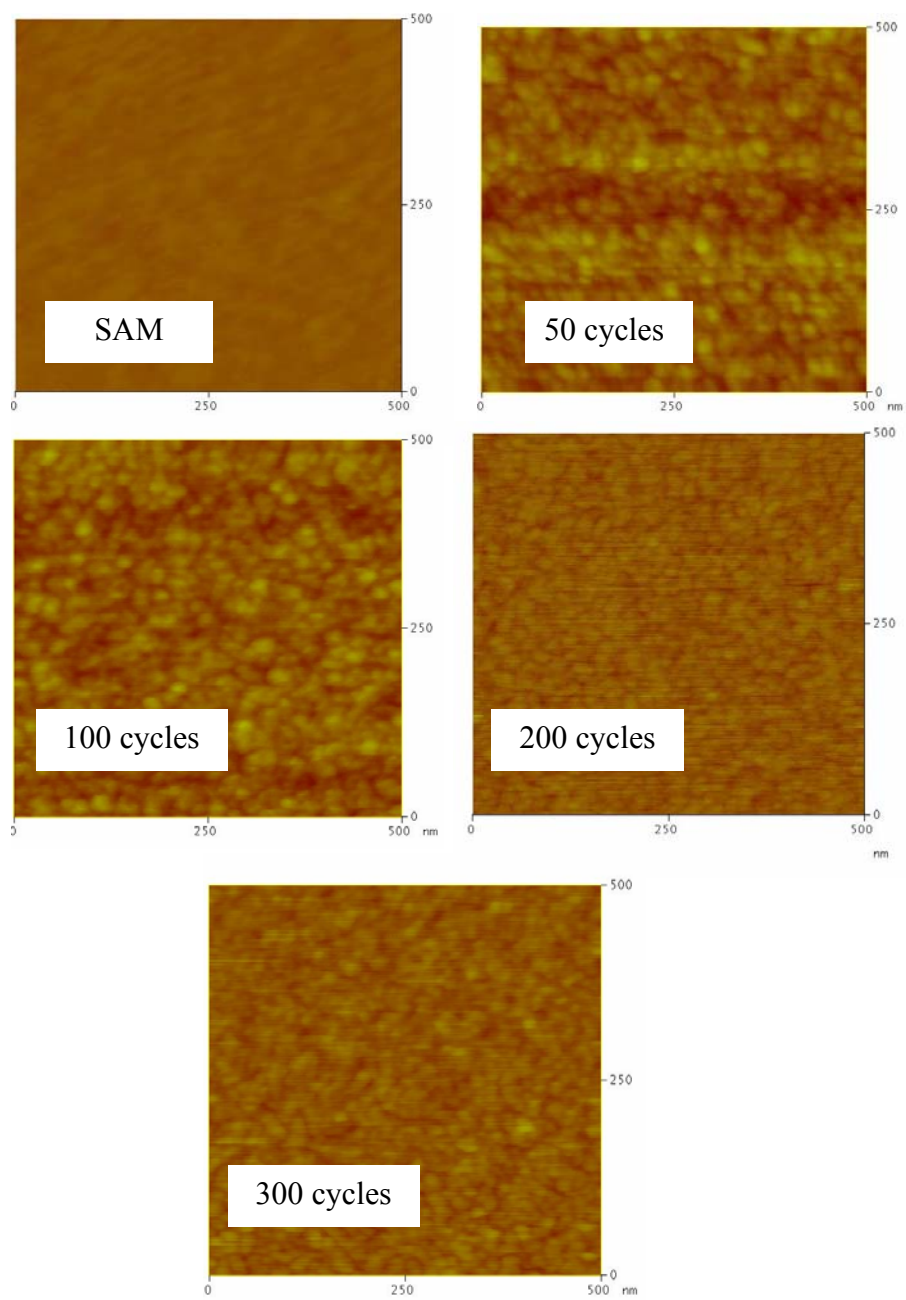
(a)

Figure 4-14 (continued)

(b)

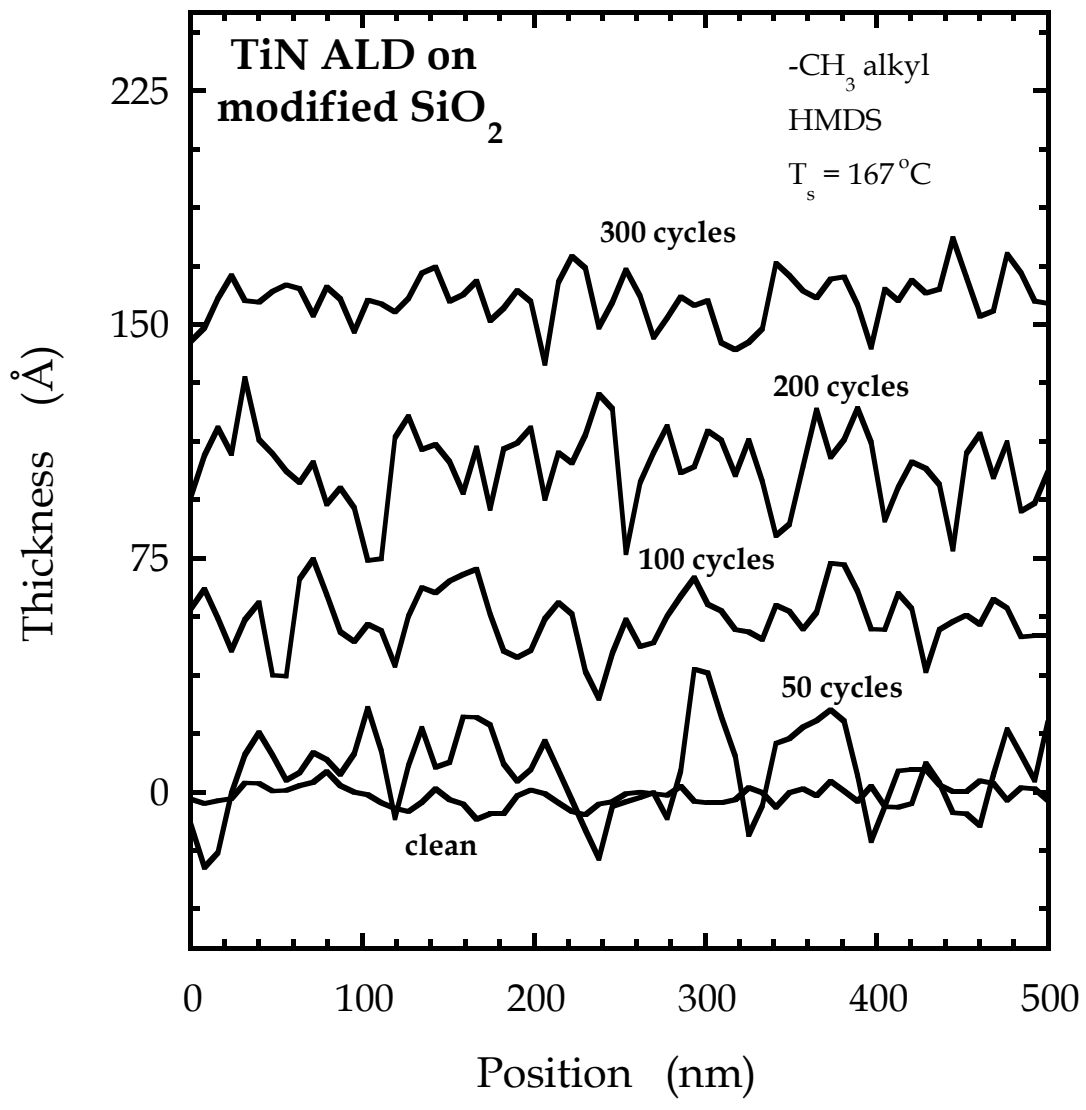


Figure 4-15: (a) Atomic force microscope images for TiN ALD at 167 °C on the -OH SAM. In each case the field of view is $0.5 \mu\text{m} \times 0.5 \mu\text{m}$. The images presented are for the SAM as well as TiN films which have been grown for 50, 100, 200, and 300 cycles. (b) Selected cross sectional line scans which have been offset by the ellipsometric thickness values, at 0, 50, 100, 200, and 300 cycles and depict the evolution of root -mean -square (RMS) roughness.

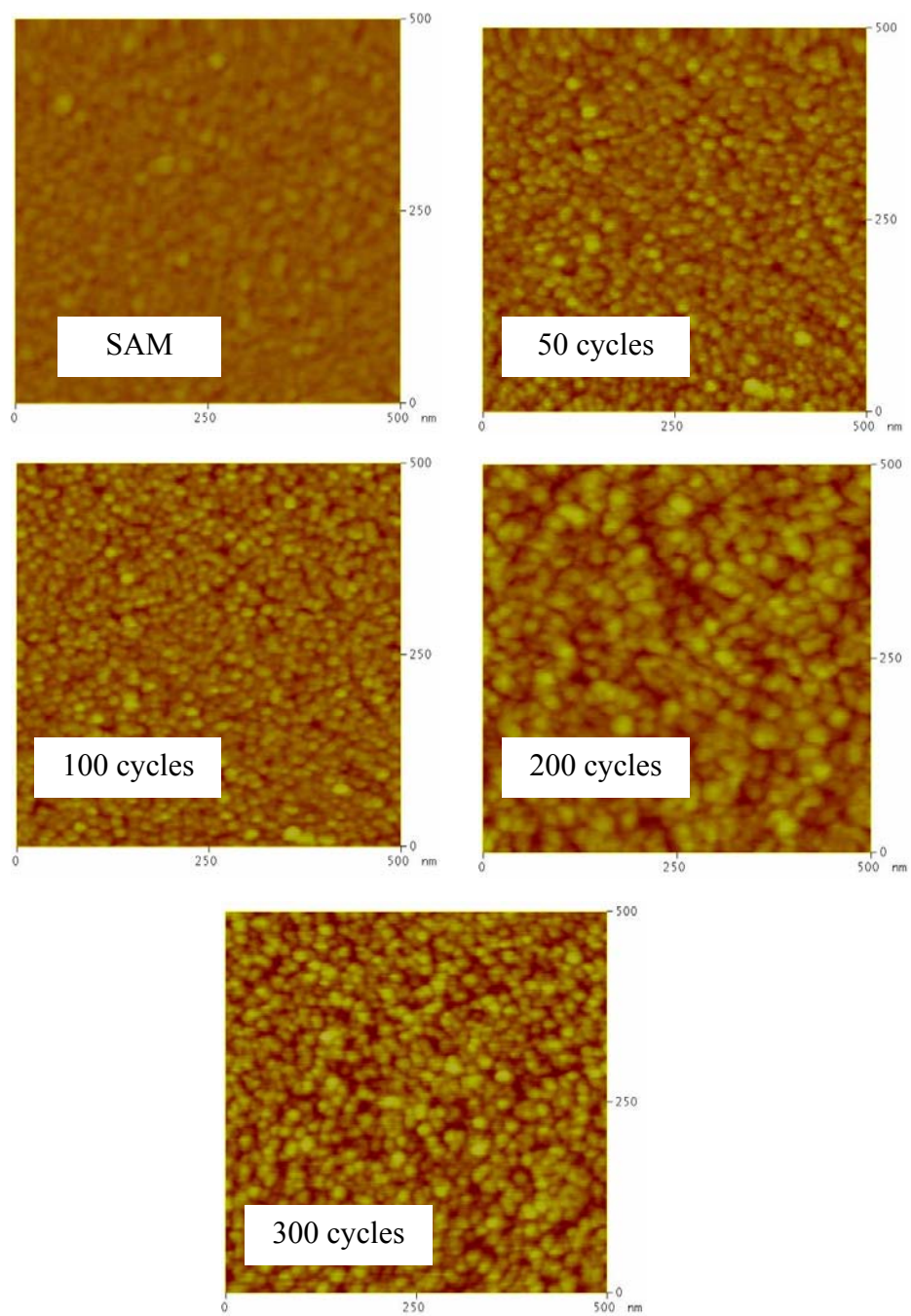
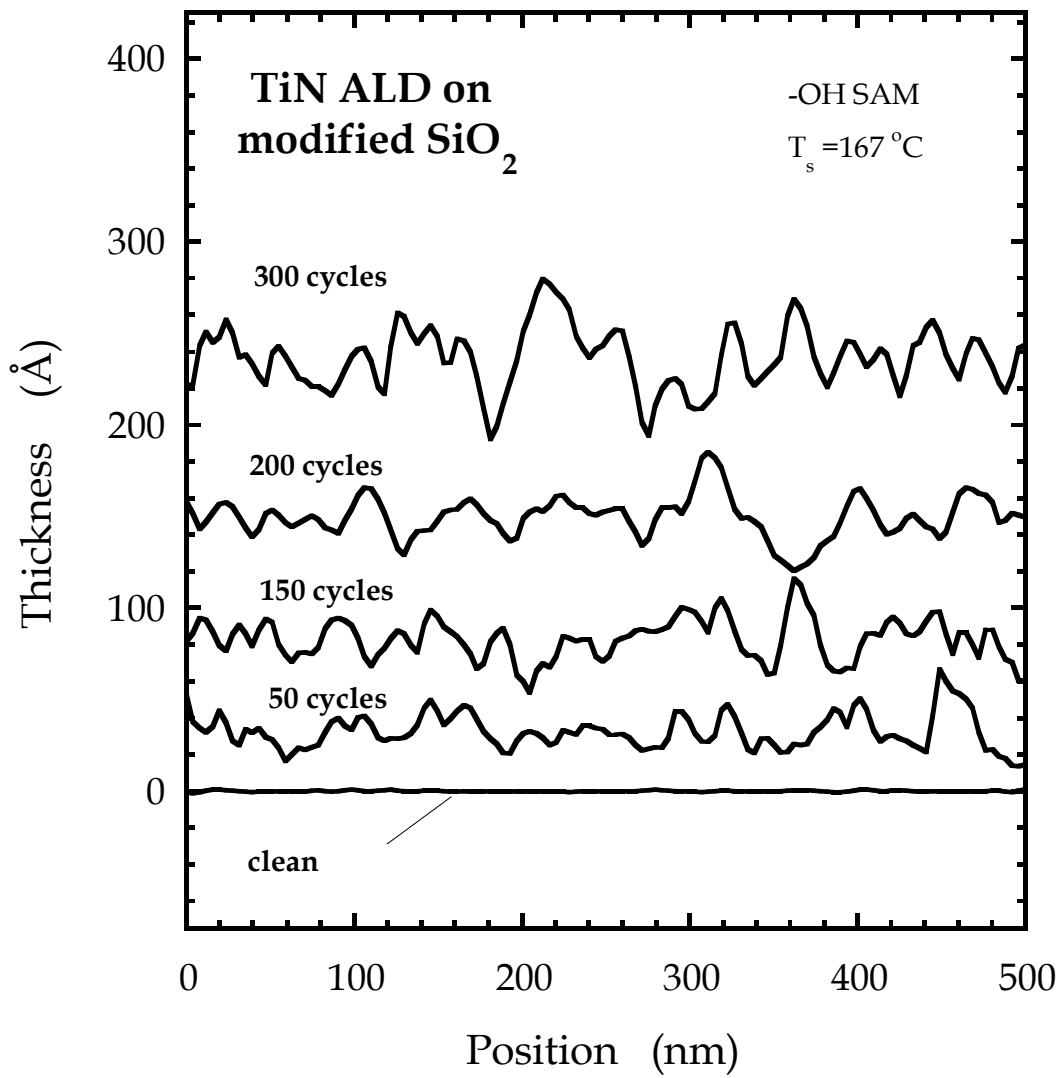
(a)

Figure 4-15 (continued)

(b)



Also plotted in Fig. 4-15(b), are the selected line scans showing the evolution RMS roughness as a function of ellipsometric thickness. Similar to the case of the Gen-1-3C SAM, the RMS roughness increases rapidly from 0 to 50 cycles and plateaus afterwards. This is indicative of relatively uniform growth in case of the -OH SAM as well.

To consider the growth morphology results altogether, the RMS roughness as a function of thickness has been plotted in Fig. 4-16. An immediate increase in roughness can be seen, going from 0 to 50 cycles for all the SAMs. The increase is more pronounced in the case of TTS, which is the thickest unreactive organic layer examined and is expected to exhibit the lowest density of vacancy /defect sites. The growth of TiN is expected to occur via islands initially in defective (vacancies, domain boundaries) and/or low density areas of the SAM, which will eventually coalesce. The onset of this phenomenon can be seen after 300 cycles in Fig. 4-13(a). In the case of unreactive SAMs, models [46, 48] would predict that the initial deposited thickness per cycle would be limited by the density of these defects. The amount of attenuation observed here, as shown in Fig. 4-6, is consistent with this picture. The roughness evolution on HMDS, in contrast to TTS, is similar to that on the reactive Gen-1-3C and -OH terminated SAMs. Here it can be argued that a much higher density of vacancy sites lead to less rough films. Growth on the SAMs bearing -NH₂ and -OH terminations, if these groups are in sufficient density, and proximity (lying nearly in a single plane), may occur initially at the SAM/vacuum interface and produce a continuous thin film quickly. This suggestion is supported by the roughness vs. thickness measurements on the Gen-1-3C and -OH SAMs.

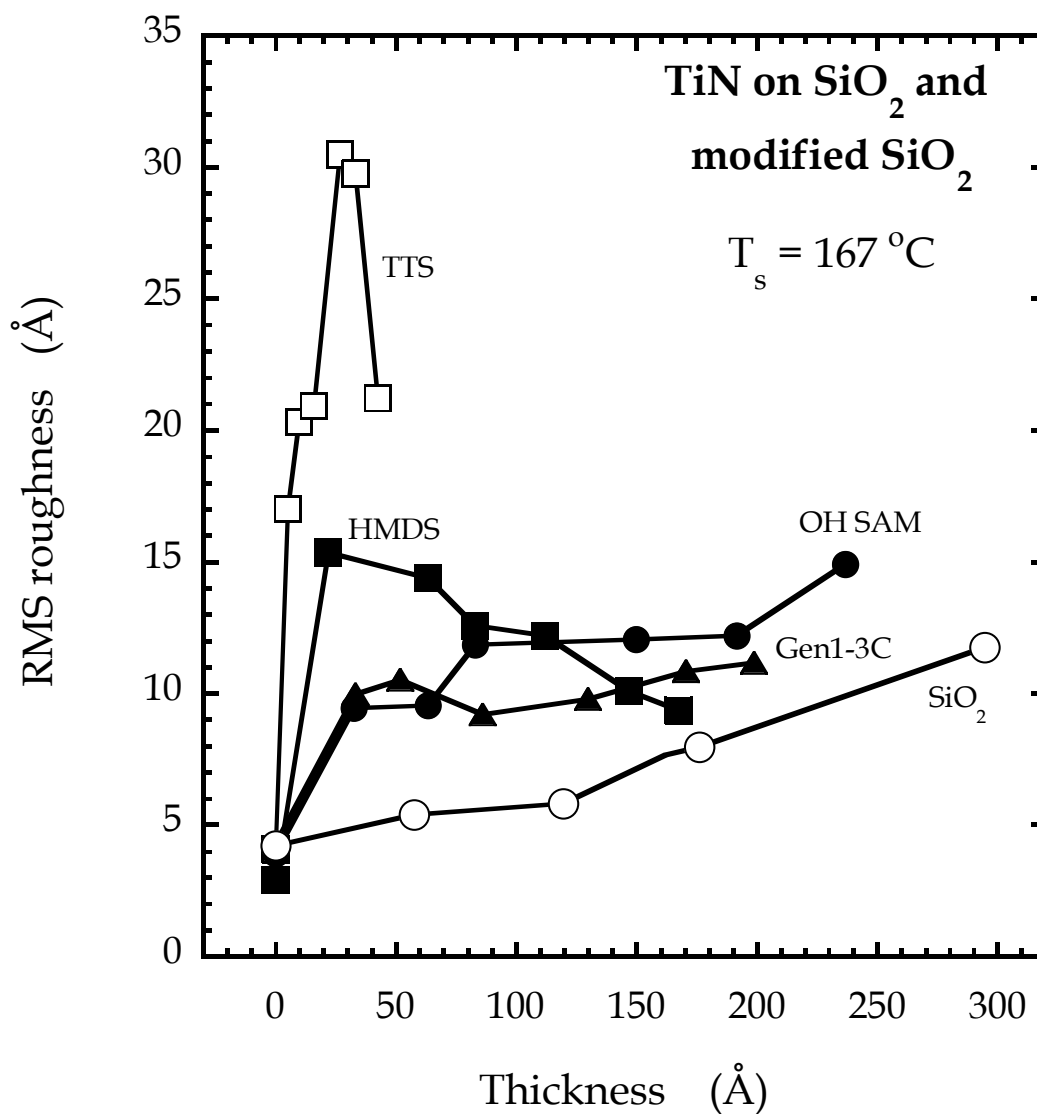


Figure 4-16: AFM determined root-mean-square (RMS) roughness as a function of measured ellipsometric thickness for TiN ALD at T_s = 167 °C on SiO₂ (open circles), Gen-1-3C (filled triangles), -OH SAM (filled circles), HMDS, and TTS SAM (filled squares).

In the case of SiO₂ a relatively modest increase in roughness was seen as a function of thickness, but unlike the reactive SAMs it doesn't plateau.

AFM data can be analyzed further to get information about the kinetic roughening mechanisms during a growth process like ALD [50]. Scaling concepts have been particularly insightful in understanding key phenomena such as surface roughening. The two quantities of interest are: Interface width (w) and the lateral correlation length (ξ). The interface width is a measure of the roughness of the surface while the lateral correlation length is a measure of spatial periodicity in the film. Average roughness is the root mean square variation (i.e. standard deviation) of the surface height profile from the mean height and is given by:

$$w = \left| \frac{1}{N} \sum_{i=1}^N (h_i - h_{mean})^2 \right|^{1/2} \quad (4-2)$$

where N is the number of data points of the profile, h_i are the points that describe the relative vertical height of the surface and h_{mean} is the mean height of the surface. Dynamic scaling theory predicts that both w and ξ increase with time according to power laws $w(t) \sim t^\beta$ and $\xi(t) \sim t^{\beta/\alpha}$. The roughness exponent α and growth exponent β are indicative of different growth mechanisms. α is obtained from 1-dimensional power spectral density (1DPSD) analysis and β from plots of film thickness as a function of roughness [50].

For example, shown in Fig. 4-17 are 1DPSD curves for TiN films grown on the Gen-1-3C SAM at 167 °C. The PSDs exhibit two distinct regions: (i) a plateau region ($1/L$) at low spatial frequencies denoting the absence of non-local correlations along the line scans, and (ii) a frequency-dependent and decaying branch indicative of the self-affine nature of the film.

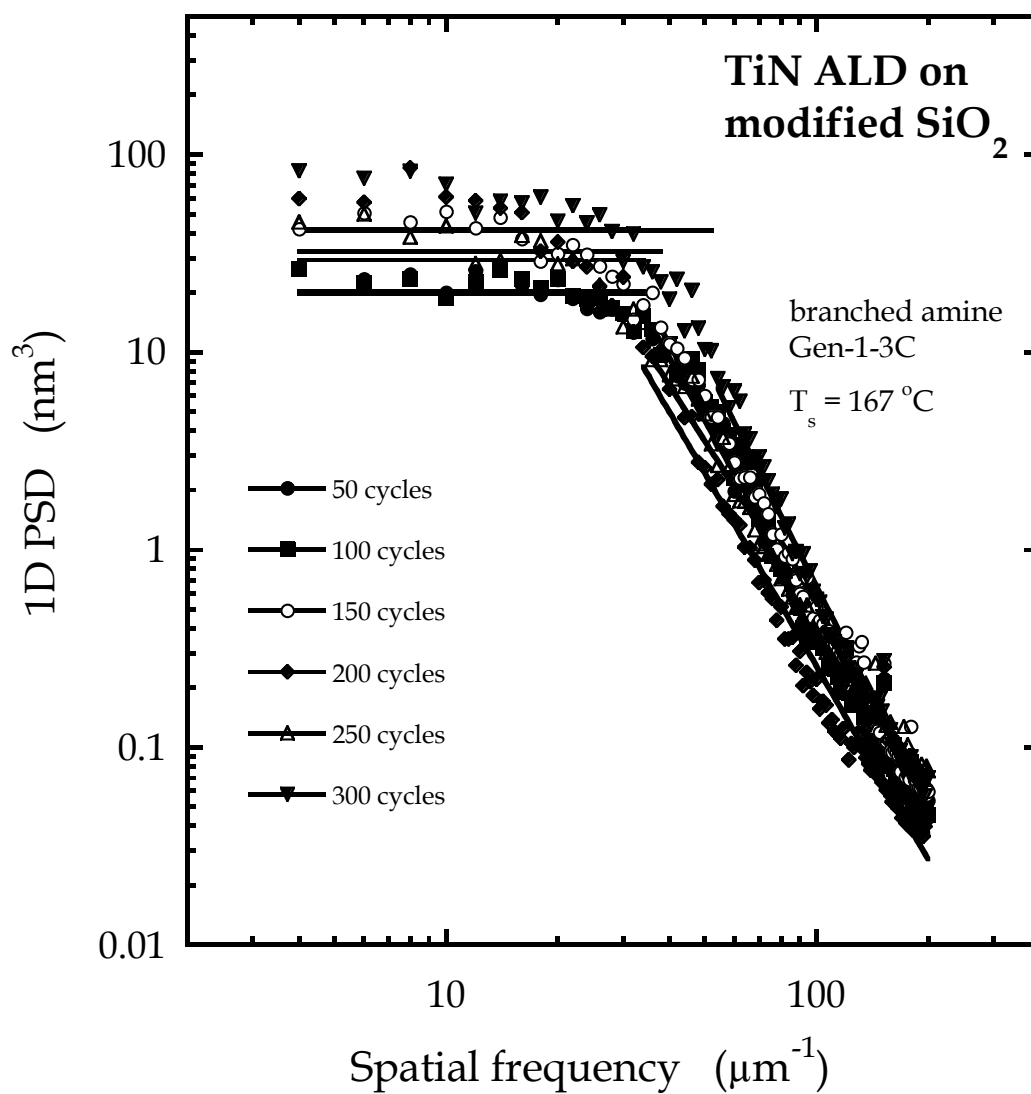


Figure 4-17: Evolution of the one-dimensional power spectral density (1DPSD) as a function of spatial frequency. Data are shown at different ALD cycles for TiN films grown at 167 °C on the Gen-1-3C SAM

The range of the intersection between the self-affine branch and the plateau defines the inverse of the correlation length (ξ):

$$\xi = \exp\left\{\frac{\ln[PSD(1/L)] - \ln K_0}{\gamma}\right\} \quad (4-3)$$

In Fig. 4-17 it can be seen that the self-affine part of the spectrum spans one order of magnitude for these films. The roughness scaling exponent α is obtained from this self-affine segment of each 1DPSD curve. This process is repeated to extract α from each AFM image for 5 different surfaces: SiO₂, TTS, HMDS, Gen-1-3C, and OH SAMs. In Fig. 4-18, the correlation length has been plotted for all the above mentioned surfaces. In the case of TTS, the correlation length is $\sim 0.1 \mu\text{m}$ from 50 to 150 cycles. During these stages, the growth is extremely non-uniform and islanded. The correlation length is a measure of the grain / island size as well [51], and it is clear from the AFM images that the early stages of growth on TTS exhibit the largest grains / islands. In Fig. 4-19, the correlation lengths are plotted as a function of RMS roughness and a trend similar to that vs. thickness is seen. Plotted in Fig. 4-20(a) are the roughness exponents α for the TTS and HMDS surfaces, as a function of ALD cycles. TTS always exhibits an $\alpha > 1$. This is a characteristic of strongly correlated fluctuations due to features large with respect to the scale length. The instability is caused by the formation of mounds, or islands and is characteristic of pyramidal growth [52, 53]. This behavior is less pronounced for HMDS, the other unreactive SAM examined. In fact, the case of HMDS is very similar to the reactive SAMs. The same data for the reactive Gen-1-3C and -OH SAMs along with chemical oxide are plotted in Fig. 4-20(b). In case of SiO₂ and all the reactive SAMs the roughness exponent spans the range of 0.7-1.

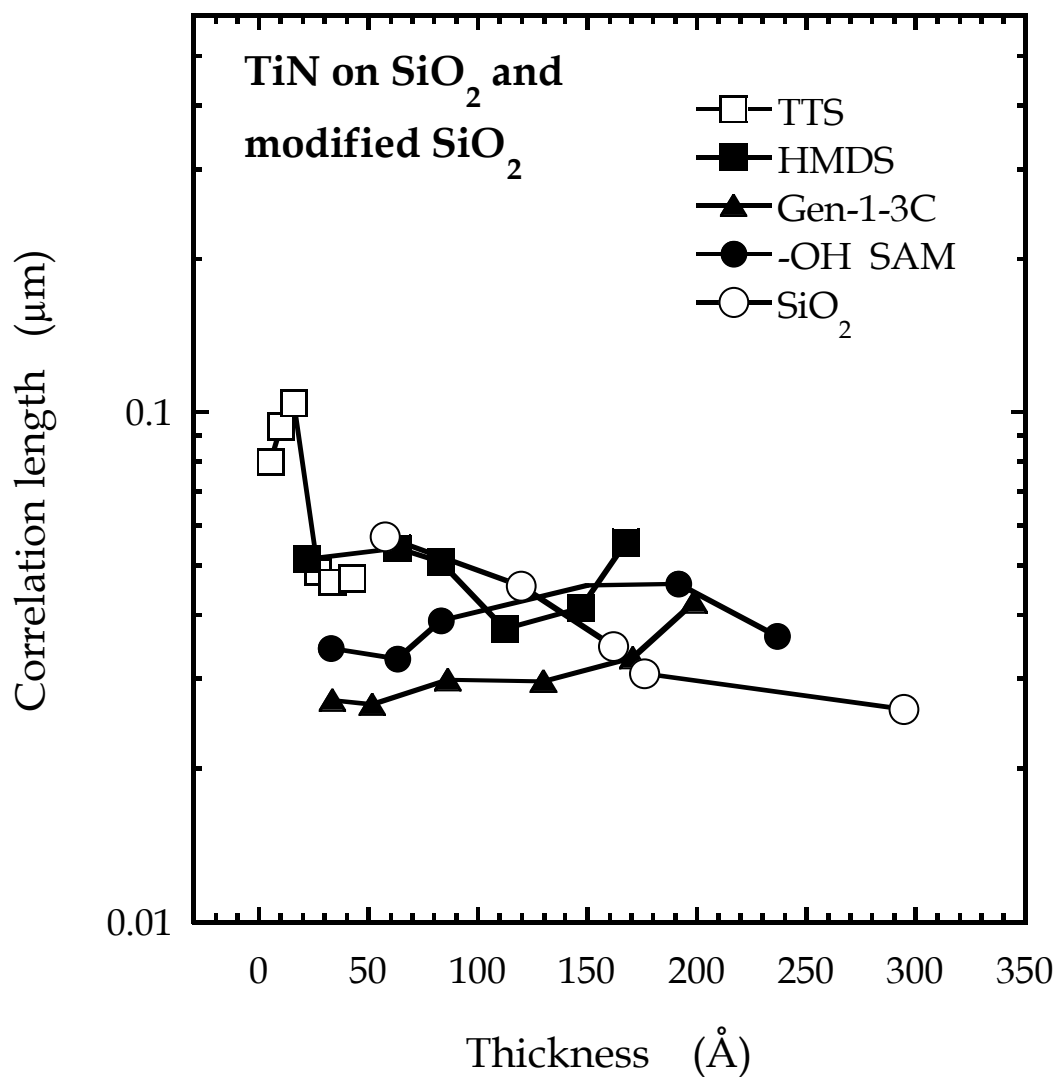


Figure 4-18: Correlation length ξ (in μm) as a function of TiN film thickness ($T_s = 167^\circ\text{C}$). ξ is obtained from the intersection of the self-affine region and the plateau region in the 1DPSD spectra for SiO₂ (open circles), Gen-1-3C SAM (filled triangles), -OH SAM (filled circles), HMDS (filled squares) and TTS (open squares).

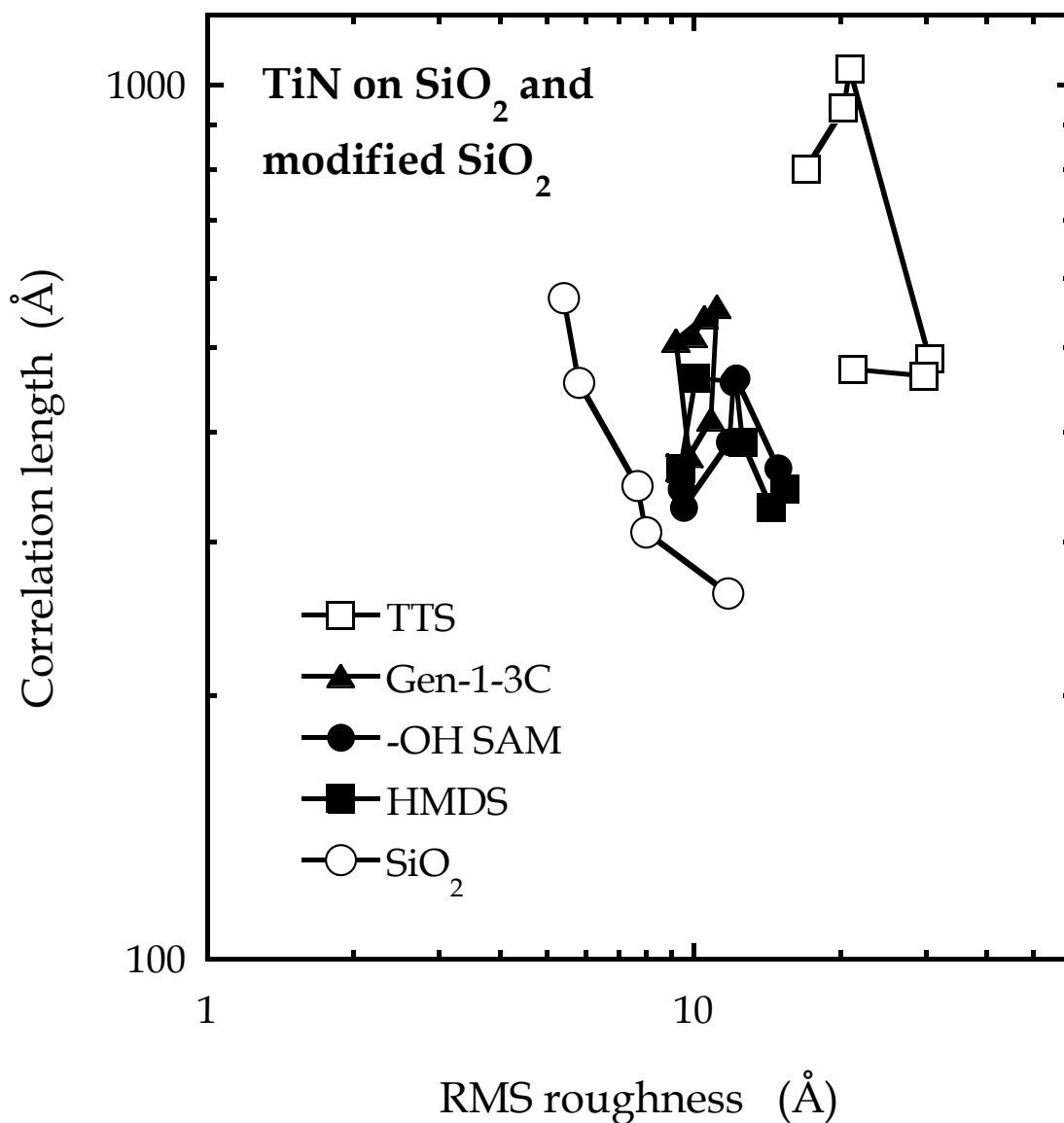


Figure 4-19: Correlation length ξ (in Å) as a function of TiN RMS roughness ($T_s = 167^\circ\text{C}$). ξ is obtained from the intersection of the self-affine region and the plateau region in the 1DPSD spectra for SiO₂ (open circles), Gen-1-3C SAM (filled triangles), -OH SAM (filled circles), HMDS (filled squares) and TTS (open squares).

Figure 4-20: (a) Roughness exponent α plotted as a function of TiN film thickness, for the TTS and HMDS SAMs ($T_s = 167^\circ\text{C}$). α is extracted from the slope of the self-affine portion of the 1DPSD spectrum. (b) Roughness exponent α plotted as a function of TiN film thickness; for SiO_2 , Gen-1-3C, and $-\text{OH}$ SAM ($T_s = 167^\circ\text{C}$).

(a)

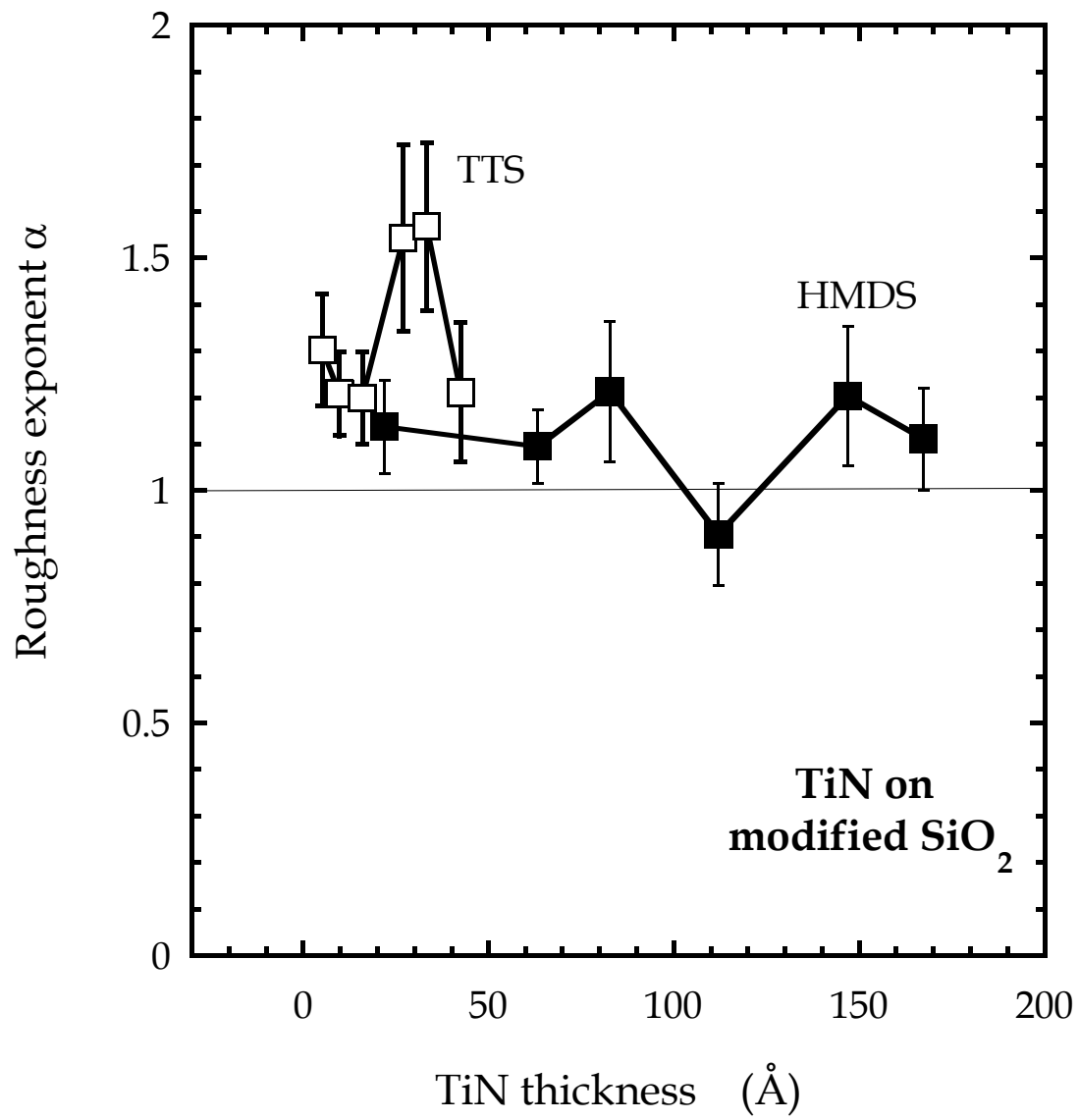
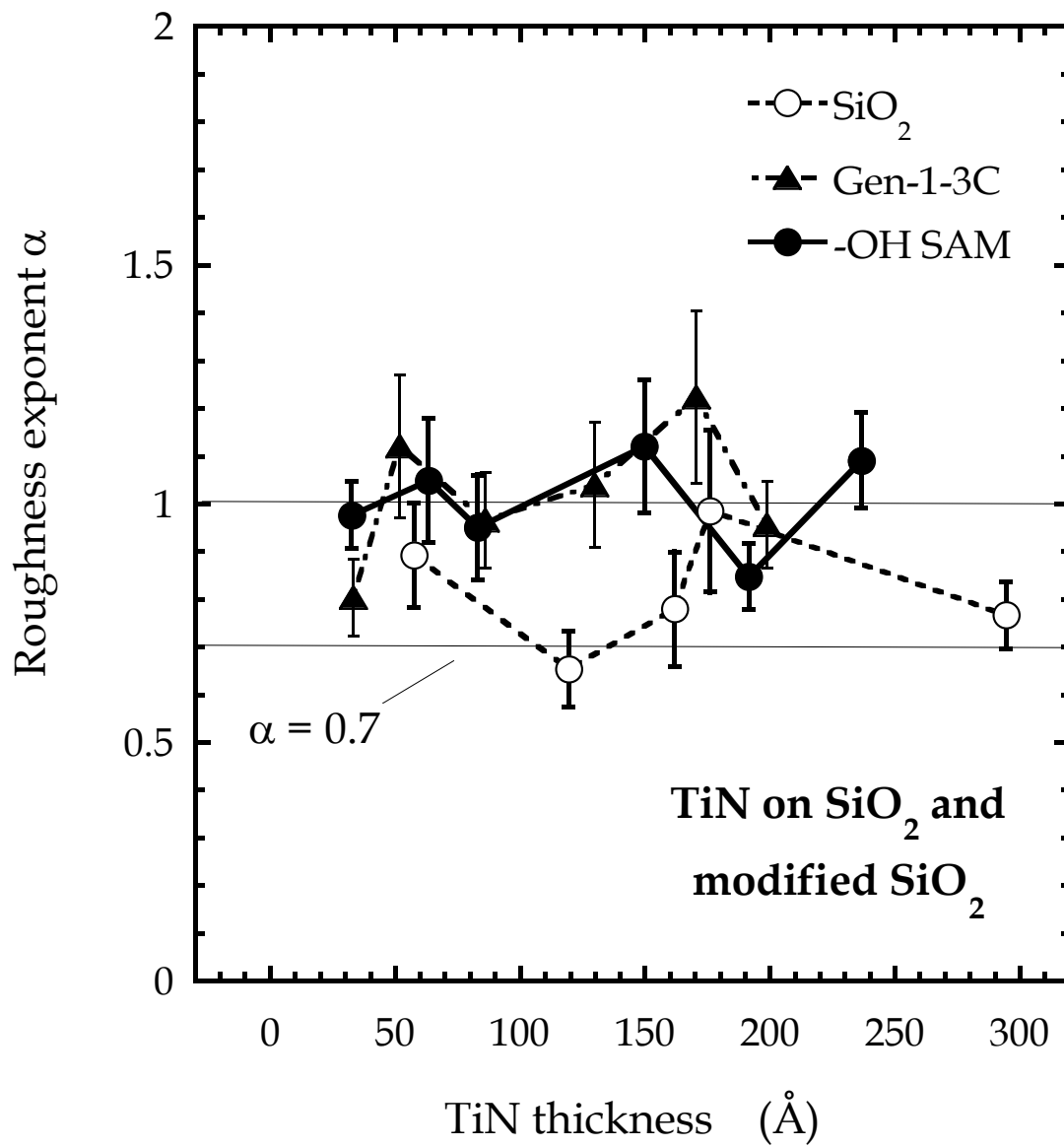


Figure 4-20 (continued)

(b)



Thus, α maps the range within the predictions of diffusion-limited aggregation ($\alpha = 1$ [50]) and molecular-beam epitaxy (MBE) growth controlled by adsorption at kink sites ($\alpha = 0.66$ [50]). The observations regarding α agree well with another report where AFM was employed to quantitatively investigate the kinetic surface-roughening phenomenon of sputter-deposited TiN thin films [54]. The values of $\alpha = 0.98$ and $\beta = 0.28$ indicated that the surface growth behavior could be adequately explained by a simple linear growth model showing surface diffusion as a smoothing effect and shot noise as a roughening effect [55]. Due to the non-linear growth behavior on all the SAMs, no attempt was made to calculate the growth exponent (β) [56]. The premise for calculating β is that the thickness should be proportional to the amount of material deposited implying that the deposition rate should be constant. Chemical oxide is the only substrate exhibiting linear growth characteristics and the roughness vs. thickness data yields a β value of 0.47 ± 0.11 . The α (0.82 ± 0.12) and β values on SiO_2 agree reasonably well with those predicted by growth models that include surface diffusion with energetic barriers at step edges ($\alpha \sim 1$ and $\beta = 0.25\text{-}0.50$) [50]. However, the assumption about existence of step-edge barriers, for quite possibly polycrystalline films in this case, with a random orientation distribution is debatable because of the absence of well defined terraces. Thus it may be argued that growth in this case is more complex with a number of processes coming into play namely: random deposition, surface diffusion, grain–grain competition, and inter-granular mass transport. A simple growth model will not be able to capture all these processes.

High-resolution scanning transmission electron microscopy (HRSTEM) was employed to further characterize the interfaces involved.

Shown in Fig. 4-21 is one such micrograph, for a specimen which is TiN (~ 120 Å) grown on the Gen-1-3C SAM at 167 °C. The layer details are depicted in a dark field image. It can be clearly seen that the TiN film conformally covers the SAM/SiO₂ layer, as seen from the similarity in undulations for both the TiN and SiO₂ layers. Conformal deposition is a benchmark for a successful ALD process. However, there is no direct evidence for the presence of a SAM. It should be noted here that all the reactive SAMs have a nominal thickness of $10 - 20$ Å which may be extremely difficult to resolve. The STEM probe was also used to acquire high resolution electron energy loss (HREELS) data which can be used to probe the chemical composition in the bulk as well as at the interfaces. Also plotted in Fig. 4-21 are the elemental HREELS depth profiles for C, Si, and Ti. The most interesting observation here is an apparent increase followed by decay in the C signal while scanning across the TiN-SiO₂ interface. This is the region where the SAM should reside. On a more cautious note, however, this data alone can not be relied upon to say with absolute certainty if the structural integrity of the SAM is preserved post deposition.

In the end, the discussion of perhaps the most interesting result in this study, which is the suppression of deposited thickness per cycle on the SAMs in comparison to SiO₂, is revisited. In case of the unreactive SAMs, it is evident that the defect-mediated nucleation process will lead to significant attenuation in deposited thickness per cycle as we saw from the comparison between HMDS (thinnest unreactive layer) and TTS (thickest unreactive layer). A more intriguing observation is the attenuation in case of the reactive SAMs. At both values of T_s examined here, a 50-70 % reduction in deposited thickness per cycle is seen. This attenuation is independent of the thickness of the reactive layer.

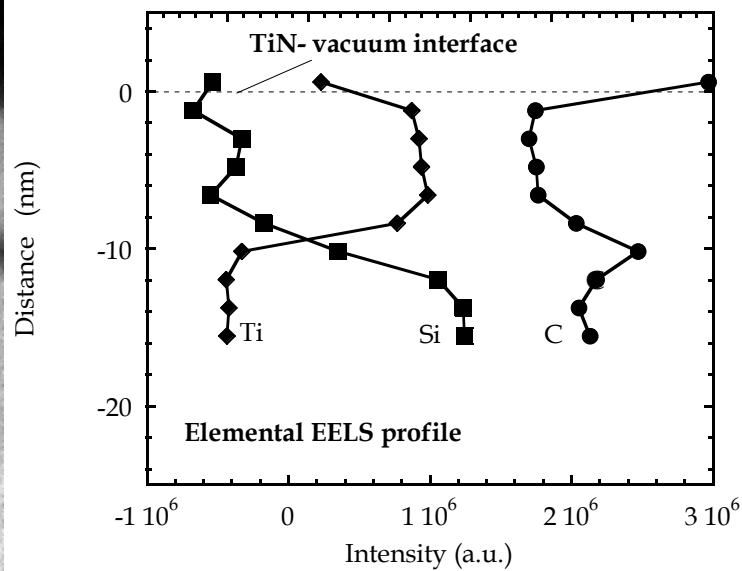
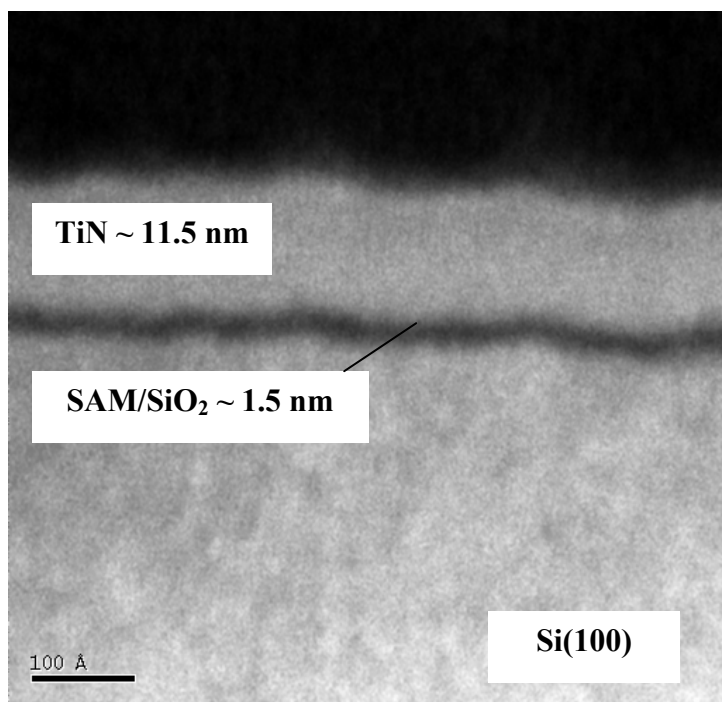


Figure 4-21: Dark field scanning transmission electron micrograph for a film grown on Gen-1-3C SAM for 300 cycles ($T_s = 167^\circ\text{C}$). High resolution electron energy loss spectra for carbon, titanium, and silicon. Plotted are the intensities as a function of distance from the surface.

Values found for the exponential decay constants m (Eq. 4-1) for the SAMs seem unphysical ($m \sim 1000-3000$). Indeed, one could argue for example for the Gen-1-3C and Gen-1-12C SAMs, that the steady-state deposited thickness per cycle has been achieved for cycles > 200 (*cf.* Fig. 4-3(a) and (b)), where D is 0.78 and 0.66 Å-cycle⁻¹ respectively (attenuation factors of 0.39 and 0.34). Some arguments can be made for and against the most likely mechanistic scenarios. First, it is deemed highly unlikely that growth, even for the reactive SAMs, is initiated at the SAM/SiO₂ interface, where the SAM layer is displaced to the surface of the growing TiN film (where it could block sites and attenuate growth)—such a scenario would contradict previous results [22], and require the efficient cleavage of no less than 3 Si-O bonds that anchor the R-SiCl₃ SAMs. Secondly, arguments involving sub-saturation deposition per cycle should be seen in all of the results, once a continuous film is formed, independent of the starting surface. Such is not the case. Thirdly, roughness might have some effect, but the difference observed (*vide supra*) would not seem sufficient to explain attenuation factors < 0.4 . Growth rate attenuation, caused by the geometrical shadowing in the arriving precursor flux, can be ruled out from the relatively low RMS roughness against the measured thickness, in all cases. One appealing explanation for different steady state D_{∞} 's is that the SAMs can induce the formation of a TiN thin film that differs from that formed on chemical oxide. Such SAM-directed assembly is known to occur in solution-based deposition [57, 58]. An appealing proposition is the formation of different orientations, where the stereochemistry of the surface determines different saturation coverages of the N(CH₃)₂ ligands, leading to different D 's. In Fig. 4-22, the growth attenuation factor α is plotted against the Ti saturation density at $T_s = 25$ °C. These densities are obtained from beam reflectivity

measurements carried out to measure reaction probability for $\text{Ti}[\text{N}(\text{CH}_3)_2]_4$ on SiO_2 , Gen-0-12C SAM, -OH SAM, and OTS [43]. A saturation exposure was carried out in these measurements. From the knowledge of the beam flux, the reaction probability and saturation coverage were calculated. There seems to be a very good linear correlation between $\dot{\alpha}$ and the Ti saturation density. It is evident that the growth rate attenuation is more pronounced for lower saturation coverage of Ti or alternatively $-\text{N}(\text{CH}_3)_2$ ligands. In a recent work on TiN ALD [59] employing TiCl_4 and NH_3 at 390°C , it was observed that an ultra thin TiN film consists of nano-crystalline domains (from TEM) which mainly grew with atomic stacking on the TiN (111) and (200) planes. It was argued that dangling bonds and surface reconstruction may be the intrinsic mechanisms causing the crystals to grow with different configurations. The surface topography of the amorphous substrate is proposed as the extrinsic mechanism which dominates the atomic stacking configurations, thus resulting in nano-polycrystalline structure in the film. Although from the AFM results it seems likely that the SAMs conformally cover the surface of the SiO_2 substrate, it is possible to have atomic level differences in surface topography leading to different growth configurations on the SAMs *vis a vis* SiO_2 . As an aside, for growth on the SAM, the TiN surface exhibiting the lowest strain energy could be expected to form, as the flexible SAM layer might accommodate the relief of strain—for crystalline TiN, that is the (111) surface [60]. A strong faceting in a preferred direction can lead to variability in growth rates. To date, however, attempts to identify ordered and/or crystalline domains in the TiN thin films deposited here by ALD have been unsuccessful. Thus this proposition remains as an intriguing possibility.

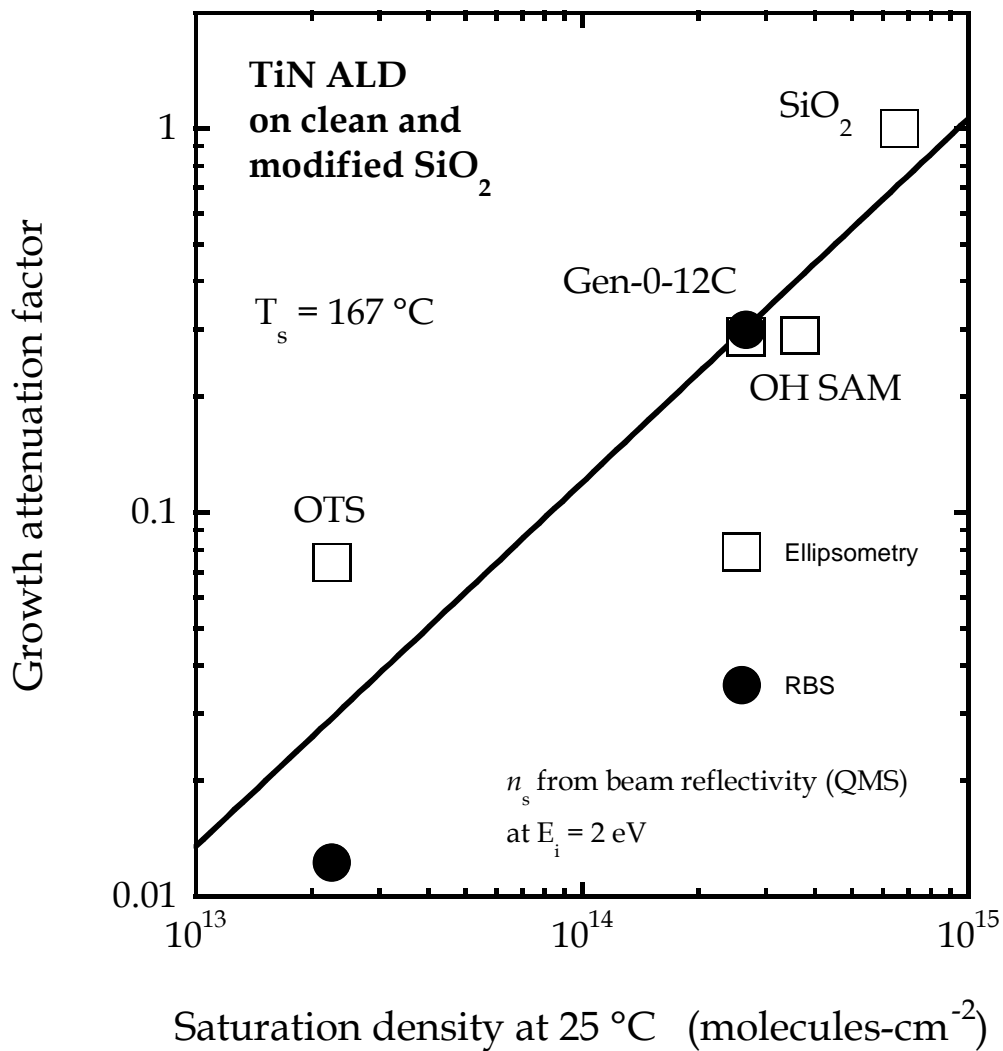


Figure 4-22: Growth attenuation factor, obtained for RBS and ellipsometry data, plotted as a function of Ti saturation densities after room temperature saturation exposures to a 2.07 eV Ti[N(CH₃)₂]₄ beam. The substrates considered were: SiO₂, Gen-0-12C, -OH SAM, and OTS. The density values have been obtained from Ref. [43].

4.5 Conclusions

The nucleation and growth during TiN ALD on SiO₂ and SiO₂ modified using interfacial organic layers in the form of SAMs, has been investigated. The SAMs possess a range of functional groups, thickness, and microstructure. They are broadly grouped into two categories: reactive towards Ti[N(CH₃)₂]₄ (-OH, -NH₂), and unreactive (-CH₃, and -CF₃). Modulated molecular beams of Ti[N(CH₃)₂]₄ and NH₃ were used as reactants. Measurement of the growth rate as a function of T_s on chemical oxide, points to a narrow ALD window between ~ 167 - 207 °C. A more interesting observation is the attenuation of growth in case of all the SAMs. For all the reactive SAMs, growth as a function of ALD cycles is non-linear and the deposited thickness per ALD cycle is suppressed by 50-70 % with respect to silicon dioxide irrespective of the termination and thickness. However, in case of the unreactive SAMs, the attenuation is a strong function of the thickness of the SAM where the thickest TTS SAM is the most effective in impeding nucleation. XPS, RBS, and AFM were employed to further probe the nature of growth. The results seem to suggest a very non-uniform and islanded growth pattern on the unreactive TTS SAM. The non-uniformities are less pronounced in the case of the unreactive but thinner HMDS, probably due to a higher defect density which promotes quicker nucleation and hence growth. In case of SiO₂ and all the reactive SAMs the growth is much more uniform. 1-D PSD analysis of the AFM data seems to suggest that the growth is pyramidal on TTS but within the limit of prediction by diffusion limited aggregation for all the other surfaces. HRSTEM results point to a highly conformal deposition process on the reactive SAMs. Taken as a whole, the results seem to suggest significant and unexpected differences in

growth patterns on SAMs in comparison to SiO_2 . The attenuation in growth rate for the unreactive SAMs is not an entirely unexpected result due to defect-mediated growth mechanism. However, in the case of the reactive SAMs, it is possible that the SAM is mediating the growth of a TiN film different in nature to that growing on the SiO_2 surface.

4.6 References

1. International Technology Roadmap for Semiconductors (www.itrs.net), **2005**.
2. *Copper interconnect technology*; Steinbrüchel, C.; Chin, B. L., SPIE Press: Washington, **2001**.
3. *Conjugated Polymer Surfaces and Interfaces, Electronic and Chemical Structure of Interfaces for Polymer Light Emitting Devices*; Salaneck, W. R., Stafstrom, S., Bredas, J. -L., Eds.; Cambridge University Press: Cambridge, **1996**.
4. Yan, L.; Gao, Y. *Thin Solid Films* **2002**, *417*, 101.
5. *Molecular Electronics: Science and Technology*, Aviram, A., Ratner, M.; Eds.; NY Academy of Science: New York, **1998**.
6. Ishii, H.; Sugiyama, K.; Ito, E.; Seki, K. *Adv. Mater.* **1999**, *11*, 605.
7. Chen, J.; Reed, M. A.; Dirk, S. M.; Price, D. W.; Rawlett, A. M.; Tour, J. M.; Grubisha, D. S.; Bennett, D. W. *NATO Sci. Ser. II: Math., Phys. Chem.* **2003**, *96*, 59.
8. Haynie, B. C.; Walker, A. V.; Tighe, T. B.; Allara, D. L.; Winograd, N. *Appl. Surf. Sci.* **2003**, *203*, 433.
9. *An Introduction to Ultrathin Organic Films, From Langmuir-Blodgett to Self-Assembly*; Ulman, A., Ed.; Academic Press :Boston, MA, **1991**.

10. Dubois, L. H.; Nuzzo, R. G. *Annu. Rev. Phys. Chem.* **1992**, *43*, 437.
11. Ulman, A. *Chem. Rev.* **1996**, *96*, 1533.
12. Niesen, T. P.; Bill, J.; Aldinger, F. *Chem. Mater.* **2001**, *13*, 1552.
13. Masuda, Y.; Jinbo, Y.; Yonezawa, T.; Koumoto, K. *Chem. Mater.* **2002**, *14*, 1236.
14. Jung, D. R.; Czanderna, A. W. *Crit. Rev. Solid State Mater. Sci.* **1994**, *19*, 1.
15. Herdt, G. C.; Jung, D. R.; Czanderna, A. W. *Prog. Surf. Sci.* **1995**, *50*, 103.
16. Jung, D. R.; Czanderna, A. W.; Herdt, G. C. *J. Vac. Sci. Technol. A* **1996**, *14*, 1779.
17. Konstadinidis, K.; Zhang, P.; Opila, R. L.; Allara, D. L. *Surf. Sci.* **1995**, *338*, 300.
18. Fisher, G. L.; Hooper, A.; Opila, R. L.; Jung, D. R.; Allara, D. L.; Winograd, N. *J. Electron. Spectrosc. Relat. Phenom.* **1999**, *98*, 139.
19. Fischer, R. A.; Weckenmann, U.; Winter, C.; Kashammer, J.; Scheumann, V.; Mittler, S. *J. Phys. IV: Proc.* **2001**, *11*, Pr3/1183.
20. Weiss, J.; Himmel, H. J.; Fischer, R. A.; Woell, C. *Chem. Vap. Depn.* **1998**, *4*, 17.
21. Wohlfart, P.; Weiss, J.; Kashammer, J.; Kreiter, M.; Winter, C.; Fischer, R.; Mittler-Neher, S. *Chem. Vap. Depn.* **1999**, *5*, 165.

22. Killampalli, A. S.; Ma, P. F.; Engstrom, J. R. *J. Am. Chem. Soc.* **2005**, *127*, 6300.
23. Chen, R.; Kim, H.; McIntyre, P. C.; Bent, S. F. *Chem. Mater.* **2005**, *17*, 536.
24. Chen, R.; Bent, S. F. *Adv. Mater.* **2006**, *18*, 1086.
25. Park, M. H.; Jang, Y. J.; Sung-Suh, H. M.; Sung, M. M. *Langmuir* **2004**, *20*, 2257.
26. Park, K. J.; Doub, J. M.; Gougousi, T.; Parsons, G. N. *Appl. Phys. Lett.* **2005**, *86*, 051903.
27. Lee, J. P.; Jang, Y. J.; Sung, M. M. *Adv. Func. Mater.* **2003**, *13*, 873.
28. Whelan, C. M.; Demas, A. -C.; Schuhmacher, J.; Carbonell L.; Maex, K. *Mater. Res. Soc. Symp. Proc.* **2004**, *812*, F2.2.
29. *Handbook of Thin Film Materials, Vol. 1, Chap. 2.*; Ritala M., Leskelä, M.; Ed. Nalwa H. S.; Academic Press: New York, **2002**.
30. Dube, A.; Sharma, M.; Ma, P. F.; Engstrom, J. R. *Appl. Phys. Lett.* **2006**, *89*, 164108.
31. Satta, A.; Vantomme, A.; Schumacher, J.; Whelan, C. M.; Sutcliffe, V.; Maex, K. *Appl. Phys. Lett.* **2004**, *84*, 4571.
32. Hoyas, A. M.; Travaly, Y.; Schuhmacher, J.; Sajavaara, T.; Whelan, C. M.; Eyckens, B.; Richard, O.; Giangrandi, S.; Brijs, B.; Vandervorst, W.; Maex, K. *J. Appl. Phys.* **2006**, *99*, 063515.

33. Green, M. L.; Ho, M.-Y.; Busch, B.; Wilk, G. D.; Sorsch, T.; Conard, T.; Brijs, B.; Vandervorst, W.; Räisänen, P. I.; Muller, D.; Bude, M.; Grazul, J. *J. Appl. Phys.* **2002**, *92*, 7168.
34. Schroeder, T. W.; Lam, A. M.; Ma, P. F.; Engstrom, J. R.; *J. Vac. Sci. Technol. A* **2004**, *22*, 578.
35. Sharma, M.; Dube, A.; Engstrom, J. R., in preparation
36. Tomalia, D. A.; Baker, H.; Dewald, J.; Hall, M.; Kallos, G.; Martin, S.; Roeck, J.; Ryder, J.; Smith, P. *Polym. J.* **1985**, *17*, 117.
37. Roadman, S. E.; Maity, N.; Carter, J. N.; Engstrom, J. R. *J. Vac. Sci. Technol. A* **1998**, *16*, 3423.
38. T. W. Schroeder, PhD thesis, Cornell University, **2004**.
39. Shirley, D. A. *Phys. Rev. B* **1972**, *5*, 4709.
40. *Practical Surface Analysis: Volume I, Auger and X-ray Photoelectron Spectroscopy*, 2nd ed.; Seah, M. P., Briggs, D., Eds.; John Wiley and Sons: Chichester, England, **1990**.
41. Conny, J. M.; Powell, C. J. *Surf. Interface Anal.* **2000**, *29*, 856.
42. Dolittle, L. R. *Nucl. Instrum. and Meth.* **1986**, *15*, 227.
43. Ma, P. F.; Dube, A.; Killampalli, A.S.; Engstrom, J. R. *J. Chem. Phys.* **2006**, *125*, 034706.
44. Elam, J. W.; Schuisky, M.; Ferguson, J. D.; George, S. M. *Thin Solid Films* **2003**, *436*, 145.

45. Kim, J. Y.; Choi, K. H.; Kim, Y. D.; Kim, Y.; Jeon, H. *Jpn. J. Appl. Phys.* **2003**, *42*, 4245.
46. Alam, M. A.; Green, M. L. *J. Appl. Phys.* **2003**, *94*, 3403.
47. Calistri-Yeh, M.; Kramer, E. J.; Sharma, R.; Zhao, W.; Rafailovich, M. H.; Sokolov, J.; Brock, J. D. *Langmuir* **1996**, *12*, 2747.
48. Puurunen, R.L.; Vandervorst, W. *J. Appl. Phys.* **2004**, *96*, 7686.
49. Dolittle, L. R. *Nucl. Instrum. and Meth.* **1986**, *15*, 227.
50. *Fractal Concepts in Surface Growth*, Barabási, A. –L.; Stanley, H. E.; Cambridge University Press: Cambridge, UK, **1995**.
51. Palasantzas, G.; Krim, J. *Phys. Rev. Lett.* **1994**, *73*, 3564.
52. Siegert, M.; Plischke, M. *Phys. Rev. Lett.* **1992**, *68*, 2035.
53. Wolf D. E.; Villain, J. *Europhys. Lett.* **1990**, *13*, 389.
54. Liu, Z.-J.; Jiang, N.; Shen, Y. G.; Mai, Y.-W. *J. Appl. Phys.* **2002**, *92*, 3559.
55. Das Sarma, S.; Tamborenea, P. I. *Phys. Rev. Lett.* **1991**, *66*, 325.
56. Krim, J.; Palasantzas, G. *Int. J. Mod. Phys. B* **1995**, *9*, 599.
57. Bunker, B. C.; Rieke, P.C.; Tarasevich, B. J.; Campbell, A. A.; Fryxell, G. E.; Graff, G. L.; Song, L.; Liu, J.; Virden, J. W.; McVay, G. L. *Science* **1994**, *264*, 48.

58. Aizenberg, J.; Black, A.J.; Whitesides, G. M. *J. Am. Chem. Soc.* **1999**, *121*, 4500.
59. Li, S.; Sun, C. Q.; Park, H. S. *Thin Solid Films* **2006**, *504*, 108.
60. See, e.g., Raushchenbach B.; Gerlach, J. W. *Cryst. Res. Technol.* **2000**, *35*, 675.

5. Atomic layer deposition of TiN on hyperbranched polymeric films and low κ dielectric substrates

5.1 Overview

The nucleation and growth of TiN via ALD on interfacial organic layers (IOLs) on silicon dioxide (SiO_2) possessing branched molecular backbones has been investigated. The nucleation and growth of TiN on porous low κ dielectric substrates and low κ substrates modified using the aforementioned IOLs has also been explored. The IOLs possess branched molecular backbones, where each branch is terminated by a reactive functional group. The growth kinetics and the structure of these organic layers were characterized using contact angle measurements, ellipsometry, and X-ray photoelectron spectroscopy (XPS). The nucleation and growth of TiN (using $\text{Ti}[\text{N}(\text{CH}_3)_2]_4$ and NH_3) thin films on these branched microstructure IOLs shows remarkably different behavior depending on the thickness of the starting organic layer. Nucleation and subsequent growth was achieved most easily on the thinnest IOL studied here. Atomic force microscopy (AFM) also suggests that film roughness increases rapidly for growth on the thicker polymer film, indicative of growth which is three dimensional (3-D) and islanded. Growth on the thinner polymer film is characterized by reduced roughness. XPS results seem to suggest very little incorporation of nitrogen in the films deposited on thicker IOLs. In case of the low κ substrates, the deposition is attenuated with respect to that on the SiO_2 surface and cross-sectional scanning transmission electron microscopy (STEM)

results show TiN penetration into the pores. Preliminary STEM results for a TiN film deposited on a low κ substrate modified using the thinnest IOL, suggest absence of penetration into the pores.

5.2 Introduction

An important strategy for increasing the speed of microelectronic circuits is to decrease the resistance-capacitance (RC) delay in the transistor interconnects. The resistance (R) has been reduced by replacing aluminum conductors with lower resistivity copper. The capacitance (C) was reduced by replacing the silica insulator (dielectric constant $\kappa = 4$) by fluorinated silica glass (FSG, $\kappa = 3.7$) and now organic-doped silica glass (OSG, $\kappa = 2.8$). Further reductions in dielectric constant will require that the dielectric contain pores ($\kappa = 1.0$) [1]. The most common methods for making porous ultra low κ dielectrics are chemical vapor deposition (CVD) or spin-coating [2]. Introducing pores into a dielectric poses several challenges *vis-à-vis* integration in traditional semiconductor manufacturing. Moisture penetrating into a porous material can increase its dielectric constant and leakage current, and hence reduce the voltage for dielectric breakdown [3]. Thus it is expected that porous low κ material in a microcircuit will need to be hermetically sealed from ambient moisture. Copper also diffuses readily through porous low κ materials, so an effective barrier is needed to confine the copper within the copper wires. The barrier to water and copper must be very thin (\sim less than 4 nm by 2012 [1]) so that it does not occupy volume needed for the current-carrying copper wires. If the barrier thickness is smaller than the largest pores, it becomes difficult to bridge the pores on the surface of the dielectric with a thin continuous barrier.

Because barriers must be deposited inside trenches and vias with high aspect ratios, the barrier material will penetrate deeply into porous dielectrics. Indeed, deposition precursors can easily penetrate entirely through porous dielectrics, causing an electrical short circuit through the insulator [4]. Sealing of porous dielectrics by plasma treatment has been proposed to provide a continuous surface on which thin barriers could be deposited [5, 6]. Although a plasma treatment can be applied to the upper surface of a porous dielectric, it is not clear that plasma particles can be projected successfully into increasingly narrow trenches and vias to seal the pores in their side-walls. The importance of interfaces in these complex device structures will prove to be critical as dimensions reach 45 nm, and, ultimately, devices that are inherently molecular will be required. At these dimensions it will be absolutely essential to fabricate interfaces with well-defined molecular structure.

Sealing porous low κ dielectrics presents two problems: many candidate materials present a low density of nucleation sites due to their molecular composition and, by definition, their void spaces provide no sites for thin film nucleation. A potential solution to this problem is to develop chemistries that involve nucleation site multipliers/amplifiers that are also intrinsically self-expanding and space filling. A cartoon representation of such hyperbranched IOLs is shown in Fig. 5-1. Chemistries exist for formation of such structures using known solution-based recipes that can be adapted for application on surfaces [7]. The backbone of these materials can involve C-C and/or Si-C linkages, and a number of organic functional groups (nucleation sites) can be produced at the surface. These hyperbranched polymer brush films would provide a chemically and mechanically robust layer to control surface properties.

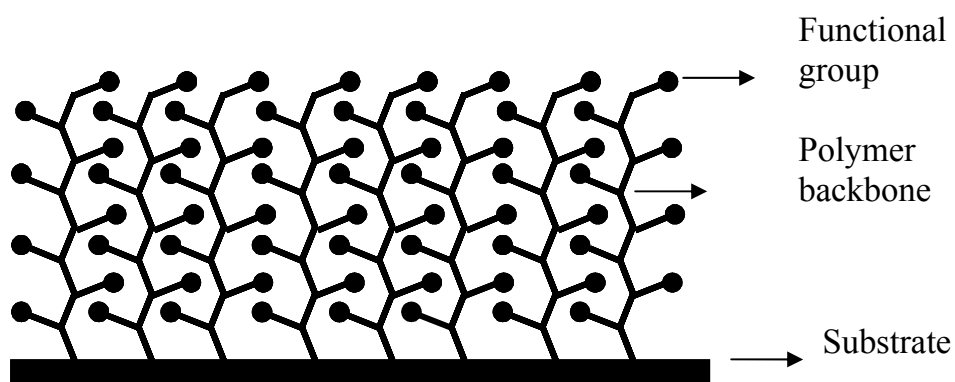
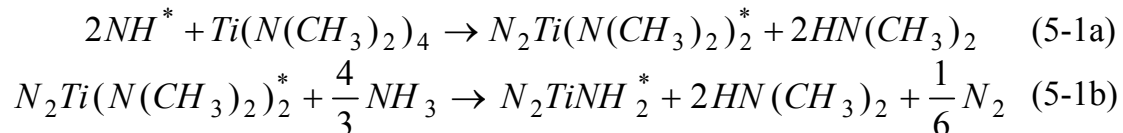


Figure 5-1: Typical schematic for a hyperbranched polymer brush film

Typically, the polymer brushes are grown from gold or Si/SiO₂ substrates that are functionalized with initiator-terminated self-assembled monolayers [8-10]. Brushes with functional groups can be used to increase the loading capacity for the covalent coupling of molecules to surfaces. Typically, dendrimers and hyperbranched polymers have been *grafted to* surfaces by reacting polymers with reactive groups on the surfaces. However, very few papers have reported the formation of surface initiated hyperbranched polymers using *grafting-from* techniques. The advantage of the grafting-from method is the higher degree of control over the placement of polymers and the opportunity to create much thicker films.

TiN is an excellent choice for a diffusion barrier with desirable electrical properties [11]. The deposition methodology is atomic layer deposition (ALD) and is used because of its self-limiting nature which affords sub-nanometer control of the growth process [12]. More importantly, ALD is characterized by relatively low temperatures and thermal budgets for growth (*vis-à-vis* CVD), making it of interest for deposition on organic materials. Deposition of TiN with CVD techniques has also received considerable attention [13-15]. CVD has been shown to deposit conformal TiN films using TiCl₄ [13] and more recently, Ti[N(CH₃)₂]₄ with the use of a second N-containing species [14]. Deposition of TiCl₄ with NH₃ has been shown to deposit clean TiN films with good conformality in demanding surface topographies. However, high substrate temperatures ($T_s > 400$ °C) make deposition from halide precursors undesirable, especially in case of organic materials. With Ti[N(CH₃)₂]₄, clean TiN films have been deposited at low temperature (< 200 °C) using a CVD technique with the addition of NH₃ [11]. More recently, ALD of TiN with Ti[N(CH₃)₂]₄ and NH₃ has been attempted in a few studies [16].

Deposition of TiN was investigated as a function of substrate temperature on Si(100) substrates at a total chamber pressure of 2 Torr. Two saturation film growth regions were observed: 175–190 °C and 200–210 °C where the growth rates were approximately 6.5 and 7.5 Å/cycle respectively. The films deposited exhibited an almost stoichiometric Ti:N ratio for all temperatures examined. In another study [17], the deposition of TiN from $\text{Ti}[\text{N}(\text{CH}_3)_2]_4$ and NH_3 was explored as a function of $\text{Ti}[\text{N}(\text{CH}_3)_2]_4$ and NH_3 exposure and substrate temperature. A binary transamination reaction sequence was proposed:



where the asterisks represents surface species. At 120 °C, the growth rate saturated at 1.2 Å/cycle for a 20 s NH_3 exposure at 0.65 Torr. The growth rate did not saturate with increasing $\text{Ti}[\text{N}(\text{CH}_3)_2]_4$ exposure and an increase in growth was seen with increasing $\text{Ti}[\text{N}(\text{CH}_3)_2]_4$ exposure. Above 180 °C, deposition was believed to occur via decomposition of $\text{Ti}[\text{N}(\text{CH}_3)_2]_4$. The apparent activation energy for deposition was dependent on $\text{Ti}[\text{N}(\text{CH}_3)_2]_4$ exposure time at $T_s > 180$ °C and was between 0.35 and 0.57 eV.

This work utilizes a grafting-from technique to form hyperbranched polyglycidol (poly-G) on SiO_2 and low κ dielectric surfaces via anionic ring-opening polymerization of glycidol. The details of the synthetic procedure have been given elsewhere [7]. The polymer brushes are grown directly from the surface using surface Si-OH groups as initiators, eliminating the need for initiator functionalized self-assembled monolayers. TiN ALD has been employed to grow the diffusion barrier films. The process is identical to that

described in earlier sections (chapter 4). To investigate nucleation the Ti precursor, $\text{Ti}[\text{N}(\text{CH}_3)_2]_4$, was introduced via a well-collimated supersonic molecular beam, and the other, NH_3 , via an effusive beam. A well collimated beam affords us the possibility of varying (i) the total number of ALD cycles (to validate the digital nature of the process), or (ii) the length of exposure to the $\text{Ti}[\text{N}(\text{CH}_3)_2]_4$ reactant (to validate the self-limiting nature of growth) on a single sample in a single experiment. This ability is critical for study of the non-steady-state stage of growth [18], i.e., nucleation. Film thicknesses were measured using single wavelength ellipsometry. *Ex situ* X-ray photoelectron spectroscopy (XPS), and Rutherford backscattering spectrometry (RBS) to determine composition, atomic density, and the extent of growth. Atomic force microscopy (AFM) was employed to track the evolution of roughness/morphology during film growth. Additionally, high-resolution scanning transmission electron microscopy (HRSTEM) and high energy resolution electron energy loss spectroscopy (HREELS) were also used to probe the growth at interfaces and hence further characterize the nature of growth.

The experimental apparatus, sample preparation, experimental procedures as well as analytical techniques employed are described in detail in chapter 2. In brief, all experiments involved four sequential stages. First, hyperbranched poly-G films were formed on SiO_2 or low κ surfaces. Second and prior to insertion into the vacuum chamber, the substrates were characterized using contact angle measurements, ellipsometry, and XPS. Third, the substrates were transferred into the thin film deposition system for TiN ALD film growth. In the fourth and last stage, the TiN samples were analyzed *ex situ* using ellipsometry, XPS, RBS, AFM, and STEM.

5.3 Results and discussion

5.3.1 Characterization of poly-G films

The kinetics of poly-G film growth on SiO₂ was quantified using ellipsometry. Plotted in Fig. 5-2 is the measured ellipsometric thickness vs. reaction time in glycidol. The thickness of the film was found to be linearly dependent on the reaction time. The poly-G IOLs were grown for 15, 30, and 60 minutes respectively and the growth rate was $\sim 1.7 \text{ \AA} \cdot \text{min}^{-1}$. The static water contact angle measured is always $< 10^\circ$ which points to the presence of an extremely hydrophilic surface in all cases. From XPS the films had C, and O in all cases. AFM results suggest that the root mean square (RMS) roughness of the 15 min film is $\sim 8 \text{ \AA}$ compared to a 4 \AA RMS roughness in case of the starting SiO₂ surface. The increase in roughness can be attributed to the hyperbranched backbone in the poly-G IOLS. The 60 min film has a slightly higher RMS roughness ($\sim 12 \text{ \AA}$). The AFMs have been shown later in the chapter. A more detailed description regarding the characterization results can be found elsewhere [19]. The thinnest poly-G IOL examined here had a reaction time of 15 min in glycidol. Prior to poly-G deposition step on low κ , the substrate was exposed to an oxygen plasma for 2 seconds which makes it relatively hydrophilic (contact angle = 30°) compared to the starting surface (contact angle = 90°).

5.3.2 TiN ALD: Film growth and characterization

Plotted in Fig. 5-3 is the TiN ellipsometric thickness as a function of number of ALD cycles at $T_s = 167^\circ \text{C}$ for SiO₂ and all three poly-G films examined here. The 15 min poly-G surface is the only one which allows TiN to nucleate with any degree of ease. The 30 and 60 min films exhibit unexpected resistance to growth in spite of a high density of $-\text{OH}$ groups.

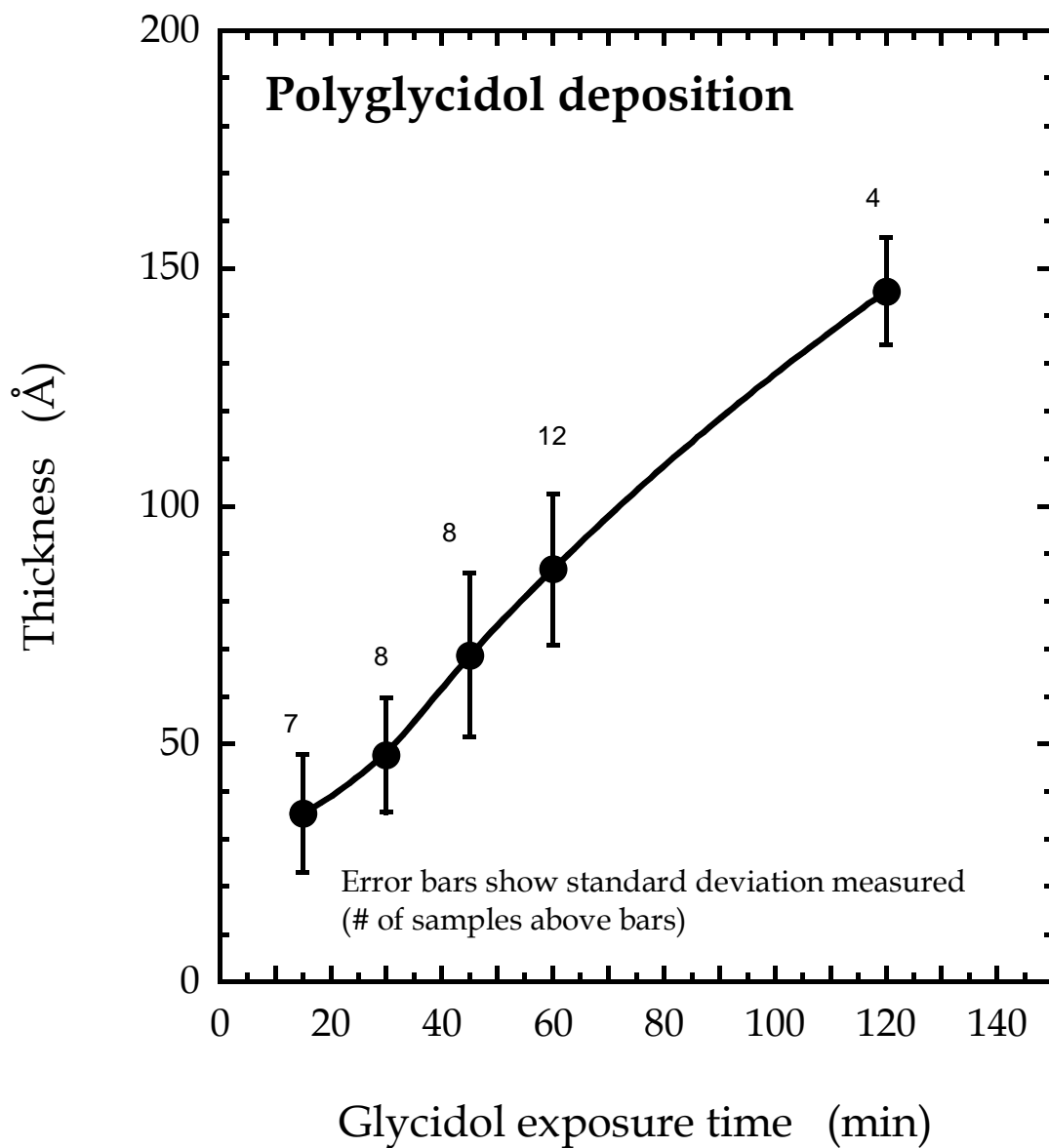


Figure 5-2: Measured ellipsometric thickness for poly-G films on SiO₂ as a function of deposition time in glycidol. The error bars have been calculated by averaging several experiments (from Manish Sharma).

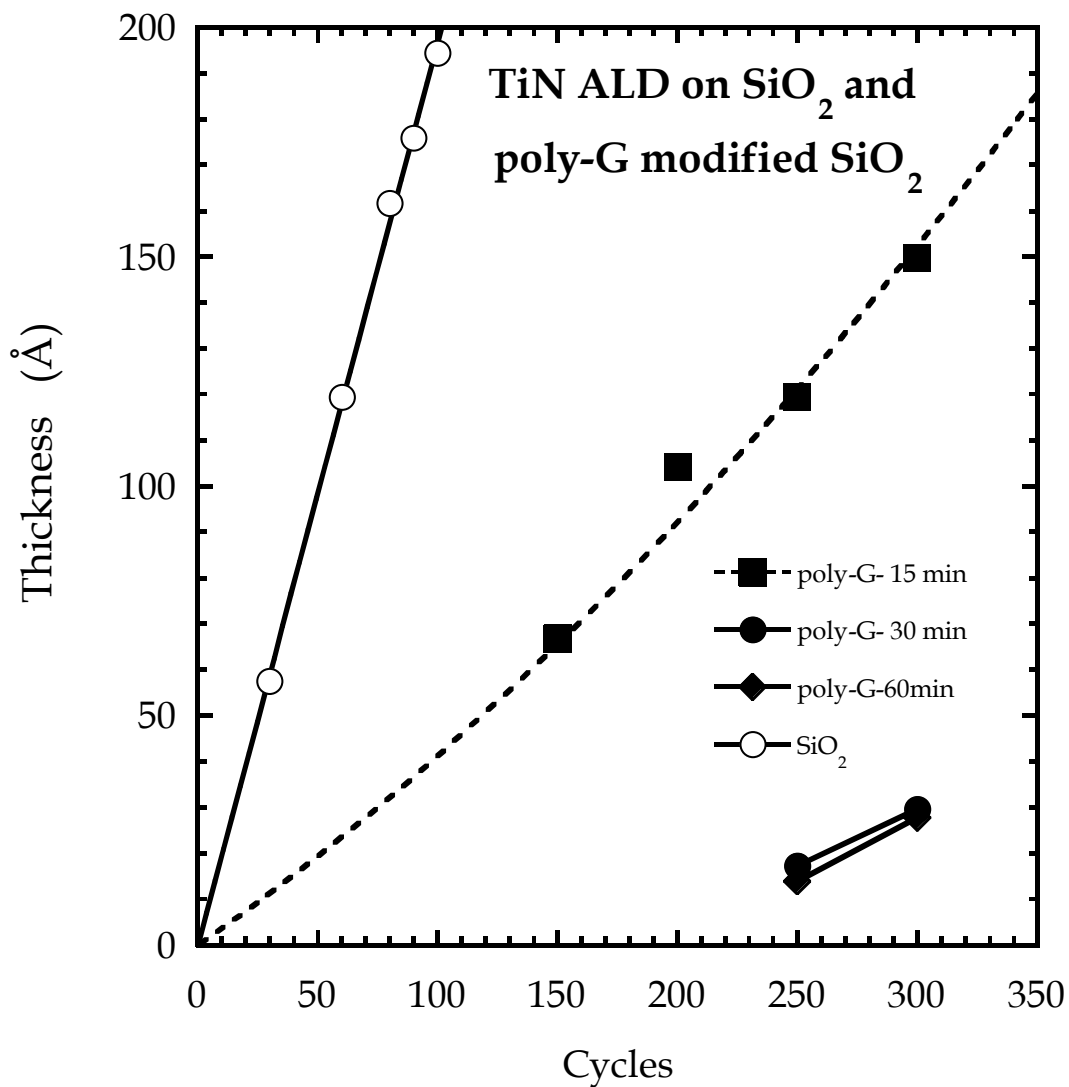


Figure 5-3: TiN ellipsometric thickness as a function of ALD cycles ($T_s = 167$ °C) on SiO₂ and poly-G modified SiO₂ of varying thickness (deposited for 15, 30 and 60 min). Data for SiO₂ and the 15 min poly-G case have been fit to the functional form in Eq. (5-2).

In another body of work in the group, done by Manish Sharma [19], ultra-high vacuum (UHV) exposure of these poly-G IOLs to pentakis(dimethylamido) tantalum, $\text{Ta}[\text{N}(\text{CH}_3)_2]_5$, was attempted. With increase in the poly-G IOL thickness, there was a clear decrease in N:Ta ratio for PDMAT chemisorbed on the surface. This indicates an increase in the loss of $-\text{N}(\text{CH}_3)_2$ ligands from $\text{Ta}[\text{N}(\text{CH}_3)_2]_5$, with an increase in poly-G thickness or alternatively the $-\text{OH}$ density. The N:Ta ratios obtained were ~ 4.5 for chemical oxide, 2.1 for 80 Å, and 0.9 for 105 Å thick poly-G film. These ratios clearly indicate that, as the density of terminal $-\text{OH}$ groups increases, $\text{Ta}[\text{N}(\text{CH}_3)_2]_5$ loses an increasingly higher number of $-\text{N}(\text{CH}_3)_2$ ligands. While the N:Ta ratio of ~ 4 hints towards a single Ta-O bond formation which was seen for chemical oxide, the ratios of ~ 2 and ~ 1 hint towards 3 and 4 Ta-O bonds forming for each reacting $\text{Ta}[\text{N}(\text{CH}_3)_2]_5$ molecule, respectively. The stoichiometries proposed here for $\text{Ta}[\text{N}(\text{CH}_3)_2]_5$ reacting with an $-\text{OH}$ terminated surface may be used to understand the difference in the growth rate of titanium nitride films in an ALD process.

To further characterize the nature of the TiN thin films grown on poly-G functionalized substrates, *ex situ* XPS was employed. Shown in Fig. 5-4 are the Ti(2p) XP spectra for all the three poly-G films examined, after 300 cycles. The Ti(2p) intensity is the strongest for TiN on the thinnest poly-G IOL, and much less intense, but about equal for TiN grown on the thicker poly-G IOLs. The Si(2p) spectra after 300 cycles are plotted in Fig. 5-5 where we see that the Si signal (representative of the underlying substrate) has been entirely attenuated by the TiN overlayer only for the case of the thinnest (15 min) poly-G IOL. The Si(2p) signal is much stronger in the cases of growth on the thicker poly-G IOLs, as the substrate is not completely covered in these cases.

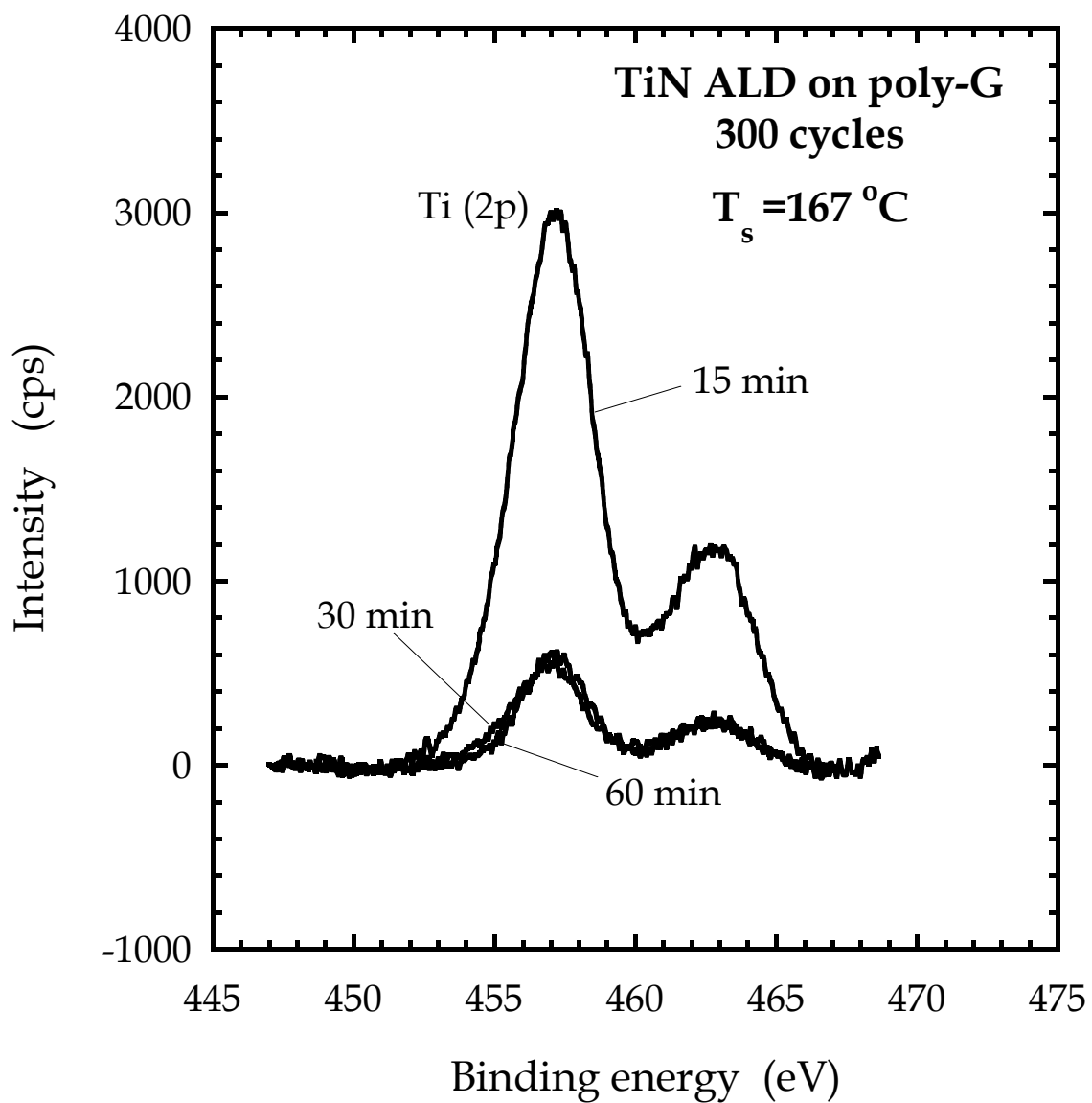


Figure 5-4: Ti (2p) XP spectra after 300 ALD cycles on poly-G films (15, 30, and 60 min deposition time on SiO₂). Two peaks are observed due to spin orbit splitting.

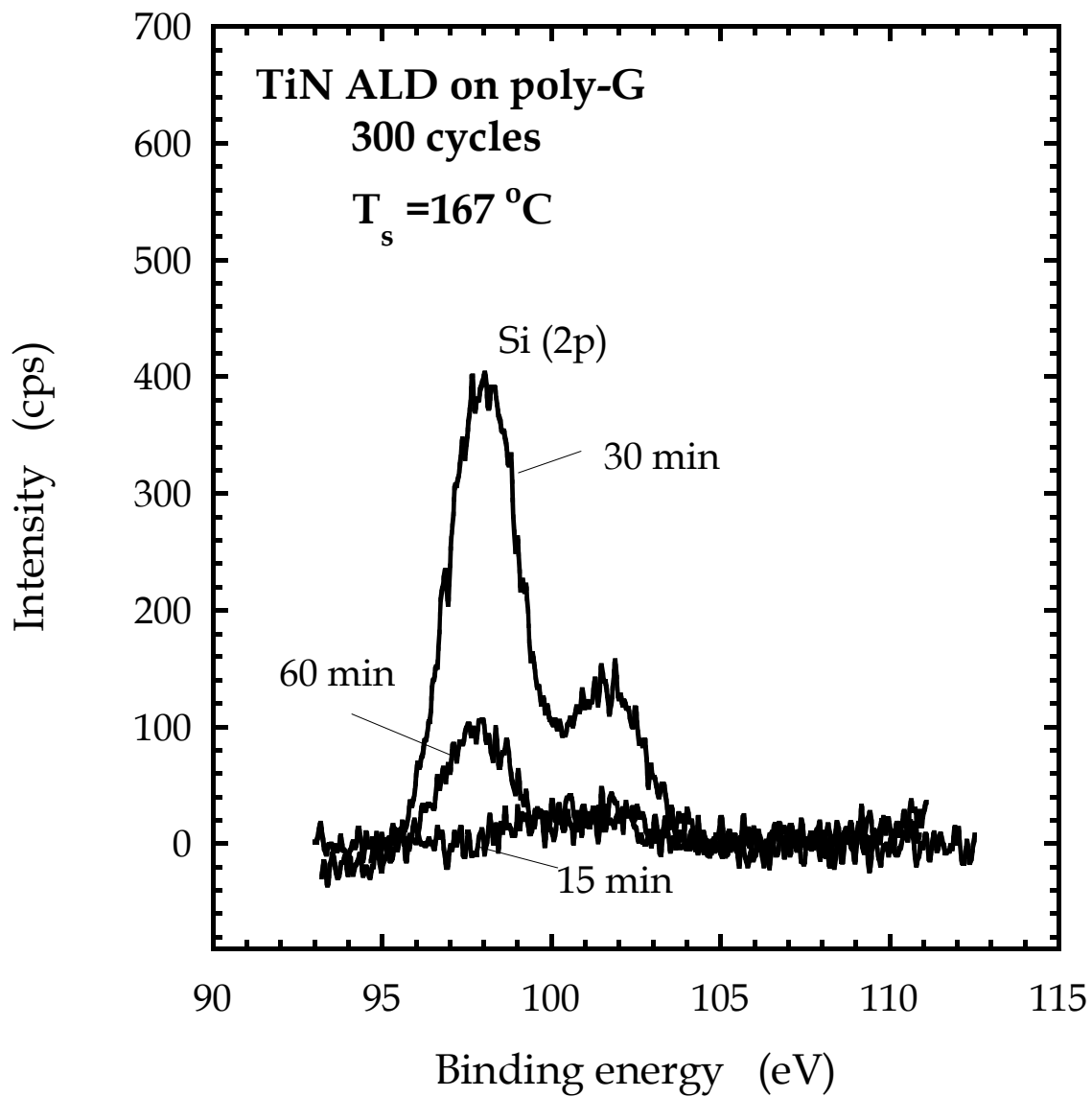


Figure 5-5: Si (2p) XP spectra after 300 ALD cycles on poly-G films (15, 30, and 60 min deposition time on SiO₂)

The Si(2p) signal is stronger in the case of the 30 min IOL as it is attenuating through a thinner organic layer, compared to case of the 60 min IOL. It should be remembered that TiN film has the same nominal thickness in both cases and hence is affecting attenuation to the same extent.

The N(1s) spectra are plotted in Fig. 5-6 where the data for 15 min case has been fit to two distinct peaks. The width is the same for both peaks and is a fit parameter. In the case of TiN on thicker poly-G thin films the N signal is very weak, indicating very little incorporation of N in the film. N incorporation is much clearer in the case of TiN deposition on the thinnest poly-G thin film, as the intensity for this peak is strong. The results presented here are indicative of the fact that increasing the number density of –OH groups would lead to more $-\text{N}(\text{CH}_3)_2$ ligand loss from the transition metal co-ordination complex. This has also been confirmed by density functional theory (DFT) calculations which predict the reaction of $\text{Ti}[\text{N}(\text{CH}_3)_2]_4$ with R-OH, where R is an alkyl group, to have an activation barrier below the vacuum level [20]. Put in other terms, the reaction of transition metal amides with –OH groups is energetically downhill. This was also confirmed experimentally via molecular beam reflectivity measurements [21]. Thus the higher the number of surface and sub-surface –OH groups, the more is the extent of the accompanied ligand loss from $\text{Ti}[\text{N}(\text{CH}_3)_2]_4$. In the case of the thicker 30 and 60 min IOLs, TiN nucleation and subsequent growth is harder to attain possibly because of the low density of $-\text{N}(\text{CH}_3)_2$ ligands post $\text{Ti}[\text{N}(\text{CH}_3)_2]_4$ exposure. The NH_3 exposure in the subsequent ALD step is ineffective, as there are not enough active sites, i.e., $-\text{N}(\text{CH}_3)_2$ ligands to initiate network formation (as illustrated in Eq. 5-1) and hence TiN growth. This is again in agreement with work done elsewhere [19].

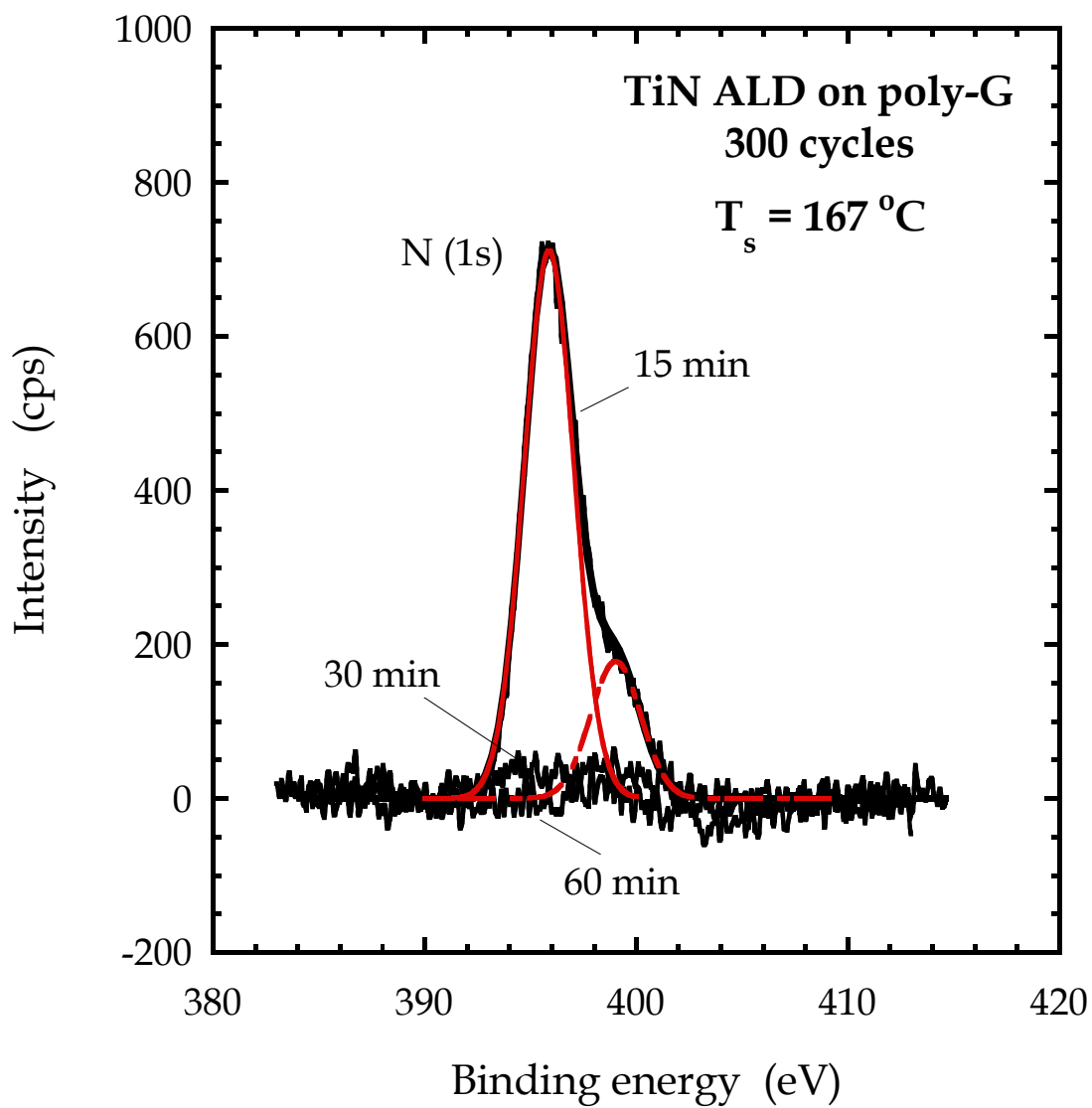


Figure 5-6: N (1s) XP spectra after 300 ALD cycles on poly-G films (15, 30, and 60 min deposition time on SiO₂). The N (1s) data for the 15 min case has been fit to a Gaussian-Lorentzian function after Shirley background subtraction. This function accounts for N present in two different chemical environments.

The asymmetry in the N(1s) signal (the shoulder on the higher binding energy side) from the TiN film on the 15 min IOL is also indicative of the fact that N exists in two different chemical environments. The N in TiN is at 396 eV [22] and is the primary peak. The secondary, higher binding energy (~ 399 eV [22]), peak can be attributed to unreacted $-\text{N}(\text{CH}_3)_2$ ligands incorporated in the film. These might still be present as there can be regions in the film where the density of $-\text{N}(\text{CH}_3)_2$ is not high enough to promote TiN formation. The data has been fit to a Gaussian-Lorentzian function (described in chapter 2) which accounts for both the peaks. The ratio of N bound to Ti and that bound to C is $\sim 3.5:1$ even after 300 cycles. The ratio has been ascertained using the curve fit parameters. The very weak N (1s) signal in the 30 and 60 min cases, can also in part be attributed to the *ex situ* nature of XPS analysis. It can be argued that these films were not very dense and hence can get completely oxidized leading to complete annihilation of the nitrogen signal.

AFM was employed to get further insight into the growth process. The topography evolution was followed with increase in number of cycles. Shown in Fig. 5-7 are $0.5 \times 0.5 \mu\text{m}^2$ AFM images for TiN ALD at 167 °C on the thinnest (15 min deposition) poly-G IOL. The images for the unreacted poly-G film as well as TiN films which have been grown for 150, 200, 250, and 300 cycles respectively are shown. In Fig. 5-8, $0.5 \times 0.5 \mu\text{m}^2$ AFM images for TiN ALD at 167 °C on a thicker (60 min growth) poly-G film have been depicted. The images for the unreacted poly-G film as well as TiN films which have been grown for 200, 250, and 300 cycles respectively are shown. To compare these two sets of results, in Fig. 5-9, the RMS roughness is plotted as a function of thickness for both cases. As may be seen, roughness increases rapidly for growth on the thick poly-G IOL, indicative of very 3-D, islanded growth.

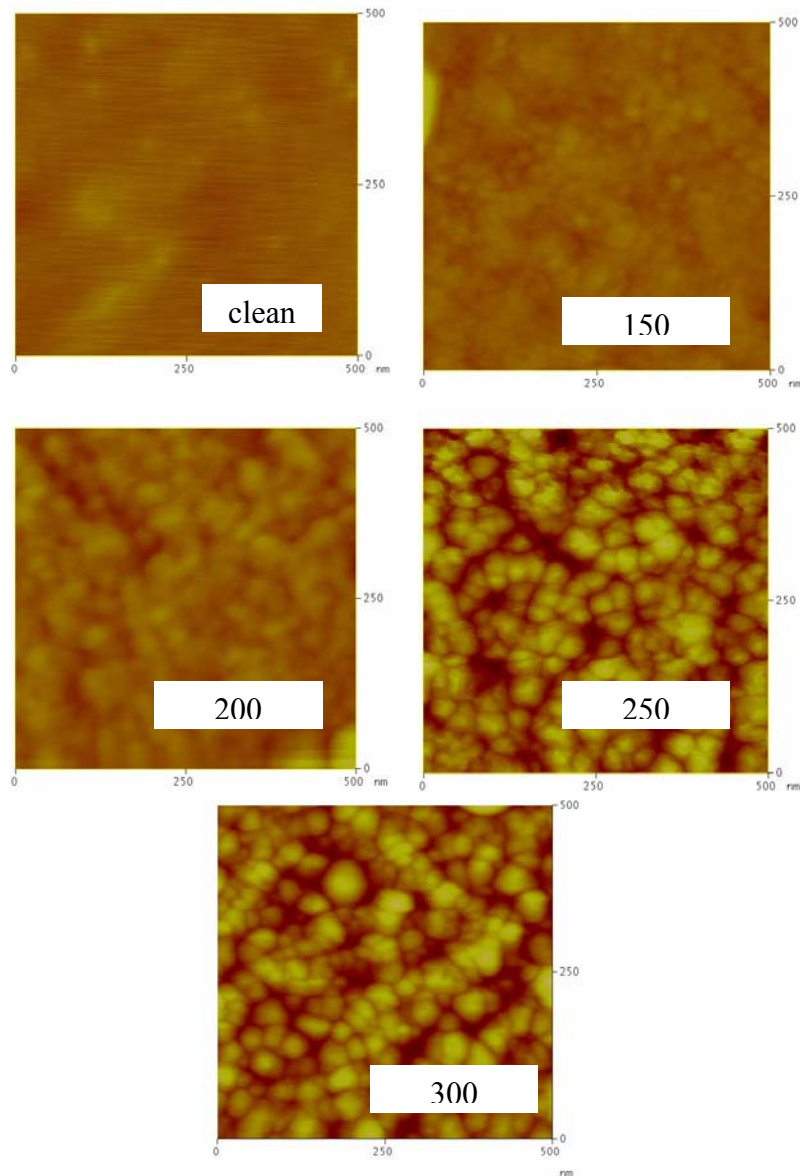


Figure 5-7: Atomic force microscope images for TiN ALD at 167 °C on 15 min poly-G films. In each case the field of view is $0.5 \mu\text{m} \times 0.5 \mu\text{m}$. The images presented are for the unreacted poly-G IOL as well as TiN films which have been grown for 150, 200, 250, and 300 cycles.

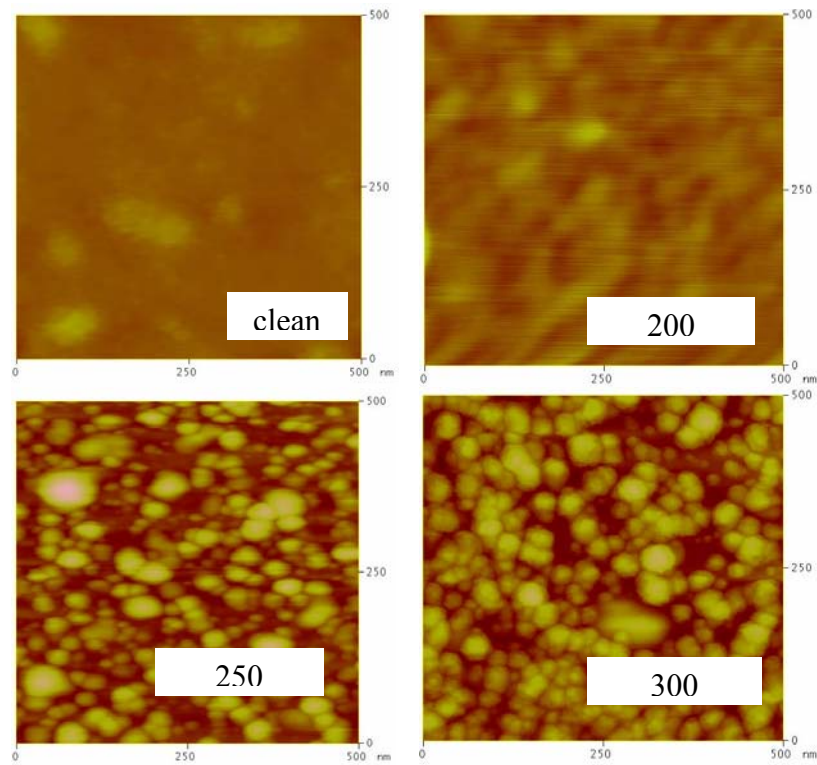


Figure 5-8: Atomic force microscope images for TiN ALD at 167 °C on 60 min poly-G films. In each case, the field of view is $0.5 \mu\text{m} \times 0.5 \mu\text{m}$. The images presented are for the unreacted poly-G IOL as well as TiN films which have been grown for 200, 250, and 300 cycles.

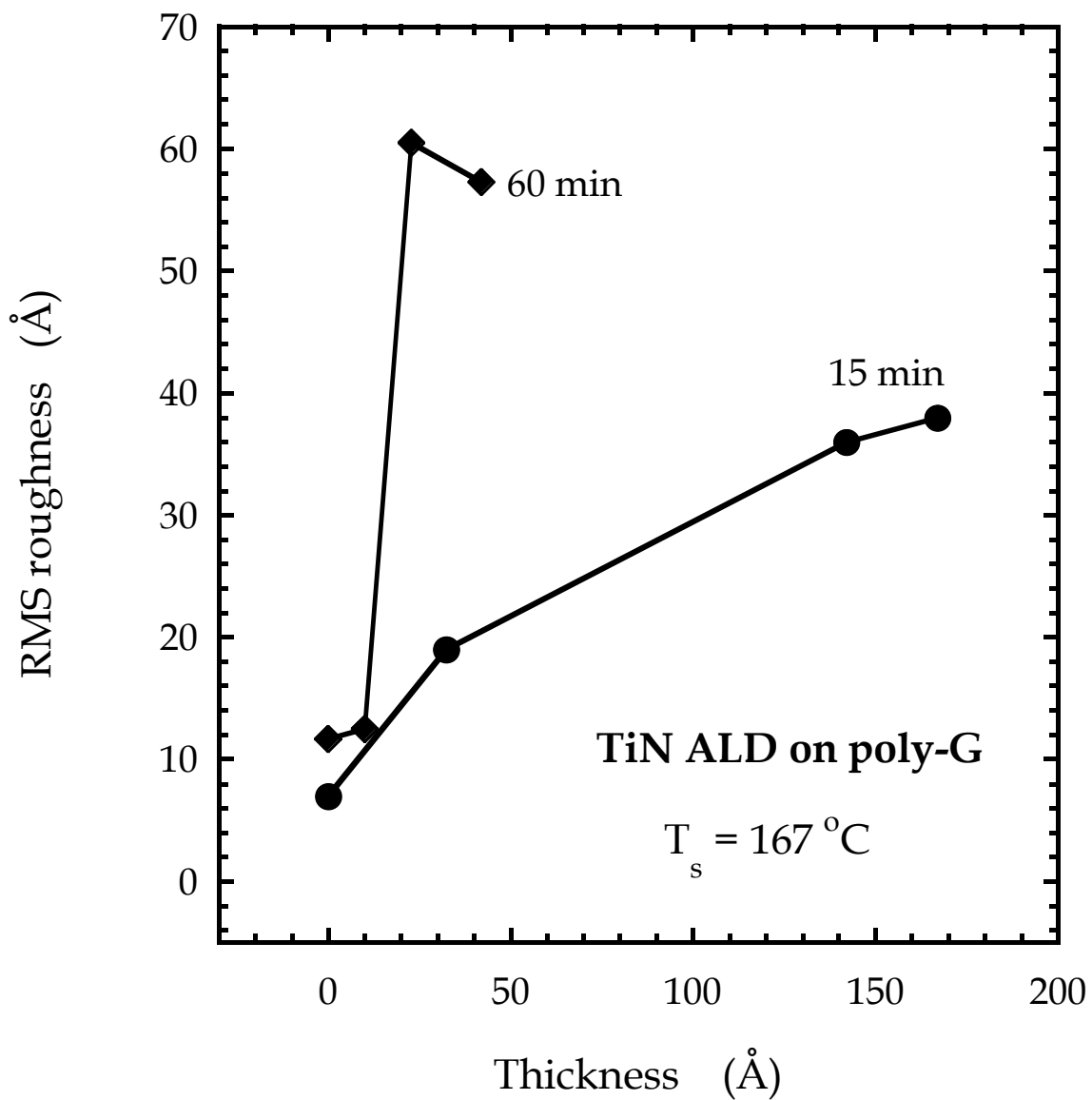


Figure 5-9: AFM determined root-mean-square (RMS) roughness as a function of measured ellipsometric thickness for TiN ALD at $T_s = 167^\circ\text{C}$ on poly-G films: 15 min (filled circles), and 60 min (filled diamonds).

AFM data can be analyzed further to get information about the kinetic roughening mechanisms during a growth process like ALD. Scaling concepts have been particularly insightful in understanding key phenomena such as surface roughening. The two quantities of interest are: Interface width (w) and the lateral correlation length (ξ). The interface width is a measure of the roughness of the surface while the lateral correlation length is a measure of spatial periodicity in the film. Detailed discussion regarding the calculation of these quantities is provided in chapter 4. Dynamic scaling theory predicts that both w and ξ increase with time according to power laws $w(t) \sim t^\beta$ and $\xi(t) \sim t^{\beta/\alpha}$. The roughness exponent α and growth exponent β are indicative of different growth mechanisms. α is obtained from 1-dimensional power spectral density (1DPSD) analysis and β from plots of film thickness as a function of roughness.

In Fig. 5-10 the α values are plotted as a function of TiN film thickness. In both cases, after an initial period, α is > 1 . This behavior is indicative of pyramidal growth and formation of mounds or 3D islands. In the initial phase the density of $-\text{N}(\text{CH}_3)_2$ ligands on the surface is not high enough to promote film growth and hence the α values are < 1 . Once the density is high enough for the surface species to start reacting with each other, a rapid increase in α is seen in both cases. The correlation lengths are plotted in Fig. 5-11. In both the cases, they are in the 0.1-0.2 μm range. These are higher in comparison to those observed on the reactive SAMs in chapter 4. The correlation length is another measure of island/grain size and it is evident that the growth is 3D and islanded in case of the poly-G films due to a loss of $-\text{N}(\text{CH}_3)_2$ ligands.

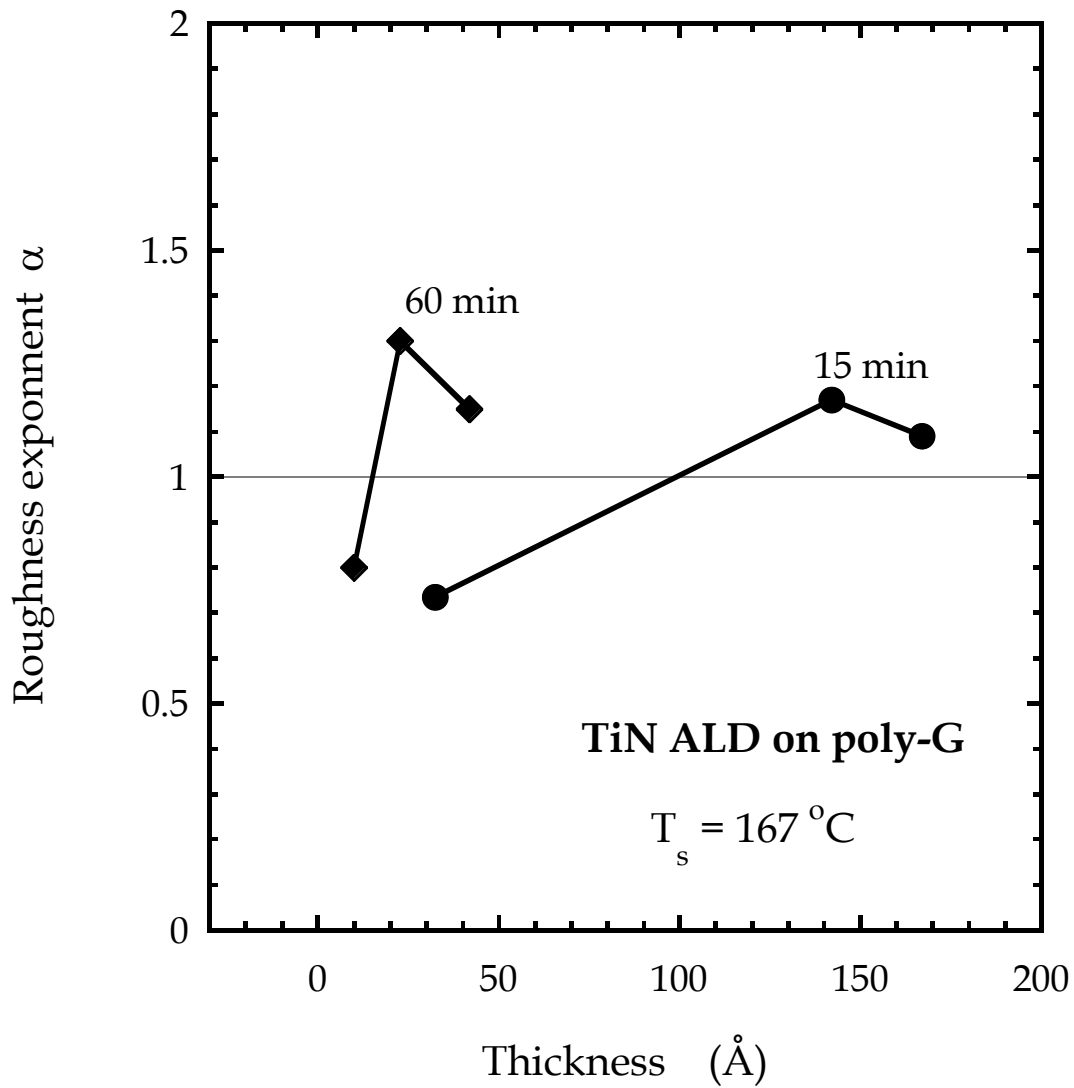


Figure 5-10: Roughness exponent α plotted as a function of TiN film thickness, for the 15 (circles) and 60 min (diamonds) poly-G films on SiO₂ (T_s = 167 °C). α is extracted from the slope of the self-affine portion of the 1DPSD spectrum.

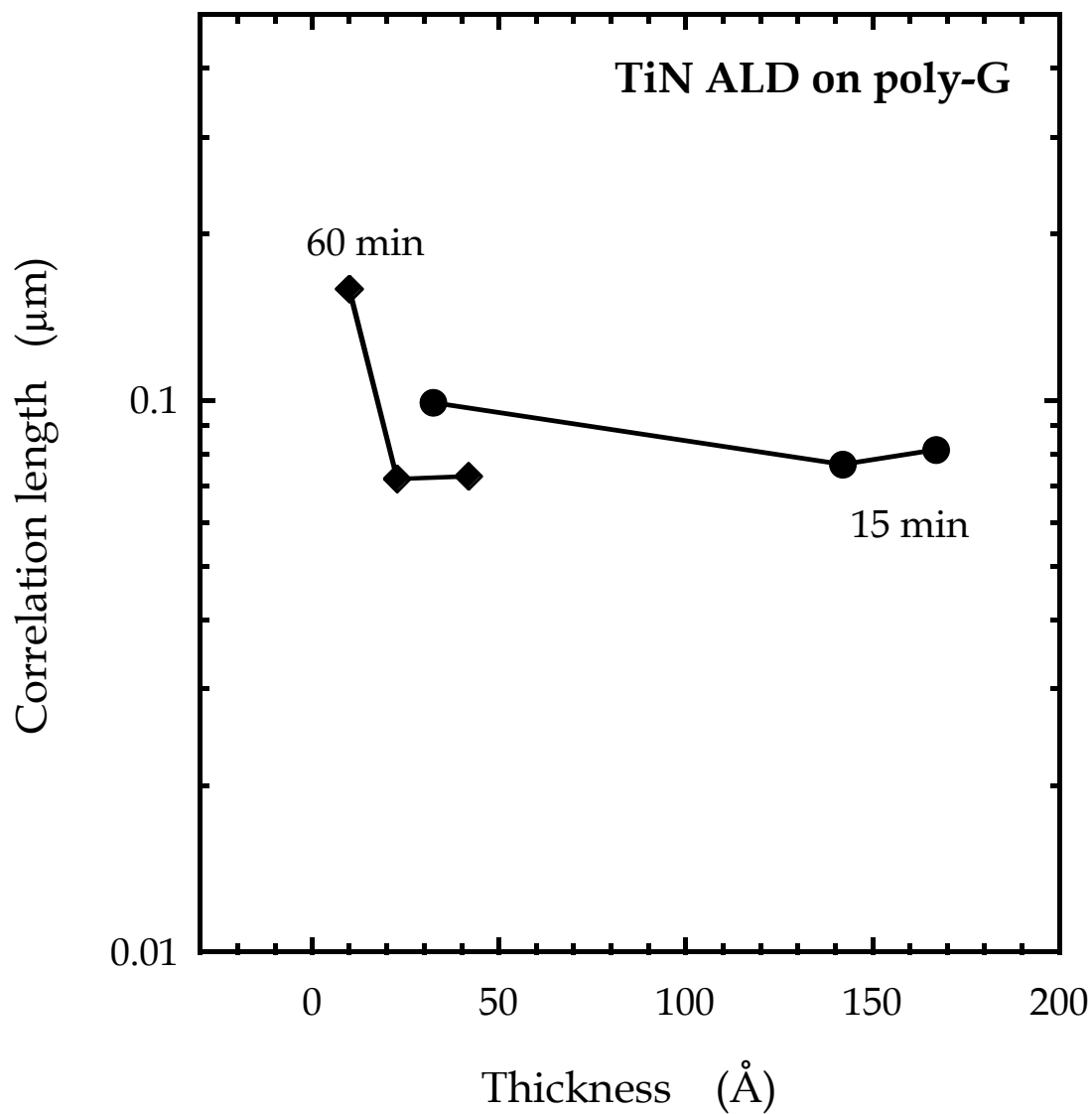


Figure 5-11: Correlation length ξ (in μm) as a function of TiN film thickness ($T_s = 167^\circ\text{C}$). ξ is obtained from the intersection of the self-affine region and the plateau region in the 1DPSD spectra for TiN films deposited on 15 min (circles) and 60 min (diamonds) poly-G modified SiO_2 .

Growth on the thinner poly-G IOL is characterized by reduced roughness, although larger than what was observed on other IOLs (reactive SAMs in chapter 4). The data confirm the growth behavior that was interpreted using the XPS data. The higher density of $-OH$ groups in the case of the 60 min IOL, causes an excessive loss of $-N(CH_3)_2$ ligands from $Ti[N(CH_3)_2]_4$. After a sufficiently large number of cycles, the density of $-N(CH_3)_2$ ligands may become high enough in certain regions and this can promote TiN growth in localized domains. This, in effect, leads to very rough and islanded films. The ligand loss effect is much less pronounced in case of the 15 min IOL due to the lower $-OH$ density. Thus the films are smoother and the nucleation much more uniform.

Cross-sectional STEM was used to further characterize the film morphology, and to try to resolve the individual layers in this inorganic-organic-inorganic thin film stack. This work was done in collaboration with Peter Ercius and Prof. David Muller (School of Applied and Engineering Physics, Cornell University). Shown in Fig. 5-12, are both the dark field and bright field STEM images for a 160 Å thick TiN film, on a 15 min IOL on SiO_2 . The deposition was carried out at 167 °C. As can be seen in both images, the TiN film is quite rough. Also, the SiO_2 layer and the IOL can not be individually resolved. The presence of a rough TiN film is in agreement with the AFM data. Additional information about film composition and interfaces can be obtained from the HREELS data. The STEM probe was also used to acquire this data. Plotted in Fig. 5-13, are the elemental EELS signals for Ti, C, and Si (both from the substrate and SiO_2 layer). These data are indicative of a scenario where TiN and SiO_2 are in direct contact with no obvious evidence for a polymeric film in between.

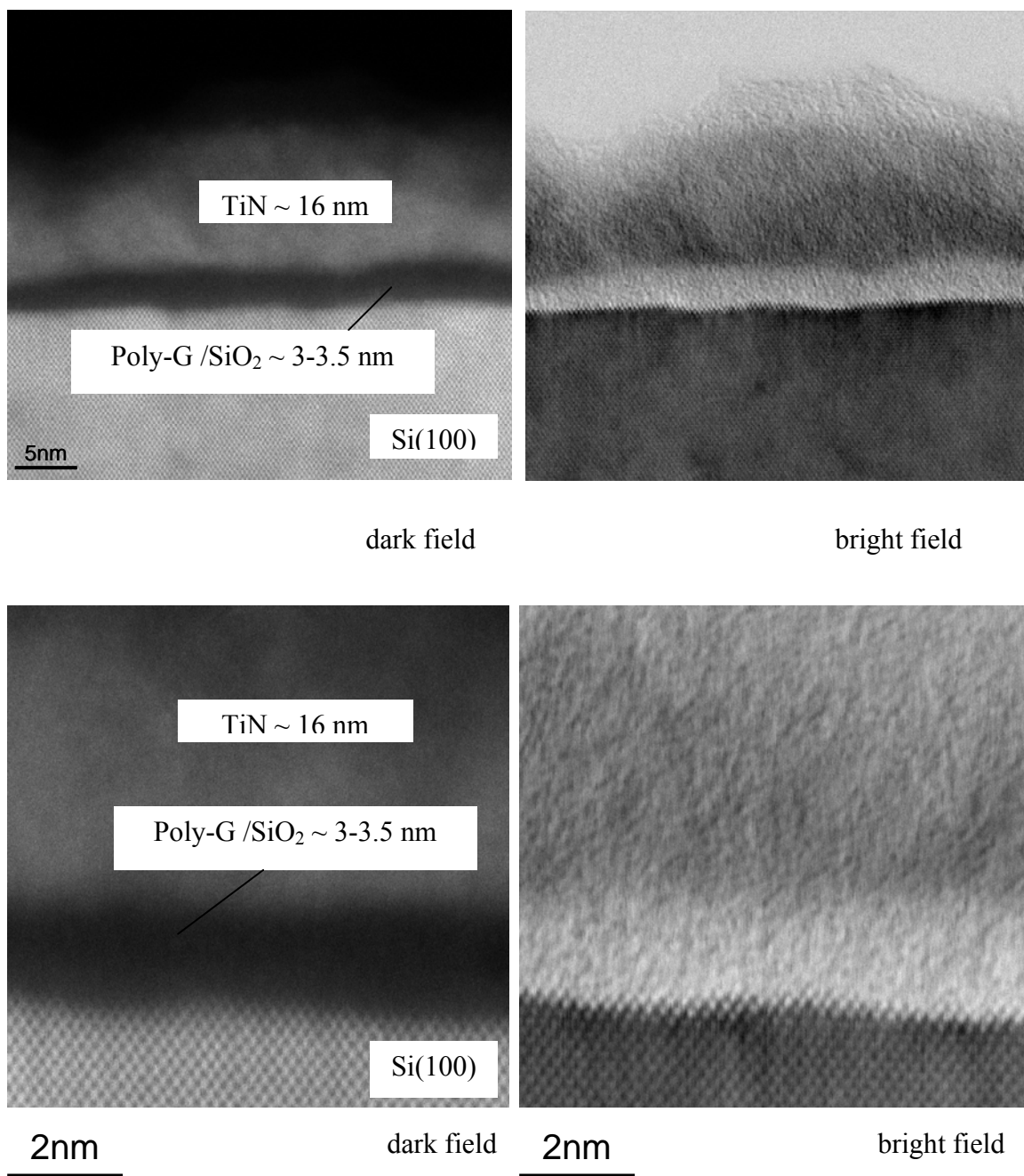


Figure 5-12: Dark and bright field scanning transmission electron micrographs (STEM) for a 160 Å thick TiN film grown on 15 min poly-G IOL at 167 °C. The images have been shown for two different magnifications.

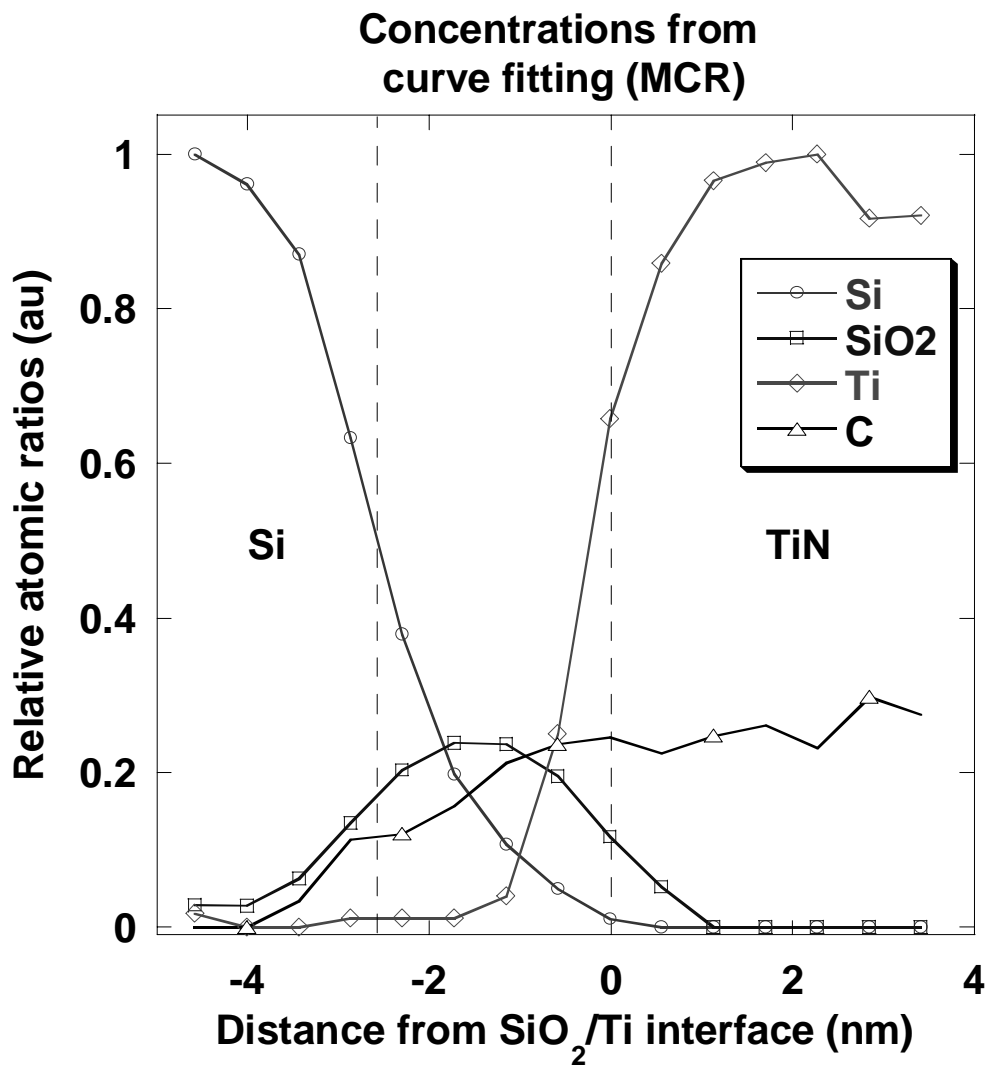


Figure 5-13: High resolution electron energy loss spectra (HREELS) for carbon, titanium, and silicon. Plotted are the intensities as a function of distance from the SiO₂/Ti interface (from Peter Ercius).

A carbon signal is detected even before any Ti is detected. This could be due to surface contamination during specimen preparation for STEM imaging. The presence of C in the TiN film could be due to $-\text{N}(\text{CH}_3)_2$ ligand incorporation occurring during the ALD process. The ALD process is by no means perfect, and some C had also been detected in the XPS analysis of the TiN films on SAMs and SiO_2 (chapter 4).

In the next set of experiments, the deposition of TiN was attempted on porous low κ dielectric substrates. The motivation was to see if these hyperbranched polymer films could be deposited on the low κ substrates to enhance nucleation sites for TiN precursors and also prevent penetration. The first set of experiments was performed on the untreated/as-received substrates, provided by the Intel Corporation. These films had the following specifications: 4500 Å in thickness, 25% porosity, 2.6 nm pore diameter, and $\kappa = 2.5$. From XPS measurements, the low κ films had Si, C, and O as elemental constituents. The films were hydrophobic and had a water contact angle of 92° . Plotted in Fig. 5-14 is the data for ellipsometric thickness vs. number of cycles on an untreated low κ sample. The ALD process was carried out at 167°C . This result is contrary to expectations as the low κ surface was expected to have a dearth of nucleation sites on the surface. It can be argued, however, that there can be surface groups inside the pores which can exhibit reactivity towards the TiN precursors. NH_3 can also play a role in functionalizing the surface with $-\text{NH}_2$ or similar groups, via reaction with any dangling bonds that may be present. These two factors taken together can contribute to nucleation after a delay of ~ 50 cycles as seen in Fig. 5-14 from a linear fit to the data.

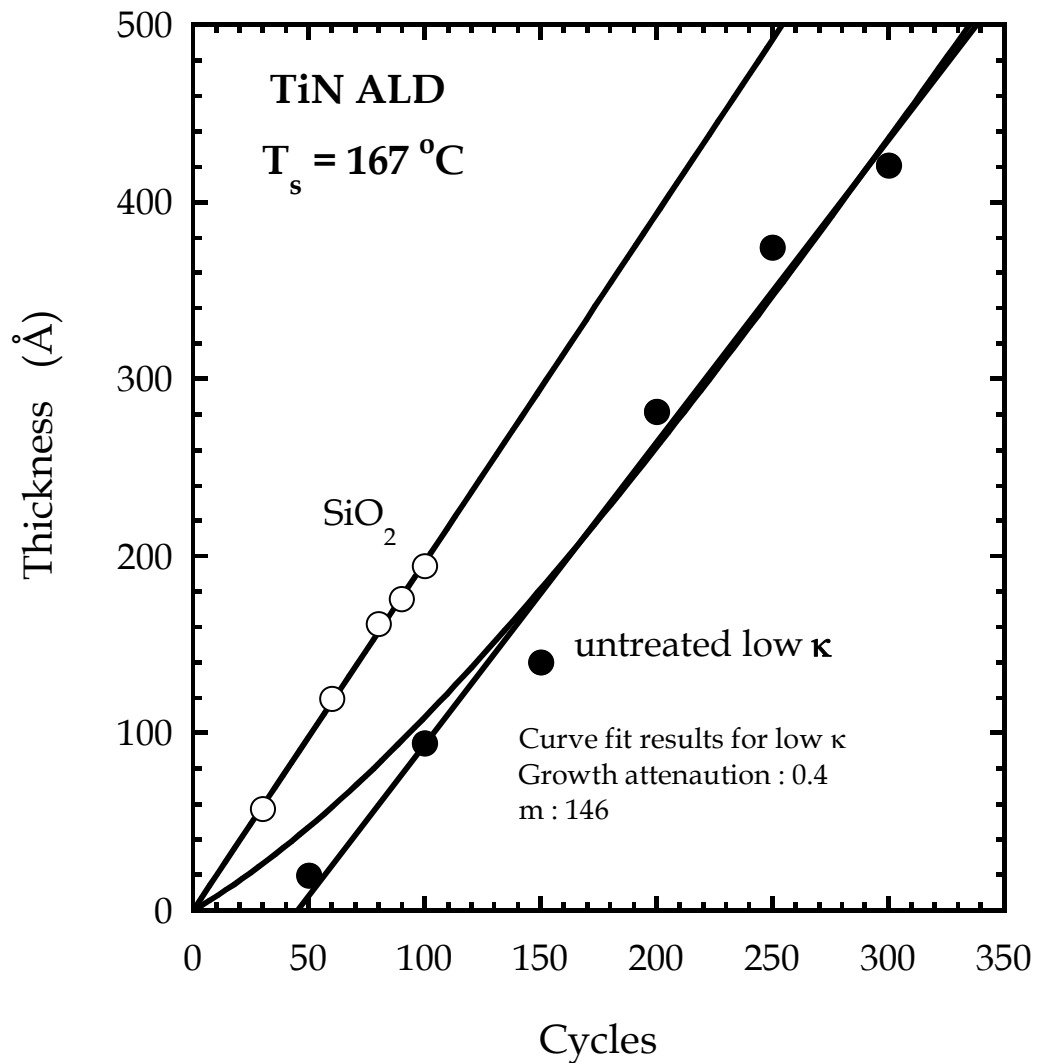


Figure 5-14: Ellipsometric thickness as a function of ALD cycles for TiN deposition on SiO₂ (open circles) and untreated low κ substrate (filled circles) at $T_s = 167$ °C. The smooth line going through the data for SiO₂ is a fit Eq. (5-2). The smooth lines going through the data for low κ are fits to two functional forms: 1) linear growth with an offset and 2) Eq. (5-2)

From a fit to this model the growth rate is $\sim 1.7 \text{ \AA-cycle}^{-1}$ (slope) with a nucleation delay of ~ 50 ALD cycles (x-intercept). The data has also been fit to the following functional form (same as chapter 4) :

$$D = D_{\infty} \{n + m(1 - \alpha)[\exp(-n/m) - 1]\} \quad (5-2)$$

where D is the film thickness, n is the number of ALD cycles, D_{∞} is the growth rate as $n \rightarrow \infty$, and α and m are parameters. This form exhibits the following characteristics: $D|_{n=0} = 0$; $dD/dn|_{n=0} = \alpha D_{\infty}$, and $dD/dn|_{n \rightarrow \infty} = D_{\infty}$, i.e., the initial growth rate is attenuated by a factor of α , but approaches its asymptotic value (D_{∞}) (which is assumed to be $\sim 2 \text{ \AA-cycle}^{-1}$: steady state growth rate on SiO_2) with an exponential decay constant of m cycles. In this model there is no “incubation” time, unlike the linear growth model. From the fit parameters a value of $\alpha \sim 0.4$ is obtained or in other words the initial growth rate is 40 % of the steady state growth rate which should be $\sim 2 \text{ \AA-cycle}^{-1}$ in all cases. Both fits, however, have a common conclusion and that is the presence of an unsteady or nucleation delay period. The incubation phase is not observed in the case of SiO_2 . Further investigations are underway to explain the reaction mechanism. However, it is important to point out that there is a need to prevent pore penetration. This discussion will be revisited a little later.

AFM was also used to track the morphology of these films as a function of ALD cycles. The results are shown in Fig. 5-15 along with RMS roughness vs. thickness data. It should be pointed out that the starting untreated low κ surface has a relatively low RMS roughness ($\sim 4.70 \text{ \AA}$). The roughness increases with increase in thickness and seems to have saturated around 12 \AA for a measured ellipsometric thickness of 420 \AA after 300 ALD cycles.

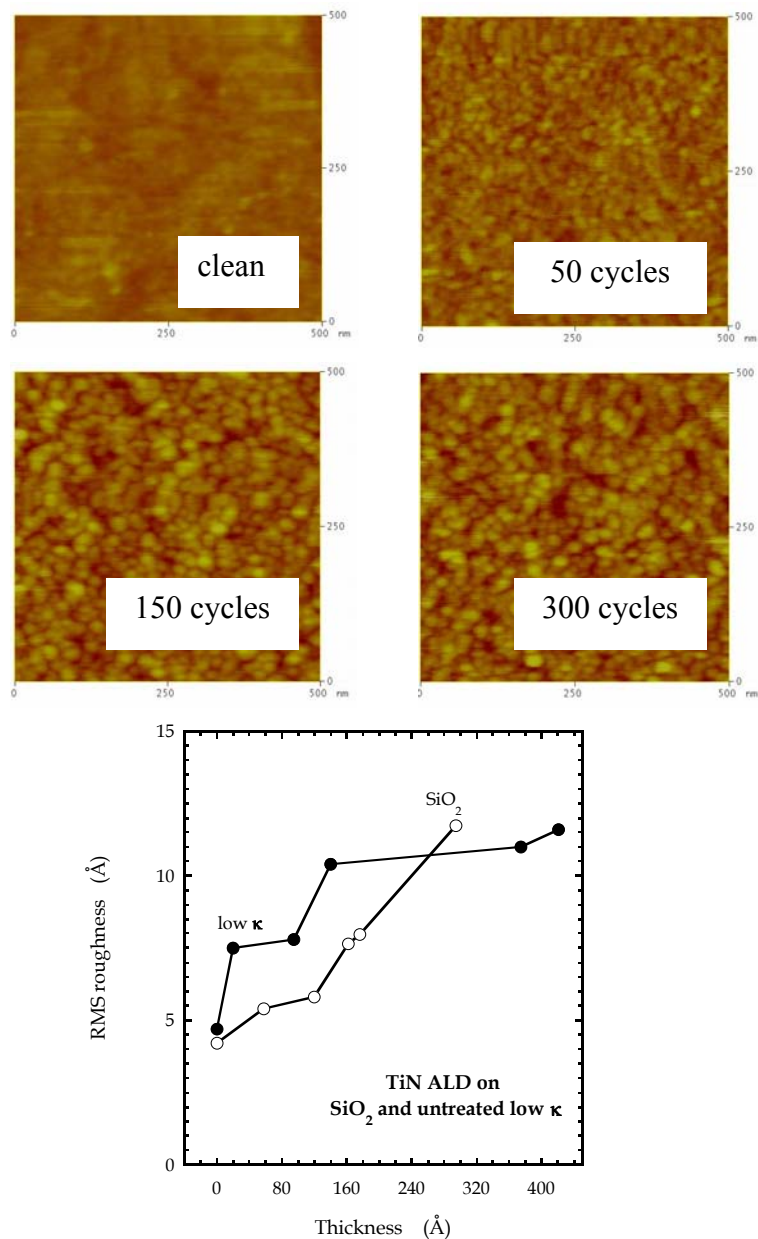


Figure 5-15: Atomic force microscope images for TiN ALD at 167 °C on untreated low κ substrates. In each case the field of view is $0.5 \mu\text{m} \times 0.5 \mu\text{m}$. The images presented are for the unreacted surface as well as TiN films which have been grown for 50, 150, and 300 cycles. Also shown is the RMS roughness vs. thickness data for SiO₂ and the untreated low κ substrates.

This result can be reconciled with the fact that the growth is extremely conformal, after an initial nucleation delay and a non-steady state growth regime, which leads to very little change in topography and hence surface roughness. Similar trends have been reported for Al₂O₃ growth on Si (100) [23] where the surface roughness is constant after 20 ALD cycles.

RBS was carried out on a 420 Å thick (300 ALD cycle) film to probe the elemental composition as well as any evidence of pore penetration. The data together with a simulation (overlying curve) are shown in Fig. 5-16. The simulation result was obtained by modeling the stack as : TiO₂/ TiN / low κ (450 nm)/ Si (100). The simulation was carried out with the aid of RUMP [24]. A TiO₂ surface layer had to be accounted for due to the fact that there is oxidation of the top few layers once the TiN surface is exposed to air. The PERT subprogram was used to search for a "best" fit to the data. It does so by varying one or more parameters of the sample description or experimental parameters (thicknesses, compositions, etc.) and comparing the resulting theoretical spectrum with the actual spectrum. PERT iterates the process until it finds the best set of parameters to match the spectrum. The definition of "best" fit is the fit which maximizes the Poisson likelihood function χ^2 between the experimental spectrum and the simulation over a selected region called the error window. χ^2 is computed using Poisson statistics [25]. In this case the compositions of the layers was fixed and the only simulation parameters were the TiN and TiO₂ thickness. In the final analysis, RBS results suggest a combined stack (TiN and TiO₂) thickness of ~ 400 Å which agrees reasonably well with the ellipsometry data.

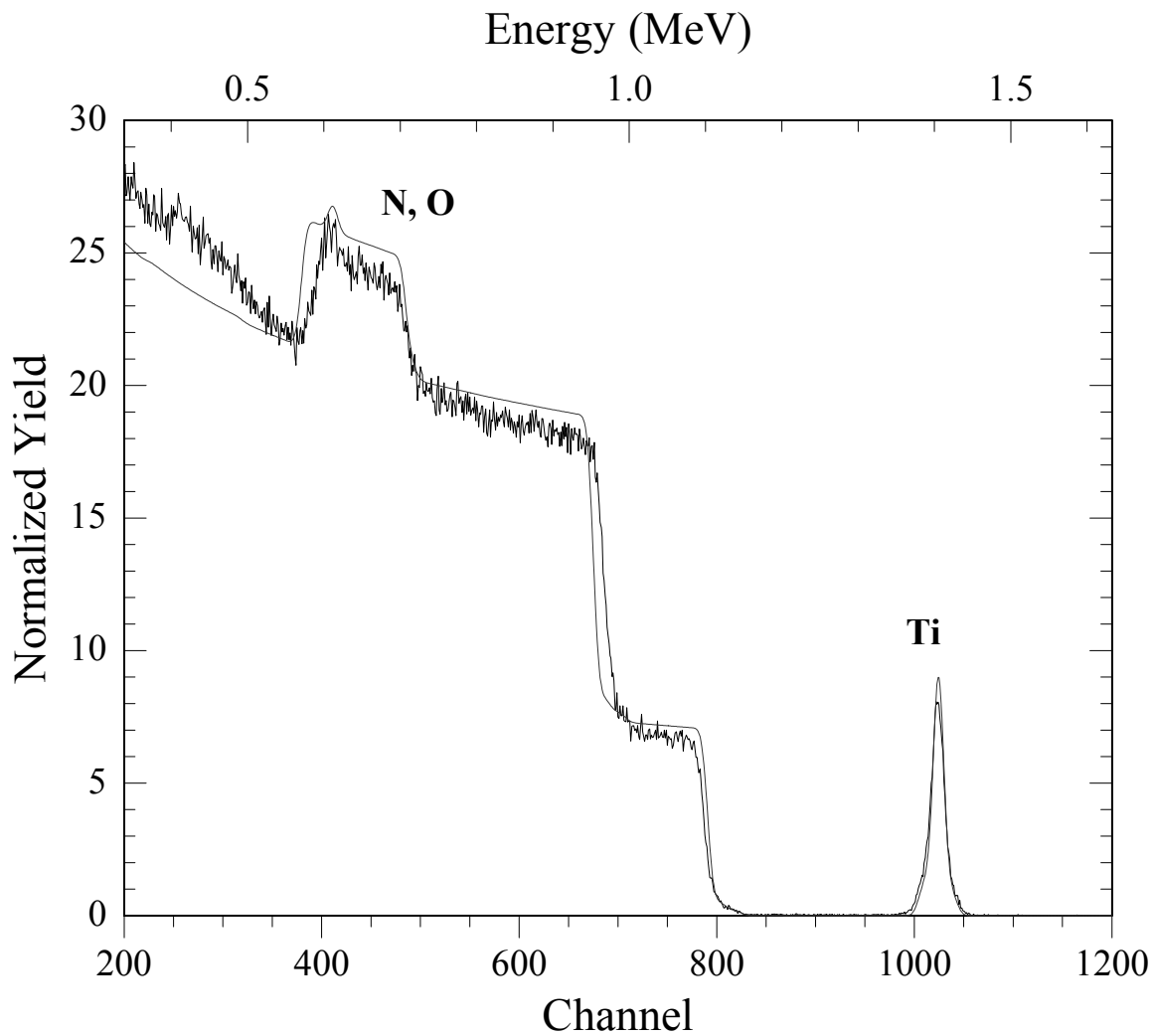
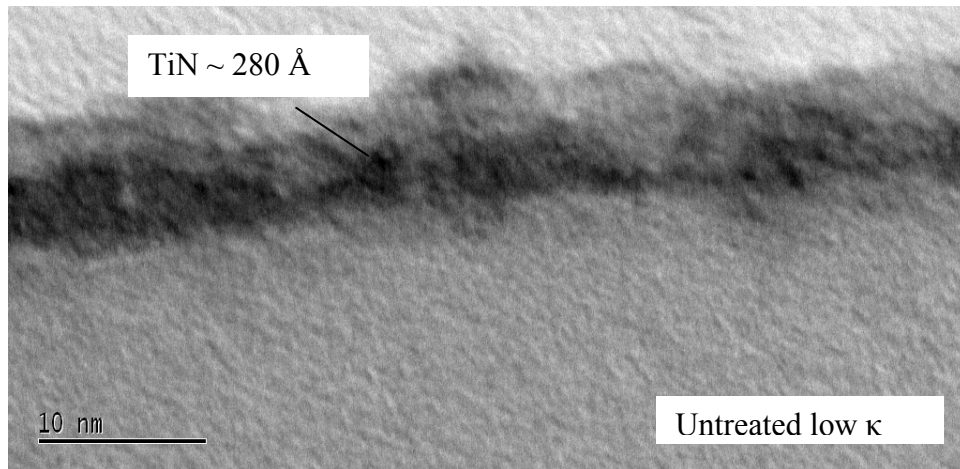


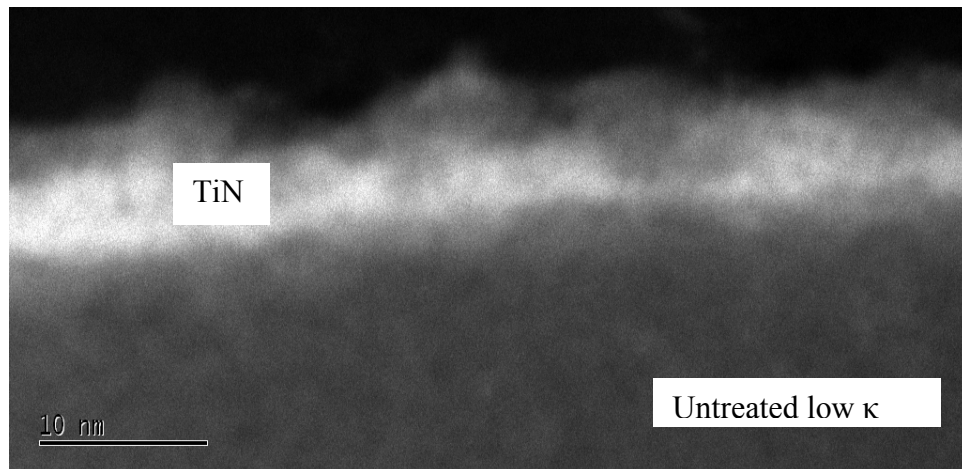
Figure 5-16: RB spectrum for a 420 Å thick (300 ALD cycle) TiN film on an untreated low κ substrate. The data together with the simulation results (overlying curve: carried out with the aid of RUMP) are presented. A TiO₂ surface layer had to be accounted for due to the formation of a native oxide on TiN.

Cross-sectional STEM data was acquired to characterize the growth process further. The dark and bright field STEM images for a 280 Å thick TiN film, on an as-received low κ substrate, are shown in Fig. 5-17. From both the images it is very clear that TiN penetrates the porous dielectric layer. The penetration depth can be quantified with the aid of HREELS data (shown in Fig 5-18). The data were acquired at three different physical locations on the specimen (labeled 36, 37, and 38). TiN penetration depth varied from 1-5 nm. Thus there is a clear need for developing techniques for the deposition of the diffusion barrier films without penetration. Penetration deteriorates the insulating properties of the dielectric layer.

The approach adopted here is to explore the use of hyperbranched glycidol films as a possible pore-sealing layer. If successful, this approach could have another advantage, namely a surface with a high density of nucleation sites in the form of $-OH$ groups. Only the thinnest (15 min) poly-G IOL was tried, as this was the case which displayed growth of least rough TiN films on IOL modified SiO_2 . Characterization using contact angle measurements, ellipsometry, and XPS suggest that the film produces a hydrophilic layer with the desired thickness on the low κ surface. Presented in Fig 5-19 are the results for TiN ALD on a low κ surface modified using a 15 min poly-G IOL. The ellipsometric thickness vs. number of cycles data suggest a longer incubation time in this case, compared to the case of untreated low κ . The linear growth model with an offset predicts a growth rate of $\sim 1 \text{ \AA-cycle}^{-1}$ with a nucleation delay of ~ 70 cycles. This was not unexpected as similar trends were seen in case of poly-G IOLs on SiO_2 . The high density of $-OH$ groups delays nucleation due to the excessive loss of $-N(CH_3)_2$ ligands from $Ti[N(CH_3)_2]_4$.



a) bright field image



b) dark field image

Figure 5-17: Bright and dark field scanning transmission electron micrographs (STEM) for a 280 Å thick TiN film grown on an untreated low κ substrate at 167 °C. The images show clear TiN penetration into the pores.

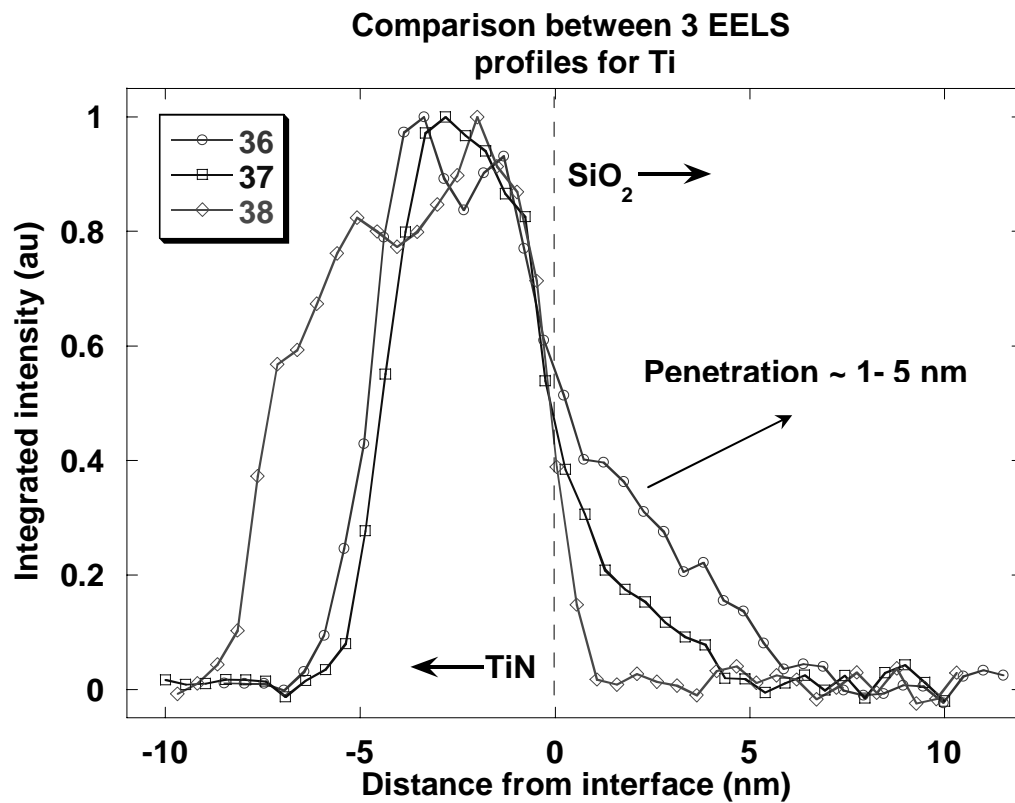


Figure 5-18: High resolution electron energy loss spectra (HREELS) for titanium at three different positions on the specimen. Plotted are the intensities as a function of distance from the low κ / Ti interface. The penetration depth is 1-5 nm in all the three measurements (from Peter Ercius).

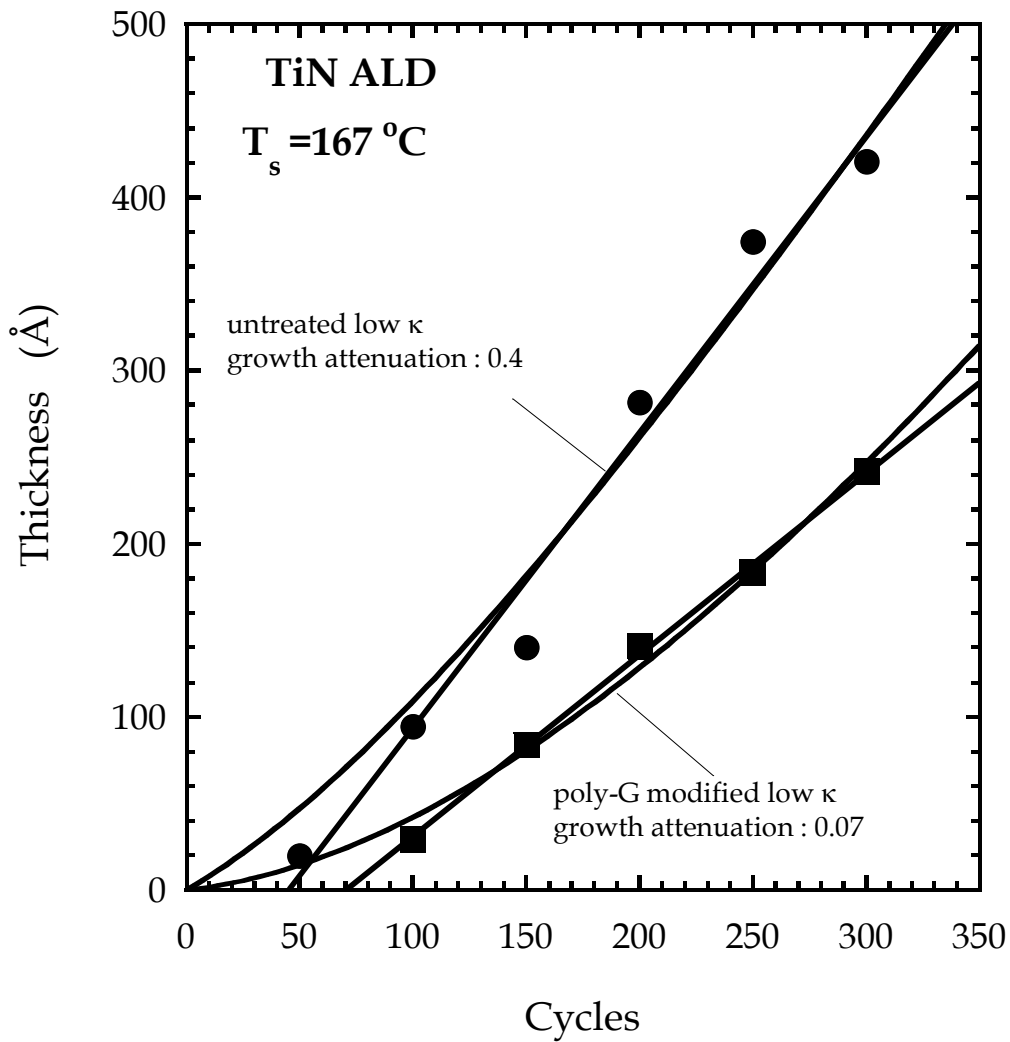


Figure 5-19: Ellipsometric thickness as a function of ALD cycles for TiN deposition on the untreated (filled circles) and 15 min poly-G treated low κ (filled squares) substrates at $T_s = 167^\circ\text{C}$. The smooth lines are fits to two functional forms: 1) linear growth model with an offset and 2) Eq. (5-2).

AFM has again been used to track film morphology as a function of ALD cycles. Shown in Fig 5-20, are the AFM images for films grown on the modified low κ films for 100, 150, and 300 cycles respectively. Also shown are data for RMS roughness vs. thickness. The data go through a maximum. This is a consequence of the localized nucleation during the early stages of growth. It can be seen that the growth occurs in many disconnected domains which may possess a high density of residual $-\text{N}(\text{CH}_3)_2$ ligands. Once these domains become large enough, film growth becomes much more uniform leading to a decrease in roughness.

RBS was again employed to characterize composition and a similar simulation was performed. The results are shown in Fig. 5-21. Ti and N were detected along with O (due to the air break between growth and *ex situ* RBS analysis). The thickness estimated from RBS is $\sim 160 \text{ \AA}$.

STEM and HREELS analysis prove to be very useful in testing the efficacy of this approach for pore sealing. The bright and dark field images for a 240 \AA thick film, on a 15 min poly-G IOL deposited on a low κ substrate, are shown in Fig 5-22. Also shown is the HREELS data. The images do not show any TiN penetration into the pores of the low κ substrate. Another key observation is that the low κ substrate and the TiN film appear to be in direct contact with each other. There is no evidence of a residual organic layer at the TiN - low κ interface. This may not be a problem for the application being considered here. As long as the organic layer is effective in preventing penetration into the pores during deposition, its fate afterwards is immaterial as it does not serve any other function. The films also look very rough, which is in part due to the fact that the top of the TiN layer has removed by ion milling. From the HREELS data in it can be seen the TiN and low κ concentrations

coincide with the interface position approximated from images of the films. The C concentration profile shows no indication of the polymeric film as seen from changes when scanning across the TiN/ low κ interface.

Finally one-dimensional power spectral density (1DPSD) analysis for the AFM images is done to get more insight into the growth mechanism for the TiN films. Plotted in Fig. 5-23 is the roughness exponent α as a function of TiN film thickness for both untreated and poly-G treated low κ substrates. In both the cases, α is always > 1 implying strongly correlated fluctuations due to features large with respect to the scale length. The instability is caused by the formation of mounds, or islands and is characteristic of pyramidal growth. The correlation lengths as a function of thickness are plotted in Fig. 5-24. The correlation lengths are in the 0.05-0.07 μm range.

Summarizing the results taken together, it is very clear that the thicker poly-G IOLs on SiO_2 (30 and 60 min) are not amenable to growing smooth and continuous films. They lead to 3D and islanded growth. This knowledge is very useful for developing a similar strategy in the case of low κ substrates. The untreated low κ film can not be used for depositing a TiN diffusion barrier without penetration into the pores. Preliminary results on 15 min poly-G IOL seem promising for depositing a barrier layer without penetration. Further characterization efforts are underway employing ellipsometric porosimetry [26] which is another metric for testing the pore sealing effectiveness.

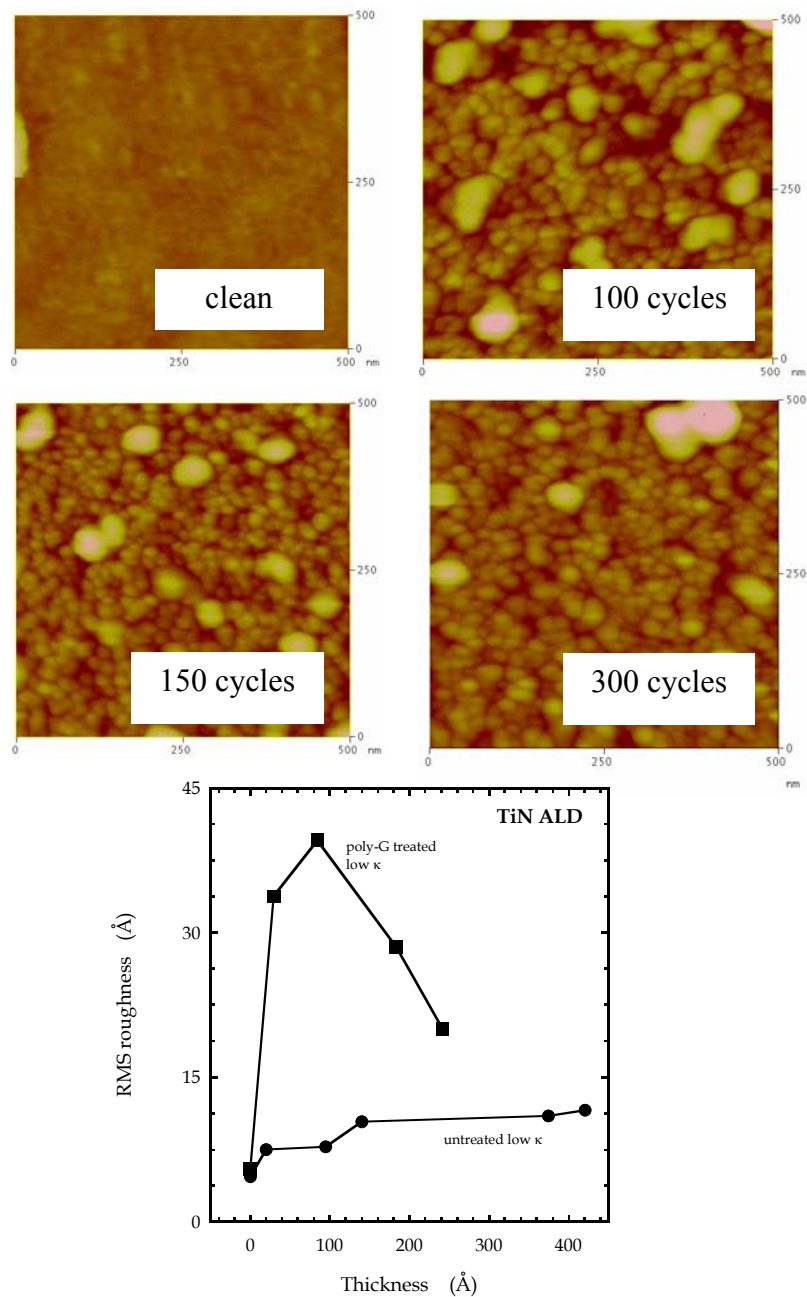


Figure 5-20: Atomic force microscope images for TiN ALD at 167 °C on 15 min poly-G treated low κ substrates. In each case the field of view is $0.5 \mu\text{m} \times 0.5 \mu\text{m}$. Also included is RMS roughness vs. thickness data for ALD films grown on untreated and poly-G treated substrates.

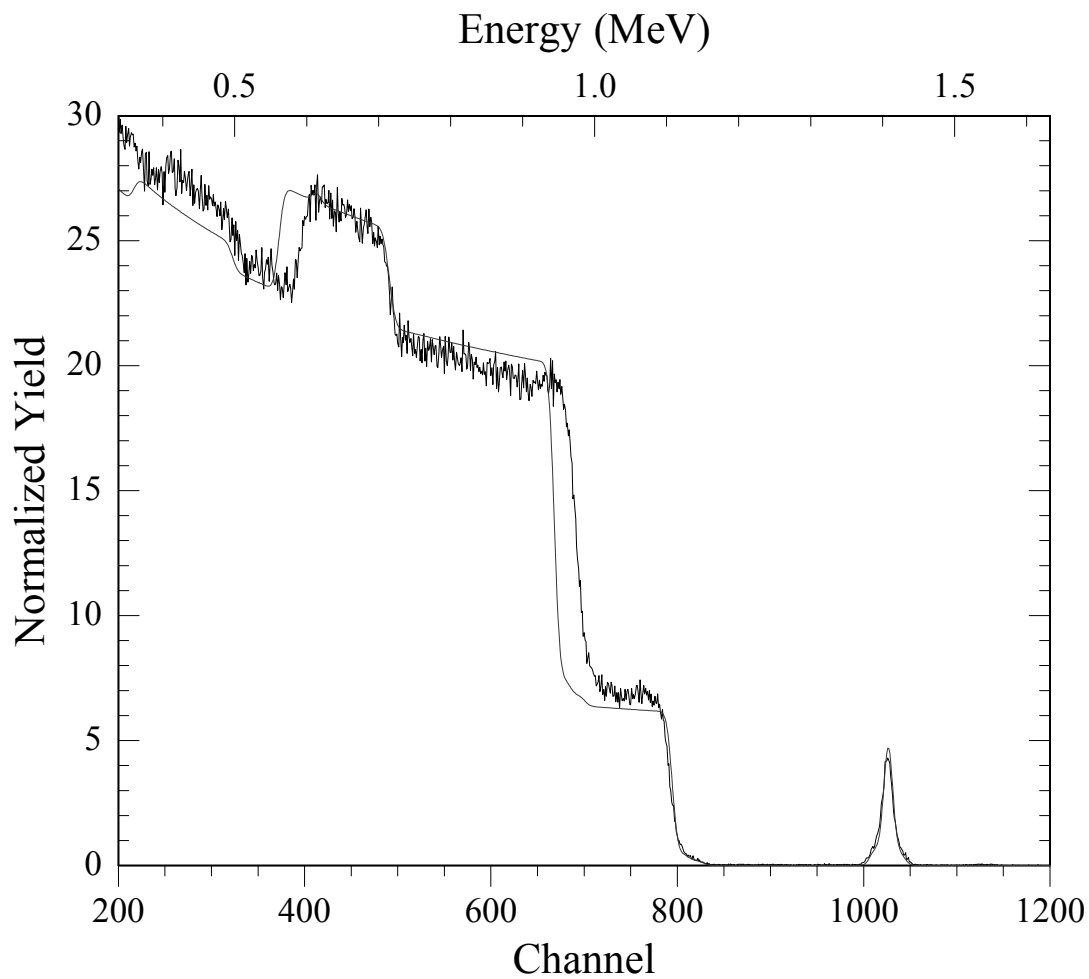


Figure 5-21: RB spectrum for a 240 Å thick (300 ALD cycle) TiN film on an poly-G (15 min) treated low κ substrate. The data and the simulation results (overlying curve) are presented. A TiO₂ surface layer had to be accounted for due to the formation of a native oxide on TiN.

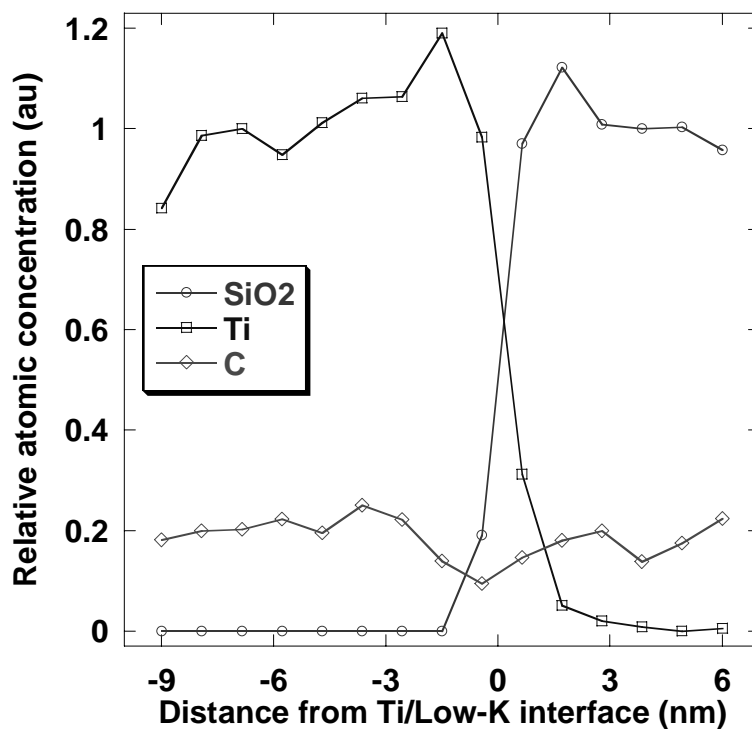
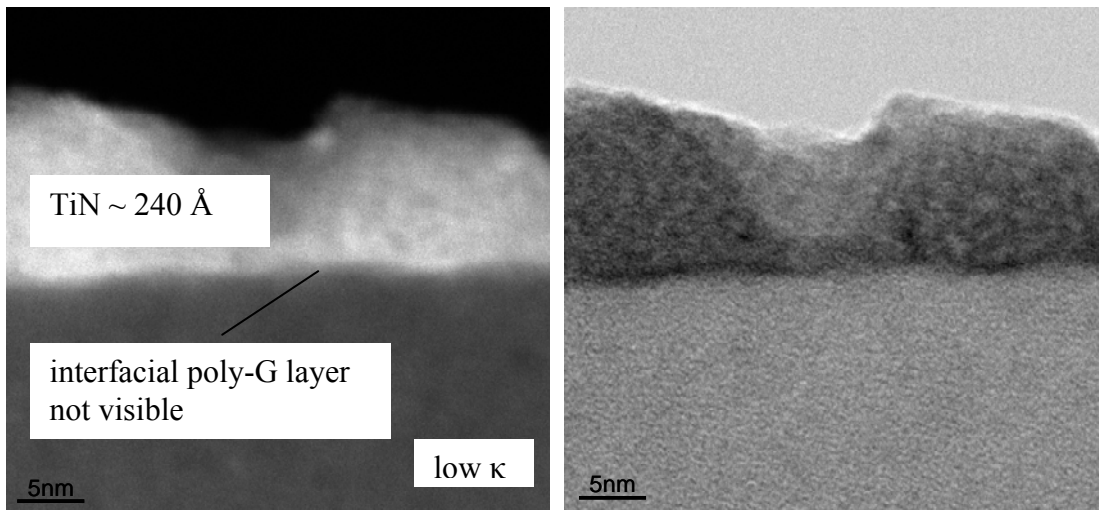


Figure 5-22: Bright and dark field scanning transmission electron micrographs (STEM) for a 240 Å thick TiN film grown on poly-G treated low κ at 167 °C. Also shown are the HREELS data for Ti, Si, and C which confirm the no penetration scenario as seen in the images.

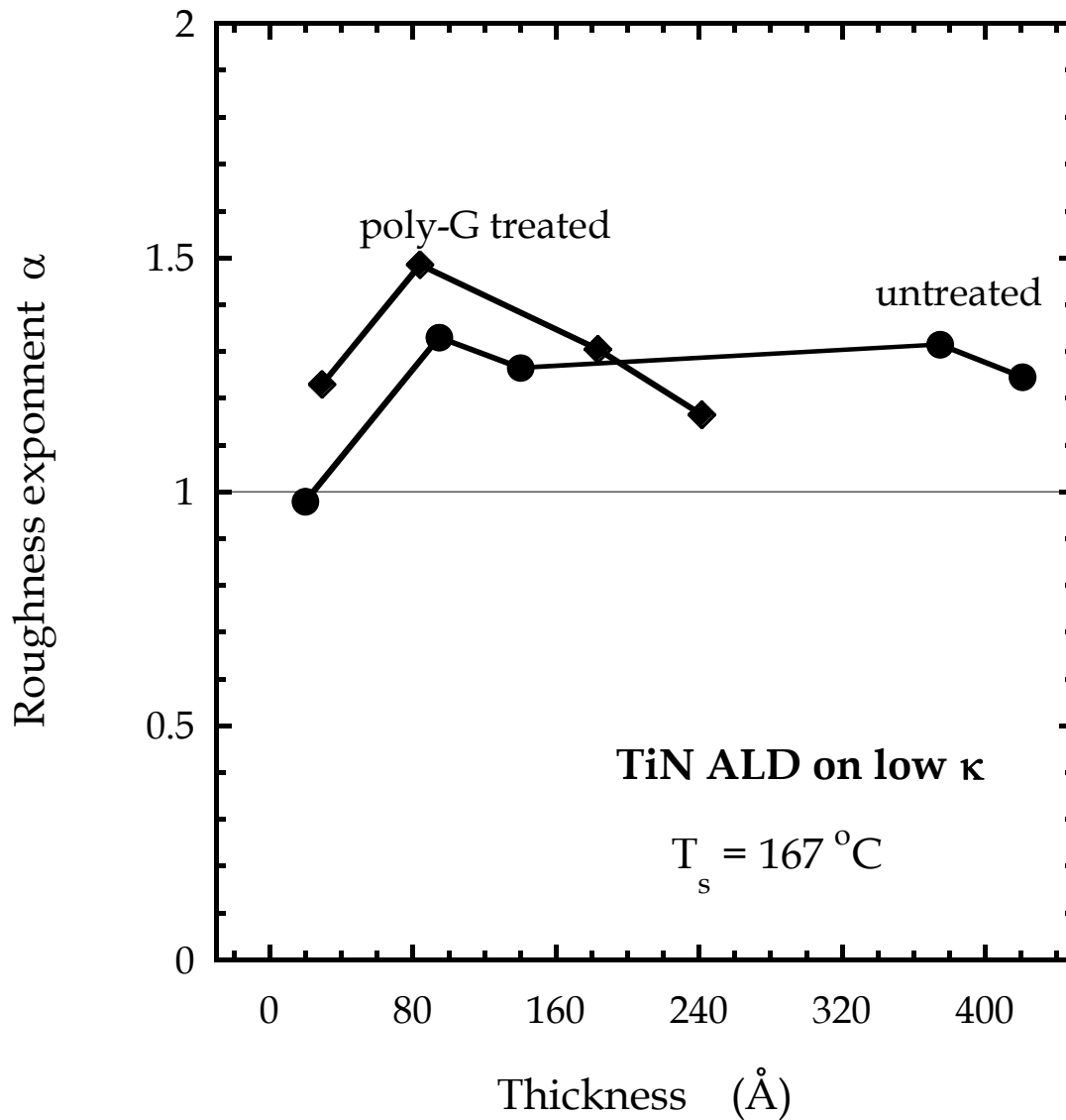


Figure 5-23: Roughness exponent α plotted as a function of TiN film thickness, for the untreated (circles) and 15 min poly-G treated (diamonds) low κ substrates ($T_s = 167^\circ\text{C}$). α is extracted from the slope of the self-affine portion of the 1DPSD spectrum.

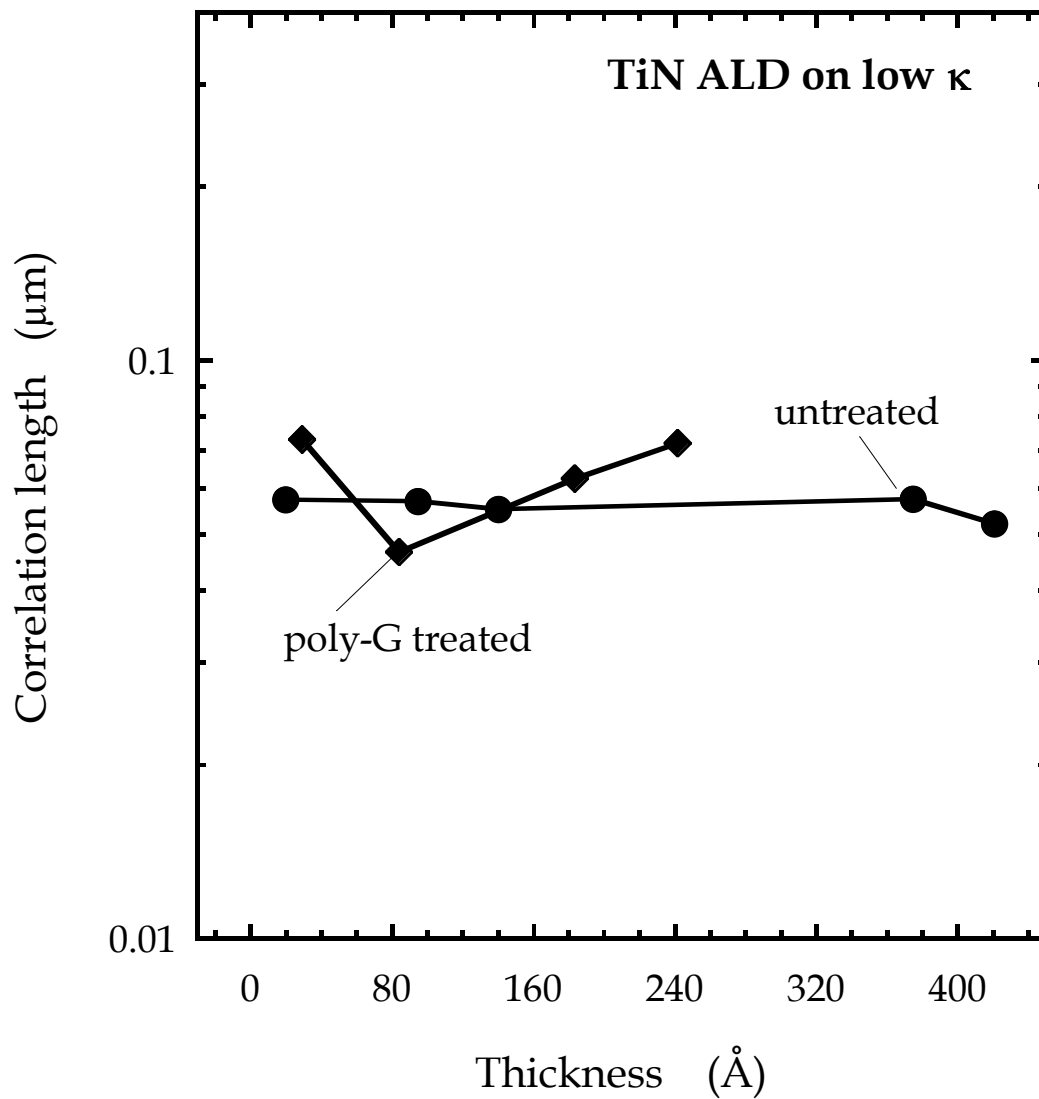


Figure 5-24: Correlation length ξ (in μm) as a function of TiN film thickness ($T_s = 167^\circ\text{C}$). ξ is obtained from the intersection of the self-affine region and the plateau region in the 1DPSD spectra for TiN films deposited on untreated (circles) and 15 min poly-G treated (diamonds) low κ substrates ($T_s = 167^\circ\text{C}$).

5.4 Conclusions

Modulated molecular beam sources have been employed to deposit TiN via ALD. The precursors were $\text{Ti}[\text{N}(\text{CH}_3)_2]_4$ and NH_3 , and all the depositions were carried out at the lower end of the ALD window: $T_s = 167$ °C. The substrates were hyperbranched polymeric (poly-G) films on SiO_2 and low κ dielectric substrates, both untreated and modified using a poly-G film. The organic surface modification was performed via anionic ring-opening polymerization of glycidol. The 15 min poly-G film on SiO_2 , which was the thinnest film studied, led to TiN films with the least roughness. For the 30 and 60 min films, the deposition results in TiN films which were islanded and extremely 3-D. This can be attributed to excessive ligand loss and hence stunted growth in case of the thicker poly-G films. STEM and HREELS data did not show conclusive evidence for an interfacial organic layer between TiN and the SiO_2 , post deposition. The results on untreated low κ surfaces were somewhat unexpected. The nucleation and subsequent growth was easier to attain than expected. This may be due to reactive groups inside the pores as well as surface functionalization by NH_3 during the ALD cycle. STEM results, however, show clear TiN penetration into the pores. To overcome the penetration problem, a 15 min poly-G film was deposited on plasma treated low κ substrate, and its viability as a potential pore sealing layer was studied. The deposition rate in this case was attenuated with respect to that on the untreated low κ substrate. Also the roughness vs. thickness data go through a maximum. The higher roughness during the initial growth phase could again be attributed to excessive ligand loss, and hence localized growth domains in the film. More importantly the preliminary STEM and HREELS data clearly demonstrate the complete

absence of penetration. In conclusion, it can be said that these surface modification techniques show early promise for pore sealing applications. Roughness is still an issue. Further investigations with organic layers having different structure, and possessing functional groups other than $-OH$, are currently underway.

5.5 References

1. International Technology Roadmap for Semiconductors, **2006**, (www.itrs.net).
2. Maex, K.; Baklanov, M. R.; Shamiryman, D.; Iacopi, F.; Brongersma, S. H.; Yanovitskaya, Y. S. *J. Appl. Phys.*, **2003**, *93*, 8793.
3. Mogilnikov, K. P.; Baklanov, M. R. *Electrochem. Solid-State Lett.* **2002**, *5*, F29.
4. Besling, W.; Satta, A.; Schuhmacher, J.; Abell, T.; Sutcliffe, V.; Hoyas, A. M.; Beyer, G.; Gravesteijn, D.; Maex, K. *Proceedings of the International Interconnect Technology Conference (IEEE)*, **2002**.
5. Lee, H. J.; Lin, E. K.; Wu, W. L.; Fanconi, B. M.; Lan, J. K.; Cheng, Y. L.; Liou, H. C.; Wang, Y.L.; Feng, M. S.; Chao, C. G. *J. Electrochem. Soc.* **2001**, *148*, F195.
6. Whelan, C. M.; Le, Q. T.; Cecchet, F.; Satta, A.; Pireaux, J. -J.; Rudolf, P.; Maex, K. *Electrochem. Solid-State Lett.* **2004**, *7*, F8.
7. Khan, M.; Huck, W. T. S. *Macromolecules* **2003**, *36*, 5088.
8. Von Werne, T.; Patten, T. E. *J. Am. Chem. Soc.* **1999**, *121*, 7409.
9. Jones, D. M.; Brown, A. A.; Huck, W. T. S. *Langmuir* **2002**, *18*, 1265.
10. Osborne, V. L.; Jones, D. M.; Huck, W. T. S. *Chem. Commun.* **2002**, *17*, 1838.

11. Berry, A.; Mowery, R.; Turner, N. H.; Seitzman, L.; Dunn, D.; Ladouceur, H. *Thin Solid Films* **1998**, *323*, 10.
12. *Handbook of Thin Film Materials, Vol. 1, Chap. 2.*; Ritala M., Leskelä, M.; ed. Nalwa H. S.; Academic Press: New York, **2002**.
13. Satta, A.; Beyer, G.; Maex, K.; Elers, K.; Haukka, S.; Vantomme, A. *Mat. Res. Soc. Symp. Proc.* **2000**, *612*, D6.5.1.
14. Ritala, M.; Asikainen, T.; Leskelä, M.; Jokinen, J.; Lappalainen, R.; Utriainen, M.; Niinistö, L.; Ristolainen, E. *Appl. Surf. Sci.* **1997**, *120*, 199.
15. Amato-Wierda, C.; Norton, E. T.; Wierda, D. A. *Electrochem. Solid-State Lett.* **1999**, *2*, 613.
16. (a) Kim, J. Y.; Choi, K. H.; Kim, Y. D.; Kim, Y.; Jeon, H. *Jpn. J. Appl. Phys.* **2003**, *42*, 4245; (b) Kim, H. Y.; Kim, J. Y.; Park, J. Y.; Kim, Y.; Kim, Y. D.; Jeon, H. *J. Kor. Phys. Soc.* **2002**, *41*, 739.
17. Elam, J. W.; Schuisky, M.; Ferguson, J. D.; George, S. M. *Thin Solid Films* **2003**, *436*, 145.
18. Schroeder, T. W.; Lam, A. M.; Ma, P. F.; Engstrom, J. R. *J. Vac. Sci. Technol. A* **2004**, *22*, 578.
19. M. Sharma et al., in preparation
20. Haran, M.; Engstrom, J. R.; Clancy, P. *J. Am. Chem. Soc.* **2006**, *128*, 836.
21. Ma, P. F.; Dube, A.; Killampalli, A.S.; Engstrom, J. R. *J. Chem. Phys.* **2006**, *125*, 034706.

22. *Practical Surface Analysis: Volume I, Auger and X-ray Photoelectron Spectroscopy*, 2nd ed.; Seah, M. P., Briggs, D., Eds.; John Wiley and Sons: Chichester, England, **1990**.
23. Ott, A. W.; Klaus, J. W.; Johnson, J. M.; George, S. M. *Thin Solid Films* **1997**, 292, 135.
24. Dolittle, L. R. *Nucl. Instrum. and Meth.* **1986**, 15, 227.
25. *Data Reduction and Error Analysis for the Physical Sciences*, 3rd ed.; Bevington, P. R., Robinson, D. K.; McGraw Hill: New York, **2002**.
26. Shamiryay, D.; Baklanov, M. R.; Maex, K. *J. Vac. Sci. Technol. B* **2003**, 21, 220.

6. Summary and future work

Inorganic-organic interfaces are playing an important role in a number of emerging technologies. A precise engineering of these interfaces will be a key in a number of areas e.g., molecular electronics, integration of porous low κ dielectrics in semiconductor manufacturing, and organic light emitting diodes. The techniques to fabricate these interfaces in a desired way are still in infancy.

The first set of experiments (described in chapter 3) dealt with the fabrication and characterization of these interfaces for molecular electronics applications. Aromatic thiophene self-assembled monolayers (SAMs) on polycrystalline Au, was the organic system chosen here. These molecules were designed to have extensive π conjugation along the back bone which will facilitate electron conduction along the molecular axis. The reaction of tetrakis(dimethylamido)titanium, $\text{Ti}[\text{N}(\text{CH}_3)_2]_4$, a TiN precursor, with *N*-isopropyl-*N*-[4-(thien-3-ylethynyl) phenyl] amine and *N*-isopropyl-*N*-(4-{[4-(thien-3-ylethynyl) phenyl]ethynyl}phenyl) amine SAMs, was studied. The structure of the SAMs themselves was also investigated. Both molecules form SAMs on polycrystalline Au bound by the thiophene group. The longer backbone molecule forms a denser SAM, with molecules characterized by a smaller tilt angle. X-ray photoelectron spectroscopy (XPS) and angle-resolved XPS were employed to examine the kinetics of adsorption, the spatial extent of reaction, and the stoichiometry of reaction. For both SAMs, adsorption was described well by first-order Langmuirian kinetics, and adsorption is self-limiting from $T_s = -50$ to 30 °C. The use of angle-resolved XPS clearly demonstrated that the $\text{Ti}[\text{N}(\text{CH}_3)_2]_4$ reacts exclusively with the iso-propylamine

end group via ligand exchange, and there was no penetration of the SAM, followed by reaction at the SAM-Au interface. Moreover, the SAM molecules remain bound to the Au surface via their thiophene functionalities. From XPS we it was concluded that, in both cases, approximately one $\text{Ti}[\text{N}(\text{CH}_3)_2]_4$ is adsorbed per two SAM molecules. Thus the approach of employing transition metal coordination complexes as initiators for inorganic-organic interface formation, is non invasive towards the structure of the organic layer itself. Further investigations are underway employing scanning tunneling microscopy (STM), which will aid in making more definitive conclusions concerning the structure of the reacted adlayers. It will also be used to probe the electrical characteristics of these interfaces.

Integration of carbon based porous low κ dielectrics into traditional semiconductor manufacturing is one of the biggest challenges for the microelectronics community. One of the more important steps in this process would be to deposit a smooth and conformal diffusion barrier on the low κ surface for preventing copper diffusion. Silane based self-assembled monolayers on SiO_2 have been used as model organic surfaces for studying the formation of these interfaces in chapter 4. The nucleation and growth during TiN ALD on SiO_2 and SiO_2 modified using interfacial organic layers in the form of SAMs, was investigated. The SAMs possess a range of functional groups, thickness, and microstructure. They were broadly grouped into two categories: reactive towards $\text{Ti}[\text{N}(\text{CH}_3)_2]_4$ (-OH, -NH₂), and unreactive (-CH₃, and -CF₃) Modulated molecular beams of $\text{Ti}[\text{N}(\text{CH}_3)_2]_4$ and NH_3 were used as reactants. Measurement of the growth rate as a function of T_s on chemical oxide, pointed to a narrow ALD window between $\sim 167 - 207$ °C. A more interesting observation was the attenuation of growth in case of all the SAMs.

For all the reactive SAMs, growth as a function of ALD cycles was non-linear and the deposited thickness per ALD cycle is suppressed by 50-70 % with respect to silicon dioxide irrespective of the termination and thickness. However, in case of the unreactive SAMs, attenuation was a strong function of the thickness of the SAM where the thickest TTS SAM was the most effective in impeding nucleation. XPS, RBS, and AFM were employed to further probe the nature of growth. The results seem to suggest a very non uniform and islanded growth pattern on the unreactive TTS SAM. The non uniformities were less pronounced in the case of the unreactive but thinner HMDS, probably due to a higher defect density which promotes quicker nucleation and hence growth. In case of SiO₂ and all the reactive SAMs the growth is much more uniform. AFM seems to suggest that the growth is pyramidal on TTS but within the limit of predictions by diffusion limited aggregation for all the other surfaces. HRSTEM results point to a highly conformal deposition process on the reactive SAMs. Taken as a whole, the results suggested significant and unexpected differences in growth patterns on SAMs in comparison to SiO₂. The attenuation in growth rate for the unreactive SAMs is not an entirely unexpected result due to defect mediated growth mechanism. However, in case of the reactive SAMs, it is possible that the SAM is mediating the growth of a TiN film which is different in nature to that growing on the SiO₂ surface. The growth of conformal films on the reactive SAMs is a promising result which could have applications in barrier layer deposition on porous low κ dielectrics.

The approach developed in chapter 4 was extended to a different organic system described in chapter 5. Hyperbranched polymeric (poly-G) films were prepared on SiO₂ as well as porous low κ dielectric substrates. The key motivation was to test the feasibility of this surface modification for pore sealing

applications. The organic surface modification was done via anionic ring-opening polymerization of glycidol on the surface for varying reaction times (15, 30 and 60 min) and leads to a high density of $-OH$ groups. Modulated molecular beam sources were again employed to deposit TiN via ALD. The precursors were $Ti[N(CH_3)_2]_4$ and NH_3 , and all the depositions were carried out at $T_s = 167^\circ C$. The 15 min poly-G film on SiO_2 , which was the thinnest organic film studied, led to TiN films with the least roughness. For the 30 and 60 min films the deposition results in TiN films which were islanded and extremely 3-dimensional. This behavior was attributed to excessive $-N(CH_3)_2$ ligand loss due to high $-OH$ density, and hence stunted growth in case of the thicker poly-G films. STEM and HREELS data did not show conclusive evidence for an interfacial organic layer between TiN and the SiO_2 , post deposition. The results on untreated low κ surface were somewhat unexpected. The nucleation and subsequent growth was easier to attain than expected. This could be attributed to reactive surface groups inside the pores as well as surface functionalization by NH_3 during the ALD cycle. STEM results however, show clear TiN penetration into the pores. To overcome the penetration problem, a 15 min poly-G film was deposited on plasma treated low κ substrate, and its viability as a potential pore sealing layer was studied. The deposition rate in this case was attenuated with respect to that on the untreated low κ . Also the roughness vs. thickness data (from AFM) goes through a maximum. The higher roughness during the initial growth phase could again be attributed to excessive ligand loss, and hence localized growth domains in the film. More importantly the preliminary STEM and HREELS data clearly demonstrate the complete absence of penetration. In conclusion, it can be said that these surface modification techniques show early promise for pore sealing applications.

Further investigations with organic layers possessing different structure and functional group, are currently underway.

Below is a list summarizing the results and their impact in the area of microelectronics research:

- For the first time, conjugated thiophene SAMs bearing reactive terminal functional groups have been prepared on polycrystalline Au substrates. The SAMs reacted with $\text{Ti}[\text{N}(\text{CH}_3)_2]_4$, a TiN precursor, in a manner desired for molecular electronics applications where the reaction was limited to the surface functional group. This approach has great merit, as the formation of the top contact was initiated without causing any structural changes to the organic layer itself. The same can not be said about the more conventional approaches making use of physical vapor deposition techniques, which lead to penetration and disruption of the organic monolayer itself.
- In the next set of experiments, TiN ALD was achieved on SiO_2 and SiO_2 modified using silane based SAMs possessing different functional terminations and microstructure. The results are significant as they represent the first ALD study carried out under ultra-high vacuum conditions using supersonic molecular beam techniques. An important conclusion was that the growth behavior is independent of the SAM thickness and the functional termination in case of the reactive functional groups. In case of the unreactive terminal groups, however, the growth pattern was a strong function of the SAM thickness with the growth being extremely islanded and three dimensional in the case of the thickest unreactive SAM examined. Thus from these results, it can be said that surface modification using SAMs is a multifarious technique

and can be used to either deposit smooth and conformal films or for preventing nucleation and hence be useful for patterning applications.

- Finally, surface modification using organic thin films deposited via hyperbranched polymerization has been employed to deposit thin and conformal TiN diffusion barrier films on porous low κ substrates. The results are significant as the surface modification technique is successful in preventing pore penetration by the TiN precursors. The untreated low κ substrates exhibit significant penetration which is an integration problem in semiconductor manufacturing. The low κ substrates treated with the polymeric film show no TiN penetration in the pores. In summary, the surface modification techniques developed here show early promise in solving the integration problems associated with porous low κ materials.

7. Appendices

7.1 Appendix A: Vapor pressure curve for $\text{Ti}[\text{N}(\text{CH}_3)_2]_4$

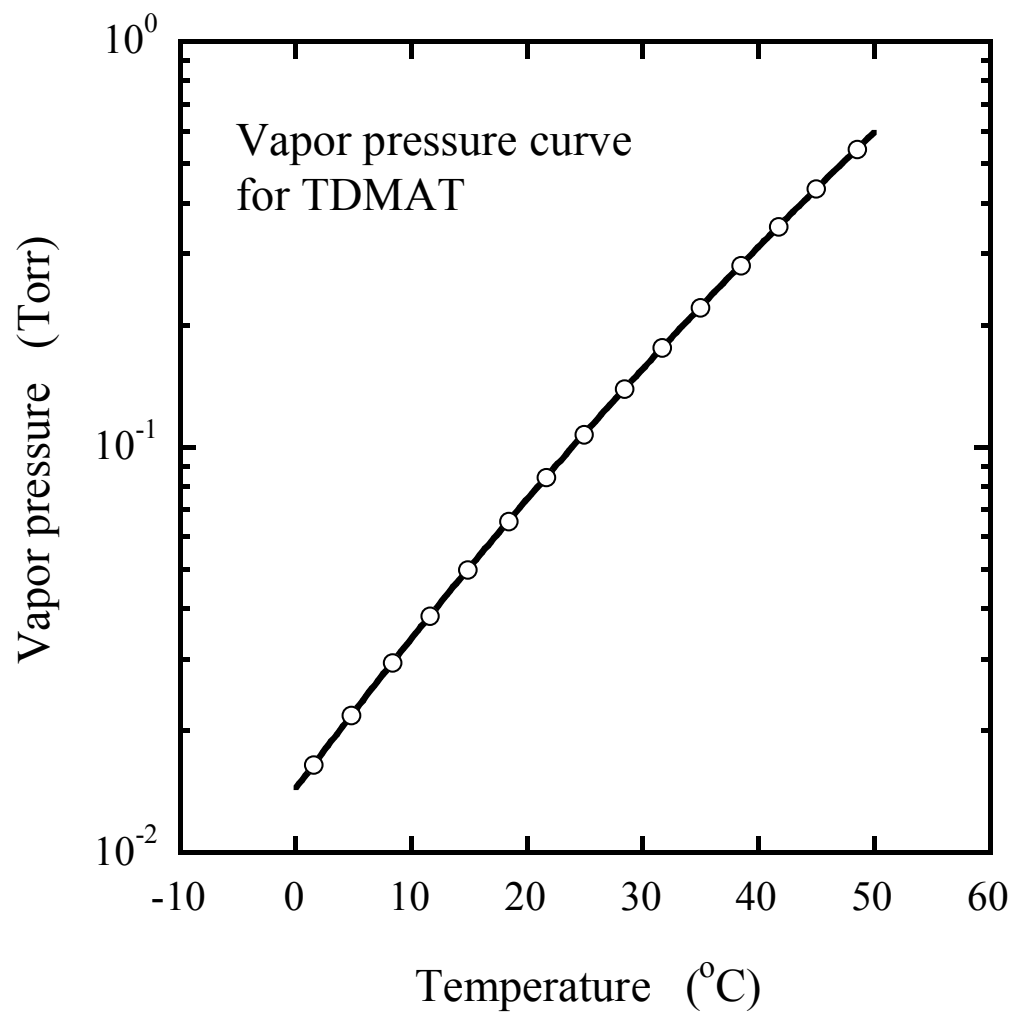


Figure 7-1: Vapor pressure curve for $\text{Ti}[\text{N}(\text{CH}_3)_2]_4$ (source: Schumacher)

7.2 Appendix B: ARXPS curve fitting results

Table 7-1: Parameters from fits to ARXPS data in chapter 3

SAM	Feature	State	$I(\theta_f = 0^\circ)$	I_0	d/λ
1P	Au(4f)	clean	22529± 629	36046± 646	0.47± 0.01
1P	Au(4f)	exposed to Ti[N(CH ₃) ₂] ₄	27263± 663	43187± 619	0.46± 0.01
1P	S(2p)	clean	174±226	944±688	1.69±0.57
1P	S(2p)	exposed to Ti[N(CH ₃) ₂] ₄	171±308	1023±1015	1.79±0.81
1P	C(1s)	clean	395±277	1445±478	0.32±0.14
1P	C(1s)	exposed to Ti[N(CH ₃) ₂] ₄	390±54	1137±71	0.42±0.04
1P	Ti(2p)	exposed to Ti[N(CH ₃) ₂] ₄	127±115	127±77	0.002±0.3
2P	Au(4f)	clean	19868± 926	32431± 863	0.49± 0.02
2P	Au(4f)	exposed to Ti[N(CH ₃) ₂] ₄	20949±1980	32204± 1756	0.43± 0.04
2P	S(2p)	clean	179± 259	1391±1106	2.05±0.65
2P	S(2p)	exposed to Ti[N(CH ₃) ₂] ₄	94± 125	326±247	1.24±0.57
2P	C(1s)	clean	577±125	1169±110	0.68±0.12
2P	C(1s)	exposed to Ti[N(CH ₃) ₂] ₄	554±28	887±18	0.98±0.05
2P	Ti(2p)	exposed to Ti[N(CH ₃) ₂] ₄	101±58	101±38	0.0±0.2
4-aminothiophenol	Au(4f)	clean	19380±1072	31634±1117	0.49±0.02
4-aminothiophenol	Au(4f)	exposed to Ti[N(CH ₃) ₂] ₄	23563±643	36955±639	0.45±0.01
4-aminothiophenol	S(2p)	clean	290±88	1063±185	1.30±0.13
4-aminothiophenol	S(2p)	exposed to Ti[N(CH ₃) ₂] ₄	288±230	1454±652	1.62±0.35
4-aminothiophenol	C(1s)	clean	628±84	1038±57	0.93±0.12
4-aminothiophenol	C(1s)	exposed to Ti[N(CH ₃) ₂] ₄	718±337	1948±413	0.46±0.15
4-aminothiophenol	Ti(2p)	exposed to Ti[N(CH ₃) ₂] ₄	84±24	94±17	0.11±0.10

7.3 Appendix C : RBS simulation methodology

7.3.1 Plotting the raw data

The raw data files usually have the .rbs extension. These files can be plotted directly using the PLOT command in RUMP. The executable file for installing the program can be downloaded free of charge from the URL www.genplot.com. Almost always the first plot will not be plotted for the whole region of interest in terms of energy range. In order to plot the data in the desired way the REGION command is used. For all the cases here the channel range was specified from 200 to 1200 to cover the energies ranging from ~ 0.5 to 1.5 MeV. The data is plotted again and an example of the output is given in Fig. 7-2.

7.3.2 Simulation

The PERT sub-routine has been utilized to create a simulation for all types of samples. The PERT subprogram is designed to work search for a "best" fit to the data. It does so by varying one or more parameters of the sample description or experimental parameters (thicknesses, compositions, equation parameters, MeV, etc.) and comparing the resulting theoretical spectrum with the actual spectrum. PERT iterates the process until it finds the best set of parameters to match the spectrum. The definition of "best" fit is the one which maximizes the Poisson likelihood function χ^2 between the experimental spectrum and the simulation over a selected region called the error window.

A normalization window using the PERT NORM command will have to be defined first. This should be in the substrate region where the simulation does not depend strongly on the parameters to be varied. An error window was selected using the PERT command WINDOW. The theory and the experiment will be compared within this window. The error window was chosen to be in the Ti peak region. Before running the simulation however, the sample structure has to be defined. In all cases it is a five layer stack (bottom to top): Si, SiO₂, SAM/organic layer, TiN, and TiO₂ (surface oxide). The first layer is defined using the OPEN command. This command has sub-commands COMPOSIT and THICKNESS which are used to fix the composition and thickness of the layer under consideration. It should be kept in mind that both of these quantities can be left as variables to make them fit parameters. However, for minimizing the number of parameters Si, SiO₂ and organic layer thickness was fixed to be the ellipsometric thickness and the composition for the organic layer was fixed as what was determined from XPS. The TiN layer was modeled as bulk TiN and surface TiO₂ due to the air break between deposition and analysis. In case of the TiN and TiO₂ layers the composition was again fixed and the thickness was left as a variable. The reported RBS thickness is the combined TiO₂ and TiN thickness. No attempt has been made to simulate the amount of C in the film because of the noise in the data. Every time a new layer has to be defined the OPEN command is used. Once the stack has been completely defined the individual layer properties can be changed by using the LAYER command. Once the simulation is complete it will output the optimized thickness values along with the mean squared error. The simulation results can be plotted by using the PLOT command. It must be remembered that the simulation data is in the active buffer once it is complete. To plot it with the raw data use the PLOT

1 command and then the overlay OVER O command. The output of such a simulation is plotted as the smooth curve in Fig. 7-2.

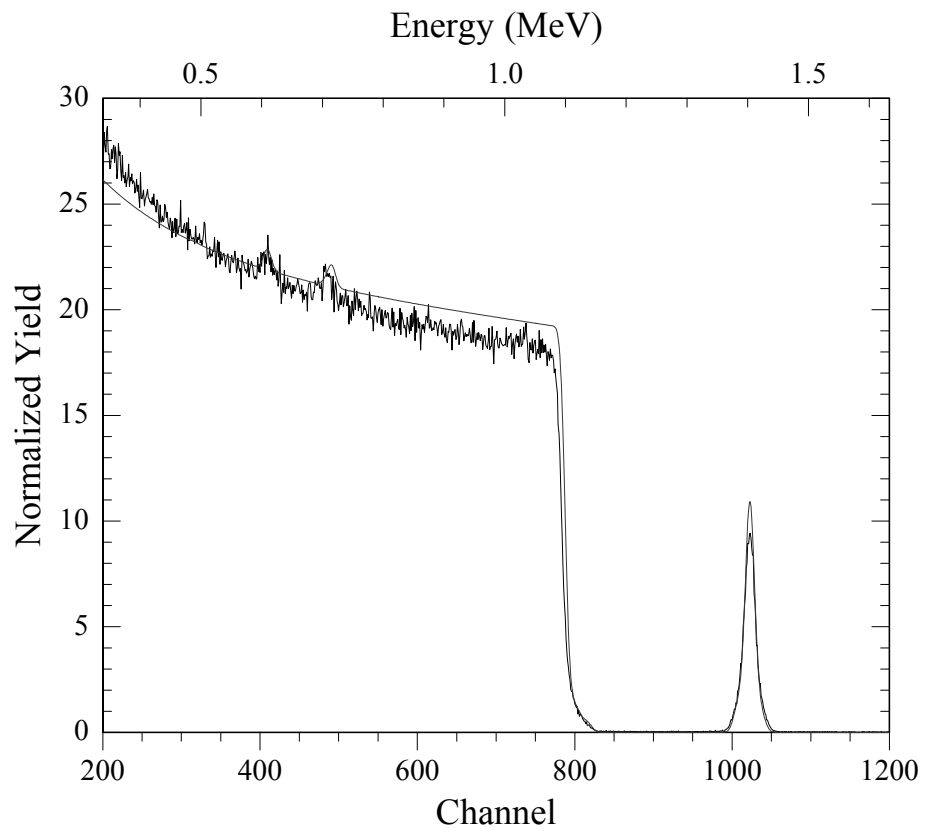


Figure 7-2: Example RB spectrum and simulation carried out with RUMP